Characterization and modeling of premixed turbulent n-heptane flames in the thin reaction zone regime

Thesis by

Bruno Savard

In Partial Fulfillment of the Requirements

for the Degree of

Doctor of Philosophy

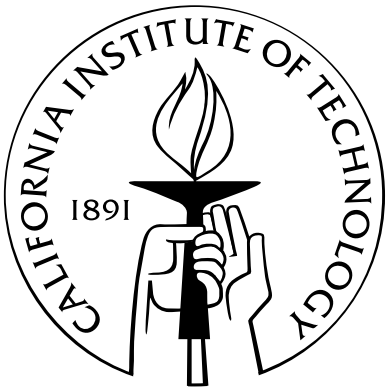

California Institute of Technology

Pasadena, California

2015

(Defended May 12, 2015)

Acknowledgments

I gratefully acknowledge funding from the Air Force Office of Scientific Research (Award FA9550-12-1-0144) under the supervision of Dr. Chiping Li, and from the Natural Sciences and Engineering Research Council of Canada (NSERC Postgraduate Scholarship D). This research used resources of the National Energy Research Scientific Computing Center, which is supported by the Office of Science of the U.S. Department of Energy under Contract No. DE-AC02-05CH11231.

I would also like to thank Dr. Andy Aspden, who kindly shared with our group the DNS data presented in Aspden *et al.* J. Fluid Mech. 680 (2011) 287-320 (used in Chapers 5 and 6).

Finally, I would particularly like to thank my advisor, Prof. Blanquart, for his continuous support and his motivation for this research project; the committee members, Prof. McKeon, Prof. Colonius, and Prof. Shepherd, for their valuable comments and suggestions to improve the quality of this work; and finally, (Prof.) Yuan Xuan, Brock Bobbitt, Simon Lapointe, and Nicholas Burali, my (ex-)office mates who have contributed to parts of this work.

Abstract

n-heptane/air premixed turbulent flames in the high-Karlovitz portion of the thin reaction zone regime are characterized and modeled in this thesis using Direct Numerical Simulations (DNS) with detailed chemistry. In order to perform these simulations, a time-integration scheme that can efficiently handle the stiffness of the equations solved is developed first. A first simulation with unity Lewis number is considered in order to assess the effect of turbulence on the flame in the absence of differential diffusion. A second simulation with non-unity Lewis numbers is considered to study how turbulence affects differential diffusion. In the absence of differential diffusion, minimal departure from the 1D unstretched flame structure (species *vs.* temperature profiles) is observed. In the non-unity Lewis number case, the flame structure lies between that of 1D unstretched flames with "laminar" non-unity Lewis numbers and unity Lewis number. This is attributed to effective Lewis numbers resulting from intense turbulent mixing and a first model is proposed. The reaction zone is shown to be thin for both flames, although large chemical source term fluctuations are observed. The fuel consumption rate is found to be only weakly correlated with stretch, although local extinctions in the non-unity Lewis number case are well correlated with curvature. All these results explain the apparent turbulent flame speeds. Other variables that better correlate with this fuel burning rate are identified through a coordinate transformation. It is shown that the unity Lewis number turbulent flames can be accurately described by a set of 1D (in progress variable space) flamelet equations parameterized by the dissipation rate of the progress variable. In the non-unity Lewis number flames, the flamelet equations suggest a dependence on a second parameter, the diffusion of the progress variable. A new tabulation approach is proposed for the simulation of such flames with these dimensionally-reduced manifolds.

Contents

List of Figures

List of Tables

Chapter 1

Introduction

1.1 Background

While considerable worldwide efforts have been made towards the development of sustainable energy sources, the U.S. Energy Information Administration projects that in 2040, more than 90 % of the world's energy consumption in the transportation sector (and more than 30 % of the world's total energy consumption) will still come from petroleum and other liquid fuels[1]. Liquid fuels remain ideal for transportation because of their high energy density, as illustrated in Fig. 1.1. This is a consequence of the large hydrocarbon species these fuels contain. Unfortunately, the combustion products of such fuels can include pollutants such as NO_x and soot.

In an effort to reduce the emission of these pollutants, most combustion devices recently developed rely on the combustion of premixed fuel/air mixtures. As opposed to non-premixed flames, in which the fuel and the oxidizer react at a local stoichiometric equivalence ratio, premixed fuel/air mixtures can be set to a low equivalence ratio (lean mixture), *i.e.* the oxidizer is in a higher relative concentration compared to stoichiometry. With lean mixtures, the burnt temperature is reduced, which results in a reduction of the NO_x concentration, and no soot is produced, as these particles are only produced under rich conditions (higher relative concentration of fuel).

The success of many of these combustion devices (in jet engines, gasoline internal combustion (IC) engines, and some homogeneous compression charge ignition (HCCI)-like engines) relies on the

[1] From the Annual Energy Outlook 2015 report (can be found at URL: http://www.eia.gov/forecasts/aeo/index.cfm/).

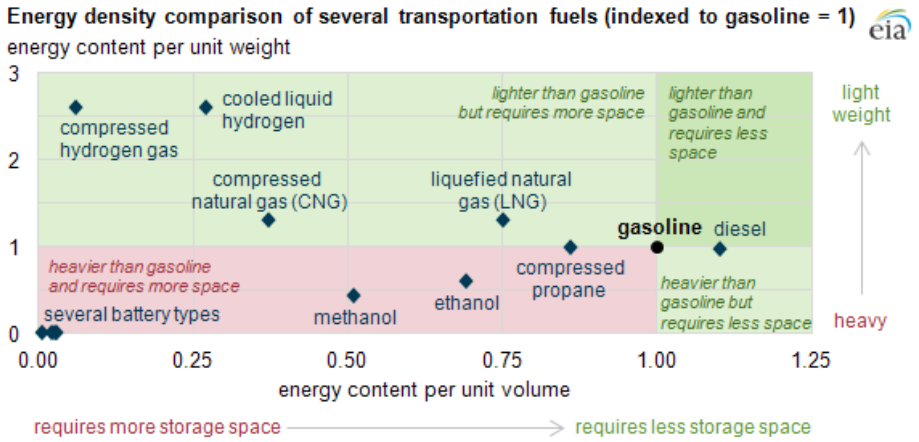

Figure 1.1: Energy density comparison of several transportation fuels (indexed to gasoline = 1). Figure taken from the U.S. Energy Information Administration official website (URL: http://www.eia.gov/todayinenergy/detail.cfm?id=14451).

presence of highly turbulent premixed flames. Turbulence enhances the flame propagation speed, which allows for a larger fuel mass flow rate in a jet engine or for larger rotation speed in IC engines. This results in an increased power output. In military applications, scramjets often use a cavity flame holder on which a turbulent premixed flame is anchored. Their performance is also affected by the turbulent flame speed.

The development process of such combustion devices relies on numerical simulation as an increasingly important tool. However, state-of-the-art numerical tools used in the industry rely on models validated at much lower turbulence intensities and with simple fuels (*e.g.* methane). The extent to which these models are adequate for highly turbulent premixed flames with large hydrocarbon fuels remains an open question.

1.2 Turbulent premixed combustion

Combustion is characterized by the following schematic reaction:

$$\text{fuel} + \text{oxidizer} \rightarrow \text{products} + \text{heat} \tag{1.1}$$

In most practical applications of combustion, the oxidizer is the oxygen contained in air. A flame can be seen as a region (in a flow field) of self-sustained combustion. Premixed flames are flames in which the reactants are mixed prior to reacting. They are characterized by a flame speed (speed at which the flame front moves with respect to the unburnt gas) and a flame thickness. Besides the nature of the fuel and the oxidizer, premixed flames are characterized by the following conditions in the unburnt side: the temperature, the pressure, and the equivalence ratio. A unity equivalence ratio corresponds to a stoichiometric mixture. If it is larger than unity, the mixture is rich, *i.e.* the oxidizer is the limiting reactant. Inversely, if the equivalence ratio is less than unity, the mixture is lean, and the fuel is the limiting reactant. A brief description of turbulent premixed combustion is provided below. Accent is put on concepts relevant to the present thesis.

1.2.1 Laminar premixed flames

For laminar flames, the flame speed is denoted S_L and the flame thickness can be defined as

$$l_F = \frac{T_b - T_u}{|\nabla T|_{\max}}, \tag{1.2}$$

with T_b the temperature in the burnt gas, T_u the temperature in the unburnt gas, and $|\nabla T|_{\max}$ the maximum temperature gradient in the flame. Figure 1.2 is representative of a large hydrocarbon one-dimensional laminar premixed flame. Representation in both physical space and temperature space is provided. The flame corresponds to a *n*-heptane/air flame with equivalence ratio of 0.9, unburnt temperature of 298 K, and unburnt pressure of 1 atm. Y_F is the fuel mass fraction and $\dot{\omega}_F$ is its chemical consumption rate, while T is the temperature and $\dot{\omega}_T$ is its chemical production rate (heat release rate). Three regions can be identified: the preheat zone, where no reaction occurs (only diffusion and convection), the reaction zone, where the fuel is burnt and most of the heat is released, and the oxidation layer, where slow oxidation reactions take place to form the products (conversion of CO to CO_2).

Representing the flame structure in temperature space is particularly useful to highlight the

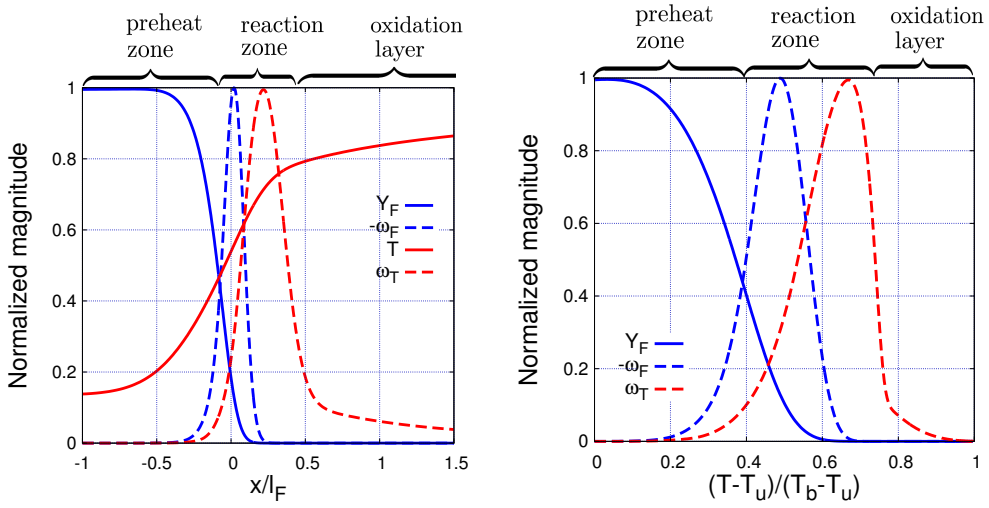

(a) physical space

(b) temperature space

Figure 1.2: Representation of a n-heptane/air flame (equivalence ratio of 0.9, unburnt temperature of 298 K, and unburnt pressure of 1 atm) in physical space and in temperature space. Y_F is the fuel mass fraction and $\dot{\omega}_F$ is its chemical consumption rate, while T is the temperature and $\dot{\omega}_T$ is its chemical production rate (heat release rate). Each quantity is normalized by its respective maximum value in the flame.

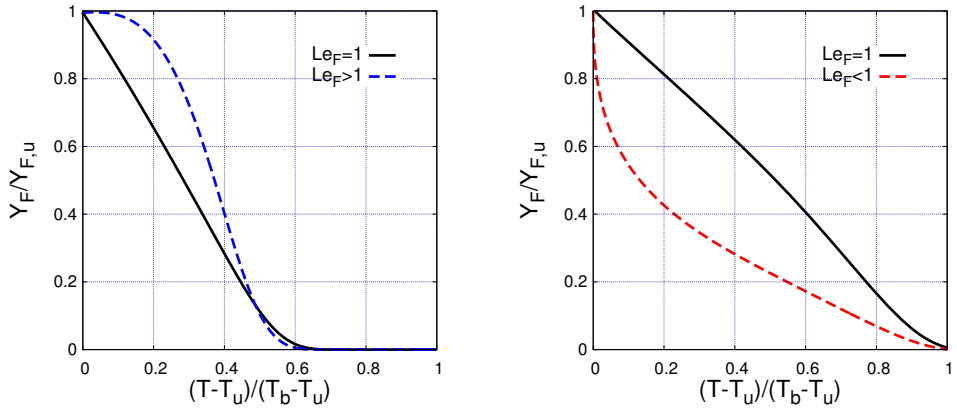

(a) n-heptane/air

(b) hydrogen/air

Figure 1.3: Normalized fuel species mass fraction *vs.* temperature profiles with non-unity Lewis numbers and unity Lewis numbers (for all species), for a n-heptane/air flame (same as in Fig. 1.2) and a hydrogen/air flame (equivalence ratio of 0.4, unburnt temperature of 298 K, and unburnt pressure of 1 atm).

effects of differential diffusion. Differential diffusion is characterized by non-unity Lewis numbers Le_i (one Lewis number for each species i), which are the ratios of the thermal diffusivity α to the species mass diffusivities D_i. Figure 1.3 shows typical fuel mass fraction *vs* temperature profiles for

fuels with different Lewis numbers. Differential diffusion is an important aspect of premixed flames. First, it has a considerable impact on the laminar flame speed. For the two flames considered (Fig. 1.4), S_L changes from 29 cm/s to 36 cm/s for *n*-heptane and from 45 cm/s to 22 cm/s for hydrogen, respectively between unity and non-unity Lewis numbers. Second, lean premixed flames with less than unity fuel Lewis numbers are thermodiffusively unstable, whereas lean premixed flames with greater than unity fuel Lewis numbers are thermodiffusively stable (for rich flames, the Lewis number of the oxidizer controls the stability). Thermodiffusively unstable laminar flames do not maintain a planar shape: cells and cusps are formed. This strongly affects the propagation speed and regions of local extinctions can be created. More details can be found in Ref. [113, 133, 114, 4, 53]. Finally, the response of flames to stretch (strain rate or curvature) is largely affected by differential diffusion (more details in Section 1.6).

Another aspect of premixed flames which will be particularly relevant to turbulence, is the evolution of the thermodynamic properties through the flame. Since the temperature and the composition of the species in the gas evolve through the flame, the thermodynamic properties are not constant, as illustrated in Fig 1.4.

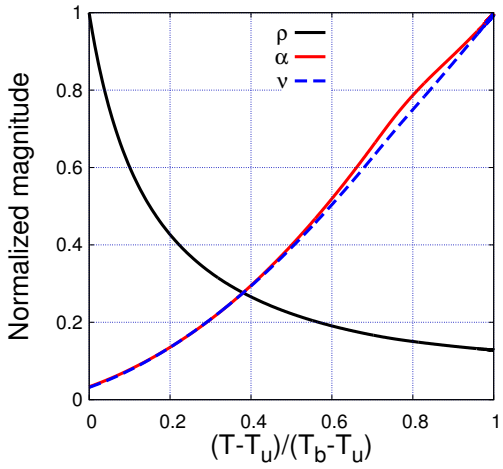

Figure 1.4: Normalized thermodynamic properties *vs.* temperature profiles for the *n*-heptane/air flame (same as in Fig. 1.2). ρ is the density and ν is the kinematic viscosity.

Note that for the purpose of this thesis, a "flamelet" will be defined as a one-dimensional unstretched flame.

1.2.2 Turbulence

As mentioned in Section 1.1, flames in practical combustion devices are always subject to a turbulent flow, which allows for an increase in the turbulent flame speed and consequently, a larger energy conversion rate, or a smaller engine. For the purpose of this thesis, only a brief description of turbulent quantities is provided. More details can be found in Ref. [178, 152].

Turbulence can be seen as a random collection of coherent structures, often called eddies. The largest turbulent length scale is called the integral length scale l. It is associated with the rms velocity fluctuations u' and the eddy turnover time

$$\tau = \frac{l}{u'}. \tag{1.3}$$

The Turbulent Kinetic Energy (TKE) is defined as

$$k = \frac{3}{2}u'^2. \tag{1.4}$$

The smallest scale, the Kolmogorov length scale η, is the scale at which the kinetic energy is converted into heat, through viscous dissipation. The length scale η is related to the dissipation rate and the kinematic viscosity ν as

$$\eta = \left(\frac{\nu^3}{\epsilon}\right)^{1/4}. \tag{1.5}$$

This dissipation rate is related to the largest scales by

$$\epsilon = \frac{u'^3}{l}. \tag{1.6}$$

The velocity associated with the Kolmogorov length scale is

$$v_\eta = (\nu\epsilon)^{1/4} \tag{1.7}$$

and the associated time scale is

$$\tau_\eta = \left(\frac{\nu}{\epsilon}\right)^{1/2}. \tag{1.8}$$

The ratio between the largest and the smallest scales is related to the turbulent Reynolds number Re_T as

$$\frac{l}{\eta} = Re_T^{3/4}, \tag{1.9}$$

with

$$Re_T = \frac{u'l}{\nu}. \tag{1.10}$$

1.2.3 Regimes of turbulent premixed flames

Turbulent premixed flames are typically characterized by the extent to which turbulence is "expected" to penetrate/disrupt the flame. The Karlovitz number

$$Ka = \frac{\tau_F}{\tau_\eta}, \tag{1.11}$$

which is the ratio of the flame time scale $\tau_F = l_F/S_L$ to the Kolmogorov time scale, provides such information [142]. The larger the Karlovitz number, the more turbulence is expected to penetrate/disrupt the flame. In order to push the characterization further, several regime diagrams have been proposed in the literature [20, 137, 1, 150]. Amongst them, Peters' regime diagram [142] is one of the most widely used (Fig. 1.5). A brief description similar to the one found in Ref. [142] is provided in this section.

For scaling purposes, it is assumed for the rest of this section only that the viscosity and the thermal diffusivity are equal, *i.e.* $\nu = \alpha$ (unity Schmidt number), and the laminar flame thickness is equal to the ratio of the thermal diffusivity and the laminar flame speed, *i.e.* $l_F = \alpha/S_L$. With these assumptions, the turbulent Reynolds number can be written as

$$Re_T = \frac{u'l}{S_L l_F}, \tag{1.12}$$

and the Karlovitz number simplifies to

$$Ka = \frac{l_F^2}{\eta^2}. \tag{1.13}$$

An additional Karlovitz number that is argued to be more appropriate for the reaction zone is defined as

$$Ka_\delta = \frac{\delta^2}{\eta^2} = \left(\frac{\delta}{l_F}\right)^2 Ka, \tag{1.14}$$

with δ the laminar reaction zone thickness. Using Eq. 1.9, the ratio u'/S_L can be related to the ratio l/l_F through the turbulent Reynolds number or the Karlovitz number

$$\begin{aligned} \frac{u'}{S_L} &= Re_T \left(\frac{l}{l_F}\right)^{-1} \\ &= Ka^{-2/3} \left(\frac{l}{l_F}\right)^{1/3}. \end{aligned} \tag{1.15}$$

Using Eq. 1.15, boundaries delimiting different regimes can be drawn in the regime diagram (Fig. 1.5). First, setting $Re_T = 1$ separates laminar flames from turbulent flames. Second, the limit of $Ka = 1$, known as the Klimov-William criterion, delimitates the thin reaction zone regime from the corrugated flamelet regime. In the thin reaction zone regime, turbulent eddies are smaller than the flame thickness and are expected to thicken the preheat zone through turbulent mixing. In the corrugated flamelet regime, eddies are too large to penetrate the flame, but are sufficiently intense to significantly corrugate the flame front. For fluctuating velocities smaller than the laminar flame speed, $u'/S_L < 1$, the flame is said to be wrinkled (as opposed to be corrugated), hence the wrinkled flamelet regime. Finally, the limit of $Ka_\delta = 1$ separates the broken/distributed reaction zone regime from the thin reaction zone regime. For $Ka_\delta > 1$, the smallest eddies are sufficiently small to penetrate the reaction zone and are expected to thicken it (distributed reaction zone) or disrupt it (broken reaction zone). δ is often assumed to be ten times smaller than l_F (for scaling purposes) and hence the $Ka_\delta = 1$ line corresponds to $Ka = 100$.

The wrinkled and the corrugated flamelet regimes have been widely studied (theoretically, experimentally, and numerically) [113, 114, 133, 4, 53]. The thin reaction zone has been explored in

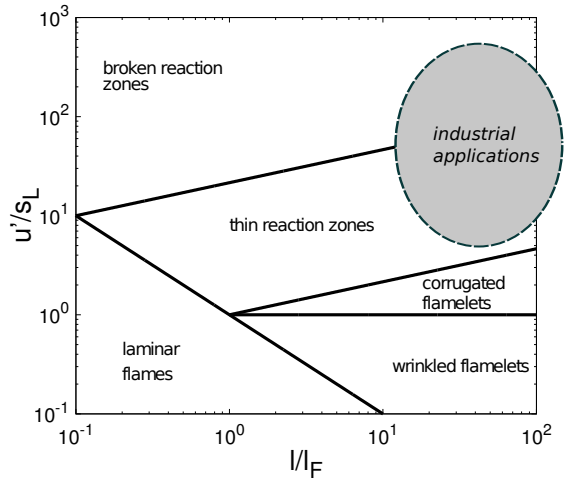

Figure 1.5: Regime diagram for turbulent premixed combustion as suggested by Peters [142]. The approximate location in this regime of turbulent premixed flames relevant to industrial applications has been added.

several studies, but most of them focused on the lower-Ka part of the regime (due to the experimental challenges and the computational cost at higher Ka) [38, 78, 160, 176, 70, 11]. The higher-Ka part of the reaction zone regime and the transition to the broken/distributed reaction zone regime have been investigated in a only a few studies [10, 9].

Most practical applications fall in the thin reaction zone regime or at the transition between the thin and broken/distributed reaction zone regimes, as shown in Fig. 1.5. Some military applications fall even further up in the broken/distributed reaction zone regime [153].

It is important to note that the regime diagram is based on scaling arguments. For instance, it does not account for any potential effect of differential diffusion, or the nature of the fuel. In addition, it does not account for the changes in thermodynamic properties through the flame (Fig 1.4).

1.3 Direct numerical simulation of high Karlovitz premixed turbulent flames

As industrial applications of turbulent premixed (and partially premixed) flames fall in the thin/broken reaction zone regimes, understanding how a flame behaves in these regimes is critical [148]. Experi-

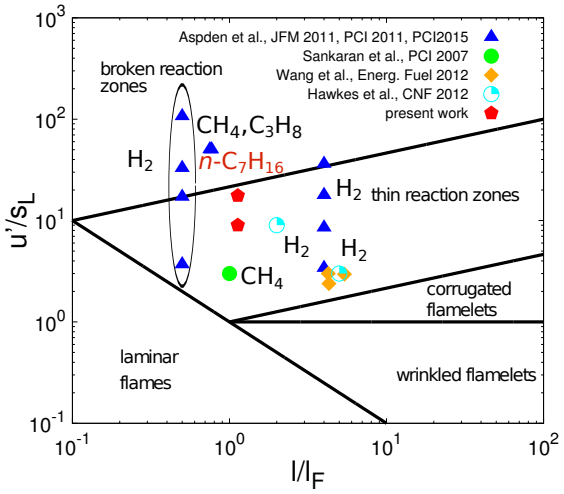

Figure 1.6: DNS of high Karlovitz turbulent premixed flames with finite-rate chemistry.

ments are difficult to conduct at high Karlovitz numbers and a limited number of them are available in the literature [38, 78]. Equivalently, due to their expensive computational costs (more details in the next section), very few Direct Numerical Simulations (DNS) of turbulent premixed flames in the broken reaction zone or the thin reaction zone regimes have been performed [10, 9, 160, 176, 70, 11]. Figure 1.6 presents all of these simulations (to the best of the authors' knowledge) in the context of the regime diagram (as proposed by Peters [142]). Note that only simulations performed with detailed finite-rate chemistry are presented (an additional study in the context of astrophysics can be found in Ref. [8]).

The only fuels that have been considered in previous simulations are hydrogen [10, 176], methane [9, 160], and propane [9]. While these fuels are used in several ground-based applications [41], most of the fuels used for transportation contain larger hydrocarbons [44, 117]. Since their chemical pathways are far more complex, and a wide range of stable species are present through the flame front, it remains unclear how turbulence influences their chemistry at high Karlovitz number.

Moreover, heavy hydrocarbons have large Lewis numbers (*e.g.* $Le_{\mathrm{C_{12}H_{26}}} \approx 3.5$). It has also been observed that for sufficiently high Karlovitz number differential diffusion effects were negligible for both H_2 ($Le_{\mathrm{H_2}} \approx 0.3$) and C_3H_8 ($Le_{\mathrm{C_3H_8}} \approx 2$) [9]. However, this similar behavior between smaller and larger than unity Lewis number fuels cannot be generalized to intermediate Karlovitz numbers

as pertinent to the transition between the thin/broken reaction zone regimes. Furthermore, while the series of lean H_2/air premixed flames performed by Aspden *et al.* [10] have provided information on how turbulence affects differential diffusion over a wide range of Karlovitz numbers, there is no such information available for heavy hydrocarbon fuels.

To tackle these questions, a series of DNS of a premixed n-C_7H_{16} turbulent flames in the thin reaction zone regime and close to the transition between the thin/broken reaction zones regimes are targetted in this thesis. n-C_7H_{16} is chosen for the fuel because it is used in surrogates for gasoline [46, 117]. In addition, it corresponds to a step towards the simulation of n-decane or n-dodecane flames (larger chemical mechanism), which species are often used in surrogates for kerosene [129, 47].

Two sets of simulations at different Karlovitz numbers are targetted. For each of these sets (higher-Ka and lower-Ka), a first simulation with unity Lewis number is considered in order to assess the effect of turbulence on the flame in the absence of differential diffusion. A second simulation with non-unity Lewis numbers (amongst which $Le_{C_7H_{16}} = 2.8$) is considered to study how turbulence affects differential diffusion.

More specifically, the following two aspects need to be characterized with these target flames:

1. the effect of turbulence on the flame structure and the impact of turbulent mixing on differential diffusion (more details in Section 1.5),

2. the effect of turbulence on the reaction zone with and without differential diffusion (more details in Section 1.6).

Modeling these effects for larger scale simulations corresponds to the subsequent challenge (more details in Section 1.7).

Before the characterization and the modeling can be achieved, the DNS need to be performed within reasonable computational time. As detailed in the next section, the time-integration of chemically reacting flows is particularly expensive because of the stiffness of the equations solved. A wide range of methods have been developed over the past few decades to overcome this issue. However, most of these methods are not optimal for the simulation of highly turbulent flames. A

detailed discussion follows.

1.4 Time-integration for stiff chemistry

Simulations of reacting flow systems using detailed finite-rate chemistry are extremely challenging [164]. The expensive nature of the chemical source terms integration comes from four main challenges: 1) their high non-linearity in the Arrhenius form of the chemical reaction rate constants (*i.e.* high computational cost for each function evaluation) [16], 2) the typically large number of species involved, 3) the strong coupling between chemistry and transport processes (convection and diffusion) [128], and 4) their very large magnitude (or equivalently small timescales) [112, 85]. As a result of all these challenges, detailed chemical mechanisms including a large number of species (above 50) and reactions (above 200) have been included in the numerical simulations of reacting flows only for relatively simple geometries (*e.g.* homogeneous or stratified reactors and statistically one-dimensional flames) [186, 135, 187, 15, 182, 9]. The number of species (and number of reactions) included in the numerical simulations of two-dimensional and three-dimensional turbulent flames has been relatively limited [17, 105, 104, 37, 9, 10]. Most of these simulations have been focused on investigating the combustion of relatively simple fuels (*e.g.* hydrogen, methane, and ethylene). Beside the work presented in this thesis, only one study has considered a turbulent flame with large hydrocarbon fuels (propane) [9] due to the large inherent simulation cost. In order to perform numerical simulations with *detailed* chemical kinetics, robust, accurate, and efficient numerical algorithms are needed for solving the coupled, highly non-linear, multi-dimensional, Partial Differential Equations (PDE) governing the unsteady evolution of these complex reacting systems. There exist various methods to improve the efficiency of chemical source term integration in reacting flow problems. These are reviewed in the following paragraphs and are organized according to the challenges mentioned above.

First, the computational cost associated with the evaluation of exponential functions in the chemical source terms (challenge #1 mentioned above) can be reduced by using single precision calculations, or by tabulating the exponential functions [124]. However, the associated efficiency gain

is not significant and the loss of accuracy might be problematic given the large range of timescales in a reacting flow simulation. Alternatively, the non-linear chemical source terms may be expanded using some type of low-order expansion [49, 156, 130]. However, it has been shown that these methods may be subject to severe time step size restrictions and stability issues when applied to combustion simulations [49], since they do not fully account for the non-linearity of the system [156].

Second, regardless of the chosen time-integration scheme, the cost of the chemical models could be alleviated by reducing the total number of species (challenge #2 mentioned above). This can be accomplished using Quasi-Steady-State (QSS) assumptions and Partial-Equilibrium (PE) approximations [107, 110], or more advanced methods such as Directed Relation Graph (DRG) [106] and DRG with Error Propagation (DRGEP) [134] before being applied to the simulation [110, 139]. Even with these techniques, it has been pointed out in previous work that the size of reduced mechanisms for practical hydrocarbon fuel surrogates is still too large to be used directly in Direct Numerical Simulations (DNS) with finite-rate chemistry [66]. Alternative chemistry reduction techniques based on separation of chemical timescales could be applied. Such techniques include the Computational Singular Perturbation (CSP) method [102] and the Intrinsic Low Dimensional Manifold (ILDM) [112] method. However, these methods require significant computational efforts to conduct chemical Jacobian decomposition and mode separation [66], which makes them not suited for the DNS of multi-dimensional reacting flows.

Third, to avoid the cost associated with the coupled reactive-transport system (challenge #3 mentioned above), most numerical frameworks rely on some variant of splitting techniques (*e.g.* Godunov [12] or Strang [166] splitting) followed by the chemical source term integration in a zero-dimensional setting. These techniques have been widely applied in the numerical simulations of turbulent reacting flows, for instance in the code developed at Lawrence Berkeley National Laboratory [52, 3]. The lagging errors introduced by the operator splitting treatment are unimportant for steady-state configurations, but may be substantial in some circumstances, for instance in the proximity of unsteady premixed flame fronts [128, 95], and become more severe when running with larger time step sizes. The effects of these errors have been the subject of many previous stud-

ies [95, 190, 189, 93, 90], and have been found to be case-dependent. Note that, with the application of these techniques, the resulting Ordinary Differential Equations (ODE) associated with the chemistry (instead of the coupled PDEs) remain stiff. To alleviate the high computational overhead associated with the integration of these stiff ODEs, methods relying on implicit numerical schemes based on Backward-Differentiation Formulas (BDF) have been developed [159, 158] and implemented in packages such as VODE [25] and DASSL [143, 23]. These packages integrate stiff chemical kinetics using BDFs with a modified iterative Newton procedure [143, 23, 155, 161], and have been widely adopted in numerical simulations of chemically reacting flows [128, 95, 190]. Despite the significant computational efficiency gain brought by the stiff chemistry integration techniques discussed above, it is important to recall that these techniques are designed for time-dependent ODE systems (and not PDE), which arise from the application of time-splitting techniques to separate the reactive (chemical kinetic) part of the PDE system (species transport equations) from the convective-diffusive part [6].

Forth, time-integration techniques designed for the coupled PDEs governing the unsteady evolution of complex reacting systems are discussed in the following. First and foremost, species chemical source terms can be integrated explicitly. For instance, an explicit time-integration scheme, along with QSS assumptions, is used in S3D [72], a massively parallel DNS solver developed at Sandia National Laboratories for the simulations of compressible, turbulent reacting flows. This code has been applied to the simulation of turbulent flames with relatively simple fuels, for instance hydrogen [121, 103], methane [160], and ethylene [188]. Heavier fuels have been considered in ignition simulations of HCCI-like systems (*e.g.* *n*-heptane [186], iso-octane [187], and ethanol [15]). The application of explicit time-integration methods are commonly limited by prohibitively small time step sizes to resolve the smallest chemical timescales present in the system (challenge #4) [66, 25]. This is the reason why the S3D code relies on "stiffness removal" techniques such as QSSA [107, 160, 110]. On the other hand, implicit time-integration methods generally yield better stability characteristics and allow for larger integration time step sizes than explicit methods [26]. Unfortunately, fully-implicit methods are generally prohibitively expensive [66], especially for unsteady problems [39],

due to the large computational overhead for chemical Jacobian inversion within each time step. This makes fully-implicit time-integration methods prohibitive for simulations of reacting flows with large hydrocarbon fuels (*e.g.* n-heptane, kerosene, and diesel), where up to hundreds of species and reactions are typically required [175, 109, 19]. Further, Krylov-based iterative methods have been proposed [16, 116, 169] to reduce the computational burden associated with the construction, storage, and inversion of large, often non-sparse, Jacobian matrices [6, 54]. Alternatively, chemical Jacobian diagonal-preconditioning has also been proposed for the time-integration of the PDE system [85, 131, 57].

While these simple diagonal preconditioners have been used for the simulation of steady-state chemically reacting flows [85, 131, 57], they were argued to be inappropriate for time-accurate simulations of unsteady flows [85]. That is why large efforts have been put in the development of iterative preconditioning methods for solving the ODEs describing 0D chemical systems. Examples of efficient methods can be found in Ref. [135, 116]. However, these methods are typically tailored for very large chemical mechanisms (thousands of species) and are considerably more computationally expensive than explicit time-integration for mechanisms of small to medium sizes (tens to hundreds of species, with hundreds of reactions). In addition, these preconditioning methods rely on a decoupling of the chemistry and transport. In other words, the inversion of the sparse-chemical Jacobian is spatially local and not global. Consequently, computationally less expensive preconditioning iterative methods applied to the PDE system are desirable. Development of such a method would allow the target flames (Section 1.3) to be simulated with reasonable computational resources.

1.5 Flame structure and differential diffusion

For non-premixed turbulent flames, the flame structure is often assumed to be similar to that of a unity Lewis number flame, even when the species have Lewis numbers far from unity [45, 144, 149]. The underlying reason is that at high turbulence levels, diffusion of species and temperature is dominated by turbulent mixing, resulting in an effective unity Lewis number. This gives good results at sufficiently high turbulence, as experimentally observed [62, 14]. To the best of the authors'

knowledge, there is no premixed flame experiment equivalent to those conducted in Ref. [62, 14] in the literature.

Aspden *et al.* [10] recently performed a series of DNS of lean ($\phi = 0.4$) premixed hydrogen flames ($Le_{\mathrm{H_2}} \approx 0.3$) at Karlovitz numbers ranging from 30 to 4200. Their results clearly show that the turbulent flame structure varies significantly between the lowest and the largest Ka flames. In agreement with the results for non-premixed flames, their largest Ka flame has a structure comparable to that of a methane flame, *i.e.* the flame behaved as an effective unity Lewis number flame. Similarly, they found that their high Karlovitz propane flame ($Le_{\mathrm{C_3H_8}} \approx 2$)(distributed reaction zone regime) also had a unity-Lewis-number-like structure [9]. These results suggest that a transition for these "effective" Lewis numbers between their laminar values and unity may be identified. Peters first suggested this concept of effective Lewis numbers [142]. However, no quantitative model has been suggested yet.

In addition, there is no such information in the literature on the flame structure of larger hydrocarbon turbulent premixed flames ($Le_{\mathrm{C_7H_{16}}} = 2.8$). Based on the results of Aspden *et. al.* [10, 9], it is likely that differential diffusion will not be fully suppressed by turbulence in the target flames considered in this thesis. This would be easily verified by comparing the unity with the non-unity Lewis number target flames. Assessing if differential diffusion effects are still present in such flames has important implications for modeling, as will be discussed in Section 1.7.

1.6 Reaction zone

The reaction zone of turbulent flames previously simulated has been shown to be affected by turbulence. In particular, fluctuations in the fuel consumption rate have been identified [73, 35, 36, 71]. Understanding the physics behind these source term fluctuations is of high interest as they directly affect the turbulent flame speed, which is one of the most important (and difficult to predict) global characteristic of a premixed turbulent flame.

Such source term fluctuations in turbulent flames have commonly been attributed to stretching effects, *i.e.* effects of curvature and strain rate [71, 22]. The idea comes from the well known

equation [133, 114]

$$S_L = S_L^0 - \mathcal{L}\left(S_L^0 \kappa + a_t\right), \tag{1.16}$$

where $\mathcal{L}$ is the Markstein length, κ is the mean curvature, a_t is the tangential strain rate, S_L^0 is the unstretched laminar flame speed, and S_L is the stretched laminar flame speed. The Markstein length is known to be dependent on the unburnt mixture conditions, and in particular on the fuel Lewis number [114]. In 1992, Haworth and Poinsot [73] investigated the effect of the fuel Lewis number on the correlation between local consumption speed and tangential strain rate/curvature in two-dimensional flames at the edge of the corrugated flamelets regime, using one-step chemistry. They found that, for non-unity Lewis number flames, the local consumption speed is more correlated with curvature than strain rate, while the opposite was found for the unity Lewis number flame.

Extending these results to high Karlovitz number turbulent flames, and, more specifically, to flames at the edge of the broken reaction zones regime, is not straightforward. First, as turbulence increases, turbulent eddies eventually penetrate the preheat zone [142, 151] and it was observed that differential diffusion effects are suppressed [10, 142, 22] (as discussed for the flame structure in Section 1.5). In addition, it is also important to note that Eq. 1.16 is only valid for small stretch [114], *i.e.* $\mathcal{L}\left(\kappa + a_t/S_L\right) \ll 1$, which may very well not be the case at high Karlovitz numbers.

At high Karlovitz numbers, similar correlations have been investigated, but only in the mean sense. Recently, using the leanest ($\phi = 0.31$) series of hydrogen/air ($Le_{\mathrm{H_2}} \approx 0.3$) flames presented in Ref. [10], Amato *et al.* [5] showed that, in terms of averaged quantities, a correlation between local consumption speed and curvature is maintained up to very high Karlovitz numbers (up to 3400). In a series of two-dimensional DNS of lean ($\phi = 0.7$) methane/air ($Le_{\mathrm{CH_4}} \approx 1$) turbulent premixed flames, Hawkes and Chen [71] showed that (in the mean sense) a correlation between local flame consumption speed and tangential strain rate could be found up to high Karlovitz numbers ($Ka \approx 300$). Unfortunately, there is no such information available in the literature for fuels with larger than unity Lewis numbers at high Karlovitz number.

Furthermore, source term fluctuations leading to local extinctions have not been previously studied using DNS data. The only local extinctions identified are for lean hydrogen/air flames which are

thermodiffusively unstable [113]. Under laminar conditions, cells (characterized by positive curvature) of intensified burning rate are formed, while being surrounded by regions of local extinctions (characterized by high negative curvature) [53]. These extinctions tend to disappear with increasing Karlovitz number and are not caused by turbulence [10, 11].

Characterization of the reaction zone of the target flames and comparison with the results (obtained for other flames) discussed above will provide valuable information. In particular, it could be determined if different modeling approaches are needed or if the existing ones are sufficient (mored details in Section 1.7).

1.7 Modeling

Direct numerical simulations of turbulent premixed flames or even non-reacting turbulent flows are limited to small turbulent Reynolds numbers only. This is due to the inherent cost of resolving a wide range of scales [152]. A popular alternative approach is the use of Large Eddy Simulations (LES), which consider only the scales larger then a specified cut-off. The smaller scales are assumed to be universal. More details on the extent of the validity of this assumption and how to properly identify this cut-off can be found in Ref. [152]. The governing equations are therefore filtered and closure for the non-resolved scales needs to be provided. These are called Sub-Grid-Scale (SGS) models. SGS models are required for both non-reacting and reacting flows.

A particular challenge for the development of SGS models in the context of turbulent flames is the number of closures required (N species) and the complexity of the terms that require closure. For instance, each of the species source term is, in general, a function of all the other species mass fractions. In practice, LES of turbulent premixed flames is done with reduced chemistry models [165, 63, 64, 98].

Chemistry reduction can be done by the use of reduced chemical mechanisms, bringing the number of transported species down to a tractable number [29], or by tabulation, reducing the number of transported scalar variables to one or two [171, 65]. Variants of the first method are described in Section 1.4 (challenge # 2). However, these methods assume a separation between

the chemical and the diffusive or convective time scales. Particularly in high Karlovitz flames, not all chemical timescales are smaller than the flow timescales. For this reason, the detailed chemical mechanisms can only be reduced down to relatively large mechanisms with these techniques.

In order to further reduce the cost associated with the chemistry, Gicquel *et al.* [65] proposed a Flame Prolongation of ILDM (FPI), *i.e.* the chemistry is represented by the ILDM at high temperatures (where the chemical timescales are small) and by flamelets at lower temperatures. van Oijen *et al.* [171] have then proposed to represent the chemistry by a Flamelet-Generated Manifold (FGM). This type of manifold "is not only based on chemical assumptions, but also takes the most important transport processes into account" [171]. With the FGM approach, only a few controlling variables (typically one or two) are transported and closure is provided through the FGM (table with as many entries as the number of controlling variables). The FGM is generated *a priori* by computing one or a series of one-dimensional flame solutions, depending on the number of controlling variables.

FGM methods are computationally very attractive for obvious reasons. However, the validity of tabulated chemistry lies on an important hypothesis: the turbulent flame structure and the chemical source terms are assumed to be similar to that of laminar flamelets. Single flamelets [63] and stretched (strained or curved) flamelets [98] have been considered to generated the FGM for LES simulations of premixed flames. These were shown to provide good accuracy at low Karlovitz numbers, namely in the wrinkled/corrugated flamet regime, and at the lower edge of the thin reaction zone regime. Based on the discussion provided in the previous two sections, it is not clear if the FGM approach should be valid at Karlovitz numbers corresponding to the flames considered in this thesis. This highlights the importance of characterizing the flame structure and the reaction zone (especially the relation with strain rate and curvature) of these flames.

Another challenge for tabulated chemistry is the choice of Lewis numbers. As discussed in Section 1.5, for non-premixed turbulent flames, tabulation is usually done with unity Lewis number flamelets, even when the species have Lewis numbers far from unity [45, 144, 149]. However, for premixed turbulent flames, chemistry tabulation is generally done by computing flamelets with full

transport [98] or constant "laminar" Lewis numbers [171]. There is clearly an inconsistency between what is done for premixed and non-premixed chemistry tabulation, hence the need for an adequate effective Lewis number model. While this may have limited impact on the simulation of methane/air flames, it is crucial for large hydrocarbon flames which exhibit important differential diffusion effects.

1.8 Objectives and outline

In view of the above discussion, the objectives of the current thesis are as follows:

1. to propose a time-integration method specifically-designed for the coupled, highly non-linear, PDEs governing the evolution of unsteady reacting flows such as highly turbulent flames;

2. to perform a series of high Karlovitz n-heptane/air premixed flames in the upper portion of the thin reaction zone regime;

3. to determine if the flame structure of these turbulent premixed flames can be mapped onto that of flamelets and to provide a model for the effective Lewis numbers that should be considered in these flamelets;

4. to assess the effects of turbulence and differential diffusion on the reaction zone characteristics, the source term fluctuations, and the turbulent flame speed;

5. to provide a modeling approach for the source term fluctuations and to propose a tabulated chemistry method for large-hydrocarbon flames in the thin reaction zone regime.

The governing equations considered and the numerical solver used are presented in Chapter 2. The new time-integration method is described and validated in Chapter 3. In Chapter 4, the configuration and the parameters of the turbulent flame simulations are presented, along with qualitative results. The flame structure is characterized and modeled in Chapter 5. The reaction zone is characterized in Chapter 6 and a modeling approach is discussed in Chapter 7. Conclusions and suggestions for future work are presented in Chapter 8.

Chapter 2

Governing equations and numerical solver

In this chapter, the governing equations considered are presented first. The numerical solver, with the exception of the modifications made on the time-integration scheme (decribed in the next chapter), is then detailed.

2.1 Governing equations

The equations governing the unsteady evolution of the chemically reacting flows considered are described in the following.

2.1.1 Fluid mechanics

The reacting mixture is assumed to contain a total number of N species and their chemistry is assumed to be given by a chemical kinetics mechanism involving K reactions, with forward and backward reactions counted separately. The chemically reacting flows of interest in the current study are of relatively low Mach number (M_a), typically below 0.3 [55, 162]. Under this condition, the acoustic waves can be ignored and the pressure field can be decomposed into a spatially-invariant, but (potentially) time-dependent component, $P_0(t)$, and a fluctuating hydrodynamic pres-

sure, $p(\mathbf{x},t)$ [55, 162, 180, 142], with

$$\frac{p(\mathbf{x},t)}{P_0(t)} = O\left(M_a^2\right). \tag{2.1}$$

Since the focus of this thesis is on turbulence-chemistry interaction, Soret and Dufour effects, body forces, and radiative heat transfer are ignored [128, 95, 162, 56]. While non-negligible Soret and Dufour effects have been observed for specific hydrogen/air flames [59], limited effects have been observed in laminar stretched *n*-heptane/air flames [181]. In particular, these effects where found to be of opposite signs in lean *vs.* rich mixtures, and are expected to be smaller with near stoichiometric mixtures. The assumption that Soret/Dufour effects can be negleceted for the flames considered in this thesis will be tested in Section 4.2.2. In addition, the species molecular diffusion is assumed to be described by the Fickian law [128, 95, 162, 180, 142]. Under these assumptions, the evolution of the system is governed by the following conservation equations of mass, momentum, energy, and species density [182, 180, 142]:

$$\frac{\partial \rho}{\partial t} + \nabla \cdot (\rho \mathbf{u}) = 0 \tag{2.2}$$

$$\frac{\partial \rho \mathbf{u}}{\partial t} + \nabla \cdot (\rho \mathbf{u} \otimes \mathbf{u}) = -\nabla p + \nabla \cdot \tau \tag{2.3}$$

$$c_p \left[\frac{\partial \rho T}{\partial t} + \nabla \cdot (\rho \mathbf{u} T) \right] = \nabla \cdot (\rho c_p \alpha \nabla T) + \sum_i c_{p,i} \rho \left(\frac{\alpha}{Le_i} \nabla Y_i + Y_i \mathbf{V_{c,i}} \right) \cdot \nabla T + \dot{\omega}_T \tag{2.4}$$

$$\frac{\partial \rho Y_i}{\partial t} + \nabla \cdot (\rho \mathbf{u} Y_i) = \nabla \cdot \left(\rho \frac{\alpha}{Le_i} \nabla Y_i \right) + \nabla \cdot (\rho Y_i \mathbf{V_{c,i}}) + \dot{\omega}_i. \tag{2.5}$$

In the above equations, ρ is the density, $\mathbf{u}$ is the velocity vector, T denotes the temperature of the mixture, and Y_i is the mass fraction of species i. In the momentum equation (Eq. 2.3), τ is the deviatoric stress tensor, defined as

$$\tau = \mu \left[\nabla \mathbf{u} + (\nabla \mathbf{u})^T \right] - \frac{2}{3} \mu (\nabla \cdot \mathbf{u}) \mathbf{I}, \tag{2.6}$$

where $\mathbf{I}$ is the identity matrix and μ is the fluid viscosity. In the energy conservation equation

(Eq. 2.4), $\dot{\omega}_T$ includes heat source terms due to chemical reactions, α is the thermal diffusivity, and c_p is the specific heat at constant pressure of the mixture, given by

$$c_p = \sum_{i=1}^{N} Y_i c_{p,i}, \tag{2.7}$$

where $c_{p,i}$ is the specific heat at constant pressure of species i. In the species conservation equations (Eq. 2.5), $\dot{\omega}_i$ is the chemical source term of species i, and Le_i is the Lewis number of species i, defined as

$$Le_i = \frac{\alpha}{D_i}, \tag{2.8}$$

with D_i the mass diffusivity for species i. The correction velocity $\mathbf{V_{c,i}}$ in Eq. 2.5 accounts for gradients in the mixture molecular weight as well as ensures zero net diffusion flux. It has the following expression [180, 142]:

$$\mathbf{V_{c,i}} = \frac{\alpha}{Le_i}\frac{\nabla W}{W} - \alpha\left(\sum_{j=1}^{N}\frac{\nabla Y_j}{Le_j}\right) - \alpha\frac{\nabla W}{W}\left(\sum_{j=1}^{N}\frac{Y_j}{Le_j}\right), \tag{2.9}$$

where

$$W = \left(\sum_{j=1}^{N}\frac{Y_j}{W_j}\right)^{-1} \tag{2.10}$$

is the local mean molecular weight of the mixture, and W_j is the molecular weight of species j.

The above set of equations is complemented by the equation of thermodynamic state

$$\rho = \frac{P_0 W}{\widehat{R}T}, \tag{2.11}$$

where P_0 is the thermodynamic pressure (see Eq. 2.1) and $\widehat{R}$ is the universal gas constant.

2.1.2 Chemical model

The overall rate of change of species i, $\dot{\omega}_i$, in Eq. 2.5 can be split into a production term, $\dot{\omega}_i^+$, and a consumption term, $\dot{\omega}_i^-$, as

$$\dot{\omega}_i = \dot{\omega}_i^+ - \dot{\omega}_i^-. \tag{2.12}$$

It is important to note that both the production term $\dot{\omega}_i^+$ and the consumption term $\dot{\omega}_i^-$ are positive.

The production rate of species i, $\dot{\omega}_i^+$, is given by the sum of the contributions from all elementary chemical reactions leading to the formation of this species:

$$\dot{\omega}_i^+ = W_i \sum_{\substack{j=1 \\ \nu_{ji}>0}}^{K} \left[k_j \prod_{s=1}^{N} \left(\frac{\rho Y_s}{W_s} \right)^{\nu_{js}} \right], \tag{2.13}$$

where ν_{js} is the stoichiometric coefficient of species s in reaction j. In the above expression, the rate constant of reaction j, k_j, is given by the Arrhenius form, $k_j\left(T\right) = A_j T^{b_j} \exp^{-T_{a,j}/T}$, where $T_{a,j}$ is the activation temperature of this reaction. Similarly, the consumption rate of species i, $\dot{\omega}_i^-$, is given by the sum of the contributions from all elementary chemical reactions leading to the destruction of this species:

$$\dot{\omega}_i^- = W_i \sum_{\substack{j=1 \\ \nu_{ji}<0}}^{K} \left[k_j \prod_{s=1}^{N} \left(\frac{\rho Y_s}{W_s} \right)^{\nu_{js}} \right]. \tag{2.14}$$

The local heat release rate is given by

$$\dot{\omega}_T = -\sum_{j=1}^{N} h_i \dot{\omega}_i, \tag{2.15}$$

where

$$h_i = h_i^0 + \int_{T_0}^{T} c_{p,i} dT \tag{2.16}$$

is the specific enthalpy of species i, and h_i^0 denotes its value under standard and reference conditions.

2.2 Numerical algorithm

In this section, a description of the flow solver and the numerical algorithms used is provided.

2.2.1 Overview of the numerical solver

The simulations in this work are performed using the structured, multi-physics and multi-scale finite-difference code NGA [55]. The NGA code allows for accurate, robust, and flexible simulations of both laminar and turbulent reactive flows in complex geometries and has been applied in a wide range of test problems, including laminar and turbulent flows [182, 183, 184] and constant and variable density flows [55, 31, 173], as well as Large-Eddy Simulations (LES) [183, 122] and Direct Numerical Simulations (DNS) [17, 173, 32]. This numerical solver has been shown to conserve discretely mass, momentum, and kinetic energy, with arbitrarily high order spatial discretization [55].

NGA uses both spatially and temporally staggered variables [55]. All scalar quantities $(\rho, p, T, Y_i, D_i, \alpha, c_p, c_{p,i}, \mu)$ are stored at the volume centers, and the velocity components are stored at their respective volume faces. The convective term in the species transport equations is discretized using the bounded quadratic upwind biased interpolative convective scheme (BQUICK) [74], and the diffusive term is discretized using a second-order centered scheme. The variables are advanced in time using the second-order semi-implicit Crank-Nicolson scheme of Pierce and Moin [145].

An iterative procedure is applied to fully cover the non-linearities in the Navier-Stokes equations. This iterative procedure has been found to be of critical importance for stability and accuracy considerations [55, 162, 145]. The numerical algorithmic sequence for one time step is described below, where a uniform time step Δt is employed. The density, pressure, and scalar fields are advanced from time level $t^{n+1/2}$ to $t^{n+3/2}$, and the velocity fields are advanced from time level t^n to t^{n+1}. A total number of Q sub-iterations is assumed.

0. Upon convergence of the previous time step, the density, $\rho^{n+1/2}$, pressure, $p^{n+1/2}$, velocity fields, $\mathbf{u}^n$, and scalar fields, $\mathbf{Y}^{n+1/2}$, are stored, where $\mathbf{Y}$ represents the vector of species mass fractions $(Y_1, ..., Y_N)$. The solutions for pressure, species mass fractions, and momentum (from

the previous time step) are used as initial best guesses for the forthcoming iterative procedure:

$$p_0^{n+3/2} = p^{n+1/2}\ ,\ \ \mathbf{Y}_0^{n+3/2} = \mathbf{Y}^{n+1/2}\ ,\ \text{and}\ \ (\rho\mathbf{u})_0^{n+1} = (\rho\mathbf{u})^n, \tag{2.17}$$

where the subscript indicates the index of the sub-iteration. The Adams-Bashforth prediction is used for the initial density evaluation:

$$\rho_0^{n+3/2} = 2\rho^{n+1/2} - \rho^{n-1/2}. \tag{2.18}$$

This ensures that the continuity equation is discretely satisfied at the beginning of the iterative procedure. The vector of chemical source terms is denoted by $\mathbf{\Omega} = (\dot{\omega}_1, ..., \dot{\omega}_N)$, and $\mathbf{\Omega}_0^{n+3/2}$ is evaluated using the thermochemical quantities obtained at the conclusion of the previous time step (explicit prediction).

For the sub-iteration $k = 1, \ldots, Q$

1. The scalar fields are advanced in time using the semi-implicit Crank-Nicolson method [55, 145] for the convective and diffusive terms, and explicit integration for the chemical source terms:

$$\mathbf{Y}_k^* = \frac{\mathbf{Y}^{n+1/2} + \mathbf{Y}_k^{n+3/2}}{2}, \tag{2.19}$$

$$\begin{aligned} \rho_k^{n+3/2}\mathbf{Y}_{k+1}^{n+3/2} &= \rho^{n+1/2}\mathbf{Y}^{n+1/2} + \Delta t\left[\left(\mathbf{C}_k^{n+1} + \mathbf{D}_k^{n+1}\right)\cdot\mathbf{Y}_k^* + \mathbf{\Omega}_k^*\right] \\ &+ \frac{\Delta t}{2}\left(\frac{\partial\mathbf{C}}{\partial\mathbf{Y}} + \frac{\partial\mathbf{D}}{\partial\mathbf{Y}}\right)_k^{n+1}\cdot\left(\mathbf{Y}_{k+1}^{n+3/2} - \mathbf{Y}_k^{n+3/2}\right). \end{aligned} \tag{2.20}$$

To simplify the discrete notations for spatial differential operators, the operators corresponding to the convective and diffusive terms in the scalar equations (Eq. 2.5) are written as $\mathbf{C}$ and $\mathbf{D}$, respectively. $\frac{\partial\mathbf{C}}{\partial\mathbf{Y}}$ and $\frac{\partial\mathbf{D}}{\partial\mathbf{Y}}$ are the Jacobian matrices corresponding to the convective and diffusive terms, respectively. $\mathbf{C}$ and $\frac{\partial\mathbf{C}}{\partial\mathbf{Y}}$ are functions of the density and the velocity, while $\mathbf{D}$ and $\frac{\partial\mathbf{D}}{\partial\mathbf{Y}}$ are functions of the density and the kinematic viscosity. They are consistently updated

at each sub-iteration. Depending on the order of discretization, these operators are generally banded diagonal matrices (*e.g.* tridiagonal for 2nd order discretization and pentadiagonal for 3rd order discretization). It is important to note that the semi-implicit Crank-Nicolson method proposed by Pierce and Moin [145] is not applied to the time-integration of the species chemical source terms, Ω_k^*. As mentioned in the introduction, this is due to the extremely high computational cost associated with the calculation of the chemical Jacobian matrix, $\left(\frac{\partial \mathbf{\Omega}}{\partial \mathbf{Y}}\right)_k^{n+1}$, and the even more expensive inversion of this matrix.

The temperature equation is advanced in time in a similar fashion:

$$T_k^* = \frac{T^{n+1/2} + T_k^{n+3/2}}{2}, \tag{2.21}$$

$$\begin{aligned} \rho_k^{n+3/2} T_{k+1}^{n+3/2} &= \rho^{n+1/2} T^{n+1/2} + \Delta t \left[\left(C_k^{n+1} + D_k^{n+1} \right) \cdot T_k^* + \Omega_{T,k}^* + S_{T,k}^* \right] \\ &+ \frac{\Delta t}{2} \left(\frac{\partial C}{\partial T} + \frac{\partial D}{\partial T} \right)_k^{n+1} \cdot \left(T_{k+1}^{n+3/2} - T_k^{n+3/2} \right), \end{aligned} \tag{2.22}$$

with $S_{T,k}^*$ being the discretized form of $\frac{\rho\alpha}{c_p} \nabla c_p \cdot \nabla T + \sum_i \frac{c_{p,i}}{c_p} \rho \left(\frac{\alpha}{Le_i} \nabla Y_i + Y_i \mathbf{V_{c,i}} \right) \cdot \nabla T$ evaluated at half time step. Note that the temperature equation is treated the exact same way as the species transport equations, with the exception of the additional source term $S_{T,k}^*$.

2. The density field is predicted from thermodynamics using

$$\rho_{k+1}^{n+3/2} = \frac{P_0 \left(\sum_{i=1}^{N} \frac{Y_{i,k+1}^{n+3/2}}{W_i} \right)^{-1}}{\widehat{R} T_{k+1}^{n+3/2}}. \tag{2.23}$$

It is important to note that this density evaluation does not ensure conservation of the species densities, ρY_i, since no density rescaling such as the one proposed by Shunn *et al.* [162] is used. However, upon convergence of the sub-iterations, this formulation is equivalent to the density treatment proposed by Shunn *et al.*

3. The momentum equation is advanced in time using a similar semi-implicit Crank-Nicolson

method as for the scalar fields

$$\mathbf{u}_k^* = \frac{\mathbf{u}^n + \mathbf{u}_k^{n+1}}{2}, \tag{2.24}$$

$$\begin{aligned} \frac{\rho^{n+1/2} + \rho_{k+1}^{n+3/2}}{2}\widehat{\mathbf{u}}_{k+1}^{n+1} &= \frac{\rho^{n-1/2} + \rho^{n+1/2}}{2}\mathbf{u}^n \\ &+ \Delta t\left[\left(\mathbf{C}_{\mathrm{u},k}^{n+1/2} + \mathbf{D}_{\mathrm{u},k}^{n+1/2}\right)\cdot\mathbf{u}_k^* + \nabla p_k^{n+3/2}\right] \\ &+ \frac{\Delta t}{2}\left(\frac{\partial \mathbf{C}_\mathrm{u}}{\partial \mathbf{u}} + \frac{\partial \mathbf{D}_\mathrm{u}}{\partial \mathbf{u}}\right)_k^{n+1/2}\cdot\left(\widehat{\mathbf{u}}_{k+1}^{n+1} - \mathbf{u}_k^{n+1}\right), \end{aligned} \tag{2.25}$$

where $\mathbf{C}_\mathrm{u}$ and $\mathbf{D}_\mathrm{u}$ are discrete operators associated with the convective and the viscous terms, respectively. $\widehat{\mathbf{u}}$ is the predicted velocity field used to compute the fluctuating hydrodynamic pressure (Step 4).

4. A Poisson equation is then solved for the fluctuating hydrodynamic pressure:

$$\nabla^2 \delta p_{k+1}^{n+3/2} = \frac{1}{\Delta t}\left[\nabla\cdot\left(\frac{\rho^{n+1/2} + \rho_{k+1}^{n+3/2}}{2}\widehat{\mathbf{u}}_{k+1}^{n+1}\right) + \frac{\rho_{k+1}^{n+3/2} - \rho^{n+1/2}}{\Delta t}\right]. \tag{2.26}$$

The Poisson equation is solved using the high-fidelity HYPRE package [55, 61]. The predicted velocity field is then updated through a projection step:

$$\mathbf{u}_{k+1}^{n+1} = \widehat{\mathbf{u}}_{k+1}^{n+1} - \frac{2\Delta t}{\rho^{n+1/2} + \rho_{k+1}^{n+3/2}}\left(\nabla \delta p_k^{n+3/2}\right) \quad \text{and} \quad p_{k+1}^{n+3/2} = p_k^{n+3/2} + \delta p_{k+1}^{n+3/2}. \tag{2.27}$$

5. Upon convergence of the sub-iterations, the new solutions are updated:

$$\rho^{n+3/2} = \rho_Q^{n+3/2},\ p^{n+3/2} = p_Q^{n+3/2},\ \mathbf{u}^{n+1} = \mathbf{u}_Q^{n+1},\ \text{and}\ \mathbf{Y}^{\mathrm{n+3/2}} = \mathbf{Y}_\mathrm{Q}^{\mathrm{n+3/2}}. \tag{2.28}$$

It is important to note that the above formulation becomes equivalent to the fully-implicit Crank-Nicolson time-integration scheme upon convergence of the sub-iterations [145].

2.2.2 Extension to multi-dimensions

For clarity, the extension to multi-dimensions is presented here only for the species equations (Eq. 2.20). An identical procedure is applied to the temperature (Eq. 2.22) and the momentum equations (Eq. 2.25).

For simpler implementation, the set of equations (Eq. 2.20) is solved in practice in its residual form:

$$\begin{aligned} & \left[\rho_k^{n+3/2}\mathbf{I} - \frac{\Delta t}{2}\left(\frac{\partial \mathbf{C}}{\partial \mathbf{Y}} + \frac{\partial \mathbf{D}}{\partial \mathbf{Y}}\right)_k^{n+1}\right] \cdot \left(\mathbf{Y}_{k+1}^{n+3/2} - \mathbf{Y}_k^{n+3/2}\right) \\ = \quad & \rho^{n+1/2}\mathbf{Y}^{n+1/2} - \rho_k^{n+3/2}\mathbf{Y}_k^{n+3/2} + \Delta t\left[\left(\mathbf{C}_k^{n+1} + \mathbf{D}_k^{n+1}\right)\cdot \mathbf{Y}_k^* + \mathbf{\Omega}_k^*\right]. \end{aligned} \tag{2.29}$$

The above equation is equivalent to

$$\mathbf{Y}_{k+1}^{n+3/2} = \mathbf{Y}_k^{n+3/2} - \Delta t \mathbf{J}^{-1}\cdot \mathbf{\Theta}_k, \tag{2.30}$$

where the matrix $\mathbf{J}$ is defined as

$$\mathbf{J} = \rho_k^{n+3/2}\mathbf{I} - \frac{\Delta t}{2}\left(\frac{\partial \mathbf{C}}{\partial \mathbf{Y}} + \frac{\partial \mathbf{D}}{\partial \mathbf{Y}}\right)_k^{n+1}, \tag{2.31}$$

and the vector

$$\mathbf{\Theta}_k = \frac{\rho_k^{n+3/2}\mathbf{Y}_k^{n+3/2} - \rho^{n+1/2}\mathbf{Y}^{n+1/2}}{\Delta t} - \left[\left(\mathbf{C}_k^{n+1} + \mathbf{D}_k^{n+1}\right)\cdot \mathbf{Y}_k^* + \mathbf{\Omega}_k^*\right] \tag{2.32}$$

is the error (residual) made on the species transport equation at the previous sub-iteration. When the sub-iterations are fully-converged, the residual, $\mathbf{\Theta}_k$, is zero.

In multi-dimensional numerical simulations, inverting the system of discrete equations presented can be of high computational cost, despite its sparse nature. The method of Approximate Factorization (AF) is therefore used to convert the single, multi-dimensional problem into multiple, one-dimensional problems that can be solved efficiently [55, 145]. The transport operator $\mathbf{F} = \frac{\partial \mathbf{C}}{\partial \mathbf{Y}} + \frac{\partial \mathbf{D}}{\partial \mathbf{Y}}$

can be split exactly into directional transport operators $\mathbf{F}_x$, $\mathbf{F}_y$, and $\mathbf{F}_z$, leading to

$$\begin{aligned}\mathbf{J} &= \rho_k^{n+3/2}\mathbf{I} - \frac{\Delta t}{2}\mathbf{F}_k^{n+1} \\ &= \rho_k^{n+3/2}\mathbf{I} - \frac{\Delta t}{2}\mathbf{F}_{x,k}^{n+1} - \frac{\Delta t}{2}\mathbf{F}_{y,k}^{n+1} - \frac{\Delta t}{2}\mathbf{F}_{z,k}^{n+1}\end{aligned} \tag{2.33}$$

in a general three-dimensional orthogonal coordinate system. Accordingly, the following factorization is used:

$$\begin{aligned}&\rho_k^{n+3/2}\mathbf{I} - \frac{\Delta t}{2}\mathbf{F}_{x,k}^{n+1} - \frac{\Delta t}{2}\mathbf{F}_{y,k}^{n+1} - \frac{\Delta t}{2}\mathbf{F}_{z,k}^{n+1} \\ = \;& \rho_k^{n+3/2}\mathbf{I} \\ \cdot \;& \left(\mathbf{I} - \frac{\Delta t}{2}\frac{1}{\rho_k^{n+3/2}}\cdot\mathbf{F}_{x,k}^{n+1}\right) \\ \cdot \;& \left(\mathbf{I} - \frac{\Delta t}{2}\frac{1}{\rho_k^{n+3/2}}\cdot\mathbf{F}_{y,k}^{n+1}\right) \\ \cdot \;& \left(\mathbf{I} - \frac{\Delta t}{2}\frac{1}{\rho_k^{n+3/2}}\cdot\mathbf{F}_{z,k}^{n+1}\right) + O\left(\Delta t^2\right).\end{aligned} \tag{2.34}$$

The AF does not degrade the temporal accuracy of the time-integration scheme, since it introduces a second-order error in time, the same order as the one introduced by the temporal discretization (Eqs. 2.19 and 2.20).

2.3 Application to turbulent reacting flows

As previously mentionned, NGA is tailored for the simulation of low Mach number variable density turbulent flows. In particular, it is optimized for massively parallel computations of such flows. These characteristics are necessary for the simulation of turbulent reacting flows such as turbulent flames. However, the solver as presented in this section integrates the scalar source terms in an explicit fashion. As mentionned in the introduction, the scalar transport equations in reacting flows are stiff and an explicit time-integration would make the simulation of such flows impracticable. Therefore, the time-integration scheme has to be adapted to treat the stiff scalar source terms in

some type of implicit fashion. This is the focus of the next chapter.

Chapter 3

Semi-implicit time-integration for stiff chemistry[1]

A semi-implicit preconditioned iterative method is proposed for the time-integration of the stiff chemistry in simulations of unsteady reacting flows, such as turbulent flames, using detailed chemical kinetic mechanisms. Emphasis is placed on the simultaneous treatment of convection, diffusion, and chemistry, without using operator splitting techniques. As such, a diagonal-preconditioned iterative (to account for the non-linearity of the system) method for the efficient integration of stiff chemistry in the numerical simulation of unsteady chemically reacting flows is proposed in a multi-dimensional setting.

The implementation of the method is presented first, followed by a description of the numerical test cases. Then, a detailed theoretical analysis of the stability and the accuracy of the scheme is provided, along with a numerical validation using the test cases. Finally, the extension of the method to other chemically reacting flows, its advantages over other methods, and its limitations are discussed.

[1]The work presented in this chapter is published in B. Savard, Y. Xuan, B. Bobbitt, and G. Blanquart, J. Comput. Phys. (2015). Yuan Xuan has contributed to the formulation of the scheme in the form of a preconditioner. He has also acted as a second advisor during the publication process. Brock Bobbitt has performed most of the one-dimensional flame simulations with NGA found in this chapter (along with the corresponding figures). The author of this thesis has contributed to the rest of the work presented in this chapter, *i.e.* the formulation of the approximate factorization with the diagonal preconditioner, the comparison of the method to the diagonal preconditioners previously found in the literature, the 3D turbulent flame, the theoretical analysis, the comparison with the numerical results, the extension of the results to other canonical flows, and the discussion.

3.1 Species *vs.* temperature equation stiffness

As discussed in the introduction (Section 1.4), in chemically reacting flows, the very large magnitude (or equivalently small timescales) of the source terms are responsible for the stiffness of the scalar transport equations [112, 85]. This stiffness is generally believed to be due to the stiff source terms in the species transport equations, but not due to the temperature transport equation [66, 112, 101]. An estimate for the temperature time scale in a n-C_7H_{16}/air premixed flame (test case presented in Section 3.4.1) gives $\tau_T \sim (T_b - T_u) \,/\, (\dot{\omega}_T / (\rho c_p))_{\max} \sim 10^{-4}$ s, where T_b and T_u are the burnt and the unburnt temperatures, respectively. This time scale is approximately an order of magnitude larger than the time step corresponding to a unity convective CFL in such a laminar flame. Therefore, the temperature equation (Eq. 2.4) is advanced in time in the exact same fashion as described in the previous chapter (Eqs. 2.21 and 2.22) without any further implicit treatment. Cases for which the temperature time scale may not be considered large are discussed in Section 3.6.3.

Consistently, improvement of the numerical procedure detailed in the previous chapter is based on modifying the time-marching step for the species mass fraction fields only (step 1 in the procedure described in Section 2.2.1). All other intermediate steps are left unchanged.

3.2 Preconditioned iterative method

The time-marching for species transport equations described in Eq. 2.30 resembles the standard preconditioned Richardson-type iterative method [154], where the matrix $\mathbf{J}$ acts as a preconditioner. More precisely, the choice of the preconditioner, $\mathbf{J}$, can be arbitrary and does not modify the discrete form of the equations to solve (*i.e.* $\mathbf{\Theta}_k = \mathbf{0}$). It only changes the convergence characteristics of the iterative method. For instance, setting

$$\mathbf{J} = \rho_k^{n+3/2} \mathbf{I} \tag{3.1}$$

is equivalent to the fully-explicit integration of the convective, diffusive, and chemical source terms

in the species transport equations, while setting

$$\mathbf{J} = \rho_k^{n+3/2}\mathbf{I} - \frac{\Delta t}{2}\left(\frac{\partial \mathbf{C}}{\partial \mathbf{Y}} + \frac{\partial \mathbf{D}}{\partial \mathbf{Y}} + \frac{\partial \mathbf{\Omega}}{\partial \mathbf{Y}}\right)_k^{n+1} \tag{3.2}$$

corresponds to the full-implicit integration of the convective, diffusive, and chemical source terms in the species transport equations.

Clearly, there is a trade-off in the choice of the preconditioner. Since it is applied at each step of the iterative method, it is preferable to have a preconditioning matrix, $\mathbf{J}$, with low computing and inversion cost. The cheapest preconditioner would therefore be the one described by Eq. 3.1 (fully-explicit integration), which leads to poor convergence performance requiring extremely small time step sizes. On the other hand, the optimal preconditioner would be the one leading to the fully-implicit integration of the various terms (Eq. 3.2). Unfortunately, since the chemical source terms of most species are generally dependent on a large number of other species, the chemical Jacobian matrix, $\frac{\partial \mathbf{\Omega}}{\partial \mathbf{Y}}$, is usually not sparse [135]. Therefore, its construction and inversion may become prohibitively expensive especially when a large number of species is considered.

Note that preconditing methods have been used in the literature for other types of problems. An exemple is the inversion of the nonlinear systems resulting from higher-order implicit Runge-Kutta steps, in which the stiffness is not specifically due to the chemistry. A wide range of iterative preconditiong methods have been proposed for such systems, including diagonal preconditioners [2, 83, 89, 167].

3.3 Semi-implicit preconditioning for stiff chemistry

3.3.1 Proposed preconditioner

In an attempt to achieve better convergence characteristics while keeping the form of the preconditioner as simple as possible, a preconditioning method for stiff chemistry, which lies between the fully-explicit and fully-implicit extremes, is proposed.

The proposed preconditioner is written as

$$\mathbf{J} = \rho_k^{n+3/2}\mathbf{I} - \frac{\Delta t}{2}\left(\frac{\partial \mathbf{C}}{\partial \mathbf{Y}} + \frac{\partial \mathbf{D}}{\partial \mathbf{Y}} - \mathbf{\Lambda}\right)_k^{n+1}, \tag{3.3}$$

where $\mathbf{\Lambda}$ is a diagonal matrix defined as

$$\mathbf{\Lambda}_{i,i} = \frac{\dot{\omega}_i^-}{Y_i}. \tag{3.4}$$

The matrix $\mathbf{\Lambda}$ may be regarded as a very good approximation of the negative of the diagonal of the chemical Jacobian:

$$\frac{\partial \dot{\omega}_i}{\partial Y_i} = \frac{\partial \dot{\omega}_i^+}{\partial Y_i} - \frac{\partial \dot{\omega}_i^-}{\partial Y_i} \approx 0 - \frac{\dot{\omega}_i^-}{Y_i} \tag{3.5}$$

as the production rate of species i (Eq. 2.13) is not a function of the species mass fraction and its consumption rate (Eq. 2.14) is often linear in Y_i. The i^{th} element of $\mathbf{\Lambda}$ represents an approximation of the inverse of the timescale corresponding to the chemical consumption of species i (approximation of the inverse of the consumption characteristic times as used in Ref. [85, 66]). The proposed preconditioner aims to suppress the small timescales due to the fast consumption of the different species in the system with stiff chemistry.

As the matrix $\mathbf{\Lambda}$ is diagonal, the preconditioner corresponds to a species-wise relaxation, similar to the Jacobi preconditioner. The proposed method accounts for the non-linearities by coupling the transport equations through the iterative procedure (Eq. 2.32).

The proposed method is inspired by the work of Eberhardt and Imlay [57], who first introduced a diagonal preconditioning in a point-implicit algorithm for the simulation of steady-state reacting flows. The diagonal elements were found by computing the L_2-norm of the corresponding row of the chemical Jacobian. However, this was found to lead to an improper approximation of the chemical time scales and resulted in a lack of elemental conservation in time-marching algorithms [85, 28, 27]. In an effort to improve the accuracy of the method, Ju [85] replaced the jth element of the diagonal preconditioner by the maximum between the inverse of the consumption characteristic time of species

j and the inverse of the production time of elementary reaction in which species j is the product. It was argued that this type of preconditioning is suited for the simulation of steady flows, but should fail to provide time-accurate solutions of unsteady flows [85]. An implicit correction with the diagonal approximation of the Jacobian would introduce errors that would accumulate over time.

In the present algorithm, the diagonal preconditioning is applied within an iterative procedure for each time step. This iterative method allows further reduction of the residuals and this is the reason why the method is suitable for the simulation of unsteady reacting flows.

3.3.2 Extension to multi-dimensions

The proposed preconditioning is compatible with the method of Approximate Factorization described in Section 2.2.2. Equation 2.33 becomes

$$\begin{aligned}\mathbf{J} &= \rho_k^{n+3/2}\mathbf{I} - \frac{\Delta t}{2}\left(\mathbf{F}-\mathbf{\Lambda}\right)_k^{n+1} \\ &= \rho_k^{n+3/2}\mathbf{I} - \frac{\Delta t}{2}\mathbf{F}_{x,k}^{n+1} - \frac{\Delta t}{2}\mathbf{F}_{y,k}^{n+1} - \frac{\Delta t}{2}\mathbf{F}_{z,k}^{n+1} + \frac{\Delta t}{2}\mathbf{\Lambda}_k^{n+1}. \end{aligned} \tag{3.6}$$

Accordingly, the following factorization is proposed:

$$\begin{aligned} & \rho_k^{n+3/2}\mathbf{I} - \frac{\Delta t}{2}\mathbf{F}_{x,k}^{n+1} - \frac{\Delta t}{2}\mathbf{F}_{y,k}^{n+1} - \frac{\Delta t}{2}\mathbf{F}_{z,k}^{n+1} + \frac{\Delta t}{2}\mathbf{\Lambda}_k^{n+1} \\ = & \left(\rho_k^{n+3/2}\mathbf{I} + \frac{\Delta t}{2}\mathbf{\Lambda}_k^{n+1}\right) \\ \cdot & \left(\mathbf{I} - \frac{\Delta t}{2}\left(\rho_k^{n+3/2}\mathbf{I} + \frac{\Delta t}{2}\mathbf{\Lambda}_k^{n+1}\right)^{-1}\cdot \mathbf{F}_{x,k}^{n+1}\right) \\ \cdot & \left(\mathbf{I} - \frac{\Delta t}{2}\left(\rho_k^{n+3/2}\mathbf{I} + \frac{\Delta t}{2}\mathbf{\Lambda}_k^{n+1}\right)^{-1}\cdot \mathbf{F}_{y,k}^{n+1}\right) \\ \cdot & \left(\mathbf{I} - \frac{\Delta t}{2}\left(\rho_k^{n+3/2}\mathbf{I} + \frac{\Delta t}{2}\mathbf{\Lambda}_k^{n+1}\right)^{-1}\cdot \mathbf{F}_{z,k}^{n+1}\right) + O\left(\Delta t^2\right). \end{aligned} \tag{3.7}$$

Similar to Section 2.2.2, this proposed factorization does not degrade the temporal accuracy of the preconditioned time-integration scheme, since it introduces a second-order error in time, the same order as the one introduced by the temporal discretization (Eqs. 2.19 and 2.20).

In the above factorization, the inversion of $\rho_k^{n+3/2}\mathbf{I} + \frac{\Delta t}{2}\mathbf{\Lambda}_k^{n+1}$ is computationally trivial since it is a diagonal matrix. As such, three simpler one-dimensional inversion problems in the x, y, and z directions can be solved sequentially using tridiagonal (2^{nd} order spatial discretization schemes) or pentadiagonal (3^{rd} order spatial discretization schemes) matrix inversion algorithms analytically, in a serial or parallel fashion. This is very important, as it keeps the overall cost of any sub-iteration linear with the number of grid points and linear with the number of species.

3.3.3 Summary

A semi-implicit preconditioning strategy is proposed, in combination with an iterative method, for the time-integration of the stiff chemistry. The proposed method takes advantage of the iterative structure of the NGA code and, more precisely, its semi-implicit formulation of the transport terms. In addition, the method is compatible with the approximate factorization (see Section 2.2.2), which is necessary to maintain the performance of the code. Note that this preconditioning method could be applied as well within any other iterative algorithm.

The proposed semi-implicit preconditioning method is based on an approximation of the diagonal of the chemical Jacobian. The hypothesis, which will be tested in Section 3.5, is that the smallest chemical timescales are well approximated by this diagonal preconditioner, allowing the use of larger integration time step sizes. Another assumption that will be tested in Section 3.5 is that a good convergence rate of the sub-iterations can be obtained with sufficiently large time step sizes. This would allow the total number of operations per time step to be very similar to that for the explicit time-integration of the chemistry. As mentioned in the introduction, other diagonal preconditioners were found to be associated with a lack of robustness and elemental conservation in non-iterative time-marching algorithms [28, 27] or were argued to lack time-accuracy [85]. However, the proposed method is iterative and, upon convergence of the sub-iterations, the fully-implicit formulation is recovered. Therefore, any issues would be alleviated by the convergence of the sub-iterations.

3.4 Test cases

The performance of the proposed iterative method will be tested in Section 3.5 on two flow configurations: a one-dimensional unstretched premixed flame and a three-dimensional high Karlovitz turbulent premixed flame.

3.4.1 One-dimensional premixed flame

The one-dimensional laminar unstretched premixed flame is selected as the first test case since it is the most canonical configuration (that includes convection, diffusion, and chemistry) and it is well suited for the quantitative evaluation of the stability and accuracy of a numerical scheme [128, 66, 95]. The condition of the present test case corresponds to a n-heptane/air flame with an equivalence ratio of 0.9 and an unburnt temperature and pressure of 298 K and 1 atm, respectively. N-heptane is used in this study as a representative of heavy hydrocarbons of relevance to transportation fuels. A reduced finite-rate chemistry model is used in the present work. The mechanism developed in Ref. [17] was reduced from 47 species and 290 reactions to 35 species and 217 reactions in an effort to alleviate the computational cost. Since the gas mixture is slightly lean, species that are only produced under rich conditions (and their associated reactions), namely C_5H_5, C_5H_6, and all aromatic species (benzene, naphthalene...) were removed from the mechanism. As the focus of the present chapter is placed on the time-integration, the Lewis numbers of all the species are set to unity (*i.e.* no differential diffusion) for the present simulation. Under these conditions, the laminar flame speed is $S_L = 29$ cm/s, and the flame thickness is $l_F = 0.43$ mm, with $l_F = (T_b - T_u)/(\partial T/\partial x)_{\max}$. It is expected that using different fuels, mixture compositions, and unburnt conditions will lead to qualitatively similar results. This is discussed in more detail in Section 3.6.

The computational domain is initialized with a fully-converged solution of a stationary flame. The flame front is initially located near the center of the domain ($x_0 = 5.5$ mm) to reduce effects of the boundaries. The left boundary is set to be a wall, and the right boundary is an open flow. Once the simulation is started, the flame front moves towards the unburnt gases (left of the domain) at a speed which corresponds to the laminar flame speed. The length of the 1D computational

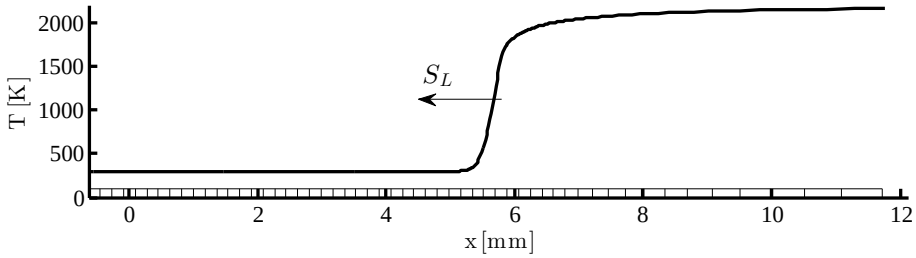

Figure 3.1: Schematic of the computational domain and initial condition.

domain is approximately 30 times the laminar flame thickness. The domain is discretized with a uniform grid cell spacing ($\Delta x = 18$ μm) except behind the initial flame location ($x > 5.5$ mm) where it is stretched with a factor of 1.1 (ratio of the grid cell size to its neighbor). A schematic of the configuration is shown in Fig. 3.1.

While arbitrarily high order (for the convective and viscous terms) is available in the NGA code, the simulations throughout this thesis rely on second-order spatial discretization of the viscous and convective terms of the Navier-Stokes equations. Grid convergence tests were performed and revealed a 2^{nd} order accuracy in space (not shown). This spatial order of accuracy was found to be independent of the proposed time-integration scheme. These tests also determined that 24 points across the flame front (l_F) is sufficient to achieve satisfactory grid independence. In the following, this grid resolution is used for all numerical tests.

3.4.2 Three-dimensional turbulent premixed flame

The second configuration chosen corresponds to the unity Lewis number flame presented in details in Chapter 4 (other simulations with differential diffusion will be presented/analyzed in Chapters 4 to 7). A brief description is provided in this section. Figure 4.1 presents a schematic of the flow configuration. The left and right ends of the domain correspond to an inflow of unburnt gases and an outflow of burnt gases, respectively. The position of the flame is statistically steady as an inflow velocity equal to the turbulent flame speed is used. Turbulent forcing is employed to avoid a fast decay of turbulence due to viscous dissipation [31]. This forcing is not used at the inlet and the outlet to avoid negative velocities. Forcing starts at $0.5L$ after the inlet and is switched off at a distance of

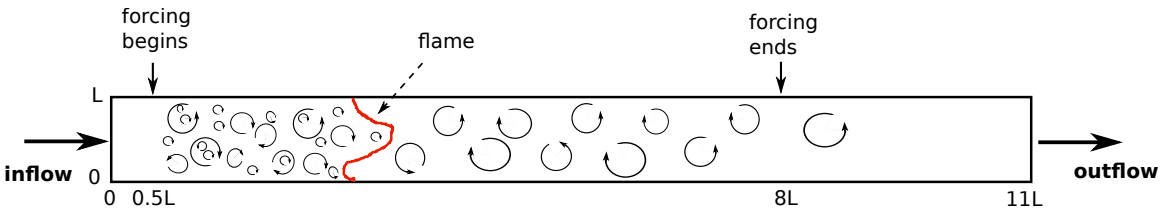

Figure 3.2: Schematic of the three-dimensional turbulent premixed flame configuration.

$3L$ from the end of the domain, with L being the domain width and height (Fig. 4.1). This distance is found sufficient for the turbulence to decay without forcing such that no negative axial velocities are found at the outlet. Note that the decay of turbulence is due to viscous dissipation.

The chemical mechanism and the flame unburnt conditions are the same as for the one-dimensional premixed flame detailed in Section 3.4.1. The Karlovitz number is 280 and the turbulent Reynolds number in the unburnt gases is 190. Other important parameters of the simulation are listed in Table 5.1. Note that prior to this simulation, the flow field is established without any flame; homogeneous isotropic turbulence is obtained in the forced region. Then, the turbulent premixed flame is simulated with finite-rate chemistry for several eddy turnover times. The simulation is performed in parallel using 1920 processors on the cluster Hopper at the National Energy Research Scientific Computing Center (NERSC). Fig. 3.3 provides visual information about the flame simulated.

The simulation is performed with a time step size of $\Delta t = 5.7 \times 10^{-7}$ s, which corresponds to a convective CFL condition of 0.8. With the proposed semi-implicit scheme, the stiffness of the chemical model was found not to impact the stability of the turbulent reacting flow simulation. More details on the stability of the numerical framework and the choice of time step size are provided in the following section.

3.5 Results

First, a theoretical analysis on the convergence of the sub-iterations for the species transport equations is presented in this section. Second, this analysis is further discussed in light of the eigenvalue content of the proposed precondition matrix. Third, the convergence of the sub-iterations is evalu-

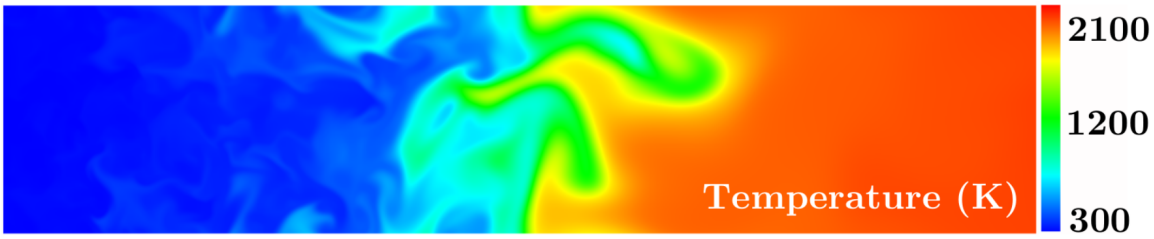

Figure 3.3: Contours of temperature on a two-dimensional slice of the three-dimensional turbulent premixed flame.

ated numerically and compared to the theoretical analysis. Fourth, the performance of the proposed method in terms of stability is presented both theoretically and numerically, using the test cases previously introduced. Fifth, since stability does not imply accuracy, the numerical accuracy of the proposed method is presented and its dependence on the time step size and the number of sub-iterations is discussed. Sixth, the performance of the proposed method in terms of elemental conservation is presented. In particular, the effects of the iterative procedure (and the number of sub-iterations used) are assessed. Finally, the computational efficiency of the method is discussed.

3.5.1 Theoretical analysis

To simplify the analysis, it is assumed transport is integrated explicitly (*i.e.* not modified by the sub-iterations). For the sub-iteration $k+1$ within a single iteration, Eq. 2.30 and 2.32 take the form

$$\mathbf{J}_k \cdot (\mathbf{Y}_{k+1} - \mathbf{Y}_k) = \rho_0 \mathbf{Y}_0 - \rho_k \mathbf{Y}_k + \Delta t \, (\mathbf{C} + \mathbf{D}) \cdot \mathbf{Y}_0 + \Delta t \boldsymbol{\Omega}_k^*, \tag{3.8}$$

where

$$\mathbf{J}_k = \rho_k \mathbf{I} + \frac{\Delta t}{2} \boldsymbol{\Lambda}_k. \tag{3.9}$$

The superscripts (n and $n+1$) have been dropped for clarity. The subscript 0 corresponds to

the final solution of the previous iteration. The terms in the equation can be reorganized as

$$\begin{aligned}\left(\mathbf{I}+\frac{\Delta t}{2}\left(\frac{1}{\rho}\mathbf{\Lambda}\right)_k\right)\cdot(\mathbf{Y}_{k+1}-\mathbf{Y}_k) = &-\mathbf{Y}_k \\ &+\frac{1}{\rho_k}\left[\rho_0\mathbf{Y}_0+\Delta t\,(\mathbf{C}+\mathbf{D})\cdot\mathbf{Y}_0\right] \\ &+\frac{\Delta t}{\rho_k}\mathbf{\Omega}^*_k.\end{aligned} \tag{3.10}$$

Expanding $\left(\frac{1}{\rho}\mathbf{\Lambda}\right)_k$, $\left(\frac{1}{\rho}\mathbf{\Omega}^*\right)_k$, and $\frac{1}{\rho_k}$ around $\mathbf{Y}_0$ gives

$$\begin{aligned}&\left(\mathbf{I}+\frac{\Delta t}{2}\left(\frac{1}{\rho}\mathbf{\Lambda}\right)_0\right)\cdot(\mathbf{Y}_{k+1}-\mathbf{Y}_k) = -\mathbf{Y}_k \\ &+\left[\frac{1}{\rho_0}+\left[\frac{\partial}{\partial\mathbf{Y}}\left(\frac{1}{\rho}\right)\right]_0\cdot(\mathbf{Y}_k-\mathbf{Y}_0)\right]\left[\rho_0\mathbf{Y}_0+\Delta t\,(\mathbf{C}+\mathbf{D})\cdot\mathbf{Y}_0+\Delta t\mathbf{\Omega}_0\right] \\ &+\frac{\Delta t}{2}\left(\frac{1}{\rho}\frac{\partial\mathbf{\Omega}}{\partial\mathbf{Y}}\right)_0\cdot(\mathbf{Y}_k-\mathbf{Y}_0)+\mathcal{O}\left(|\mathbf{Y}_k-\mathbf{Y}_0|^2\right).\end{aligned} \tag{3.11}$$

Subtracting Eq. 3.11 evaluated at two consecutive sub-iterations, and neglecting the second-order terms yields

$$\begin{aligned}&\left(\mathbf{I}+\frac{\Delta t}{2}\left(\frac{1}{\rho}\mathbf{\Lambda}\right)_0\right)\cdot(\mathbf{Y}_{k+1}-2\mathbf{Y}_k+\mathbf{Y}_{k-1}) = -(\mathbf{Y}_k-\mathbf{Y}_{k-1}) \\ &+\left[(\rho\mathbf{Y}+\Delta t\,(\mathbf{C}+\mathbf{D})\cdot\mathbf{Y}+\Delta t\mathbf{\Omega})\otimes\frac{\partial}{\partial\mathbf{Y}}\left(\frac{1}{\rho}\right)\right]_0\cdot(\mathbf{Y}_k-\mathbf{Y}_{k-1}) \\ &+\frac{\Delta t}{2}\left(\frac{1}{\rho}\frac{\partial\mathbf{\Omega}}{\partial\mathbf{Y}}\right)_0\cdot(\mathbf{Y}_k-\mathbf{Y}_{k-1}).\end{aligned} \tag{3.12}$$

A simpler expression reads

$$\mathbf{Y}_{k+1}-\mathbf{Y}_k = \mathbf{A}_0\cdot(\mathbf{Y}_k-\mathbf{Y}_{k-1}), \tag{3.13}$$

with

$$\mathbf{A}_0 = \mathbf{I}-\left(\mathbf{I}+\frac{\Delta t}{2}\left(\frac{1}{\rho}\mathbf{\Lambda}\right)_0\right)^{-1}\left(\mathbf{I}-\frac{\Delta t}{2}\left(\frac{1}{\rho}\frac{\partial\mathbf{\Omega}}{\partial\mathbf{Y}}\right)_0-\mathbf{T}_0\right), \tag{3.14}$$

where

$$\mathbf{T}_0 = \left[\left(\rho \mathbf{Y} + \Delta t \left(\mathbf{C} + \mathbf{D} \right) \cdot \mathbf{Y} + \Delta t \boldsymbol{\Omega} \right) \otimes \frac{\partial}{\partial \mathbf{Y}} \left(\frac{1}{\rho} \right) \right]_0 . \tag{3.15}$$

The convergence of the sub-iterations is assured as long as the absolute values of all eigenvalues of $\mathbf{A}_0$ are less than unity, *i.e.* the spectral radius of $\mathbf{A}_0$ is less than unity. The opposite implies a divergence (in the linear sense) of the sub-iterations which is likely to be associated with an unstable simulation. Without surprise, in the limit of $\Delta t \to 0$, the spectral radius of $\mathbf{A}_0$ goes to zero and the convergence of the sub-iterations is ensured. For practical time step sizes, large eigenvalues of $\mathbf{A}_0$ can be due to the large magnitude of the chemical Jacobian $\left(\frac{1}{\rho} \frac{\partial \boldsymbol{\Omega}}{\partial \mathbf{Y}} \right)_0$ or the matrix $\mathbf{T}_0$. However, it can be easily shown that the only eigenvalue of $\mathbf{T}_0$ is a ratio of densities (density of the explicit prediction *vs.* initial density) which is of order one and is negligible compared to the large eigenvalues of the chemical Jacobian (more details in Section 3.5.2). Consequently, the matrix $\mathbf{T}_0$ is neglected in the present theoretical analysis. This simplification will be further justified by the numerical tests in Section 3.5.4.2. Therefore, the rest of the theoretical analysis will consider the following matrix:

$$\mathbf{A}_0' = \mathbf{I} - \left(\mathbf{I} + \frac{\Delta t}{2} \left(\frac{1}{\rho} \boldsymbol{\Lambda} \right)_0 \right)^{-1} \left(\mathbf{I} - \frac{\Delta t}{2} \left(\frac{1}{\rho} \frac{\partial \boldsymbol{\Omega}}{\partial \mathbf{Y}} \right)_0 \right), \tag{3.16}$$

which is only a function of the full chemical Jacobian, and the approximate (diagonal) Jacobian. The convergence of the sub-iterations is then assured as long as the spectral radius of $\mathbf{A}_0'$ is less than unity.

Alternatively, one can consider the residuals in the relative species mass fractions instead of the residuals in their absolute values. These relative residuals are evaluated as follows:

$$\mathbf{Y}_{k+1}^{\mathrm{rel}} - \mathbf{Y}_k^{\mathrm{rel}} = \mathbf{A}_0'' \cdot \left(\mathbf{Y}_k^{\mathrm{rel}} - \mathbf{Y}_{k-1}^{\mathrm{rel}} \right), \tag{3.17}$$

where $\mathbf{Y}^{\mathrm{rel}} = \mathbf{G}^{-1} \mathbf{Y}$, with $\mathbf{G} = \mathrm{diag}\left(Y_{0,1}, \ldots, Y_{0,N} \right)$. $Y_{0,i}$ is the mass fraction of species i obtained at the end of the previous iteration. The matrix $\mathbf{A}_0''$ reads

$$\mathbf{A}_0'' = \mathbf{G}^{-1}\mathbf{A}_0'\mathbf{G} = \mathbf{I} - \left(\mathbf{I} + \frac{\Delta t}{2}\left(\frac{1}{\rho}\mathbf{\Lambda}\right)_0\right)^{-1}\left(\mathbf{I} - \frac{\Delta t}{2}\mathbf{G}^{-1}\left(\frac{1}{\rho}\frac{\partial \mathbf{\Omega}}{\partial \mathbf{Y}}\right)_0\mathbf{G}\right). \tag{3.18}$$

Note that both the absolute and the relative value system of equations are analytically equivalent. In particular, the eigenvalues of $\mathbf{A}_0''$ are identical to those of $\mathbf{A}_0'$.

3.5.2 Eigenvalue analysis

It is clear from Eq. 3.16 that if the approximation of the diagonal of the chemical Jacobian (Eq. 3.4), further referred to as the precondition matrix, were to be equal to the full chemical Jacobian, $\frac{\partial \mathbf{\Omega}}{\partial \mathbf{Y}}$, the scheme would be, in the linear sense, unconditionally stable (recall that $\mathbf{T}_0 = 0$ is assumed). In all other cases, the first pertinent analysis to justify the choice of the preconditioner (Eq. 3.3) is to evaluate the eigenvalue content of the precondition matrix and compare it to that of the full chemical Jacobian. To ensure a good convergence rate of the sub-iterations, the eigenvalue content of the precondition matrix should be close to that of the full Jacobian. This assumption is tested in the following.

More specifically, the eigenvalues of the chemical Jacobian $\frac{\partial \mathbf{\Omega}}{\partial \mathbf{Y}}$ correspond to the inverse of the chemical timescales (τ) present in the system. These timescales are associated with the rate of change of the species (or a combination of species) mass fractions in the system in the absence of transport. The idea of using a preconditioner is to allow the use of a time step larger than the smallest of these timescales. Consequently, given a time step Δt, it is important that the chemical timescales smaller than Δt be well represented by the precondition matrix, such that the source terms associated with these timescales are properly integrated over Δt. Note that the eigenvalues of the proposed diagonal precondition matrix correspond to an approximation of the reciprocal species lifetimes.

The species lifetimes obtained for the precondition matrix (Eq. 3.4) and the chemical timescales obtained with the full Jacobian are compared in Fig. 3.4. These are evaluated with the mixture composition and the temperature ($T = 1615$ K) corresponding to the peak rate of heat release in a one-dimensional flame similar to that presented in Section 3.4.1. For this *a priori* analysis, the one-

dimensional flame is computed with FlameMaster [146]. Note that, *a posteriori*, virtually identical results were obtained when the NGA solution was considered (Section 3.4.1). This is not surprising, as the precondition matrix and the Jacobian only depend on the local mixture composition and temperature, which should not be dependent on the solver used. It is interesting to associate species to each of the chemical timescales shown in Fig. 3.4. However, it is important to note that not every chemical timescale corresponds to a species lifetime. The timescales are ordered from the smallest to the largest. They are then compared, entry by entry, between the preconditioned and the full Jacobian.

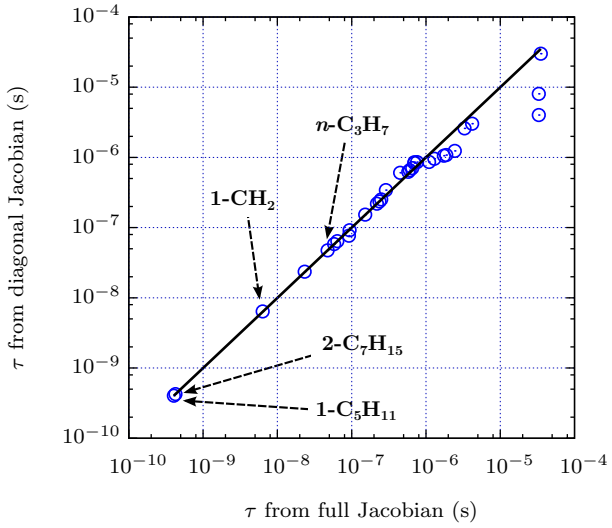

Figure 3.4: Comparison of the chemical timescale (τ) of the full chemical Jacobian to the species lifetime of the preconditioned chemical Jacobian.

It is well known that because of elemental conservation, n_k of the eigenvalues of the full Jacobian are zero, with n_k the number of elements in the chemical system [112]. Only one of them is zero for the precondition matrix, *i.e.* the one associated with N_2, as its source term is identically zero. This is to be expected from the definition of the precondition matrix. Therefore, only the 31 smallest timescales are shown in Fig. 3.4.

Although Fig. 3.4 does not provide direct information on the stability limit, it can be observed that all the timescales smaller than about 10^{-5} s are well approximated by the precondition matrix. In other words, the diagonal matrix represents accurately the smallest chemical timescales in the

system. As mentioned previously, the proposed method is similar to the Jacobi method, which is guaranteed to converge in diagonal-dominant problems (but it can also converge in other cases). It is therefore interesting to assess if the matrix $\mathbf{I} - \frac{\Delta t}{2}\left(\frac{1}{\rho}\frac{\partial \mathbf{\Omega}}{\partial \mathbf{Y}}\right)_0$ (Eq. 3.16) is diagonal dominant for $\Delta t < 10^{-5}$ s. Figure 3.5(a) shows that the matrix is clearly not diagonal dominant for $\Delta t = 5 \times 10^{-6}$ s. However, the corresponding normalized matrix introduced in Eq. 3.18, $\mathbf{I} - \frac{\Delta t}{2}\mathbf{G}^{-1}\left(\frac{1}{\rho}\frac{\partial \mathbf{\Omega}}{\partial \mathbf{Y}}\right)_0 \mathbf{G}$ is close to be diagonal dominant for the same Δt, as shown in Fig. 3.5(b), *i.e.* all the terms of each row are smaller in magnitude than the corresponding term on the diagonal. Since both of these matrices have the same eigenvalue content and the same terms on the diagonal, it becomes clear why the precondition matrix approximates adequately the smaller timescales of the full Jacobian.

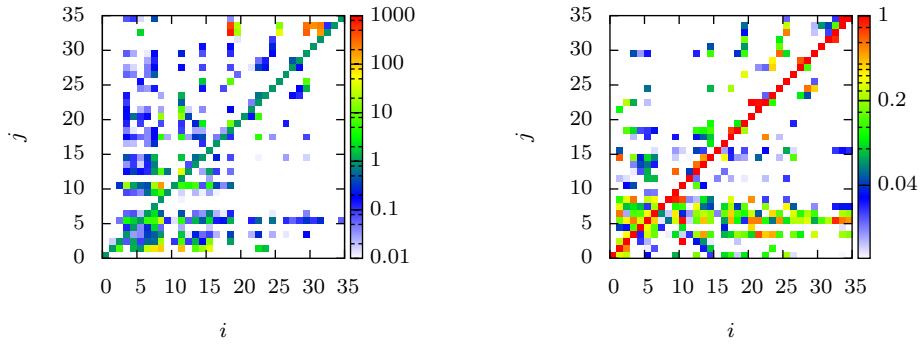

(a) $\mathbf{I} - \frac{\Delta t}{2}\left(\frac{1}{\rho}\frac{\partial \mathbf{\Omega}}{\partial \mathbf{Y}}\right)_0$ (b) $\mathbf{I} - \frac{\Delta t}{2}\mathbf{G}^{-1}\left(\frac{1}{\rho}\frac{\partial \mathbf{\Omega}}{\partial \mathbf{Y}}\right)_0 \mathbf{G}$

Figure 3.5: Relative magnitude of the elements of each row compared to the element on the respective diagonals. $\Delta t = 5 \times 10^{-6}$ s.

The results from Fig. 3.5(b) suggest that the Jacobi method may be successfully applied to such a matrix (it is guaranteed to converge if the matrix is diagonal dominant). This will be verified in the following sections as the stability and the convergence rate of the method is analyzed considering the spectral radius of $\mathbf{A}_0'$ (or, equivalently, $\mathbf{A}_0''$).

3.5.3 Convergence of the sub-iterations

The one-dimensional flame test case is used to evaluate numerically the convergence of the sub-iterations. The maximum density residual over the whole domain is considered as its convergence is

controlled by the convergence of all the chemical species. Figure 3.6 displays the residual through two complete time steps for four different time step sizes. As the time step size decreases, the residuals decrease faster. The rate of convergence of the sub-iterations is observed to follow an exponential relationship, *i.e.* $\mathrm{Res_k} \sim \mathrm{r^k}$ with r the convergence rate. The numerical convergence rate r is computed by fitting an exponential curve to the density residuals. Since density is an analytical function of the species mass fractions, its convergence rate should tend towards that of the slowest converging species mass fraction. In other words, this convergence rate should be close to the spectral radius of $\mathbf{A}'_0$ (Eq. 3.16).

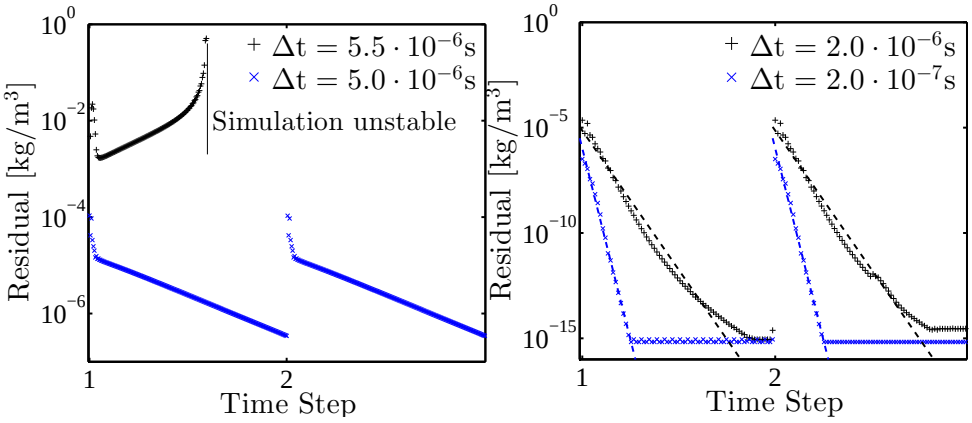

(a) At the stability limit

(b) Far from the stability limit

Figure 3.6: Evolution of the density residual as a function of sub-iterations over two time steps for the proposed semi-implicit time-integration scheme. The dashed lines correspond to fitted exponential curves averaged over several time steps.

The numerical and theoretical (spectral radius) convergence rates are compared in Fig. 3.7. The numerical convergence rates are in relatively good agreement with the theoretical values. This further justifies neglecting the variable density matrix, $\mathbf{T}_0$, in the present theoretical analysis (Section 3.5.1). Using the spectral radius (*i.e.* the largest eigenvalue) as a measure of the convergence rate is a worst case scenario, as the projection of the density residuals on the associated eigenvector might be identically zero (to machine precision). This might explain partially better numerical convergence rates than theoretically predicted.

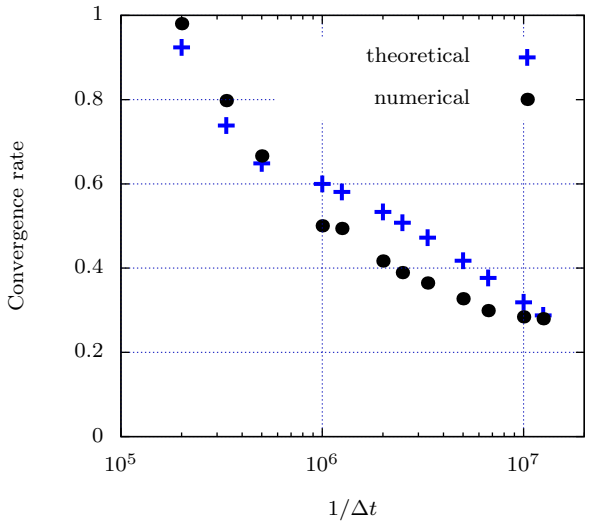

Figure 3.7: Rate of convergence of the sub-iterations: comparison between theoretical (largest spectral radius of $\mathbf{A}_0'$) and numerical (rate of convergence of the largest density residuals) results for the one-dimensional flame.

3.5.4 Stability

The stability of the preconditioned iterative method relies on the stability of the sub-iterations. By stability, it is meant that the solution remains bounded in time. Note that stability does not require the sub-iterations to be fully converged, nor does it imply accuracy. Due to the high non-linearity and the complexity of the governing equations, the stability condition for the proposed preconditioned iterative method and its relation to sub-iteration convergence rate are investigated theoretically (simplified system) and numerically in the present section.

3.5.4.1 Theoretical stability

Assuming the residuals of the species mass fractions at each sub-iteration remain sufficiently small for the linear analysis presented in Section 3.5.1 to be valid, then the sub-iterations do not diverge if the spectral radius of $\mathbf{A}_0'$ (Eq. 3.16), is less than 1. In other words, if this spectral radius is less than 1, stability is ensured, independently of the number of sub-iterations used. However, the accuracy of the solution will be affected by the number of sub-iterations (discussed in Section 3.5.5).

The spectral radius of $\mathbf{A}_0'$ is plotted as a function of temperature in Fig. 3.8(a) for different values

of Δt. The matrices $\left(\frac{1}{\rho}\mathbf{\Lambda}\right)_0$ and $\left(\frac{1}{\rho}\frac{\partial \mathbf{\Omega}}{\partial \mathbf{Y}}\right)_0$ are evaluated from the one-dimensional flame solution, computed with FlameMaster [146]. Note that the maximum of each curve corresponds to a point in Fig. 3.7. The spectral radius is shown to be a strong function of temperature. It is not surprising that the chemical system is more sensitive to perturbations at higher temperatures (where the Arrhenius rate constants are larger). It is important to remember that the stability limit in a reacting flow also depends on the nature of the transport terms, which have been ignored for the present analysis, as well as the coupling between the scalar transport and the Navier-Stokes equations. In particular, the most unstable location may not systematically occur at the highest temperature in the domain.

For comparison, the matrix corresponding to $\mathbf{A}'_0$ using an explicit time-integration of the chemical source term is introduced:

$$\mathbf{A}'_{0,\text{exp}} = \frac{\Delta t}{2}\left(\frac{1}{\rho}\frac{\partial \mathbf{\Omega}}{\partial \mathbf{Y}}\right)_0. \tag{3.19}$$

The spectral radius of $\mathbf{A}'_{0,\text{exp}}$ is plotted against temperature in Fig. 3.8(b) for different values of Δt. The (theoretical) stability limit for the explicit scheme is $\Delta t = 5.6 \times 10^{-11}$ s, whereas it is $\Delta t = 6.1 \times 10^{-6}$ s for the semi-implicit scheme. Under the present conditions, it can be clearly observed that the proposed method has the potential to increase the stability limit by several orders of magnitude.

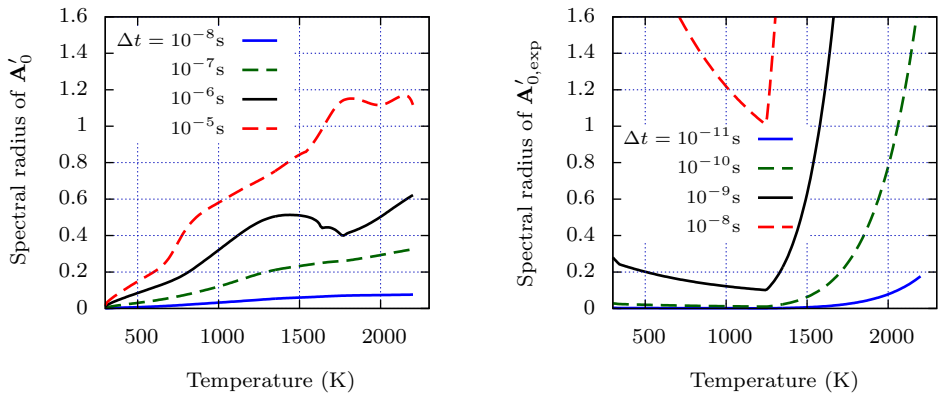

(a) Proposed semi-implicit

(b) Explicit

Figure 3.8: Spectral radius of $\mathbf{A}'_0$ and $\mathbf{A}'_{0,\text{exp}}$ as a function of temperature in the one-dimensional premixed flame.

3.5.4.2 Numerical stability

The previous section provided a stability criterion through theoretical analysis of a system of reduced complexity. In this section, the stability of the complete scheme is analyzed numerically. Note that, while the theoretical analysis was done assuming explicit transport, the test cases are performed with semi-implicit transport (as described in Section 2.2), which is used in turbulent flame simulations. It is important to demonstrate the performance of the proposed preconditioning method within the algorithmic setting used in practical simulations. For the present tests, the same stability limits were found for the transport terms treated explicitly and implicitly. This is not surprising because the convective CFL number is less than unity for all test cases. It also confirms that the transport terms may be neglected in the previous theoretical analysis (Section 3.5.1).

The 1D test case is considered first. For all time step sizes tested, it was found that converging (as opposed to *converged*) sub-iterations implied a stable simulation. In other words, unless the sub-iterations diverge, the simulation remains stable. As shown in Fig. 3.6(a), the largest time step size that can be used for the simulation to be stable is found to be $\Delta t = 5 \times 10^{-6}$ (with $\Delta t = 5.5 \times 10^{-6}$ leading to unstable results). This value is very close to the theoretical stability limit of $\Delta t = 6.1 \times 10^{-6}$ s (Section 3.5.4.1). Note that the largest numerically stable time step size using an explicit time-integration of the chemical source term is $\Delta t = 2 \times 10^{-10}$ s, also close to the theoretical stability limit ($\Delta t = 5.6 \times 10^{-11}$ s). These stability limits are summarized in Table 3.1.

	Numerical	Theoretical
Proposed scheme	5×10^{-6} s	6.1×10^{-6} s
Explicit scheme	2×10^{-10} s	5.6×10^{-11} s

Table 3.1: Largest stable time step size for the proposed semi-implicit scheme and the explicit time-integration of the chemical source terms for the 1D flame test case. Numerical and theoretical results (see Section 3.5.4.1) are compared.

These results suggest that the stability limit can be well approximated by the theory, *i.e.* the maximum Δt such that the spectral radius of $\mathbf{A}_0'$ (Eq. 3.16) is less than unity. As such, this should also correspond to the numerical stability limit for the 3D turbulent premixed flame. However, $\Delta t = 5 \times 10^{-6}$ s corresponds to a convective CFL number of approximately 7, which is too large for

the overall spatio-temporal scheme to be stable. In other words, for the turbulent case, the largest stable time step size is constrained not by the time-integration of the chemical source terms but by the convective CFL condition. This allowed the simulation to be performed with a convective CFL of 0.8 (see Section 3.4.2), which corresponds to $\Delta t = 5.7 \times 10^{-7}$ s.

To understand why such a large time step size could be used for the turbulent flame simulation, the spectral radius of $\mathbf{A}'_0$ (Eq. 3.15) is plotted against temperature throughout the whole domain of the 3D simulation in Fig. 3.9. For reference, the one-dimensional equivalent is added on top of the scatter plot. This plot suggests that the stability of the chemical system alone (Eq. 3.8) is only slightly altered by turbulence.

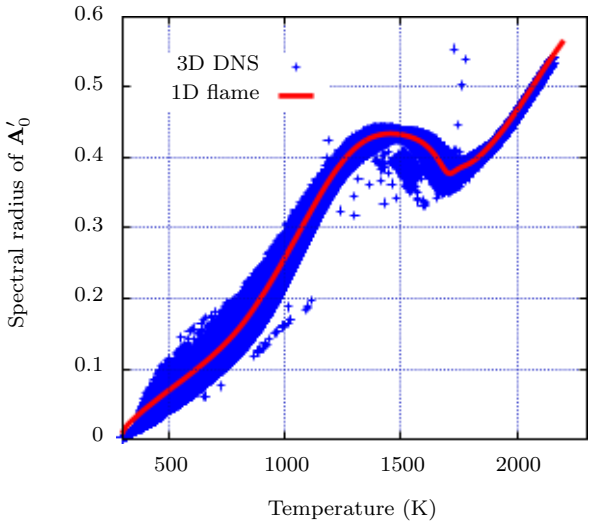

Figure 3.9: Scatter plot of the spectral radius of $\mathbf{A}'_0$, with $\Delta t = 5.7 \times 10^{-7}$ s, as a function of temperature in the three-dimensional turbulent flame. The one-dimensional profile is added for comparison.

3.5.4.3 Summary

It was shown in the present section that the stability limit of the proposed method is well approximated by the largest Δt such that the spectral radius of $\mathbf{A}'_0$ is less than 1. This stability limit is independent of the number of sub-iterations used. On the other hand, the number of sub-iterations does affect accuracy, and it will be discussed in the next section.

An important result is the fact that the stability of the three-dimensional turbulent flame was

constrained by the convective CFL limit, rather the time-integration of the chemical source terms. This means that the proposed method has a great potential, in terms of stability, for such flow simulations. Theoretical estimates of the stability limits for other types of flows, fuels, conditions, and chemical mechanisms will be discussed in Section 3.6.1.

3.5.5 Accuracy

In the previous subsection, we established the stability limit(s) of the proposed scheme. We now investigate the accuracy for a given stable simulation.

3.5.5.1 Order of accuracy

The order of accuracy (*i.e.* the power-dependence of the error as the time step size is reduced) of the proposed method is determined for the 1D (freely propagating) flame test case. In the absence of chemistry, the algorithm used in NGA can be formally shown to be second-order accurate if two or more sub-iterations are used [145]. In practice, four sub-iterations are typically used (to improve stability and to achieve adequate accuracy of the fractional-step) [55, 31, 173]. For the present test case, four sub-iterations are also used to evaluate the order of accuracy. The impact of the number of sub-iterations on the absolute magnitude of these errors is discussed in the next sub-section.

Simulations with different time steps are performed and results are presented in Fig. 3.10. The errors for various quantities are evaluated as the absolute difference of their integrated value in temperature space compared with a reference solution obtained with $\Delta t = 2 \times 10^{-8}$ s. The species n-C_7H_{16}, OH, CO, and H_2O are chosen as representatives of reactants, radicals, intermediates, and products. All of these quantities are found to demonstrate second-order accuracy in time, as shown in Fig. 3.10. It is interesting to note that the expected order of accuracy is already recovered with only four sub-iterations.

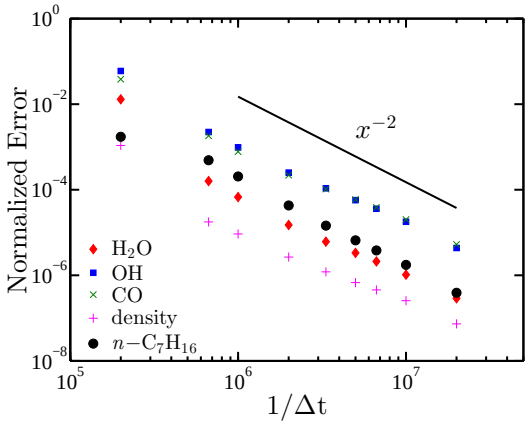

Figure 3.10: Temporal accuracy of the method as a function of the time step size for the one-dimensional, propagating flame. The errors for the various species mass fractions are evaluated as the absolute difference of their integrated value in temperature space compared with a reference solution obtained with $\Delta t = 2 \times 10^{-8}$ s.

3.5.5.2 Magnitude of errors

It is important to distinguish order of accuracy (as the time step size goes to zero) and absolute magnitude of errors. In order to illustrate the quality of the solution using various time step sizes, Table 3.2 compares the laminar flame speeds, Fig. 3.11(a) presents the temperature profiles in physical space (shifted to coincide at $T = 400$ K), and Fig. 3.11(b) shows the intermediate species n-C_3H_7 mass fraction *vs.* temperature profiles. The first two quantities are chosen, as they correspond to the two most important quantities associated with a laminar flame. The n-C_3H_7 mass fraction *vs.* temperature profile is chosen, as it is the quantity the most sensitive to the time step size (small reciprocal lifetime where its mass fraction is non-zero). It is clear that, up to a time step size of $\Delta t = 2 \times 10^{-6}$ s, errors are negligible even with only four sub-iterations (0.3% error in laminar flame speed and virtually no difference in the temperature and species profiles). At the stability limit ($\Delta t = 5 \times 10^{-6}$ s), the solution is deteriorated when only four sub-iterations are used. However, using a large number of sub-iterations, the solution reaches similar level of accuracy.

These results demonstrate that, for time step sizes smaller than $\Delta t = 2 \times 10^{-6}$ s, sufficiently accurate solutions for the 1D flame are obtained with as little as four sub-iterations. For time step sizes between $\Delta t = 2 \times 10^{-6}$ s and the stability limit, more sub-iterations are needed to reach sufficient accuracy. This is a direct consequence of the decreasing convergence rates with increasing

Δt (s)	Q	$\rho_{\max}(\mathbf{A}_0')$	S_L (cm/s)
2×10^{-7}	4	0.42	28.65
2×10^{-6}	4	0.65	28.57
5×10^{-6}	4	0.92	26.93
5×10^{-6}	200	0.92	28.64

Table 3.2: Laminar flame speed obtained from simulations with various time step sizes and number of sub-iterations. $\rho_{\max}(\mathbf{A}_0')$ is the theoretical maximum spectral radius of $\mathbf{A}_0'$ in the flame.

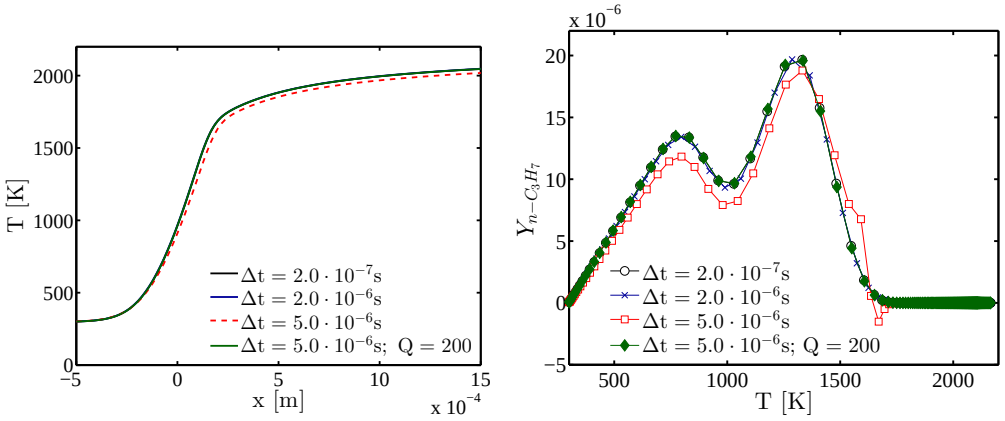

(a) Temperature *vs.* distance

(b) n-C_3H_7 mass fraction *vs.* temperature

Figure 3.11: Impact of time step size and number of sub-iteration on the accuracy of 1D propagating flames. When not mentioned, four sub-iterations are used ($Q = 4$).

time step sizes, as presented in Fig. 3.7. There should exist a pair of time step size/number of sub-iterations such that performance is optimized for a given level of accuracy. However, since the method is meant to be used with turbulent flames, and not 1D flames, such optimization would be of limited interest since the largest time step size allowed by the convective CFL condition in the turbulent flame is smaller than $\Delta t = 2 \times 10^{-6}$ s. Because the spectral radius in the turbulent flame is similar to that of the 1D flame (see Fig. 3.9), four sub-iterations should be sufficient to obtain accurate solutions. This is further tested below.

As mentioned in the previous section, the turbulent premixed flame simulation was performed with a convective CFL number of 0.8 ($\Delta t = 5.7 \times 10^{-7}$ s). In order to evaluate the quality of the solution, a comparative simulation was performed with a smaller time step size, $\Delta t = 8 \times 10^{-8}$ s (four sub-iterations are used for both simulations). Note that this comparative simulation was also run until statistically steady state was reached. While the time step size varies by a factor of 7

between the two simulations, virtually no differences could be identified between the simulations. Figure 3.12 shows a representative comparison of joint probability density functions of the species mass fraction *vs.* temperature. This type of joint probability density functions is used to evaluate the impact of turbulence on the chemistry (Chapter 5) and it is important to make sure that any deviation away from a laminar flame is not due to numerical artifacts. The results obtained using both time step sizes are virtually identical, which is consistent with the observations made with the one-dimensional flame test case.

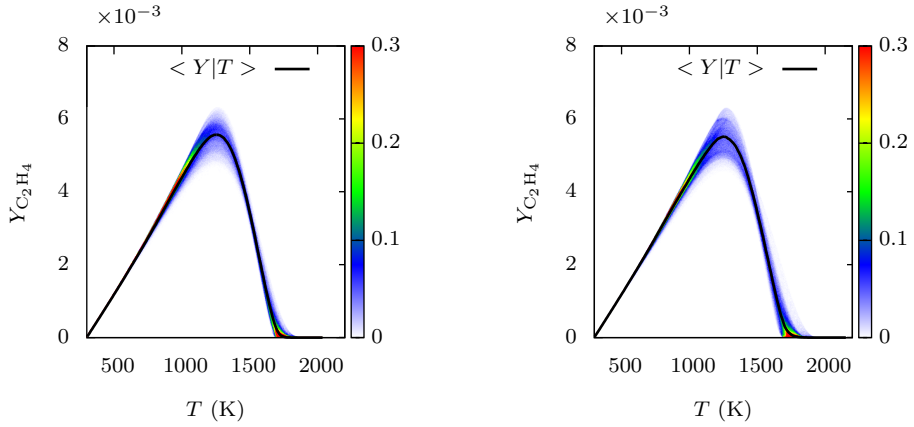

(a) $\Delta t = 5.7 \times 10^{-7}$ s (CFL= 0.8)

(b) $\Delta t = 8 \times 10^{-8}$ s

Figure 3.12: Comparison between the joint probability density function of the C_2H_4 mass fractions *vs.* temperature obtained with different time step sizes.

3.5.6 Mass conservation

As it can be noted from the presentation of the method in Section 2.2, the sum of the species mass fraction is not implicitly recovered. In other words, with the proposed diagonal preconditioner, the sum of mass fraction is not guaranteed to remain equal to unity. While element conservation is not ensured with the proposed scheme using only one sub-iteration, in practice, with the number of sub-iterations used, elemental mass fractions were found to be adequately conserved. This can be observed in Fig. 3.13 for the 3D turbulent premixed flame, at a CFL of 0.8 with only four sub-iterations being used. Under the assumption of unity Lewis number transport, the elemental mass

fractions (Y_{C}, Y_{H}, Y_{O}) should remain perfectly at their inlet values. Any deviations are evidence of mass conservation errors. The maximum deviations in the domain are only about 1% of the inlet values. These maximum deviations are found to occur in the oxidation layer of the turbulent flame.

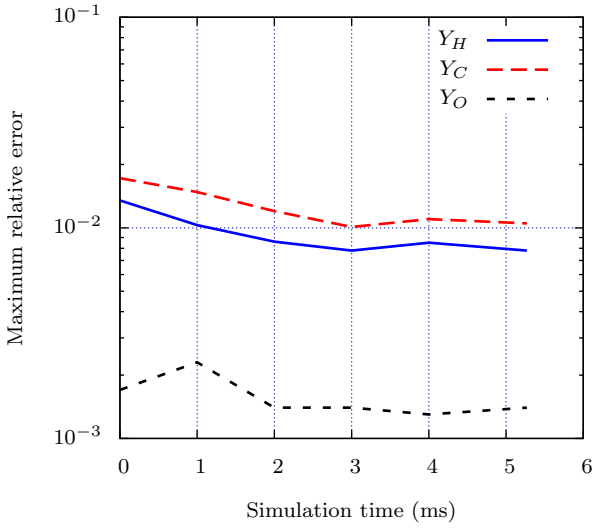

Figure 3.13: Maximum deviation in the domain from the inlet elemental mass fractions *vs.* simulation time. The results shown are for the three-dimensional turbulent flame with $\Delta t = 5.7 \times 10^{-7}$ s and four sub-iterations.

Using more sub-iterations leads to better elemental conservation, as shown in Fig. 3.14 for the 1D flame test case with $\Delta t = 2 \times 10^{-6}$ s. In particular, the rate of convergence of these elemental mass fraction residuals follows the theoretical spectral radius of 0.65. Note that each of these simulations were performed with a different number of sub-iterations Q until a constant propagation speed (flame speed) and a constant flame structure were reached.

3.5.7 Computational efficiency

As presented in Section 2.2, the cost per sub-iteration with the proposed semi-implicit scheme is virtually identical to that using an explicit time-integration of the chemical source terms. In addition, with the proposed scheme, a number of four sub-iterations was found to be sufficient in practice to achieve adequate accuracy and elemental conservation. As previously mentioned, this number of sub-iterations is typically used for the simulation of non-reacting flows [55, 31, 173] and reacting

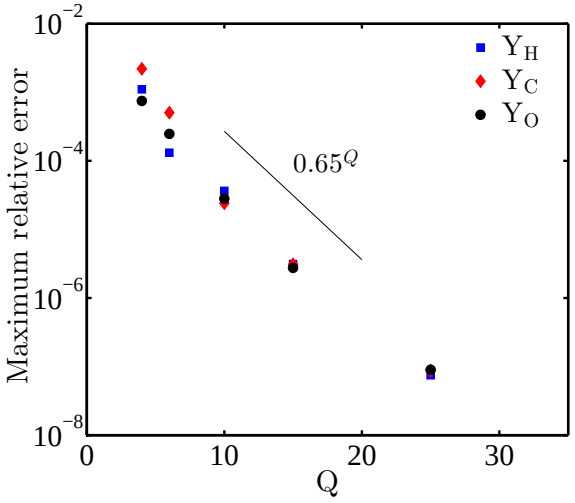

Figure 3.14: Maximum deviation in the domain from the inlet elemental mass fractions *vs.* number of sub-iterations, Q. The results shown are for the one-dimensional, propagating flame using $\Delta t = 2 \times 10^{-6}$ s. The theoretical convergence rate is added for comparison.

flows with explicit time-integration. Therefore, the cost per iteration with the proposed scheme is (in practice) similar to that using an explicit time-integration of the chemical source terms.

Since the proposed scheme does not alter the cost per iteration compared to an explicit time-integration of the chemical source terms, the increase in efficiency (speed-up) is equal to the increase in largest stable time step size. For unsteady flames, the optimal time step size corresponds to the convective CFL limit (the theoretical limit is unity, but 0.8 is the target within our numerical framework). While the time step size in the 1D flame simulations was limited by the chemistry, the convective CFL number was 0.2 ($\Delta t = 2 \times 10^{-6}$ s). This means that for turbulent flames with $u_{\max}/S_{L,b}$ larger than 4, with $u_{\max}$ the maximum velocity in the domain and $S_{L,b}$ the laminar flame speed in the burnt gas ($u_{\max}/S_{L,b} = 1$ for a 1D flame), the time step size will be limited by the convective CFL limit. This was the case with the 3D turbulent flame test case in which $u_{\max}/S_{L,b} \approx 14$. Consequently, the proposed time-integration method is optimally efficient for such turbulent flames, in the context of the numerical framework of NGA.

3.6 Discussion

The proposed preconditioner was shown to exhibit very good performance for the test cases analyzed, and in particular it allowed the use of a time step size limited by the convective CFL (3D turbulent flame). In this section, in light of the results presented previously, the theoretical analysis of the stability limit using the proposed scheme is extended to various flames, fuels, unburnt conditions, and kinetic mechanisms. An ignition case is also considered. Additional validation of the numerical stability is provided for a few selected cases. A quantification of the accuracy of the solutions obtained with the proposed method is also presented for these cases. Then, the advantages of the proposed preconditioner over alternative methods are highlighted. Subsequently, the limitations of the present method are discussed. The objective of this section is to help one decide if the proposed method is well suited for a specific unsteady reacting flow simulation.

3.6.1 Extension

The theoretical analysis presented in Section 3.5.1 is general and does not depend on the fuel, the chemical mechanism, the flow configuration, or the unburnt conditions. In particular, the eigenvalue analysis (Section 3.5.2) and the theoretical stability conditions (Section 3.5.4.1) can be applied to any reacting flow. These analyses, which consider a dependence on the local mixture composition and the temperature only, were further validated in a one-dimensional flame configuration (Section 3.5.4.2). The results were also argued to be independent of the transport terms. Finally, it was shown that, even in a highly turbulent three-dimensional flame, the departure from a one-dimensional flame solution was not sufficient to significantly influence the stability (both theoretical and numerical). In summary, the theoretical analysis (without transport) is sufficient to determine the stability and the convergence rate of any laminar or turbulent reacting flow.

As such, the theoretical results are extended in this section by considering a wide range of one-dimensional flame and zero-dimensional ignition solutions (each computed with FlameMaster [146]). First, for premixed flames, the effects of the fuel, the unburnt conditions, and the chemical mechanism on the theoretical stability limits are investigated. Then, the analysis is performed for non-

premixed flamelets with different scalar dissipation rates and a 2D coflow diffusion flame. Finally, a homogeneous ignition case at constant pressure is considered.

3.6.1.1 Premixed flames

The theoretical performance of the proposed semi-implicit method is tested on a series of one-dimensional unstretched premixed flames.

First, the unburnt conditions are kept fixed and various fuels are considered. Four additional fuels are tested: H_2 combined with the chemical model presented in Ref. [77] (9 species 52 reactions), CH_4 with GRI-MECH 3.0 [163] (36 species 422 reactions), *i*-C_8H_{18} with CaltechMech v2.1 [18] (171 species 1835 reactions), and *n*-$C_{12}H_{26}$, also with CaltechMech. The analysis performed in Section 3.5.2 is repeated with these fuels. The species lifetimes at the location of the peak heat release obtained from the semi-implicit precondition matrix (Eq. 3.4) are compared to the chemical timescales obtained from the full chemical Jacobian in Fig. 3.15. Same as observed in Section 3.5.2, for all fuels (and mechanisms) tested, the diagonal Jacobian (precondition matrix) approximates very well almost all the timescales smaller than 10^{-5} s. Similarly, as presented in Table 3.3, the stability limits using the proposed scheme are very close to the one found in Section 3.5.4.1.

Second, the same *n*-C_7H_{16} premixed flame with the unburnt conditions presented in Section 3.4.1 is computed using CaltechMech. Again, the stability limit (Table 3.3) is only marginally affected by the chemical mechanism.

Third, a series of unburnt conditions are used for the *n*-C_7H_{16} premixed flame (using the mechanism introduced in Section 3.4.1). As the unburnt conditions encountered in practical combustion devices correspond typically to higher temperature and pressure, both these quantities are increased in this series of tests. Then, the equivalence ratio, which can significantly vary in a combustion device, is modified in the test cases to cover a wide range centered around stoichiometry. Table 3.3 presents the theoretical stability limit for all these cases. Again, the largest (theoretically) stable time step size varies only slightly throughout all cases.

An important conclusion can be drawn from the results shown in Table 3.3: the stability limit,

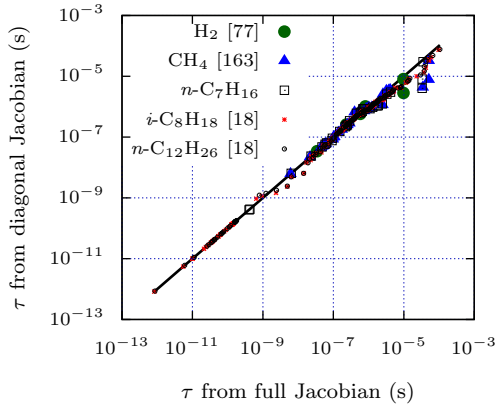

Figure 3.15: Comparison of the chemical timescale (τ) of the full chemical Jacobian to the species lifetime of the preconditioned chemical Jacobian at the peak rate of heat release, considering various fuels and chemical mechanisms.

using the proposed iterative semi-implicit preconditioning method, is only marginally sensitive to the fuel, the unburnt condition, and the mechanism used. As mentioned in Section 3.5.7, the target time step size is the convective CFL limit. An effective CFL number is therefore computed for each of these 1D premixed flame (see Table 3.3), assuming 24 grid points per flame thickness (see Section 3.4.1) are necessary for accurate simulation of a 1D laminar flame ($u_{\max} = S_{L,b}$). The effective CFL number would be larger for turbulent flames and would increase with the turbulent intensity. From these results, it is obvious that even for moderately turbulent flames, the time step size would be restricted by the convective CFL, rather than the chemistry.

These results relate to the stability limit only, and do not suggest anything about accuracy. As shown in Section 3.5.5, the accuracy is a function of the spectral radius, which is a function of the time step size, and the number of sub-iterations used. Depending on the flow configuration considered (turbulent, laminar, strained,...), four sub-iterations may be sufficient for the solution to be accurate, even at the stability limit. However, the opposite is also possible. Under such circumstance, either the time step size has to be decreased or the number of sub-iterations has to be increased. This choice depends on the spectral radius *vs.* time step size profile (previously shown in Fig. 3.7).

Figure 3.16 presents such profiles for flames corresponding to each of the chemical mechanisms

Fuel	ϕ	P_0 (atm)	T_u (K)	$\Delta t_{\max}$ (s) explicit	$\Delta t_{\max}$ (s) semi-implicit	Equivalent convective CFL
H_2 [77]	0.9	1	298	5.2×10^{-8}	1.6×10^{-6}	1.2
CH_4 [163]	0.9	1	298	2.7×10^{-9}	5.0×10^{-6}	0.47
n-C_7H_{16}	0.9	1	298	5.6×10^{-11}	6.1×10^{-6}	0.76
i-C_8H_{18} [18]	0.9	1	298	2.3×10^{-14}	4.7×10^{-6}	0.45
n-$C_{12}H_{26}$ [18]	0.9	1	298	2.2×10^{-14}	4.6×10^{-6}	0.55
n-C_7H_{16} [18]	0.9	1	298	4.5×10^{-14}	4.6×10^{-6}	0.58
n-C_7H_{16}	0.9	1	400	4.3×10^{-11}	5.2×10^{-6}	0.89
n-C_7H_{16}	0.9	1	600	2.7×10^{-11}	3.8×10^{-6}	1.1
n-C_7H_{16}	0.9	2	298	5.2×10^{-11}	6.2×10^{-6}	1.3
n-C_7H_{16}	0.9	10	298	5.0×10^{-11}	6.5×10^{-6}	3.1
n-C_7H_{16}	0.7	1	298	2.1×10^{-10}	9.5×10^{-6}	0.58
n-C_7H_{16}	1.1	1	298	3.9×10^{-11}	4.3×10^{-6}	0.62
n-C_7H_{16}	1.3	1	298	7.4×10^{-11}	4.3×10^{-6}	0.43

Table 3.3: Theoretical largest stable time step size for the proposed semi-implicit scheme and the explicit time-integration of the chemical source terms with various unstretched one-dimensional premixed flames.

used in this section (and presented in Table 3.3). The first three mechanisms, although used for different flame conditions, exhibit very similar profiles. This means that, with these mechanisms, a moderate decrease in time step size from the stability limit translates in an appreciable decrease in spectral radius. For the 1D test case analyzed in Section 3.4.1, a time step size three times smaller than the theoretical stability limit was shown to provide sufficient accuracy with only four sub-iterations.

Interestingly, the spectral radius profile exhibits a plateau just below the stability limit over a wide range of time step size with CaltechMech. This means that, in order to obtain a minimal level of convergence of the sub-iterations, either a very large number of sub-iterations or a very small time step size would be needed. However, this is not what is observed numerically, as shown in Fig. 3.17, since accurate solutions are obtained with time step sizes as large as half the numerical stability limit, still with only four sub-iterations.

This result is better understood by considering the density residuals *vs.* sub-iterations for the *n*-C_7H_{16} flame with CaltechMech, with $\Delta t = 2 \times 10^{-6}$ s, presented in Fig. 3.18 (similar to Fig. 3.6). Their convergence rate is found to be much closer to the third largest eigenvalue of $\mathbf{A}'_0$ (0.689), as opposed to its largest one (*i.e.* spectral radius), corresponding to 0.997. In other words, the

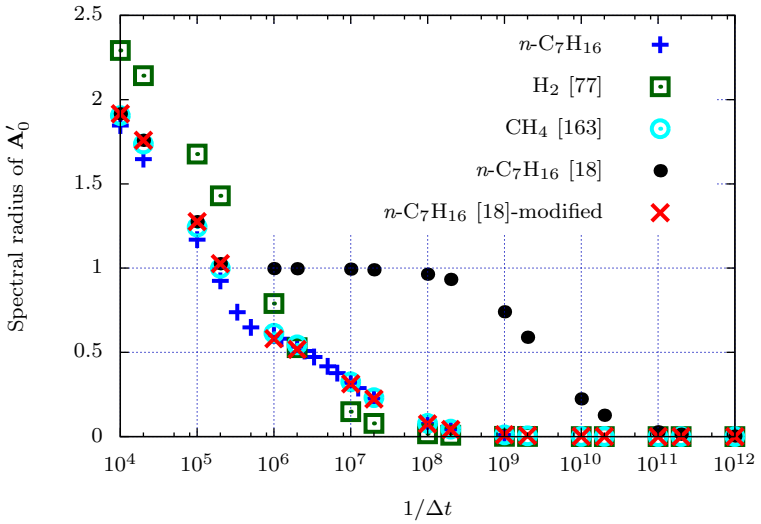

Figure 3.16: Spectral radius of $\mathbf{A}'_0$ *vs.* the inverse of the time step size for various cases presented in Table 3.3. The red cross symbols correspond to the profile for the n-C_7H_16/air flame with the stiff reaction (Eq. 3.20) removed from CaltechMech.

projection of the species mass fractions residuals on the eigenvectors associated with the two largest eigenvalues is negligible. This is consistent with the fact that these two largest eigenvalues are only due to the presence in the chemical mechanism of the following fast reversible reaction:

$$A_1C_2H_2{-}C_8H_7 \rightleftarrows A_1C_2H_3^\star{-}C_8H_7, \tag{3.20}$$

which involves species that have negligible mass fractions in the flame simulated (these species are soot precursors and should not be present in the lean flames considered in this chapter). The high pressure limit rate constant (the only one available in the literature) was prescribed for this reaction. Such rate constant is obviously too large, especially for the present atmospheric flames. The spectral radius *vs.* time step size profile obtained when this reaction is removed from the chemical mechanism is shown in Fig 3.16 (red cross symbols). The profile is virtually identical to the one obtained with the 35-species mechanism introduced in Section 3.4.1. This means that the proposed method is also efficient with a mechanism as large as CaltechMech, which is far larger than any other mechanism used for the simulation of three-dimensional turbulent premixed flames [9, 10, 160, 176, 70, 53, 11].

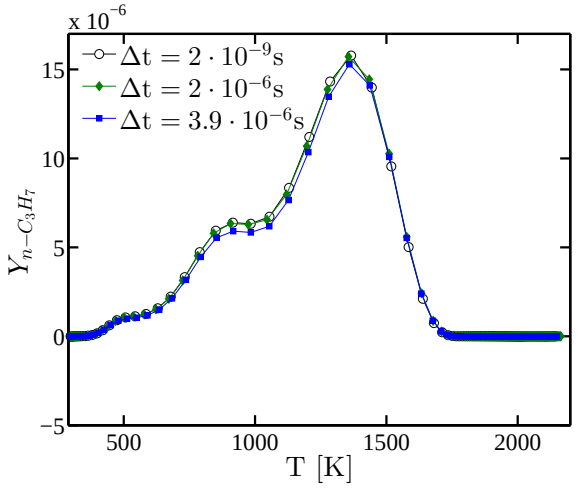

Figure 3.17: Profiles of n-C_3H_7 mass fraction *vs.* temperature in the one-dimensional, n-C_7H_{16} propagating flame (similar to the test case of Section 3.4.1) with CaltechMech. The solutions from using three different time step sizes, each with 4 sub-iterations, are compared.

3.6.1.2 Non-premixed flames

The theoretical stability limit using the proposed scheme is now evaluated for a series of (unity Lewis number) non-premixed flamelets [136]. These one-dimensional flamelets correspond to solutions close to the axis of symmetry of counter-flow diffusion flames and to local solutions close to the stoichiometric isosurface of mixture fraction of turbulent flames.

First, two n-C_7H_{16}/air flamelets are considered: one with a small scalar dissipation rate (typically found in laminar co-flow diffusion flames and turbulent diffusion flames, at moderate Reynolds number) and one with a large scalar dissipation rate, corresponding to half the dissipation rate leading to extinction. The results are shown in Table 3.4. Once again, the stability limits using the proposed scheme are very similar to the values found for the series of premixed flames (previous section). Additionally, the dissipation rate does not seem to have a strong effect on the stability of the scheme.

Second, two C_2H_4/air flamelets are considered: again, one with a small scalar dissipation rate, and one with a large dissipation rate. These two flamelets are used to estimate theoretically the stability limit of a 2D-coflow diffusion flame. The 2D flame corresponds to an International Sooting Flame Workshop target flame (more details in Ref. [88, 87]). The ethylene fuel (17.6% by mass)

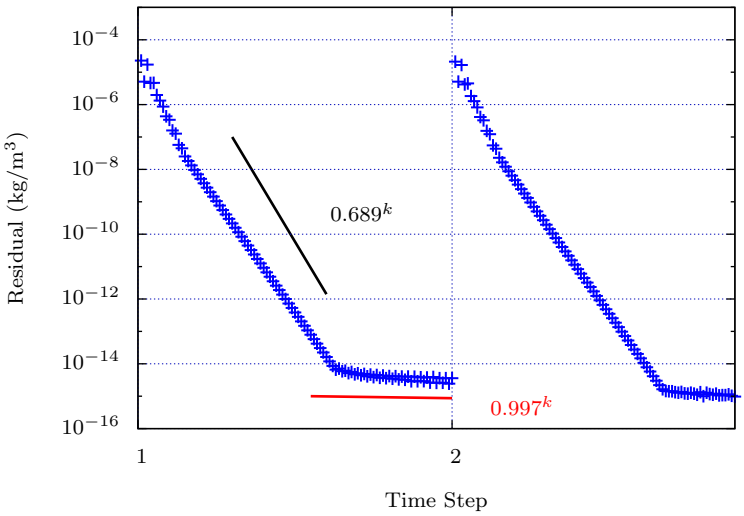

Figure 3.18: Evolution of the density residual as a function of sub-iterations over two time steps for the n-C_7H_{16} flame with CaltechMech using the proposed time-integration scheme with $\Delta t = 2\times10^{-6}$ s. The convergence rates given by the first (red) and the third (black) largest eigenvalues are shown for comparison. k references to the sub-iteration index.

is diluted with nitrogen (82.4% by mass) (in both the flamelets and the 2D flame). The steady-state solution for the temperature field is shown in Fig. 3.19. The two dissipation rates considered in Table 3.4 correspond to the maximum and minimum values found in the 2D simulation. As expected, the more restrictive time step size is encountered at the largest dissipation rate. In contrast, the 2D numerical simulation was found to be stable up to a time step size of $\Delta t = 4.0 \times 10^{-6}$ s, which is larger than the theoretical prediction of $\Delta t = 2.7 \times 10^{-6}$ s. With this "practical" time step, the maximum spectral radius of $\mathbf{A}_0'$ found in the 2D domain (see Fig. 3.19) is about 0.97. This difference can be partially explained by the fact that, in the region of largest dissipation rates (at the burner exit), the flame is extinguished and does not compare well with a flamelet.

3.6.1.3 0D ignition

Although the proposed time-integration scheme was developed primarily for the simulation of multi-dimensional turbulent flames, it could potentially be applied to the simulation of flows with ignition events. In order to partially assess the potential of the method for such flows, a canonical 0D, constant pressure ignition case is considered. The initial conditions as well as the theoretical stability

Fuel	χ_{st} (1/s)	P_0 (atm)	T_f (K)	T_o (K)	$\Delta t_{\max}$ (s) explicit	$\Delta t_{\max}$ (s) semi-implicit
n-C_7H_{16} [17]	1	1	400	800	1.4×10^{-11}	3.7×10^{-6}
n-C_7H_{16} [17]	320	1	400	800	8.3×10^{-11}	2.9×10^{-6}
C_2H_4 [17]	0.025	4	298	298	4.4×10^{-11}	4.9×10^{-6}
C_2H_4 [17]	138	4	298	298	1.4×10^{-10}	2.7×10^{-6}

Table 3.4: Theoretical largest stable time step size for the proposed semi-implicit scheme and the explicit time-integration of the chemical source terms with non-premixed flamelets. χ_{st} is the scalar dissipation rate at stoichiometry, T_f the temperature on the fuel side, and T_o the temperature on the oxidizer side. The oxidizer is air and the chemical mechanism considers 47 species and 290 reactions [17].

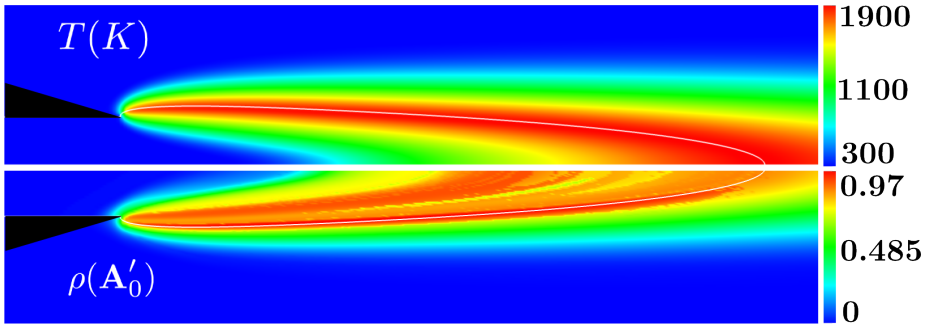

Figure 3.19: Contours of temperature (top) and spectral radius of $\mathbf{A}_0'$ (bottom) from the two-dimensional coflow laminar flame, obtained with a time step of 4.0×10^{-6} s.

limits (computed from a FlameMaster solution) are listed in Table 3.5. These conditions are meant to be representative of ignition events in HCCI-like engines [186, 86]. All simulations are performed with the CaltechMech mechanism.

Fuel	ϕ	P_0 (atm)	T_0 (K)	$\Delta t_{\max}$ (s) explicit	$\Delta t_{\max}$ (s) semi-implicit
n-C_7H_{16} [18]	0.7	30	850	1.1×10^{-12}	3.7×10^{-7}

Table 3.5: Theoretical largest stable time step size for the proposed semi-implicit scheme and the explicit time-integration with a 0D isobaric ignition case. T_0 is the initial temperature.

The same numerical simulation is performed with the present semi-implicit scheme in NGA to evaluate the practical stability limit. The stability limit identified numerically is $\Delta t = 5.2 \times 10^{-7}$ s, which is close to the theoretical limit. Unfortunately, at such large time step size, using four sub-iterations, the solution is deteriorated: the ignition delay time is over-predicted and the burnt

temperature is under-predicted. This is also observed at the theoretical stability limit, as shown in Table 3.6. Interestingly, with only four sub-iterations and using a time step size of $\Delta t = 2 \times 10^{-7}$ s, the solution is very close to the FlameMaster prediction, as seen in Table 3.6. While only a limited analysis, the present results show the applicability of the proposed semi-implicit scheme for ignition events.

Framework	Δt (s)	t_{ign} (ms)	T_b (K)
FlameMaster		1.560	2129
NGA	3.7×10^{-7}	1.703	2002
NGA	2.0×10^{-7}	1.566	2126

Table 3.6: Comparison of the ignition delay time t_{ign} and the burnt temperature obtained with FlameMaster, and with the proposed framework using two different time step sizes. Four sub-iterations are used.

3.6.2 Advantages over other methods

The performance of the proposed preconditioner is compared to that of the fully-implicit preconditioner, operator-splitting methods, and stiffness removal through QSSA in the following.

3.6.2.1 Fully-implicit method

As mentioned in the introduction, the use of fully-implicit time-integration of the chemical source terms is known to be prohibitively expensive for the simulation of turbulent reacting flows [66], as the inversion of the full chemical Jacobian, $\frac{\partial \mathbf{\Omega}}{\partial \mathbf{Y}}$, at every point of the domain and at every time step becomes very expensive when more than 10-20 species are considered. Another problem that would arise using a fully-implicit preconditioner with the numerical framework presented in Section 2.2 is that the extension to multi-dimensions using the approximate factorization introduced in Section 2.2.2 could no longer be applied, as the fully-implicit chemical Jacobian is not a diagonal matrix. Such a factorization is necessary for the efficiency of the overall procedure.

The major advantage of fully-implicit time-integration of the chemical source terms over the proposed semi-implicit scheme is the use of a time step size not restricted by the chemistry. For steady-state problems, this might be justified/useful. However, for turbulent reacting flows (such

as the one presented in Section 3.4.2), the characteristic hydrodynamic timescales of the turbulent flow (relative to the turbulence and the chemistry) need to be resolved. These are often sufficiently small that the cost increase for the fully-implicit method is not justified anymore.

3.6.2.2 Operator-splitting methods

The preconditioned iterative method integrates simultaneously the chemical, diffusive, and convective terms at the *same* effective time level. This guarantees that the numerical scheme used is free of lagging errors. These errors are of particular importance in unsteady reacting flows, where chemistry, diffusion, and convection are closely coupled, especially close to the thin flame fronts [128].

Using operator-split formulations, the chemical source terms are decoupled from the diffusive and the convective terms in order to be integrated using stiff ODE solvers. Therefore, the application of these methods for the simulation of reacting flow problems leads typically to integration accuracy degradation [49, 67, 191]. This is demonstrated in Fig. 3.20 for the mass fraction of n-C_3H_7. Using Godunov splitting, large numerical errors due to operator-splitting are observed with $\Delta t > 5 \times 10^{-7}$ s (the ODE solver used is DVODE [25] with 10^{-8} and 10^{-20} for the relative and absolute tolerances, respectively [116]). At this point, the numerical time step size surpasses the diffusion timescales. In contrast, the proposed preconditioned iterative method does not suffer from these errors, since the convection, diffusion, and chemistry are all integrated simultaneously. Note that, while Strang splitting is known to perform generally better than Godunov splitting, its extension to a low Mach number code based on spatial and temporal staggering is not trivial. This is the reason why Godunov splitting, easily implementable on a staggered grid, was used for comparison.

Figure. 3.21 presents the computational cost per grid point per simulation time using 1) the proposed preconditioned iterative method, 2) Godunov splitting, and 3) explicit time-integration of the chemical source terms. For all cases, four sub-iterations are used. Without surprise, the cost using small time step sizes ($\Delta t < 5 \times 10^{-8}$ s) is similar for all methods. For Godunov splitting, it is computationally as cheap as the explicit method when the chemical source terms are not stiff, which is the case at small time step sizes. However, using large time step sizes, the chemical source

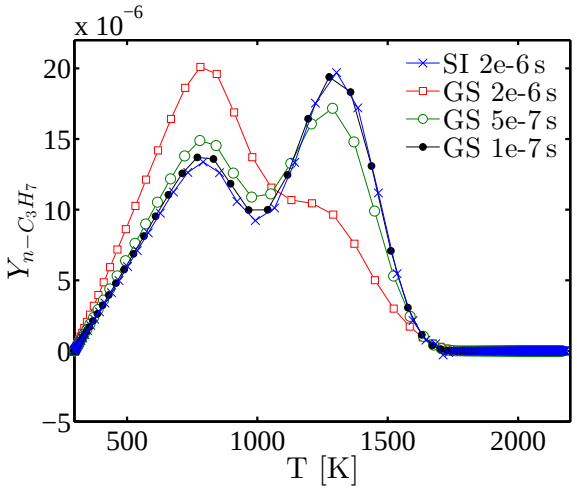

Figure 3.20: n-C_3H_7 mass fraction of from the 1D (freely propagating) flame solution. Solutions from using Godunov splitting (GS) are compared, for different time step sizes, to the solution using the proposed preconditioning method.

terms become stiff and the cost associated with solving the stiff ODEs increases. At large time step sizes, the cost associated with Godunov splitting increases up to twice larger than that associated with the proposed method. On the other hand, for the proposed preconditioned iterative method, as mentioned earlier, the total number of operations per time step is virtually the same as that associated with an explicit time-integration of the chemical source terms. In particular, the cost per iteration does not vary with time step size. As such, the computational cost per grid point per simulation time is proportional to the inverse of the time step size. In summary, for the present 1D flame test case, with a time step of $\Delta t = 2 \times 10^{-6}$ s, the computational cost associated with the proposed method is smaller than that associated with Godunov splitting, while being free of lagging errors (see Fig. 3.20).

In the simulation of turbulent flames, the chemical source terms are zero almost everywhere (unburnt/burnt regions in a premixed flame; fuel/oxidizer streams in a non-premixed flame) except at the flame front. This means that, if the domain is partitioned in the direction perpendicular to the flame, the cost of a single time step, using an operator-splitting method, will vary between the different partitions. Unfortunately, a partition cannot advance faster in time than the others. Therefore, the computational time is dictated by the slowest partition. For the three-dimensional simulation test case, this made the simulation impracticable using Godunov splitting. This could

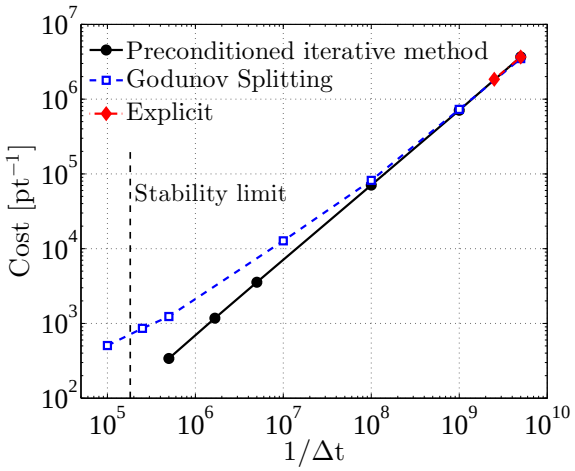

Figure 3.21: Computational cost of 1D stationary flame simulation for different chemical integration methods. Cost is calculated as cpu time per point (s/pt), per second of simulation time (s). All cases use four sub-iterations.

be partially alleviated by considering load balancing [75] at the cost of making the code more complicated.

3.6.2.3 Stiffness removal through QSSA

As mentioned in the introduction, a way to remove the stiffness of the species transport equations (and reduce the number of transport equations) is to put the species with small chemical timescales in Quasi Steady State (QSS) [107]. It can be assumed that these species concentrations are entirely controlled by non-QSS species. As such, an algebraic equation for their concentrations is obtained and these QSS species are not transported in the simulation. This algebraic equation is used to replace these QSS species in the reactions in which they are involved. More details can be found in Ref. [140].

Application of this method is particularly interesting for compressible codes, for which the stability limit is controlled by either chemistry or acoustics [72]. The acoustics timescale is smaller than the convective timescale (subsonic flows) and may be relatively close to the smallest chemical timescales. As seen in Fig. 3.4, it is very likely that only a few species (and their associated reactions) are responsible for the small chemical timescales. After removal of these species (and their associated reactions), using QSSA, the stability of the solver would be limited by the acoustics only.

However, putting the species with the smallest associated timescales in quasi-steady state may not always be justified. With the quasi steady state assumption, algebraic expressions can be found for these species. In Fig. 3.22, these expressions are compared to their true values in the 3D turbulent premixed flame (see Section 3.4.2). Several species typically placed in QSS in previous studies [160, 108] are considered. It is obvious that the QSSA is valid for 1-CH_2, but not for n-C_3H_7 nor 2-C_7H_{15} in the present turbulent premixed flame. This can be explained by the fact that the timescales corresponding to these species, although very small at high temperature, are very large at low temperatures, as can be seen in Fig. 3.23. A way to counter this behavior that has been used in the literature [105] is to preheat the unburnt mixture to make the flame more "robust", *i.e.* to make sure that the species responsible for the stiffness of the system can be put in quasi-steady state. However, this obviously modifies the nature of the flame simulated. Note that a recently developed dynamic stiffness removal relies on local, rather than global, QSSA [110]. However, to the best of the authors' knowledge, the method has only been applied to the simulation of ignition problems [186, 110].

3.6.3 Limitations

A first limitation of the method is that it is only efficient for the simulation of unsteady reacting flows, in which the interplay between the flow field and the chemistry has to be captured through adequate temporal resolution (small time step size). While one might decide to use the present method to reach the solution of a steady-state problem, as shown in Section 3.6.1.2 for the 2D-coflow diffusion flame, the associated cost would be large. In such a case, the use of a large time step size is desirable to reach the time-independent solution. For all the examples provided, the largest stable time step size is of the order of 1×10^{-6} s, which makes the method inefficient to reach a steady-state flow solution.

Second, the method behaves poorly when a fast reversible reaction is present in the chemical mechanism, since this leads to a spectral radius of $\mathbf{A}_0'$ close to unity over a wide range of time step sizes (as discussed in Section 3.6.1.1). Although such fast reaction was found to be unphysical in

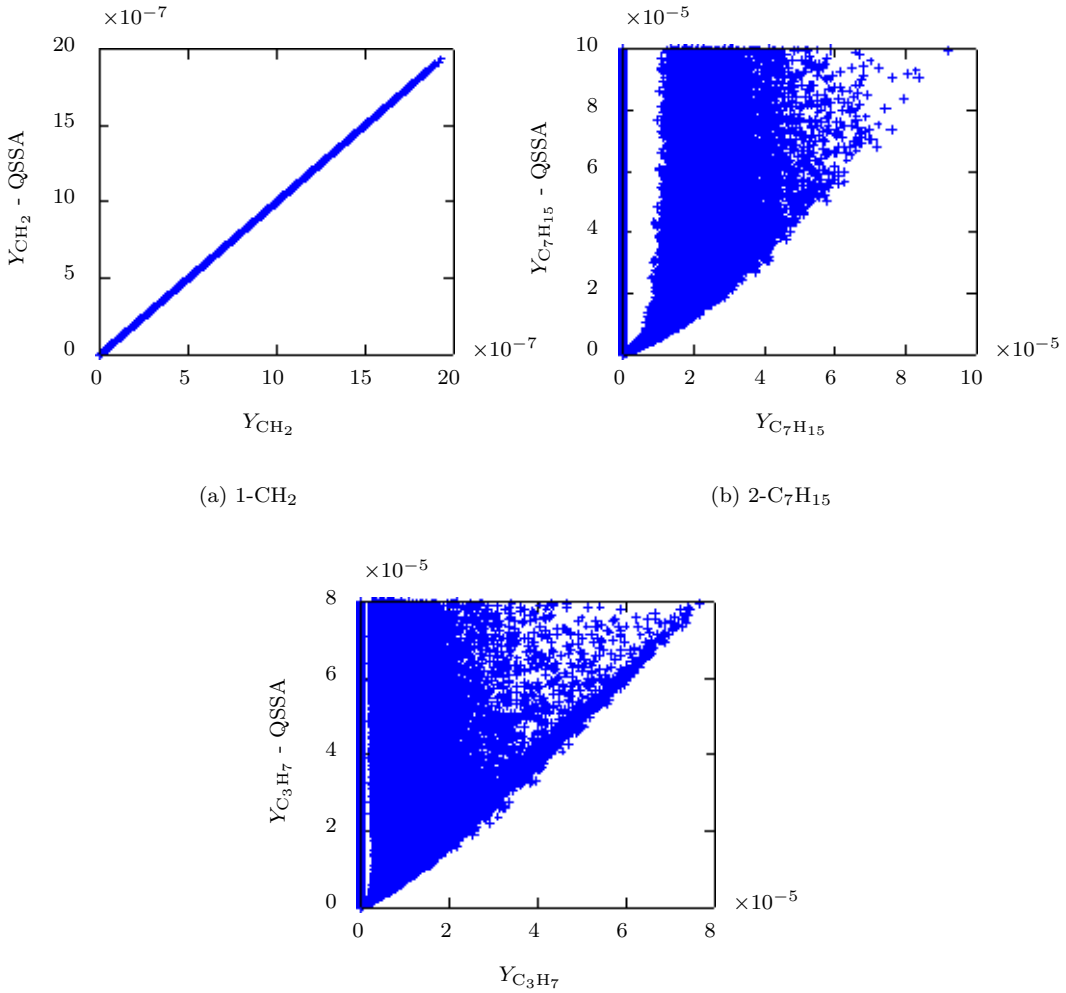

(a) 1-CH_2

(b) 2-C_7H_{15}

(c) *n*-C_3H_7

Figure 3.22: Scatter plots of species mass fractions computed from the algebraic expression assuming QSS *vs.* their actual value in the three-dimensional turbulent flame. A straight line ($y = x$) is expected for perfect QSS species.

CaltechMech (a better reaction rate should be implemented), it is not clear if it is always the case. More importantly, for very large mechanisms such as those developed at the Lawrence-Livermore National Laboratories (LLNL) such reactions are present. It is impractical to identify each of these reactions and assess if they can or cannot be removed for the specific reacting flow being simulated (as was done in Section 3.6.1.1 with CaltechMech). A time-integration method used with such mechanisms has to be efficient even in the presence of such reactions (an example can be found in Ref. [116]). This is achieved at the cost of making the preconditioner more complex (and non-

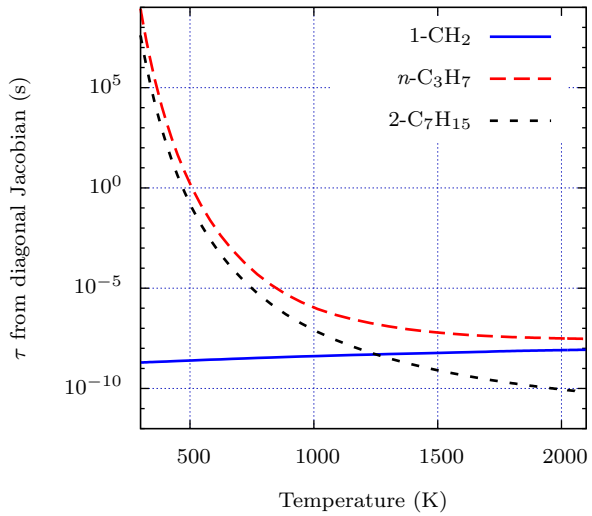

Figure 3.23: Chemical consumption timescale associated with 1-CH_2, 2-C_7H_{15}, and n-C_3H_7 *vs.* temperature in the one-dimensional flame.

diagonal). Therefore, the proposed method is not expected to be efficient for the simulation of reacting flows with very large chemical mechanisms such as those developed at LLNL. However, these mechanisms are mainly used for 0D ignition calculations and are too large to be used for the simulation of turbulent flames.

Third, the temperature equation is integrated explicitly, which may limit the largest stable time step size in some reacting flow configurations. For the laminar n-heptane/air flame (Section 3.4.1), the temperature time scale (related to heat release) is of the order of 10^{-4} s. This temperature time scales goes down to 10^{-5} s for the 30 atm 0D ignition case (section 3.6.1.3). For turbulent reacting flows, the convective CFL limit is generally more restrictive than any of these time scales. Therefore, explicit treatment of the chemistry in the temperature equation should not affect the performance of the proposed scheme for the applications it is intended for, *i.e.* unsteady reacting flows such as turbulent flames. If the method were to be used to simulate flows in which the temperature time scale is smaller than the convective CFL limit, then a similar implicit treatment of the temperature equation as the one proposed for the species equations may be desirable.

Fourth, the proposed approximation of the diagonal of the chemical Jacobian (Eq. 3.5) may, in some cases, introduce non-negligible deviation from the exact diagonal. For species whose con-

sumption rate is mostly due to recombination reactions, the corresponding term in the approximate diagonal may be up to twice smaller (in magnitude). For instance, for the *n*-heptane/air flame tested with the 35-species mechanism, the reaction OH + OH $\rightarrow$ O + H_2O accounts for most of the consumption rate of OH. As a consequence, the exact term in the diagonal of the chemical Jacobian corresponding to OH is about 1.7 times larger than its approximation. However, when the approximation is replaced by the exact diagonal of the Jacobian, the increase in efficiency of the method was found to be negligible. More specifically, the stability limit increases by only 25%, and the convergence rate is unaffected for time step sizes smaller than 2×10^{-6} s. Since computing the exact diagonal requires additional operations, the proposed implementation is marginally more efficient. Under other circumstances, for instance in wall/flame interactions, where the importance of the H recombination reaction has been shown [68], or in hypersonic flows, replacing the approximate diagonal by the exact diagonal may lead to better efficiency.

In summary, use of the proposed preconditioner is particularly relevant to moderately to highly turbulent (premixed or non-premixed) flames (high Karlovitz numbers for premixed flames) in which the convective CFL limit is more restrictive than the largest stable time step size (due to the chemistry) with the proposed time-integration method.

3.7 Summary

A semi-implicit preconditioning strategy, applied to an iterative method, is proposed for the time-integration of the stiff chemistry in the simulation of unsteady reacting flows, such as turbulent flames. The preconditioner consists of an approximation of the diagonal of the chemical Jacobian. It is integrated into the iterative procedure already implemented in the NGA code, in order to account for the non-linearities of the governing equations. Upon convergence of the sub-iterations, the fully-implicit Crank-Nicolson method is recovered. Therefore, the stability of the scheme is dictated by the stability of the sub-iterations.

The performance of the proposed method was numerically tested on two flow configurations: a one-dimensional unstretched premixed flame and a three-dimensional turbulent premixed flame,

both with an unburnt mixture of air and *n*-heptane. First, the species lifetimes evaluated from the preconditioned chemical Jacobian represent appropriately the smallest chemical timescales. Second, a theoretical approximation of the rate of convergence of the sub-iterations was derived and shown to be in good agreement with numerical results. Third, the stability limit was found to be well approximated by the theoretical analysis. It was also shown that the stability limit does not depend on the number of sub-iterations. Fourth, the method was shown to be second-order accurate in time, even with only four sub-iterations. Increasing the number of sub-iterations led to a reduction of the magnitude of the errors. With a time step size as large as a third of the stability limit, four sub-iterations were shown to be sufficient to achieve acceptable accuracy. Fifth, while other methods using diagonal preconditioned chemical Jacobians have been shown to lack elemental conservation or were argued to not be time-accurate [85, 28, 27], the proposed method was shown to conserve properly elements over time thanks to the sub-iterations. Sixth, the computational cost of a single iteration with the proposed method is similar to that of an explicit time-integration scheme (since the same number of sub-iterations are used). Therefore, the simulation speed-up achieved with the proposed method corresponds to the increase in the largest stable time step size. For the three-dimensional turbulent premixed flame, the simulation could be performed with a convective CFL of 0.8 (optimal, with or without chemistry).

The theoretical analysis for stability and convergence rate is general and is not limited by the type of fuel, chemical mechanism, or flow configuration. Therefore, it was repeated, in the context of one-dimensional premixed flames, with several fuels, unburnt conditions, and chemical mechanisms. It was also performed with non-premixed flamelets using different scalar dissipation rates. The method provided good convergence rates of the sub-iterations close to the stability limit for all the chemical mechanisms considered. Consequently, the proposed preconditioning method showed great potential for the efficient time-integration of turbulent flames. Although not a primary target, the method was also shown to work for a homogeneous ignition case.

Finally, the proposed method is more suited than other methods for reacting flows in which the convective timescales are of the order of 10^{-6} s or less. These correspond to moderately to highly

turbulent (non-premixed or premixed) flames (high Karlovitz for premixed flames).

Chapter 4

Direct numerical simulations[1]

Relying on the time-integration scheme introduced in the previous chapter, a series of direct numerical simulations (DNS) of high Karlovitz n-C_7H_{16}/air premixed turbulent flames are performed. In Section 4.1, the numerical approach is presented. The chemistry and transport models are validated in Section 4.2. Grid-independence is verified in Section 4.3. Section 4.4 presents qualitative results from the turbulent flame simulations.

4.1 Numerical approach

The flow configuration is first introduced, followed by a few additional details on the equations solved (not mentionned in Chapter 2). Finally, the turbulence forcing method is described.

4.1.1 Flow configuration

Figure 4.1 presents a schematic diagram of the flow configuration. This is the same configuration as the one briefly presented in Section 3.4.2. A statistically-planar, freely-propagating flame was chosen in order to isolate the effects of turbulence on the flame from mean flow shear and curvature effects. Furthermore, since both an inflow and an outflow are present, the simulation can be run for an unbounded arbitrary time, allowing the turbulent flame to reach a statistically-stationary state.

The unburnt gas is a slightly lean ($\phi = 0.9$) n-C_7H_{16}/air mixture at standard temperature

[1] Most of the work presented in this section is published in B. Savard, B. Bobbitt, and G. Blanquart, Proc. Comb. Inst. (2015) and in B. Savard and G. Blanquart, Combust. Flame (2015). Brock Bobbitt has contributed to the choice of the turbulent flame parameters. Unless otherwise mentioned, the author of this thesis has contributed to all the work presented in this chapter.

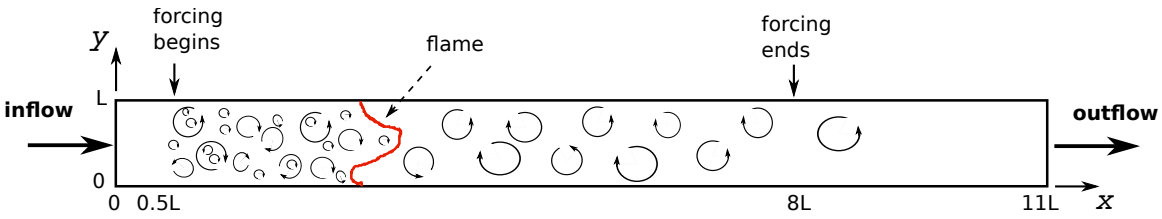

Figure 4.1: Schematic diagram of the flow configuration.

(T_u = 298 K) and pressure (P_0 = 1 atm). These standard conditions were chosen in order to match the experimental conditions of most premixed turbulent flames [30]. Two sets of simulations are considered: one at a higher Karlovitz number, and one at a lower Karlovitz number[2]. For each of these sets, two simulations are performed: one with non-unity Lewis numbers and one with unity. The parameters for both simulations are presented in Table 4.1. Given this choice of unburnt conditions, the other parameters are chosen to maximize the Karlovitz number (for the higher-Ka), while keeping a sufficiently large l/l_F, where $l = {u'}^3/\epsilon$ is the integral length scale and $l_F = (T_b - T_u)/|\nabla T|_{\max}$ is the laminar flame thickness. u' is the rms velocity fluctuation, ϵ is the dissipation rate, T_b is the temperature in the burnt gas, and $|\nabla T|_{\max}$ is the maximum temperature gradient throughout the flame. The Karlovitz number is defined as the ratio of the flame time scale to the Kolmogorov time scale, *i.e.* $Ka = t_F/t_\eta = (l_F/S_L)(\epsilon/\nu)^{1/2}$, where ν is the kinematic viscosity in the unburnt mixture. The only difference between the two sets of simulations is u'. The Karlovitz numbers chosen are sufficiently high that the first set of flames is expected to fall at the transition between the thin/broken reaction zones regimes (see Fig. 1.6), while the other set should lie in the thin reaction zone regime, further away from the broken reaction zones regime. Note that the parameters for the higher-Ka simulations were chosen optimally such that the computational cost is constaint by both the chemistry (resolving the flame front) and the turbulent flow (resolving the Kolmogorov lenght scale).

The turbulent flame speed is not known *a priori*. A first simulation was performed with tabulated chemistry [97] (unity Lewis number) to obtain an estimate of the turbulent flame speed. The flame was allowed to slightly drift for more than 100τ, where τ is the eddy turnover time defined as $\tau = k/\epsilon$,

[2]The lower-Ka set of flames was simulated in collaboration with Simon Lapointe and can be found in S. Lapointe, B. Savard, and G. Blanquart, Combust. Flame (2015) under review.

	higher-Ka		lower-Ka	
	unity Le	non-unity Le_i	unity Le	non-unity Le_i
Domain size	$L \times L \times 11L$		$L \times L \times 11L$	
L (m)	2.3×10^{-3}		2.3×10^{-3}	
Grid	$128 \times 128 \times 1408$		$128 \times 128 \times 1408$	
Δx (m)	1.8×10^{-5}		1.8×10^{-5}	
η (m)	9×10^{-6}		1.5×10^{-5}	
n_F	23	21	23	21
ϕ	0.9		0.9	
S_L (m/s)	0.29	0.36	0.29	0.36
l_F (mm)	0.43	0.39	0.43	0.39
l/l_F	1.0	1.1	1.0	1.1
u'/s_L	21	18	10	9.0
$Ka = t_F/t_\eta$	280	220	91	78
$Re_t = (u'l)/\nu$	190		83	

Table 4.1: Parameters of the simulation. Δx is the grid spacing (uniform), η the Kolmogorov length scale in the unburnt gas, n_F the number of grid points through the laminar flame thickness, Δt the time step, ϕ the equivalence ratio, and Re_t the turbulent Reynolds number in the unburnt gas.

with k the turbulent kinetic energy (TKE). From this simulation, the turbulent flame speed was estimated and the inlet velocity was changed to match this estimate. Then, the finite-rate chemistry simulations (either with unity or with non-unity Lewis numbers) were started from the statistically steady (tabulated) simulation. The simulations were run until statistically steady state was reached (run for 10τ, almost two flame brush through times, which corresponds to the ratio of the turbulent flame thickness to the mean bulk velocity). The data was collected over at least the next 10τ. The unity Lewis number flame drifted by less than $0.1L$ from its initial position ($x = 3.5L$), and the non-unity Lewis number flame by less than $0.3L$. More details on the drift of the flame front (and the associated turbulent flame speed) will be provided in Section 6.3.

The simulated flames are characterized by an important velocity ratio u'/S_L (about 20). This is a direct consequence of the large Karlovitz number. Consequently, a special treatment has to be applied to the inlet and the outlet in order to avoid negative inflow/outflow velocities (for numerical stability). The unburnt gas is injected with a low TKE, such that there are no negative inlet velocities. This inflow is generated from a separate homogenous isotropic turbulence simulation [157, 31]. Velocity field forcing (subsection 2.3) maintains this low TKE over a distance of $0.5L$, after which the forcing magnitude is increased such that the TKE reaches the desired value. This nominal velocity field forcing is stopped after a distance of $8L$, allowing the turbulence to decay sufficiently

that there are no negative axial velocities at the outlet. The forcing method used is described in subsection 2.3.

Note that unless otherwise mentioned, the analysis throughout this thesis is done on the higher-Ka flames. The lower-Ka flames will be used only as a validation tool for the models presented in the next chapters (more details in Section 4.4.3).

4.1.2 Governing equations

The governing equations solved are described in Section 2.1, with the exception of the momentum equation, to which a forcing term is added:

$$\frac{\partial}{\partial t}\left(\rho \boldsymbol{u}\right) + \nabla \cdot \left(\rho \boldsymbol{u} \otimes \boldsymbol{u}\right) = -\nabla p + \nabla \cdot \boldsymbol{\sigma} + \boldsymbol{f}, \tag{4.1}$$

where, $\boldsymbol{f}$ is a forcing term used to maintain the presence of turbulent fluctuations (see subsection 4.1.3).

The species and enthalpy production terms are taken from the reduced, *n*-heptane chemical model which contains 35 species and 217 elementary reactions introduced in Section 3.4.1. This model corresponds to a slightly reduced version of that found in Ref. [17]. A validation is presented in Section 4.2.1.

The species viscosities μ_i are computed by standard kinetic theory [76] and the mixture viscosity μ is calculated using Wilke's formula [179]. The mixture thermal conductivity is obtained following Mathur *et al.* [115], where the species thermal conductivities λ_i are computed by Eucken's formula [60]. In order to reduce the computational cost of the simulation, the species diffusivities are computed as $D_i = \alpha / Le_i$, with the Lewis numbers Le_i assumed to be constant throughout the flame. For the non-unity Lewis number simulation, these species Lewis numbers Le_i are extracted from the simulation of a one-dimensional, laminar premixed flame with full transport properties, using FlameMaster [146]. The Lewis numbers are evaluated in the burnt gas such that deviations from the full transport solution are negligible. These are listed in Table 4.2. A validation of the

constant Lewis number assumption is presented in Section 4.2.2.

N_2	0.99	HCO	1.22	A-C_3H_5	1.79
1-CH_2	0.94	CH_2O	1.23	*n*-C_3H_7	1.81
3-CH_2	0.94	CH_3	0.96	C_2H_6	1.40
O	0.69	CO_2	1.37	P-C_3H_4	1.68
H_2	0.28	CH_4	0.97	A-C_3H_4	1.68
H	0.16	C_2H_3	1.28	C_3H_6	1.80
OH	0.70	C_2H_4	1.28	1-C_4H_8	1.99
H_2O	0.79	C_2H_5	1.39	1-C_5H_{10}	2.27
O_2	1.06	C_2H	1.25	1-C_5H_{11}	2.08
HO_2	1.07	HCCO	0.86	2-C_7H_{15}	2.84
CH	0.64	C_2H_2	1.27	*n*-C_7H_{16}	2.84
CO	1.07	C_3H_3	1.6		

Table 4.2: Constant species Lewis numbers used in the turbulent flame simulations (evaluated in the burnt gas from a one-dimensional flame solution).

The governing equations are solved numerically using the energy conservative, finite difference code NGA [55], described in Section 2.2. The scheme used is second-order accurate in both space and time. The semi-implicit Crank-Nicolson time integration described in Chapter 3 is used. The third-order Bounded QUICK scheme, BQUICK [74], is used as the scalar transport scheme to ensure the transported species mass fractions and temperature remain within their physical bounds.

4.1.3 Turbulence forcing

As all other similarly high Ka numerical simulations from the literature [10, 9, 151], the present configuration misses the generation of turbulence due to large scale flow straining (larger than the domain size). As a result, the turbulence is expected to decay. The decay of the TKE ahead of the flame (in the unburnt gas) in the absence of velocity field forcing can be estimated theoretically by analogy to decaying isotropic turbulence, considering $\mathrm{d}k/\mathrm{d}t = -k/\tau$. With U the mean bulk/inlet velocity, the characteristic length scale over which the TKE decays is $U\tau = 0.1$ mm, which is too small compared to the laminar flame thickness (about 0.4 mm, see Table 4.1). As a consequence, the use of velocity field forcing is necessary.

In previous work, spectral forcing techniques were often used to offset the decay of TKE and maintain the turbulence characteristics [10, 151]. In the present work, the linear velocity forcing method [111, 157, 32] was preferred for its more physical nature and good stability properties [31].

The linearly forced turbulent field under comparable Reynolds number was analyzed in Ref. [32] and it was shown that the second- and third-order structure functions and the energy spectrum are self-consistent and in agreement with experimentally obtained data [126] of decaying grid turbulence. The linear forcing method *mimics* the missing large scale straining by appending a source term to the momentum equation (Eq. 4.1) [111, 157].

The method is adapted to take into account the axially evolving nature of the flow. Consequently, the forcing term $\boldsymbol{f}$ in Eq. 4.1 takes the following form:

$$\begin{aligned} \boldsymbol{f}(x,y,z,t) &= A\frac{k_0}{k(x,t)} \\ &\times \left(\rho(x,y,z,t)\,\boldsymbol{u}(x,y,z,t) - \overline{\rho\boldsymbol{u}}(x,t)\right), \end{aligned} \tag{4.2}$$

where $A = \epsilon_0/(2k_0)$ is the forcing coefficient (computed as $A = (2/27)^{1/2}\left(k_0/l^2\right)^{1/2}$ [31]), which takes the form of the inverse of a time scale, k_0 is the desired TKE, ϵ_0 is the corresponding desired dissipation rate, and k is the planar Favre-averaged TKE, defined as

$$k = \frac{1}{2}\left(\widetilde{(u'')^2} + \widetilde{(v'')^2} + \widetilde{(w'')^2}\right). \tag{4.3}$$

Planar Favre averages are defined as

$$\widetilde{\boldsymbol{\phi}} = \frac{\overline{\rho\boldsymbol{\phi}}}{\overline{\rho}}, \tag{4.4}$$

with the standard (Reynolds) planar average

$$\overline{\boldsymbol{\phi}}(x,t) = \frac{1}{L^2}\int_0^L\int_0^L \boldsymbol{\phi}(x,y,z,t)\,\mathrm{d}y\mathrm{d}z. \tag{4.5}$$

With the forcing method used, homogeneous isotropic turbulence is imposed upstream of the flame. A slight decrease in the TKE through the flame and a relaxation back to the imposed TKE further downstream was found, as shown in Fig. 4.2. This evolution is consistent with the experimental results of Cheng *et al.* [40]. While the trends agree, in both studies the variations in

TKE through the flame remain marginal, which has also been observed computationally [160].

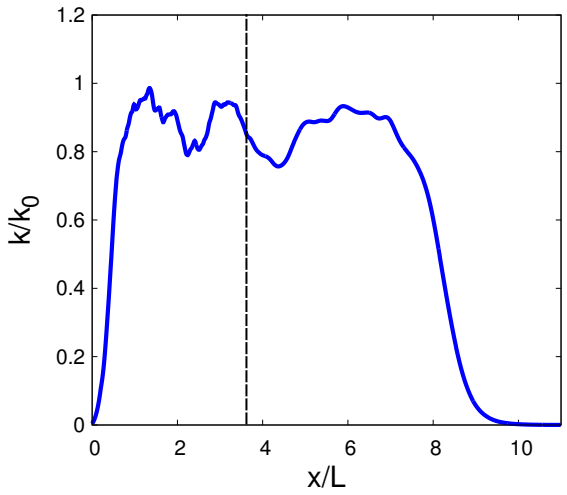

Figure 4.2: Time-averaged (over 10 eddy turnover times), planar Favre-averaged TKE *vs.* x for the non-unity Lewis number flame. The average flame position is shown by the dashed line (more details on the flame position are given in Section 6.3.1).

Figure 4.3 presents the energy spectra (computed as in Ref [152]) in the unburnt gases for both the lower- and the higher-Ka flames[3]. First, it is important to note that, as expected, both profiles collapse on each other. Second, the presence of an inertial sub-range is very limited. This is to be expected given the turbulent Reynolds numbers (Table 4.1). Finally, for both cases, the turbulent kinetic energy is contained over two decades of length scales. This is also to be expected given the turbulent Reynolds numbers of approximately 100. This range of length scale is limited by the inherent computational cost.

4.2 Chemistry and transport models validation

In this section, we provide additional justifications and validation for the choice of chemical model and transport model.

[3]The profiles were computed by Simon Lapointe and can be found in S. Lapointe, B. Savard, and G. Blanquart, Combust. Flame (2015) under review.

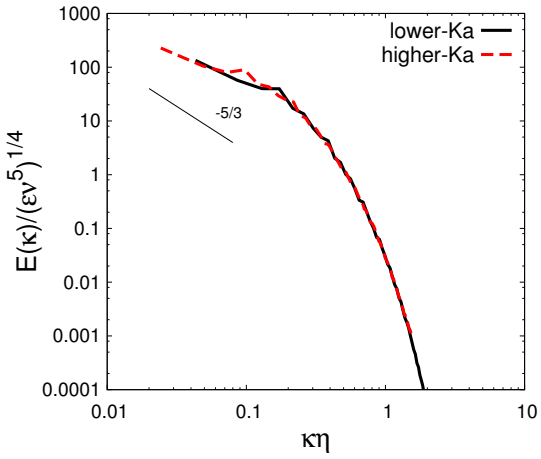

Figure 4.3: Normalized energy and dissipation spectra for the higher- and lower-Ka non-unity Lewis number flames. The two-dimensional three components spectra taken in a y-z plane in the unburnt gases (averaged over time). $\kappa = 2k\pi/L$, for $k = 1, 2, ..., N_y/2$, with N_y the number of points in the y- or z-direction, is the wavenumber.

4.2.1 Reduced mechanism performance

The turbulent flame speed is one of the most important quantity that characterizes a turbulent premixed flame. This overall consumption rate is a strong function of the local flame speed. An effect of differential diffusion is to modify the local equivalence ratio in locations where the flame is curved [142, 113]. Since highly turbulent flames are subject to locally large curvatures, the mechanism should predict adequately the local flame speed over a range of equivalence ratios. In order to validate the performance of this reduced mechanism (presented in Section 3.4.1), the flame speed *vs.* equivalence ratio profile is compared to experimental data in Fig. 4.4. The flame speeds are obtained from one-dimensional unstretched flames simulated with the same reduced mechanism with FlameMaster [146]. Two solutions are compared: one using full transport (mixture-averaged diffusivities and Soret diffusion) and one using constant Lewis numbers (as listed in Table 4.2) without Soret diffusion. The laminar flame speeds obtained with both transport models are in very good agreement with experimental data over a wide range of equivalence ratios.

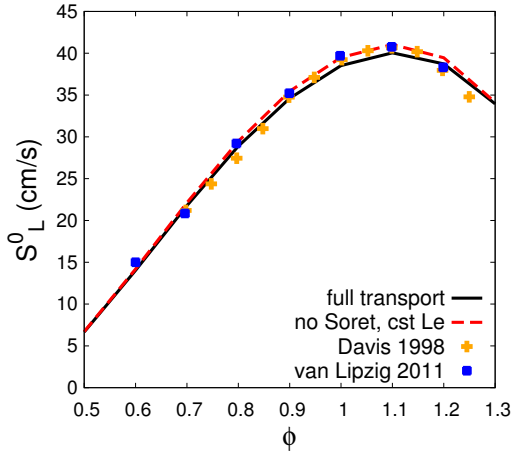

Figure 4.4: Laminar flame speed *vs.* equivalence ratio profiles obtained numerically with the 35-species mechanism and experimentally [51, 170]. The numerical simulations were performed with full transport (solid line) and constant Lewis numbers (dashed line).

4.2.2 Transport model validation

The transport model is further tested on a one-dimensional unstretched flame simulated with FlameMaster. The same unburnt gas parameters (T_u, P_0, ϕ) as in the DNS are used. The mass fraction *vs.* temperature profiles for the fuel (n-C_7H_{16}), an intermediate species (CH_2O), and a product (H_2O), obtained from full transport (mixture-averaged diffusivities and Soret diffusion), mixture-average transport without Soret diffusion, and constant Lewis numbers without Soret diffusion solutions, are shown in Fig. 4.5(a) to 4.5(c). Similarly, the source term *vs.* temperature profiles are shown in Fig. 4.5(d) to 4.12(b) for the same species. It is clear from these figures that the constant Lewis number assumption introduces virtually no deviation from the mixture-averaged transport solution. Soret diffusion has a noticeable effect only in the fuel mass fraction *vs.* temperaure profile. This effect would, however, be attenuated in turbulent flames as turbulent transport is especially important at low temperature in the preheat zone (more details in Chapter 5). The good agreements shown in Fig. 4.5 are particularly important given the computational cost reduction of using fixed, constant Lewis numbers without Soret diffusion.

Note that while the simplified transport model gives good agreement with the full transport model in a one-dimensional laminar setting, it is unclear to what extent it should perform equally well in a

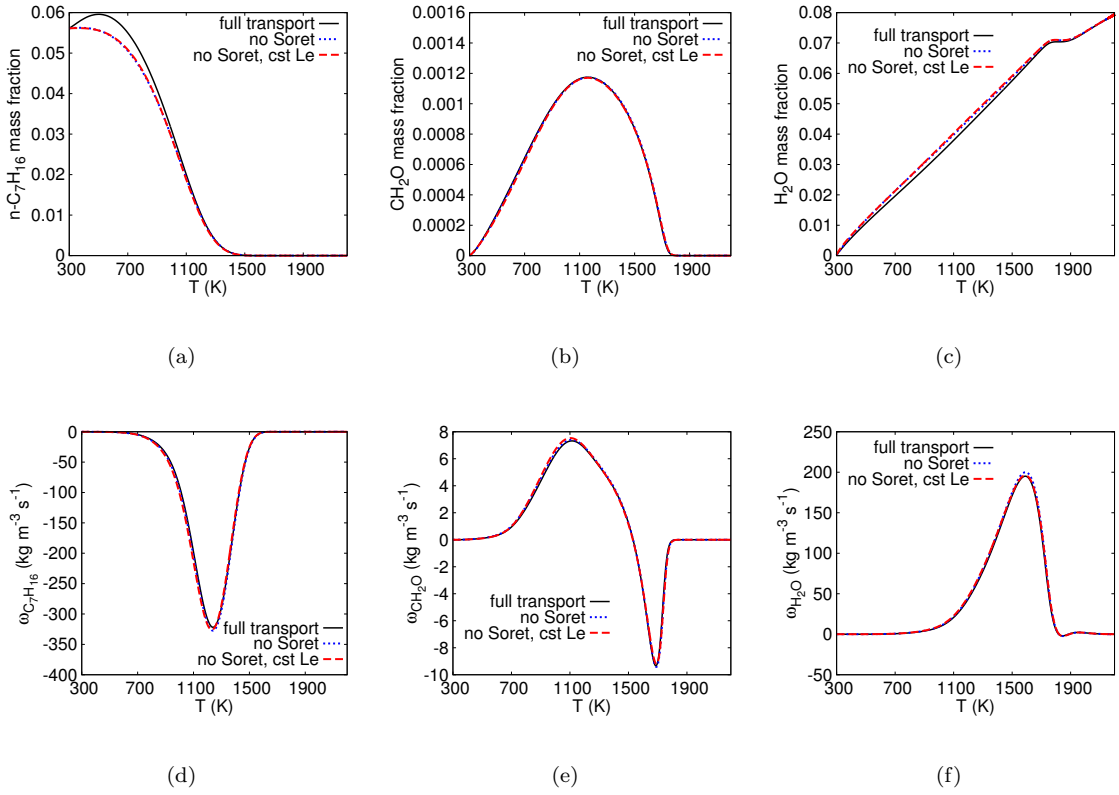

Figure 4.5: Comparison of species mass fraction (top row) and source term (bottom row) *vs.* temperature profiles for n-C_7H_{16}, CH_2O, and H_2O between the one-dimensional, unstretched, flame solutions obtained with full transport (solid lines) and constant Lewis numbers (dashed lines). The unburnt conditions are the same as in Section 4.1.

three-dimensional turbulent setting. In order to partially asses the validity of this transport model in the turbulent flame, the non-unity simulation was performed with mixture-averaged diffusivities by Nicholas Burali[4]. Given the cost of the simulation, it was performed for 13 eddy turnover times. Figure 4.6 compares the fuel burning rate statistics for the two simulations. The last 3 turnover times of the mixture-averaged simulation are considered (the first ten being considered a transient period). The fuel burning rate is shown as it will be investigated extensively in the next chapters. This quantity is also chosen because the species source terms are much more sensitive to turbulent fluctuations than the species mass fractions (more details in the following chapters). Figure 4.6 shows that only marginal differences can be identified between the two flames. This means that the effect of turbulence is captured independently of the transport model.

[4]N. Burali and G. Blanquart, Combust. Flame, in preparation.

Finally, the effect of Soret diffusion in the turbulent flame should be analyzed in more details in future work.

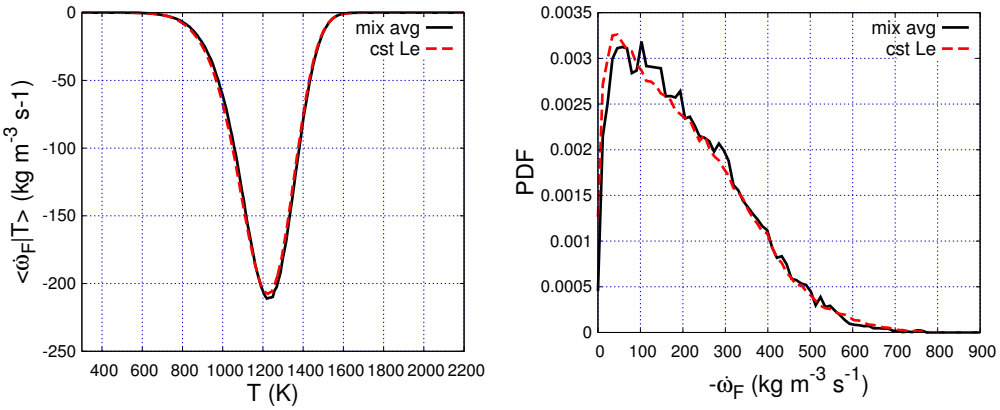

(a) Conditional mean

(b) Conditional PDF ($T = 1240$ K)

Figure 4.6: Comparison of the fuel burning rate statistics in the non-unity Lewis number turbulent flame with mixture-averaged diffusivities and constant Lewis numbers.

4.3 Grid refinement

The grid spacing is chosen such that $\kappa\eta > 1.5$ everywhere in the domain, and is limited by the turbulence in the unburnt gases, where η is the smallest. In order to verify the quality of the solution, a non-unity Lewis number simulation with twice the number of grid points per direction is performed for 13 eddy turnover times (limited by the cost of such a simulation). Figure 4.7 compares the fuel burning rate statistics for the nominal- and refined-grid simulations. Again, the last 3 turnover times are considered for the refined-grid simulation. Only small differences can be identified. It will become more clear in Chapter 6 that these differences are marginal for the purpose of the analysis made in this work. The conclusions made in the next chapters should therefore be grid independent.

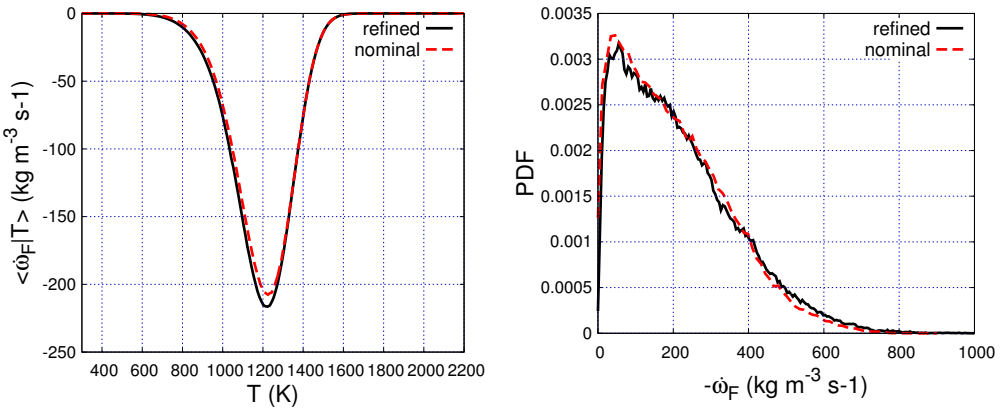

(a) (b)

Figure 4.7: Comparison of the fuel burning rate statistics in the non-unity Lewis number turbulent flame with refined and nominal grids.

4.4 Turbulent flame

In this section, qualitative results for the non-unity Lewis number flame are presented. Further analysis will be performed in Chapters 5 to 6 (using both the non-unity and the unity Lewis number flames).

4.4.1 Thickened flame

At high Karlovitz numbers, the spatial structure of a premixed flame is expected to depart from that of a laminar flame, as turbulent structures are sufficiently small enough to penetrate the preheat zone, and potentially the reaction zone. Figure 4.8 presents contours of vorticity, n-C_7H_{16} and CH_2O mass fractions, and temperature through the flame brush on a two-dimensional horizontal slice of the non-unity Lewis number turbulent flame. This figure is representative of both the unity and the non-unity Lewis number turbulent flame brushes.

As expected the preheat zone appears largely thickened [142] (approximately 10 times larger than the laminar flame). It is interesting to note that smaller turbulent structures are observed upstream of the flame (*i.e.* in the preheat zone) compared to close to the reaction zone. This is partially-explained by the fact that the kinematic viscosity increases (by up to a factor of 30) and

the Kolmogorov length scale, $\eta = \left(\nu^3/\epsilon\right)^{1/4}$, increases through the flame by about a factor of 13.

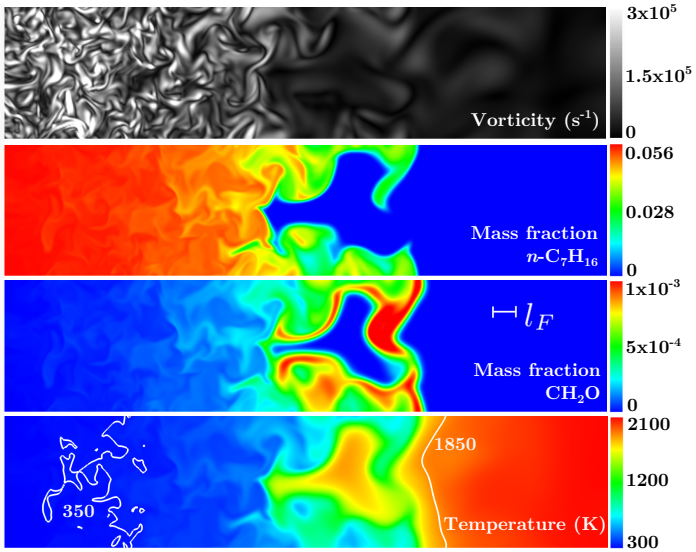

Figure 4.8: Contours of vorticity, n-C_7H_{16} and CH_2O mass fractions, and temperature through the flame brush on a two-dimensional horizontal slice. The laminar flame thickness l_F is added for comparison.

4.4.2 Reaction zone

Contours of the source term of n-C_7H_{16} and H_2O for the non-unity Lewis number flame are shown in Fig. 4.9 on the same two-dimensional slice as in Fig. 4.8. For a Karlovitz numbers as large as 220, scaling arguments suggest that turbulent structures should be sufficiently small enough to penetrate the reaction zone [142]. However, two observations can be made from Fig. 4.9: 1) the reaction zone appears to be thin and 2) signs of local extinctions (broken reaction zone) can be observed in the fuel consumption zone, but cannot be observed in the H_2O production zone.

The first observation could seem inconsistent with the fact that the Kolmogorov length scale in the unburnt gas is 10 times smaller than the laminar reaction zone thickness. However, as mentioned above, the Kolmogorov length scale increases through the flame due to the increasing kinematic viscosity, and becomes as large as the laminar reaction zone thickness as it reaches the burnt side.

To simplify the following analysis, only the fuel consumption will be further investigated in this

thesis. This is first justified because only the consumption rate of the fuel shows local extinction. Second, the magnitude of the relative fluctuations in the fuel chemical source term is amongst the largest of all species source terms. Third, besides hydrogen (atomic and molecular), the fuel has the Lewis number furthest from unity, which makes it a good candidate to analyze differential diffusion effect, and, in particular, greater-than-unity Lewis number effects.

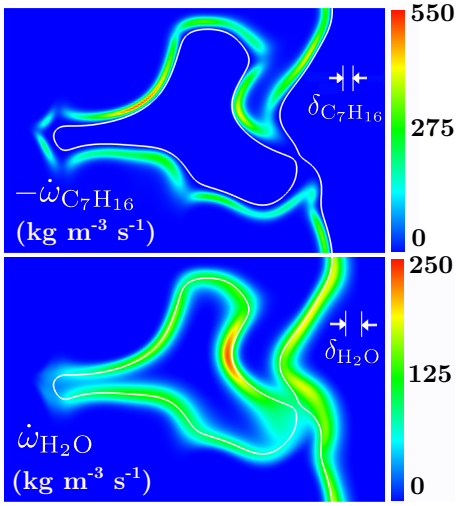

Figure 4.9: Contours of the source terms of n-C_7H_{16} (top) and H_2O (bottom) on the same two-dimensional horizontal slice as in Fig. 4.8. The isoterm $T = 1500$ K (white) is also shown. The laminar reaction zone thicknesses (full width at half-height) of n-C_7H_{16} ($\delta_{C_7H_{16}}$) and H_2O (δ_{H_2O}) are also shown for comparison.

The qualitative results presented in this section and the previous one are summarized in Figure 4.10: turbulence is affected as it progresses through the flame (increased viscosity resulting in an increased Kolmogorov length scale), the flame is largely thickened (increased turbulent mixing in the preheat zone), and the reaction zone is thin and locally broken.

4.4.3 Lower-Ka flame

Results from the lower-Ka flame are qualitatively similar, but the effects of turbulence identified for the higher-Ka flame are less pronounced, as illustrated in Fig. 4.11 and 4.12. For this reason, only the higher-Ka flame will be characterized in Chapters 5 and 6. The lower-Ka flame will be used to validate the models developed in Chapters 5 and 7, as these should hold through the thin reaction zones regime.

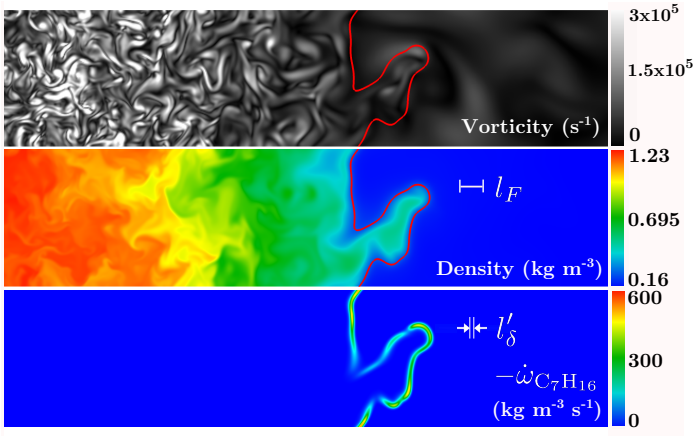

Figure 4.10: Contours of vorticity, density, and fuel burning rate through the flame brush on a two-dimensional horizontal slice of the non-unity Lewis number flame. The $T = 1240$ K isocontour is also shown (red).

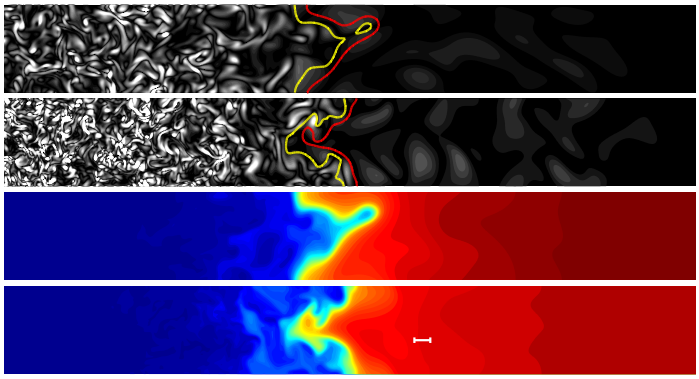

Figure 4.11: Two-dimensional slices showing the vorticity and temperature for the non-unity Lewis number flames. The yellow line indicates the $T = 940$ K isocontour and the red line indicates the $T = 1540$ K isocontour. The vorticity ranges are satureated at [0,8e4] (s^{-1}) and [0,1.6e6] (s^{-1}). The temperature ranges are both [298,2200] K.

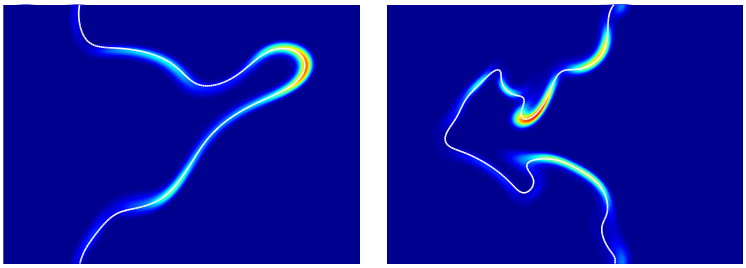

(a) $Ka = 78$ (b) $Ka = 220$

Figure 4.12: Two-dimensional slices showing the fuel consumption rate for the non-unity Lewis number flames. The fuel consumption rate range is saturated at [0,650] (kg m^{-3} s^{-1}). The $T = 1240$ K isocontour is also shown (white).

Chapter 5

Characterization and modeling of the flame structure[1]

The qualitative results from the previous chapter show that the flame is significantly affected (thickened) by turbulence. The objective of this chapter is to characterize the effect of turbulence on the flame structure and to model the effect of turbulent mixing on this mean structure. The flame structure is characterized first. Second, an *a priori* model for the flame structure of non-unity Lewis number turbulent flames is developed/validated using a set of DNS of turbulent hydrogen/air flames (simpler chemistry) performed by Aspden *et al.* [10] for a wide range of Karlovitz numbers. Finally, the model is tested on the present non-unity *n*-heptane/air flame. A discussion on the validity and the limitations of the model for this flame is also provided.

5.1 Structure of the *n*-heptane flame

In this section, the structure of both the unity and the non-unity Lewis number flames are presented. The effects of turbulence in the absence of differential diffusion are presented first (unity Lewis number flame). Second, the differential diffusion effects are highlighted with the non-unity Lewis number flame.

[1]The first two sections of this chapter are published in B. Savard, B. Bobbitt, and G. Blanquart, Proc. Comb. Inst. (2015) and in B. Savard and G. Blanquart, Combust. Flame (2014), respectively. The author of this thesis has contributed to all the work presented in this chapter.

5.1.1 Turbulent flame structure in the absence of differential diffusion

The effects of turbulence on the flame are illustrated in Fig. 5.1. By comparing this figure to Fig. 4.8, the unity and the non-unity Lewis number flames look very similar qualitatively. In particular, both flames look very different from a one-dimensional flame.

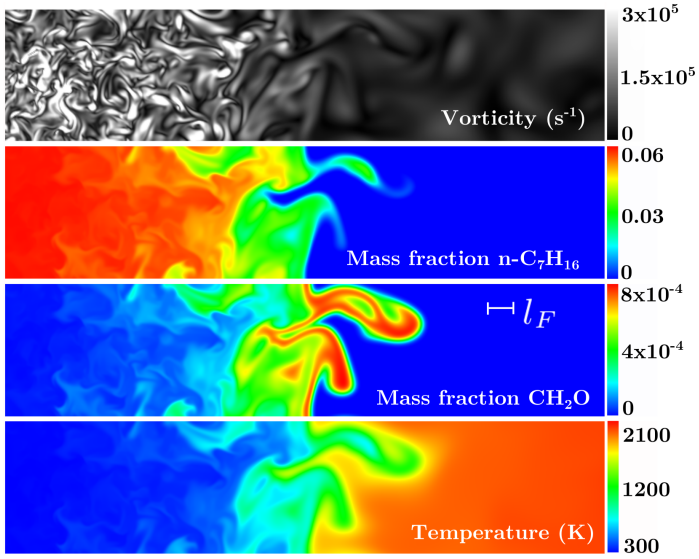

Figure 5.1: Contours of vorticity, n-C_7H_{16} and CH_2O mass fractions, and temperature through the flame brush on a two-dimensional horizontal slice. The laminar flame thickness l_F is added for comparison.

To properly assess the influence of turbulence on the flame structure, one can analyze the correlation between species and temperature (or any other progress variable). As such, the flame structure can be adequately compared to that of a one-dimensional laminar flame, which is well represented in temperature space. Any departure from a one-dimensional laminar flame due to turbulence should be captured by these species mass fraction profiles.

In this sense, several species mass fractions are plotted against temperature and are compared to their one-dimensional laminar flame equivalent. Figure 5.2 shows joint probability densities of n-C_7H_{16}, C_2H_4, and CO_2 mass fraction, *vs.* temperature. These species correspond to a reactant, an intermediate species, and a product, respectively. The conditional mean of these species mass fraction (conditional on temperature) is also shown. This figure is representative of the overall flame structure as the mass fractions of other species show similar behaviors. These results suggest that

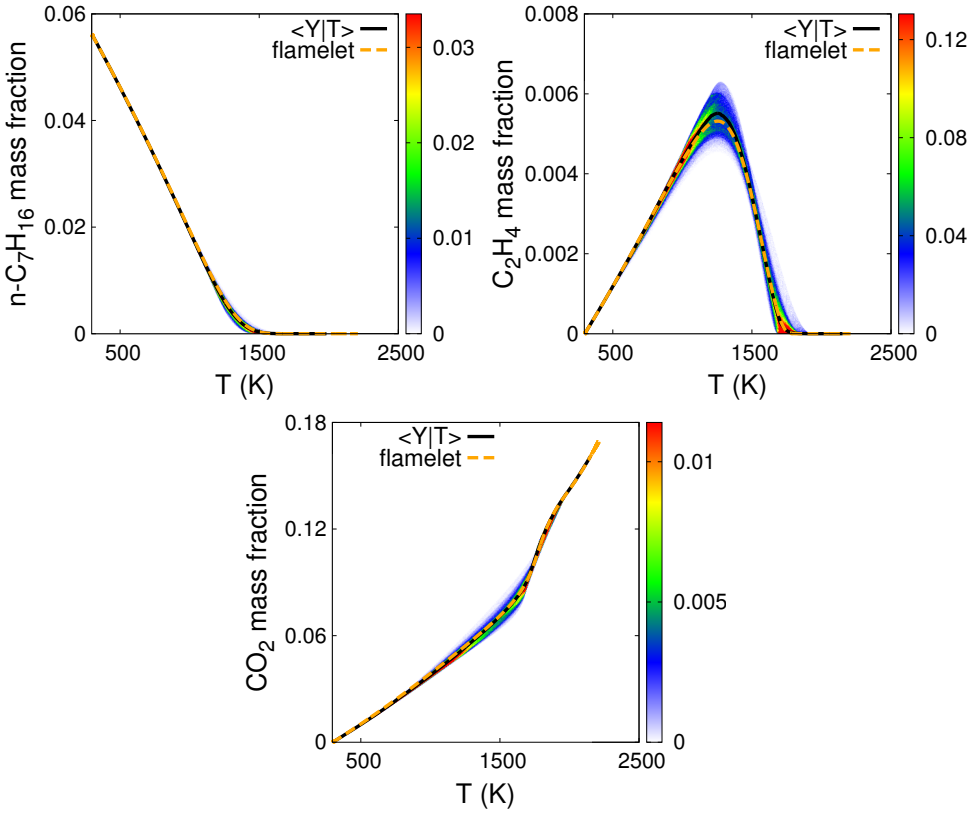

Figure 5.2: Joint PDF and conditional mean (solid line) of the n-C_7H_{16} (top left), C_2H_4 (top right), and CO_2 (bottom) mass fraction *vs.* temperature from the unity Lewis number DNS. The unity Lewis number flamelet solution is also shown (dashed line).

the influence of turbulence on the flame structure in the absence of differential diffusion is very limited as the spread of the joint PDF is limited (this has also been observed by Aspden *et al.* for a high-Ka CH_4/air flame [9]). More interestingly, the conditional mean profiles of these species follow very closely the profiles of a one-dimensional, unstretched laminar flame at the same condition. This result is surprising, as the turbulent flame is clearly not in the flamelet regime and does not look like a flamelet.

Although the last result may be surprising, an expected first order effect of turbulence on species transport is the increase in the effective diffusivity through increased mixing. Assuming turbulence mixes all scalars the same way, the turbulent diffusivities (D_T) may be assumed equal for all of these

scalars, and the effective diffusivity becomes

$$D_{\text{eff}} = D + D_T. \tag{5.1}$$

To assess the effect of diffusivity on the flame structure, additional laminar flamelet solutions were obtained varying this diffusivity. Whereas the resulting laminar flame speeds and flame thicknesses were accordingly altered by a factor of $(D_{\text{eff}}/D)^{1/2}$, the flame structure was virtually unaffected, as shown in Fig. 5.3.

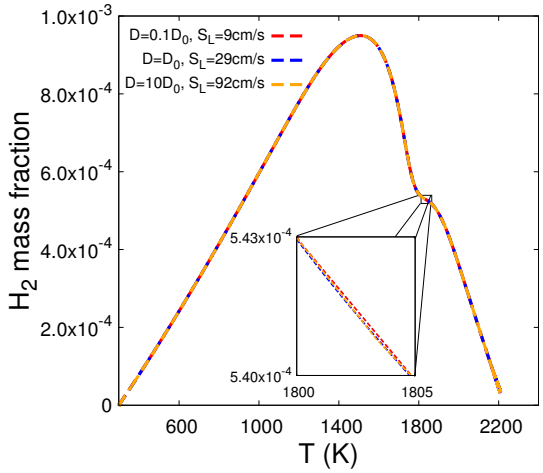

Figure 5.3: Flamelet solutions of the H_2 mass fraction *vs.* temperature with varying diffusivity coefficients.

In summary, while the turbulent flame is thickened by turbulence and is clearly not a thin flame, its *structure* is similar to that of a flamelet. This may suggest that the use of a progress variable with tabulated chemistry [171, 65, 97] would be justified and sufficient even at such high Karlovitz number.

5.1.2 Turbulent flame structure with differential diffusion

Similarly to Fig. 5.2, Fig. 5.4 presents the structure of C_2H_4 through the non-unity Lewis number flame. The full-transport flamelet solution is also added for comparison. While turbulence has almost no impact on the structure of the unity Lewis number flame, it has a clear effect on that of a

non-unity Lewis numbers flame. In this case, the turbulent flame structure lies between that of a full transport and a unity Lewis number flamelet. Once again, a first order effect of turbulence on scalar transport is an increase in the effective diffusivity of each scalar (including species mass fractions and temperature) through increased mixing. As a result, the effective species Lewis number take the following from:

$$Le_{i,\text{eff}} = \frac{\alpha + D_T}{D_i + D_T}. \tag{5.2}$$

A similar expression for these effective Lewis numbers was first suggested by Peters [142]. More details on D_T and $Le_{i,\text{eff}}$ and how they relate to the scalar transport equations will be provided in Section 5.2.2.3. Equation 5.2 suggests that if the turbulence were sufficiently intense, the non-unity Lewis number case would behave the same as the unity Lewis number case, *i.e.* turbulence would suppress differential diffusion effects.

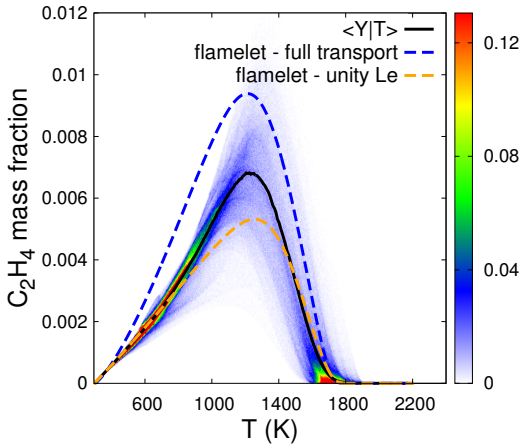

Figure 5.4: Joint PDF and conditional mean (solid line) of the C_2H_4 mass fraction *vs.* temperature from the non-unity Lewis number DNS. The non-unity and unity Lewis number flamelet solutions are also shown (dashed line).

This behavior is observed at low temperatures (*i.e.* in the preheat zone), where the data from the DNS collapse perfectly with the unity Lewis number flamelet solution. However, at higher temperatures, the structure deviates from that of a unity Lewis number flamelet. This can be attributed to the fact that the Kolmogorov length scale grows through the flame, and therefore the "local Karlovitz number" is reduced. As a result, preferential diffusion effects may still be present,

especially towards the reaction zone. These effects are disscussed in more details in the following chapter.

5.2 Effective species Lewis numbers

In this section, a model for the effective species Lewis numbers (Eq. 5.2) is provided. Given the complexity of the *n*-heptane/air flame studied, another set of turbulent premixed flames is chosen to verify/develop the model. A series of Direct Numerical Simulations of lean hydrogen/air flames performed by Aspden *et al.* [10] is considered. The reason behind this choice of flames is three-fold: 1) the hydrogen/air flame has far simpler chemistry (similar to one-step chemistry) than the *n*-heptane/air flame, 2) the viscosity ratio across the flame is considerably lower in the hydrogen/air flame (13 *vs* 30 for the *n*-heptane/air flame), and 3) the hydrogen/air flames were performed over a wide range of Karlovitz numbers, such that the transition between the purely laminar to the fully turbulent flame structure can be studied.

Section 5.2.1 presents the flame structure obtained from the DNS data of Aspden *et al.* and compares it to corresponding laminar unstretched flamelets. Section 5.2.2 derives an *a priori* model from simplified species and temperature balance equations. Section 5.2.3 compares the model against the effective Lewis numbers computed from the DNS. Section 5.2.4 discusses different approaches to derive a model for these effective Lewis numbers. A Reynolds number versus a Karlovitz number dependency is especially emphasized. Finally, Section 5.2.5, in addition to disscussing the model's sensitivity, applicability, and practical use, presents the impacts of the effective Lewis numbers on the laminar flame speed and the laminar flame thickness, the effective Karlovitz number and the regime diagram, and the turbulent flame speed models.

The validity and the limitations of the model for the *n*-heptane/air flame will be discussed in Section 5.3.

5.2.1 Turbulent flame structure

In this section, the flame structure from the series of Direct Numerical Simulations performed by Aspden *et al.* [10] is compared to the structure of laminar unstretched flamelets. A schematic diagram of the flow configuration used for the DNS is presented in Fig. 5.5. The complete set of parameters describing the DNS cases can be found in Ref. [10] and are summarized in Table 5.1. Note that Aspden *et al.* used a different definition for the Karlovitz number than the one presented in the introduction, *i.e.* $Ka = (u'/S_L)^{3/2} (l/l_F)^{-1/2}$. Based on scaling arguments, the two definitions are equivalent [142]. The one used by Aspden *et al.* assumes $S_L l_F = \nu$. The reactants are a lean ($\phi = 0.4$) hydrogen-air mixture. A reduced version of GRI-MECH 2.11 was used as the chemical mechanism (9 species, 27 reactions; all carbon-based species and associated reactions were removed). Soret and Dufour effects as well as radiation were not included in the DNS [10]. As confirmed in Ref. [10] and shown in Fig. 5.6, the transition from the thin reaction zone to the broken reaction/distributed burning zone is covered by the simulation cases.

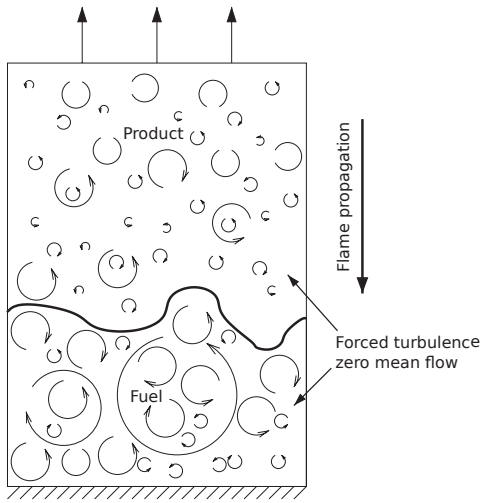

Figure 5.5: Schematic diagram of the flow configuration used by Aspden *et al.* [10]. Diagram taken from Ref. [10].

The laminar flame counterparts are simulated using FlameMaster [146]. The equivalence ratio is fixed to 0.4; the same chemical model as in the DNS is used; and Soret and Dufour effects and

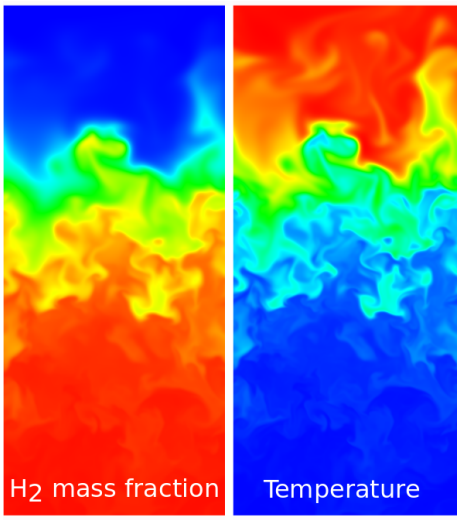

Figure 5.6: Contours of hydrogen mass fraction and temperature on a two-dimensional vertical slice of the DNS case D [10].

Case	A	B	C	D
Equivalence ratio (ϕ)	0.4	0.4	0.4	0.4
Laminar flame speed (S_L) (m/s)	0.224	0.224	0.224	0.224
Laminar flame thickness (l_F) (mm)	0.629	0.629	0.629	0.629
Length ratio (l/l_F)	0.5	0.5	0.5	0.5
Velocity ratio (u'/S_L)	3.69	17.1	32.9	106.8
Turbulent Reynolds number based on viscosity of unburnt gases (Re_T)	14.2	65.8	126.1	410.7
Karlovitz number ($Ka = (u'/S_L)^{3/2} (l/l_F)^{-1/2}$)	10	100	266	1526

Table 5.1: Parameters for the series of turbulent premixed hydrogen flame DNS performed in Ref. [10].

radiation heat losses are ignored.

The conditional means of the mass fractions with respect to temperature $< Y_i \mid T >$ are calculated for several instantaneous snapshots of the established (statistically steady) propagating flame. Figure 5.7 shows the conditional mean hydrogen mass fraction as a function of temperature for cases A through D. The temperature is used here as a progress variable. The profiles for laminar unstretched flamelets with full transport [177, 91] and unity Lewis numbers are also shown in Fig. 5.7. The "full transport" and "unity Lewis numbers" laminar flames correspond to limiting cases of purely laminar and fully turbulent premixed flames, respectively. A clear trend is observed: the DNS profiles gradually move from the purely laminar towards the fully turbulent limiting cases. It

is important to stress that all DNS data are "bracketed" by these two limiting cases. As mentioned earlier, one of the objectives of this section is to model this transition between the purely laminar to the fully turbulent flame structure.

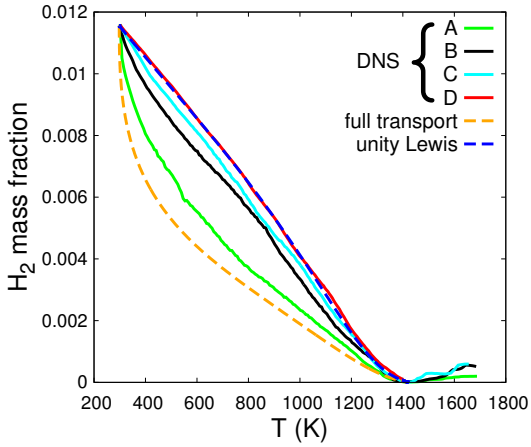

Figure 5.7: Conditional mean hydrogen mass fraction profiles as a function of temperature for the DNS cases A through D and unstretched laminar flames with full transport and unity Lewis numbers. DNS from Aspden *et al.* [10]

The effects of thermo-diffusive instabilities are revealed by the presence of hot-spots in Fig. 5.7, *i.e.* by the extension of the DNS profiles to temperatures higher than the adiabatic flame temperature ($T_{\text{ad}} \approx 1400$ K). However, the present analysis is aimed to address the turbulent transport problem only. The hot spots are in particular not relevant to the *n*-heptane/air flames considered in this thesis as they are thermo-diffusively stable (more details in Chapter 6). Unfortunately, in the hydrogen/air flames, the turbulent transport is influenced by these thermo-diffusive instabilities. While these instabilities have an important impact on laminar flames [53], they are expected to be less important as turbulence increases, *i.e.* as preferential diffusion becomes negligible due to turbulent mixing. This is observed for the highest Ka DNS case (D). The qualitative behavior of the turbulent flame structures shown in Fig. 5.7 and, as it will be presented in Section 5.2.3, the good agreement of the proposed model suggest that these instabilities have limited impact on the statistical mean structure. As the hot spots and the super-adiabatic temperatures are not a consequence of turbulent transport (of concern in this chapter) and are entirely due to those instabilities, they are not considered in this work. Computing the conditional mean as $< Y_i \mid T >$ instead of $< T \mid Y_i >$

Species	Le_i
N_2	1.169
O	0.772
O_2	1.223
H	0.202
OH	0.787
H_2	0.325
HO_2	1.195
H_2O_2	1.203
H_2O	0.932

Table 5.2: Lewis numbers used in the constant, non-unity Lewis numbers model. These Lewis numbers are evaluated at 723 K from a full transport flamelet solution.

allows one to isolate these hot spots.

In order to simplify the theoretical analysis in the following sections, the full transport model will be replaced by a constant, non-unity Lewis numbers model. Figure 5.8 shows that flamelets with full transport and constant Lewis numbers have virtually the same hydrogen mass fraction profiles. This indeed justifies the assumption of constant Lewis numbers through the flame. Regardless of the temperature at which the constant Lewis numbers are evaluated, the deviation from the full transport profile is negligible. This deviation was, however, minimized by evaluating the Lewis numbers at 723 K, *i.e.* at the beginning of the reaction zone. These constant Lewis numbers are listed in Table 5.2.

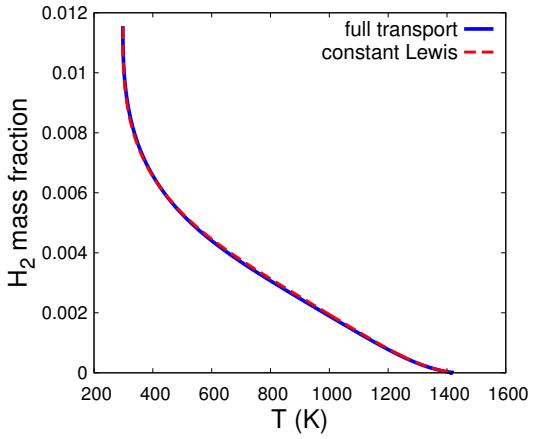

Figure 5.8: Hydrogen mass fraction profiles as a function of temperature for flamelets with full transport and constant Lewis numbers.

5.2.2 Proposed model

In this section, we develop a model for the effective Lewis numbers in a turbulent flame.

5.2.2.1 Species transport equation

The species transport equation (Eq. 2.5) presented in Section 2.1 is also relevant to the hydrogen/air flame:

$$\frac{\partial \rho Y_i}{\partial t} + \underbrace{\nabla \cdot (\rho \mathbf{u} Y_i)}_{\text{advection}} = \overbrace{\nabla \cdot \left(\rho \frac{\alpha}{Le_i} \nabla Y_i \right)}^{\text{diffusion}} + \underbrace{\dot{\omega}_i}_{\text{chemical source}} + \overbrace{\nabla \cdot (\rho Y_i \mathbf{V_{c,i}})}^{\text{velocity correction}} . \tag{5.3}$$

Figure 5.9 shows the contribution from each term in Eq. 2.5 for H_2, in the case of the constant, non-unity Lewis numbers (Table 5.2) unstretched laminar flamelet (same unburnt conditions as in Section 5.2.1). The unsteady term is obviously absent. The conclusion is that the diffusion term associated with the correction velocity is negligible in comparison to the other terms.

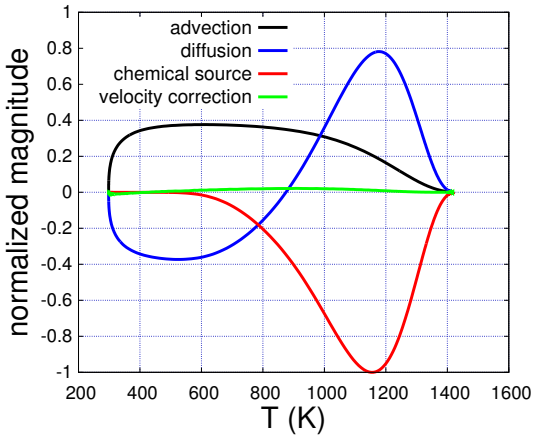

Figure 5.9: Contribution from each term in the species transport equation for H_2 as a function of temperature, obtained for an unstretched laminar flamelet with constant, non-unity Lewis numbers. Each contribution is normalized by the largest absolute value of all contributions.

5.2.2.2 Temperature equation

The temperature equations (Eq. 2.4) presented in Section 2.1 can also be written in the following form:

$$\frac{\partial \rho T}{\partial t} + \underbrace{\nabla \cdot (\rho \mathbf{u} T)}_{\text{advection}} = \overbrace{\nabla \cdot (\rho \alpha \nabla T)}^{\text{diffusion}} + \underbrace{\frac{\dot{\omega}_T}{c_p}}_{\text{chemical source}} + \overbrace{\frac{\rho \alpha}{c_p} \nabla c_p \cdot \nabla T + \sum_i \frac{c_{p,i}}{c_p} \rho \left(\frac{\alpha}{Le_i} \nabla Y_i + Y_i \mathbf{V_{c,i}} \right) \cdot \nabla T}^{\text{others}} . \tag{5.4}$$

Figure 5.10 shows the contribution from each term in Eq. 5.4 calculated for the same flamelet as in subsection 5.2.2.1. As shown, the sum of the last two terms on the right hand side of Eq. 5.4 has negligible contribution.

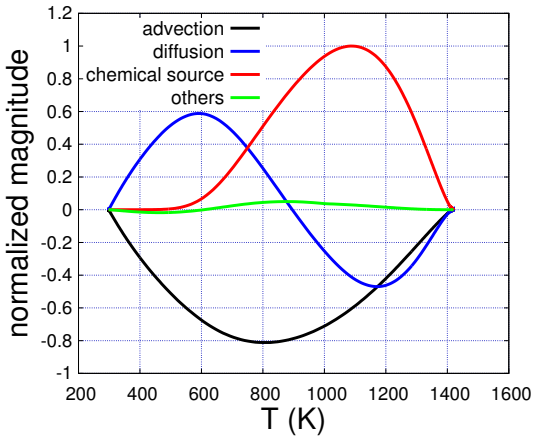

Figure 5.10: Contribution from each term in the temperature equation as a function of temperature, obtained for an unstretched laminar flamelet. Each contribution is normalized by the largest absolute value of all contributions.

5.2.2.3 Effective Lewis numbers

Any model should at least capture the mean of the turbulent flame (in a statistical sense). Reynolds-averaged transport equations provide information about the ensemble/statistical average of the transported quantity. Hence, the choice of a RANS formalism is made. Omitting the terms found to be negligible in subsections 5.2.2.1 and 5.2.2.2, the Reynolds-averaged species and temperature

balance equations can be written as

$$\frac{\partial}{\partial t}\left(\overline{\rho}\widetilde{Y}_i\right) + \nabla\cdot\left(\overline{\rho}\tilde{\boldsymbol{u}}\widetilde{Y}_i\right) = \nabla\cdot\left[\overline{\rho}\left(D_i + D_T\right)\nabla\widetilde{Y}_i\right] + \overline{\dot{\omega}_i} \tag{5.5}$$

$$\frac{\partial}{\partial t}\left(\overline{\rho}\widetilde{T}\right) + \nabla\cdot\left(\overline{\rho}\tilde{\boldsymbol{u}}\widetilde{T}\right) = \nabla\cdot\left[\overline{\rho}\left(\alpha + D_T\right)\nabla\widetilde{T}\right] + \overline{\left(\frac{\dot{\omega_T}}{c_p}\right)}, \tag{5.6}$$

where $\bar{\cdot}$ denotes a Reynolds average and $\widetilde{\cdot}$ a Favre average. D_T is the eddy diffusivity and is assumed to be identical for all species and temperature. This result is a direct consequence of assuming turbulence mixes all scalars the same way. A similar assumption is made in transported PDF methods [174, 152]. From Eq. 5.5 and 5.6, an effective Lewis number can be obtained for each species:

$$Le_{i,\text{eff}} = \frac{D_{\text{heat}}}{D_{\text{mass}}} = \frac{\alpha + D_T}{D_i + D_T} = \frac{1 + \frac{D_T}{\alpha}}{\frac{1}{Le_i} + \frac{D_T}{\alpha}}. \tag{5.7}$$

As previously stated, a similar expression for the effective/turbulent Lewis number was first proposed by Peters [142].

5.2.2.4 Turbulent model

Using a k-ϵ model for the eddy viscosity ν_T [178], the eddy diffusivity can be written as

$$D_T = \frac{\nu_T}{Pr_T} = \frac{C_\mu k^2}{Pr_T \epsilon}, \tag{5.8}$$

where ϵ is the turbulent dissipation rate, k is the turbulent kinetic energy, C_μ is the k-ϵ model coefficient, and Pr_T is the turbulent Prandtl number. Using the same definition for the integral length scale l as in Ref. [10],

$$l = \frac{u'^3}{\epsilon} \tag{5.9}$$

and the turbulent kinetic energy

$$k = \frac{3}{2}u'^2, \tag{5.10}$$

one obtains

$$D_T = \frac{9}{4}\frac{C_\mu u' l}{Pr_T}, \tag{5.11}$$

with u' the root-mean-square velocity fluctuation. Using the definition of the mixture Prandtl number Pr, the ratio of the eddy to the thermal diffusivities can be written as

$$\frac{D_T}{\alpha} = \frac{9}{4}\frac{C_\mu u' l Pr}{\nu Pr_T} = \frac{9}{4} C_\mu \frac{Pr}{Pr_T} Re_T, \tag{5.12}$$

where ν is the mixture kinematic viscosity and $Re_T = u'l/\nu$ is the turbulent Reynolds number. The species effective Lewis number becomes

$$Le_{i,\text{eff}} = \frac{1 + a^{\text{RANS}} Re_T}{\frac{1}{Le_i} + a^{\text{RANS}} Re_T}, \tag{5.13}$$

where

$$a^{\text{RANS}} = \frac{9}{4} C_\mu \frac{Pr}{Pr_T}. \tag{5.14}$$

In Eq. 5.13, Le_i and Re_T are the inputs. Le_i is known for all species and can be obtained from a one-dimensional flame simulation (Table 5.2) and Re_T is a known quantity from the DNS parameters.

The parameter a^{RANS} is a function of several quantities. An exact *a priori* evaluation of this parameter is difficult. However, an estimate can be provided. First, we set $C_\mu = 0.09$ from a standard k-ϵ model [178]. Second, Pr is a function of temperature and mixture composition and can be obtained from a one-dimensional flame simulation. It is bounded by its value in the unburnt mixture ($Pr_u = 0.54$) and its value in the burnt mixture ($Pr_b = 0.70$). Third, the turbulent (eddy) Prandtl number Pr_T has to be estimated. Since the thermal and species eddy diffusivities are assumed equal, it is of the same order of approximation to assume that the eddy viscosity is also equal to the eddy diffusivities. It is therefore reasonable to assume Pr_T to be unity. A similar assumption is made in transported PDF methods [174, 152]. However, other values for the turbulent Prandtl number have been reported in the literature: in the case of free shear flow, a constant value of 0.7 for the turbulent Prandtl number was found to give better agreement between experiments

and analytical predictions [152]. We therefore assume that Pr_T is bounded by 0.7 and 1. With these parameters, an estimated range for the parameter a^{RANS} is obtained:

$$a^{\mathrm{RANS}} \approx 0.1\text{–}0.2. \tag{5.15}$$

However, it is important to note that a large uncertainty exists on this parameter. Regardless, this gives the order of magnitude one should obtain for a^{RANS}. Note that this parameter is used as a fitting coefficient in the following section.

5.2.3 Evaluation of the effective Lewis numbers and model validation

In this section, we evaluate the effective Lewis numbers from the DNS data and compare the results with the model proposed in the previous section. In order to identify an adequate method for the evaluation of these effective species Lewis numbers from the DNS data, a sensitivity analysis of the flamelet structure to the species Lewis numbers is first performed.

5.2.3.1 Sensitivity analysis to species Lewis numbers

The laminar unstretched flamelet profiles are not equally sensitive to all species' effective Lewis number. For instance, O_2 has a "laminar" Lewis number already close to unity ($Le_i \approx 1.2$ for O_2) and therefore as its effective Lewis number progresses towards unity, very small changes in the laminar flame profile should be expected. On the other hand, the effective Lewis number of H_2 will change from around 0.3 to unity. Therefore, it is useful to perform a sensitivity analysis first.

One species Lewis number at a time is modified, the other ones being fixed to the species Lewis numbers obtained for a laminar flame with full transport. Multiple flamelets are simulated for each modified species, their Lewis number varying from their "laminar" value towards unity. The resulting H_2 and OH mass fractions versus temperature profiles are compared with the DNS profiles. Figure 5.11 shows these profiles for H_2 (top) and OH (bottom) mass fractions for modified Lewis numbers of H_2, H, and all species but H_2 and H, respectively, from left to right. Note the presence

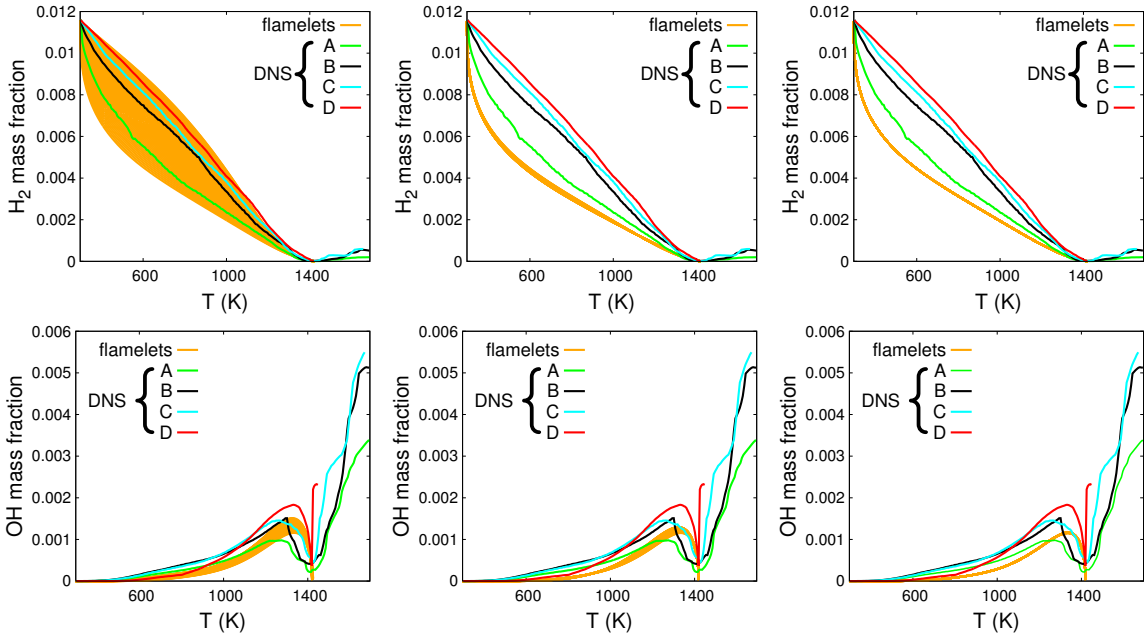

Figure 5.11: Comparison of H_2 and OH mass fraction profiles between DNS conditional means and flamelets with modified H_2 (left), H (center), and all species but H_2 and H (right) Lewis numbers. DNS from Aspden *et al.* [10]

of hot spots in Fig. 5.11 (for $T > 1400$ K). As mentionned in Section 5.2.1, these are beyond the scope of this thesis and will not be further considered.

Modifying the Lewis number of H_2 has by far the most influence, whereas modifying the Lewis number of H has small effect on H_2 mass fraction and small but non negligible effect on OH mass fraction. Modifying the other species' Lewis number has negligible influence on the flame structure. It is not surprising that the Lewis numbers of H_2 and H have the most influence. Two explanations are suggested and cannot be differentiated in this study: 1) H_2 and H are the species with Lewis numbers the furthest away from unity and 2) H_2 being the limiting reactant and H the most important radical, their diffusion controls the flame structure.

5.2.3.2 Computing the effective Lewis numbers

Based on the sensitivity analysis performed in the previous subsection, the unstretched laminar flame structure is very sensitive to the H_2 Lewis numbers. Therefore, one should be able to identify the H_2 Lewis number that leads to the best flame structure when compared to each DNS data set.

This "optimized" Lewis number is referred to as the effective Lewis number. One such effective Lewis number can be evaluated for each DNS data set. Unfortunately, the unstretched laminar flame structure is almost insensitive to the other species Lewis numbers (except H to some extent), which means that the effective Lewis numbers for these species cannot be identified directly.

As a first step, only the Lewis number of H_2 is modified. The L2-norm of the error between the conditional mean profiles from DNS and the laminar profiles is minimized to obtain the best estimate of the hydrogen effective Lewis number, *i.e.*, for each DNS case (A through D):

$$\begin{aligned} Le_{\mathrm{H_2,eff}} &= \underset{Le^*_{\mathrm{H_2}}}{\arg\min} \frac{1}{N} \sum_{i=1}^{N} \left(Y^{lam}_{\mathrm{H_2}}(Le^*_{\mathrm{H_2}}, T_i) - Y^{DNS}_{\mathrm{H_2}}(T_i) \right)^2 \\ &\text{subject to } Le^*_{\mathrm{H_2}} \in [Le_{\mathrm{H_2}}, 1] \,, \end{aligned} \tag{5.16}$$

where $Y^{DNS}_{\mathrm{H_2}}(T_i)$ corresponds to the interpolated value of $< Y_{\mathrm{H_2}} \mid T >$ (from the DNS) at $T = T_i$, and $Y^{lam}_{\mathrm{H_2}}(Le^*_{\mathrm{H_2}}, T_i)$ corresponds to the value of $Y_{\mathrm{H_2}}$ obtained from the laminar unstretched flamelet simulation with $Le_{\mathrm{H_2}} = Le^*_{\mathrm{H_2}}$, interpolated at $T = T_i$. The temperature is discretized uniformly from the minimum temperature in the domain T_u to the adiabatic flame temperature T_{ad} such that $T_i = T_u + \frac{i}{N+1}(T_{ad} - T_u)$. Once again, the hot spots are not considered.

Table 5.3 presents the effective Lewis numbers obtained and Fig. 5.12 compares them against the model presented in Section 5.2.2. The parameter a^{RANS} in Eq. 5.13 was used as a fitting coefficient and was set to 0.05 to obtain a better agreement with the data. Note that this value is only a factor of two away from the estimate given by Eq. 5.15. In addition, the value of a^{RANS} does not change the slope in the semilog plot of Fig. 5.12. With this slight adjustment, the results are in very good agreement with the model. More specifically, the model captures the evolution of the Lewis number over the range of Reynolds numbers from its laminar value towards unity.

The proposed model does not make a difference between a species or another, *i.e.* all species Lewis numbers should be adjusted. Recognizing that all the parameters in Eq. 5.13 are the same

Case	A	B	C	D
$Le_{\mathrm{H_2,eff}}$ obtained through Eq. 5.16 (only $Le_{\mathrm{H_2}}$ modified)	0.436	0.638	0.795	0.897
$Le_{\mathrm{H_2,eff}}$ obtained through Eq. 5.18 (all Le_i modified)	0.446	0.682	0.871	0.995

Table 5.3: Effective Lewis numbers obtained from the DNS (average from three instantaneous snapshots separated by several eddy turnover times).

for each species, each Lewis number is modified according to

$$Le_{i,\mathrm{eff}} = \frac{1+\gamma}{\frac{1}{Le_i}+\gamma}, \tag{5.17}$$

where $\gamma = a^{\mathrm{RANS}} Re_T$. Defining $\mathbf{Le}_{\mathrm{eff}}$ as the vector containing all species effective Lewis numbers, this vector is obtained, equivalently to Eq. 5.16, as

$$\begin{aligned} \mathbf{Le}_{\mathrm{eff}} = \arg\min_{\mathbf{Le}^*} & \tfrac{1}{N}\sum_{i=1}^{N}\left(Y_{\mathrm{H_2}}^{lam}(\mathbf{Le}^*, T_i) - Y_{\mathrm{H_2}}^{DNS}(T_i)\right)^2 \\ \text{subject to} & \begin{cases} Le_j^* = \frac{1+\gamma}{\frac{1}{Le_j}+\gamma}, \\ \gamma \in [0, +\infty)\,. \end{cases} \end{aligned} \tag{5.18}$$

The hydrogen effective Lewis numbers obtained are presented in Table 5.3. They are also compared against the model in Fig. 5.12. The effective Lewis numbers are virtually the same as obtained with changing only H_2 for the low Reynolds number cases (A and B). Only a small difference is registered for the higher turbulent cases (C and D). Regardless, the agreement with the model remains relatively good. It is interesting to note that the slope predicted by the model seems to be slightly off, which would suggest that the power dependence on Re_T in Eq. 5.13 may be incorrect, or equivalently the Reynolds number may not be the best variable to use in Eq. 5.13.

5.2.4 Model dependence on Reynolds versus Karlovitz number

The model proposed in Section 5.2.2 suggests that the effective Lewis numbers depend on the turbulent Reynolds number. The eddy diffusivity that appears in the equation for the effective Lewis numbers (Eq. 5.7) was approximated using a k-ϵ turbulent model and a model based on Re_T was obtained (Eq. 5.13). One could however argue that the effective Lewis numbers are mostly relevant

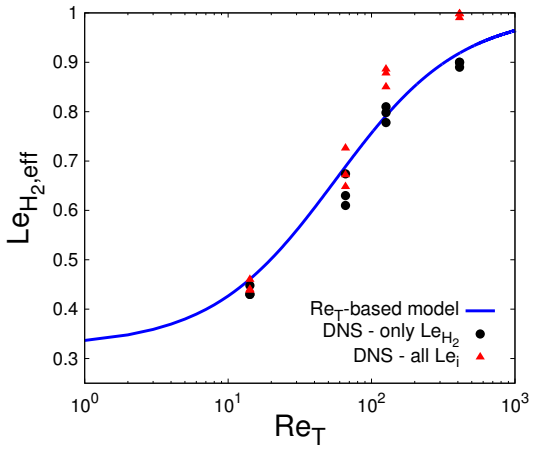

Figure 5.12: Effective Lewis number for H_2 versus turbulent Reynolds number obtained by L2-norm minimization from the DNS where only H_2 (black circles) or all Lewis numbers (red triangles) are modified in the flamelet simulations (three instantaneous snapshots separated by several eddy turnover times for each case).

within the flame, where large scalar gradients are present. Based on this argument, the flame characteristics should appear in the scaling for the eddy diffusivity. The following subsections consider and compare different approaches to obtain this scaling and, as a result, a possible dependence of the proposed model on the Karlovitz number instead of the turbulent Reynolds number is suggested.

5.2.4.1 RANS-based approach

The RANS-based approach used to derive the model (in Section 5.2.2) assumes that the eddy diffusivity scales as the product of the integral length scale and the velocity fluctuation, *i.e.*

$$D_T \propto lu'. \tag{5.19}$$

Consequently, using Eq. 5.7, the model for the effective Lewis numbers can be expressed as

$$Le_{i,\text{eff}}^{\text{RANS}} = \frac{1 + a^{\text{RANS}} Re_T}{\frac{1}{Le_i} + a^{\text{RANS}} Re_T}, \tag{5.20}$$

where a proportionality constant a^{RANS} is used. With this approach, the effective Lewis number does not depend on any flame characteristic. This result is rather surprising as such a dependency should be expected.

5.2.4.2 Flame thickness-based approach

Another approach is to assume that the eddy diffusivity is controlled by eddies of the size of the flame. This leads to the following scaling:

$$D_T \propto l_F u_F, \tag{5.21}$$

where u_F is the turnover velocity of an eddy of size l_F. This velocity is obtained by [142]

$$u_F = (\epsilon l_F)^{1/3}. \tag{5.22}$$

Using Eq. 5.9, 5.21, and 5.22, one obtains

$$D_T \propto \frac{l_F^{4/3}}{l^{1/3}} u' \tag{5.23}$$

or

$$\frac{D_T}{\alpha} \propto Ka^{2/3}. \tag{5.24}$$

A model for the effective Lewis numbers follows

$$Le_{i,\mathrm{eff}}^{l_F} = \frac{1 + a^{l_F} Ka^{2/3}}{\frac{1}{Le_i} + a^{l_F} Ka^{2/3}}, \tag{5.25}$$

where a^{l_F} is a proportionality constant.

5.2.4.3 Time scale-based approach

A third approach is to consider the response time of the flame to unsteady perturbations. This response time is expected to scale like the flame time t_F. Eddies of turnover time corresponding to the flame time should then be used in the scaling for the eddy diffusivity, *i.e.*

$$D_T \propto l(t_F)u(t_F), \tag{5.26}$$

where $l(t_F)$ and $u(t_F)$ are respectively the size and eddy turnover velocity of an eddy of turnover time t_F. Peters [142] derived a mixing length scale based on the quench time and showed that this quench time is of the order of the flame time scale [138]. Therefore, the scaling results derived here are equivalent to Peters' approach.

The relevant eddy size is obtained by

$$l(t_F) = \left(\epsilon t_F^3\right)^{1/2}. \tag{5.27}$$

Recall that the flame time scales as

$$t_F \propto \frac{l_F^2}{\alpha}. \tag{5.28}$$

The turnover velocity $u(t_F)$ is obtained as

$$u(t_F) = \left(\epsilon t_F\right)^{1/2}. \tag{5.29}$$

Using Eq. 5.9, 5.27, and 5.29 in Eq. 5.26, one obtains

$$D_T \propto \frac{u'^3}{l}\frac{l_F^4}{\alpha^2}. \tag{5.30}$$

Equivalently,

$$\frac{D_T}{\alpha} \propto Ka^2. \tag{5.31}$$

As a consequence, one can obtain a model for the effective Lewis numbers as

$$Le_{i,\text{eff}}^{t_F} = \frac{1 + a^{t_F} Ka^2}{\frac{1}{Le_i} + a^{t_F} Ka^2}, \tag{5.32}$$

where a proportionality constant a^{t_F} is used.

5.2.4.4 Integral length scale limit

Subsections 5.2.4.2 and 5.2.4.3 made use of eddies of specific sizes (l_F and $l(t_F)$). However, the largest size these eddies can be is the integral length scale. Consequently, the length scale l_F used in subsections 5.2.4.2 should be replaced by the smallest value between l_F and l, *i.e.* $\min(l_F, l)$. Equivalently, $l(t_F)$ used in subsection 5.2.4.3 should be replaced by $\min(l(t_F), l)$. In the limit where $l_F > l$ and $l(t_F) > l$, the original RANS-based model is recovered for both cases. Nevertheless, it is important to remember that expressions 5.24 and 5.31 are only scaling arguments and a (unknown) proportionality coefficient should be used.

For the DNS simulations used in this section, the integral length scale is smaller than both the flame thickness l_F and the length scale $l(t_F)$ introduced in subsection 5.2.4.3. They are, however, of the same order of magnitude. As a result, it is difficult to assess which length scale is really the limiting quantity.

Another particularity of the series of simulations performed in Ref. [10] is that the l/l_F ratio is fixed. In other words, we have the following scaling

$$Re_T \propto Ka^{2/3}. \tag{5.33}$$

Consequently, the effects of Ka cannot be differentiated from those of Re_T. Using Eq. 5.33, one could have replaced Re_T by $Ka^{2/3}$ in the Re_T-based model (Eq. 5.13 or equivalently Eq. 5.20). Note that the resulting model would correspond to Eq. 5.25.

5.2.4.5 Comparison with DNS results

Based on the observation made in subsection 5.2.3.2, the exponent of Re_T in the Re_T-based model was found to be slightly off. Furthermore, it seems reasonable that the effective Lewis numbers should depend on laminar flame characteristics, as discussed in subsections 5.2.4.1-5.2.4.3. Towards that end, we have proposed two new scalings based on the Karlovitz number. The t_F approach predicts an exponent of 2 to the Karlovitz number, whereas the l_F approach predicts an exponent of 2/3 (for fixed l/l_F the RANS approach also predicts an exponent of 2/3). The predictions with these models are compared against the effective Lewis numbers presented in Table 5.3 (obtained from Eq. 5.18), and are depicted in Fig. 5.13. An additional empirical model is considered in which the Re_T is simply replaced by Ka in Eq. 5.13:

$$Le_{i,\text{eff}}^{Ka} = \frac{1 + a^{Ka} Ka}{\frac{1}{Le_i} + a^{Ka} Ka}. \tag{5.34}$$

For each of these models, the proportionality coefficient is adjusted to best fit the data ($a^{Ka} = 0.05$). The best agreement is found to be with an exponent of 1 (Eq. 5.34), which is bounded by the 2/3 and 2 exponents. The agreement with the DNS values is very good and in particular better than for the Re_T-based model. This better agreement with the empirical Ka-based model raises interesting questions.

However, as mentioned in subsection 5.2.4.4, since the l/l_F ratio is fixed in the DNS used, the Reynolds and Karlovitz numbers are related to each other (Eq. 5.33). As such, the dependence of the model to the Reynolds or the Karlovitz number cannot be verified. Nevertheless, the Ka-based model is still prefered due to its more physical nature and better agreement with the DNS data.

5.2.5 Discussion

In this section, the empirical Ka-based model (Eq. 5.34) is considered. As discussed in Section 5.2.4, this Ka-based model was found to agree the best with the DNS results.

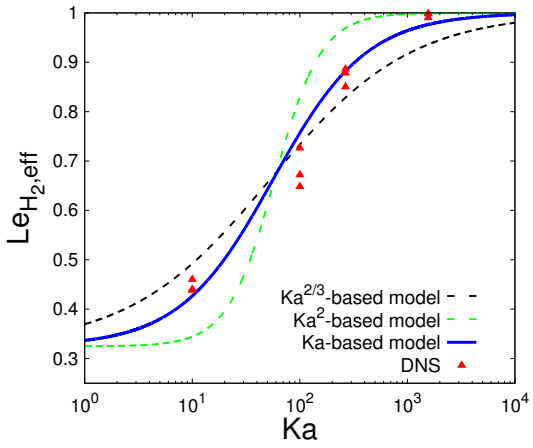

Figure 5.13: Comparison of the effective Lewis number for H_2 versus Karlovitz number for three different models.

5.2.5.1 Model's sensitivity to unburnt pressure, temperature, and equivalence ratio

Only four DNS datasets were used to assess the model's validity. Unfortunately, the number of available datasets suitable for the present study is limited. Nevertheless, one might wonder what the model's sensitivity is to the unburnt equivalence ratio, pressure, and temperature, and in what context the model could be used. Three points are discussed in this subsection: 1) the form of the model, 2) the parameter's sensitivity to the unburnt conditions, and 3) the range of applicability of the model.

First, the model for the effective species Lewis numbers maps a pair of species Lewis number-Karlovitz number to an effective species Lewis number. In other words, one can define a function f such that

$$Le_{i,\text{eff}} = f\left(Le_i, Ka\right), \tag{5.35}$$

where

$$f\left(\xi_1, \xi_2\right) = \frac{1 + a^{Ka}\xi_2}{\frac{1}{\xi_1} + a^{Ka}\xi_2}. \tag{5.36}$$

The function f is derived from ensemble-averaged equations (Eq. 5.5 and 5.6). Its form is therefore independent from the unburnt equivalence ratio, pressure, and temperature.

Second, while the form of the function is fixed, the parameter a^{Ka} in the function f is expected to

vary somewhat with the unburnt equivalence ratio, pressure, and temperature. Its sensitivity to the unburnt conditions is expected to be similar to that of a^{RANS} appearing in the Re_T-based model. This parameter's sensivity is itself expected to follow closely that of Pr (Eq. 5.14), as the other two parameters, namely Pr_T and C_μ, come from turbulent models that are independent of these unburnt conditions. The Prandtl number is the ratio of the thermal diffusivity and the kinematic viscosity. These two quantities scale the same way with respect to temperature and pressure. More specifically, we have the following scaling:

$$\nu, \alpha \propto T^{3/2} p^{-1}. \tag{5.37}$$

Since the Prandtl number is the ratio of these two quantities, its sensitivity to the unburnt temperature and pressure is expected to be low. Its sensitivity to the unburnt equivalence ratio appears through the mixing rules for the thermal diffusivity and the kinematic viscosity of the mixture [177]. Pr is therefore bounded by the Prandtl number of air and that of the fuel. In summary, we expect a weak sensitivity to the unburnt equivalence ratio, pressure, and temperature for the parameters a^{RANS} and a^{Ka}.

Third, the model was derived and validated considering only statistically flat, unstretched flames, and therefore might not be applicable outside this context. However, as mentioned above, the model should remain valid independently from the unburnt conditions. Furthermore, the model should be applicable to any range of Karlovitz numbers, as the effective Lewis numbers predicted are bounded by their laminar values and unity.

5.2.5.2 Practical use of the model

While the model presented in this work was developed from the RANS equations, it may be applied equally well to LES and DNS.

The results of the previous sections show that the structure of a turbulent flame resembles that of a laminar flame (from a statistical point of view) with an appropriate choice of effective Lewis numbers. In other words, all chemical quantities may be expressed as a function of a single progress

variable (such as temperature or product mass fraction). Such methodology is often refered to as tabulated chemistry. The model presented in this chapter should be used in the generation of such a chemistry table.

Lewis numbers appear at two places in the simulation of premixed flames with tabulated chemistry (either RANS, LES, or DNS): 1) in the transport equations for the species in the one-dimensional, unstretched laminar flame simulations (used to tabulate the chemistry), and 2) in the transport equation for the progress variable in the computational fluid dynamics (CFD) code. The model presented in this chapter is only relevant to the Lewis numbers that appear at the first place (1D flame simulations for tabulation).

Note that additional impacts of the effective species Lewis number model are detailed in Appendix A.

5.3 Use of the effective species Lewis number model with the *n*-heptane flame

In this section, the effective species Lewis number model presented in the previous section is tested on the non-unity *n*-heptane/air flame. First, the Ka-based model (Eq. 5.34) is used to compute a set of effective species Lewis numbers. The same proportionality coefficient as used in Section 5.2.4.5, $a^{Ka} = 0.05$, is considered. Note that given the definition of the Karlovitz number used in Section 5.2, a Karlovitz number of 73 is obtained for the *n*-heptane/air flame. As such, the effective Lewis number for the fuel is 1.16. The solution of an unstretched laminar flame with this set of effective species Lewis numbers is obtained with FlameMaster. The species mass fraction *vs.* temperature profiles are compared, in Fig. 5.14, to the corresponding conditional means from the DNS for the fuel, C_2H_4, and CO_2. Although differences are noticeable, especially for the product, the effective Lewis number model captures fairly well the effect of turbulent mixing on the mean flame structure. It is important to highlight the fact that the model was proposed/validated with a series of lean hydrogen/air flames,

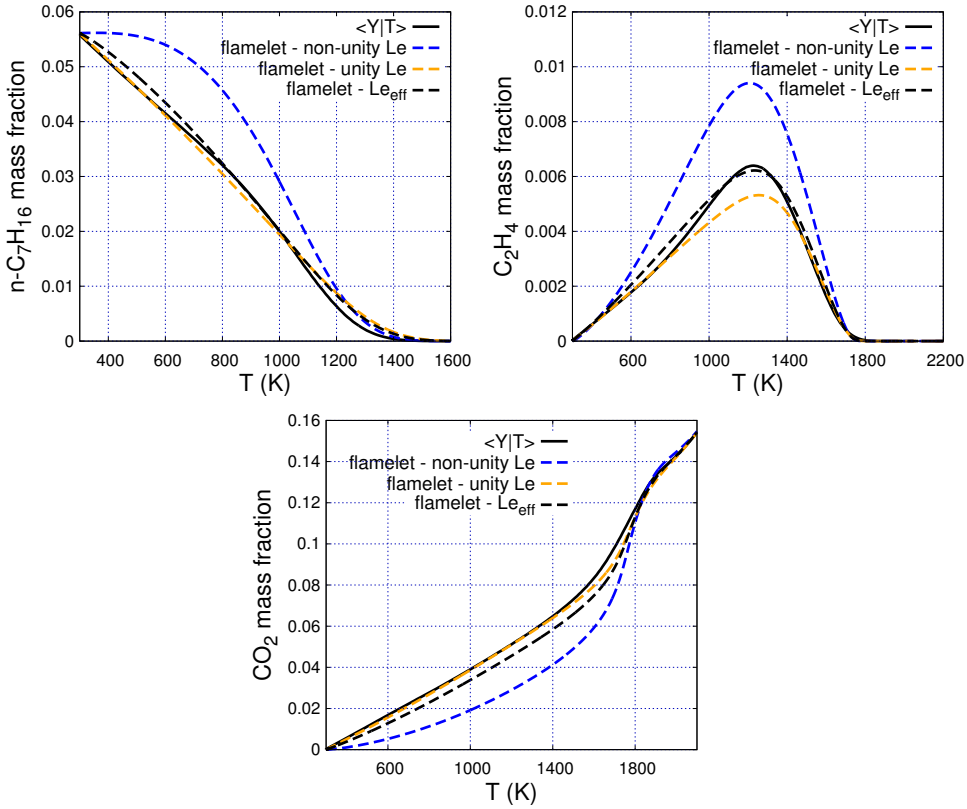

Figure 5.14: Conditional mean (solid line) of the n-C_7H_{16} (top left), C_2H_4 (top right), and CO_2 (bottom) mass fraction *vs.* temperature. The non-unity, the unity, and the effective Lewis number flamelet solutions are also shown (dashed line).

but is also relevant to the present n-heptane/air flame, without any modification needed.

Second, the procedure described in Section 5.2.3.2 is followed, *i.e.* Eq. 5.18 is solved considering the n-heptane *vs.* temperature profile. The results are compared in Fig. 5.15 to those obtained for the hydrogen/air flames. Since both fuels have very different Lewis numbers, the effective diffusivity is presented instead (corresponding to $\gamma = D_T/\alpha$ in Eq. 5.18). This diffusivity is also computed for the lower-Ka flame (introduced in Chapter 4). Independently of the flame, the data is in fairly good agreement with the model, at least for moderate Ka, corresponding to the thin reaction zones regime.

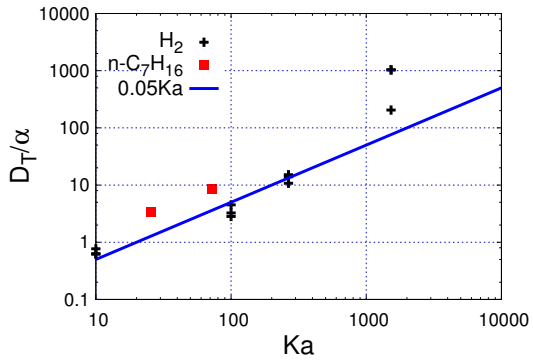

Figure 5.15: Normalized effective diffusivity obtained by solving Eq. 5.18 for the respective fuels (hydrogen and *n*-heptane) *vs.* Karlovitz number ($Ka = (u'/S_L)^{3/2} (l/l_F)^{-1/2}$ to be consistent with the analysis in Section 5.2). The solid line represents $D_T/\alpha = a^{Ka} Ka$ (corresponding to Eq. 5.34) with $a^{Ka} = 0.05$.

5.4 Limitations of the model

As mentioned in Section 5.1.2, a single set of effective species Lewis numbers is not sufficient to entirely capture the mean structure of the non-unity Lewis number *n*-heptane/air flame, as shown in Fig. 5.14. We argued that this is due to the evolving nature of turbulence through the flame. As such, the "local D_T" should vary accross the flame. Again, it is clear from Fig. 5.14 that the flame structure is more unity Lewis number-like at lower temperatures than higher temperatures. Modeling this "local D_T" with scaling arguments (as was done is Section 5.2.4) is not an easy task since relevant local scales need to be identified.

Finally, it was argued in Section 5.1.1 that the use of a progress variable with tabulated chemistry could be justified in the unity Lewis number flame, since the species mass fractions can be mapped unto a single progress variable. Similarly, it was discussed in Section 5.2.5.2 that a progress variable approach could be used for the hydrogen/air flames analyzed in Section 5.2, as long as the proper effective species Lewis numbers are considered. However, it is unclear how this would apply to the non-unity Lewis number *n*-heptane/air flame, in which a single set of effective species Lewis numbers cannot properly characterize both the preheat and the reaction zones. This will be discussed in more details in Chapter 7.

Chapter 6

Characterization of the reaction zone[1]

In this chapter, a characterization of the reaction zone is provided. The effects of turbulence on the reaction zone are assessed in the first section. The mechanism by which stretching affects the fuel consumption rate is then investigated. In the third section, the turbulent flame speed is evaluated and the mechanism through which turbulence affects this flame speed is described. Finally, a short discussion is provided.

All throughout this chapter, the effects of differential diffusion are highlighted by comparing the results between the unity and the non-unity Lewis number flames. Note that the results from the previous chapter indicate that effects of differential diffusion should not be fully suppressed by turbulent mixing at the reaction zone.

6.1 Turbulent reaction zone

The first subsection recalls some of the observations made in Section 4.4.2 on the turbulent reaction zone and provides quantitative information on the fuel source term fluctuations, and the effect of differential diffusion is highlighted. In the second subsection, the structure of the reaction zone in temperature space is analyzed.

[1]The work presented in this chapter is published in B. Savard, B. Bobbitt, and G. Blanquart, Proc. Comb. Inst. (2015) and in B. Savard and G. Blanquart, Combust. Flame (2015). The author of this thesis has contributed to all the work presented in this chapter.

6.1.1 Source term fluctuations and differential diffusion effect

Figure 6.1(a) shows contours of the source term of n-C_7H_{16} for the unity Lewis number flame. Similarly, Fig. 6.1(b) shows the same plot but for the non-unity Lewis number flame. For both flames, the turbulent reaction zone is locally of the same thickness as that of a one-dimensional flat flame (as already shown in Section 4.4.2 for the non-unity flame). These plots suggest that the flames belong to the thin reaction zones regime. As mentioned already, the Kolmogorov length scale increases through the flame due to the increasing kinematic viscosity, and becomes as large as the laminar reaction zone thickness as it reaches the burnt side. Consequently, turbulence has limited impact on the reaction zone thickness. The location in temperature space of the reaction zone is also virtually unaffected. This is evidenced in Fig. 6.1(a) and 6.1(b) by the solid black lines which are isocontours of the respective temperatures of peak source term in a one-dimensional flame (more details in the next section). Nevertheless, the species source terms fluctuate by up to 100% around the laminar value on these isocontours, as highlighted in Fig. 6.1(c). This figure shows both source terms of n-C_7H_{16}, normalized by their peak value in a corresponding laminar flame, extracted along the isocontour corresponding to the temperature of that peak source term, T_{peak}. Note that $T_{\text{peak}} = 1364$ K for the unity Lewis number flame, and $T_{\text{peak}} = 1240$ K for the non-unity Lewis number flame. These fluctuations are suspected to be a consequence of stretching, as observed in Ref. [71, 22] for lower Karlovitz number flames. This will be assessed in Section 6.2.

Interestingly, while little deviations from the laminar flame structure were found (Fig. 5.2) in the unity Lewis number flame, the source terms fluctuate by up to 100% around the laminar value (Fig. 6.1(c)). Although the species mass fractions correlate very well with temperature, small deviations from the laminar profiles are present (see Fig. 5.2), especially around the peak fuel consumption temperature ($T = 1300$ K). These small absolute deviations from the laminar profiles can result in large relative fluctuations and hence large fluctuations in the chemical source terms.

Although source term fluctuations are present for both flames, extinction events seem to be more present with differential diffusion (Fig. 6.1(b) and Figure 6.1(c)). This is confirmed by Fig. 6.2, which presents the distribution of the normalized fuel consumption rate on the isocontour $T = T_{\text{peak}}$

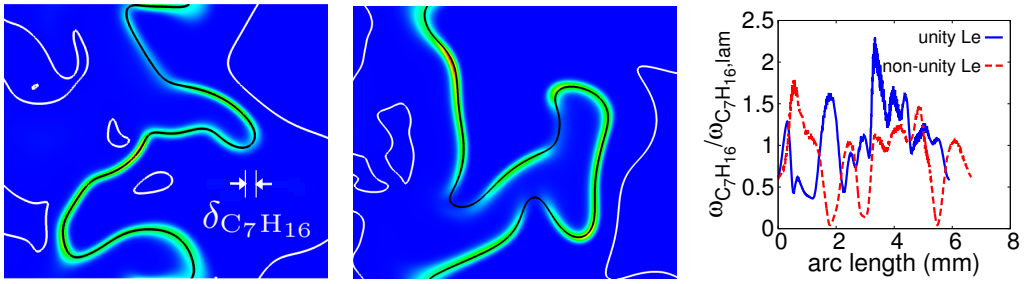

(a) $\dot{\omega}_{C_7H_{16}}$; $T_{peak} = 1364$ K (b) $\dot{\omega}_{C_7H_{16}}$; $T_{peak} = 1240$ K (c) $\dot{\omega}_{C_7H_{16}}$ at T_{peak}

Figure 6.1: (a,b) Contours of n-C_7H_{16} source term normalized by its peak laminar value on a two-dimensional horizontal slice. Also shown are three temperature isocontours: 600 K (white, left of the reaction zone), temperature of peak source term T_{peak} (black), and 1850 K (white, right of reaction zone). The laminar reaction zone thicknesses of n-C_7H_{16}, $\delta_{C_7H_{16}}$ is also shown for comparison. (c) Normalized n-C_7H_{16} source term *vs.* distance along the isocontour $T = T_{peak}$.

(surface in three dimensions) for both flames. The distributions are surface-area weighted and averaged over 10 eddy turnover times. While both distributions have similar shapes, a clear shift to smaller fuel consumption rates is observed with the presence of differential diffusion. Local extinction events are found in the non-unity Lewis number flame, but are absent in the unity Lewis number flame. This is further evidence that the effective diffusivity is not sufficiently high at the reaction zone to suppress the effects of differential diffusion.

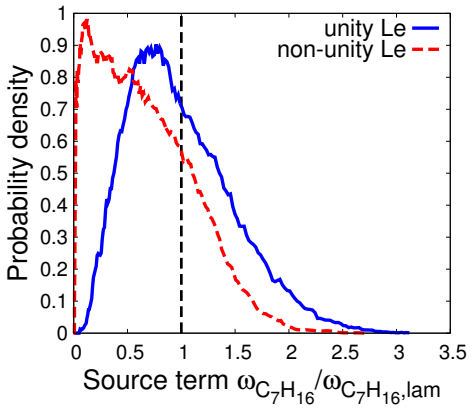

Figure 6.2: Probability density, at $T = T_{peak}$, of n-C_7H_{16} source term, $\dot{\omega}_{C_7H_{16}}$, normalized by its peak laminar value for both the non-unity and the unity Lewis number cases.

It is important to note that the reaction zone is thin and broken at several locations, but not distributed. It may be argued that the Karlovitz number is not sufficiently high to lead to a

distributed reaction zone. Interestingly, Aspden *et al.* [10] have shown that a lean H_2/air flame could transition from a thin reaction zone to a distributed reaction zone behavior (as the Karlovitz number is increased) without showing signs of a broken reaction zone. These different observations may be due to the fact that H_2 has a Lewis number less than unity ($Le_{H_2} \approx 0.3$), whereas n-C_7H_{16} has a greater than unity Lewis number ($Le_{C_7H_{16}} = 2.8$). A more diffusive flame may be expected to be more resistant to turbulent effects/perturbations.

6.1.2 Fuel consumption at T_{peak}

Although the extinction events are linked to differential diffusion, it is not clear through which mechanism. Many authours have previously suggested that extinctions (and, more generally, source term fluctuations) can be a consequence of stretching [71, 22]. These possible correlations (on curvature and strain rate) will be investigated in Section 6.2.3. Before performing such analysis, it is practical to reduce the analysis of the reaction rate from a volumetric (3D) analysis to a surface (2D) analysis.

The integrated fuel consumption speed has often been used in the literature and would be ideal to identify such extinction events [53]. This method requires the integration of the fuel consumption term in a direction normal to the isoterm corresponding to $T = T_{\text{peak}}$. Unfortunately, since the reaction zone is highly curved and sometimes "folded" on itself, the fuel consumption term cannot be computed with both significance and robustness for the present flames. As a consequence, a more local quantity would be preferred.

Figure 6.3(a) shows the joint probability density of the normalized fuel consumption rate as a function of temperature for the unity Lewis number flame. The mean of the source term conditional to temperature is also shown. This profile is compared to its unstretched one-dimensional flame equivalent. While the mean profile is very close to that of the one-dimensional flame, fluctuations around this mean are relatively large. Alternatively, Fig. 6.3(b) presents the joint probability density of the fuel consumption term away from the flame front (at local temperature T) normalized by the consumption term of the closest point on the flame front (*i.e.* normaly projected on the iso-surface

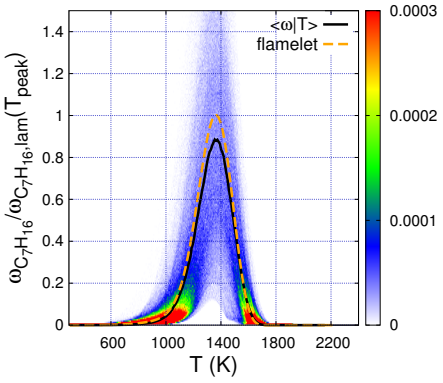

(a) $Le = 1$

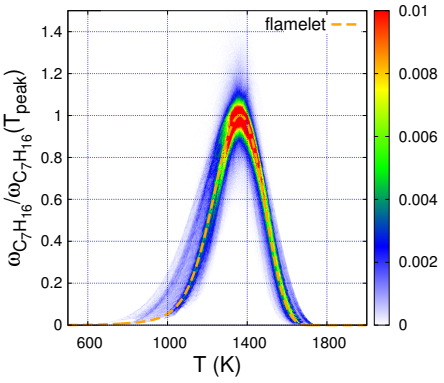

(b) $Le = 1$; normalized by closest point on isoterm $T = T_{\text{peak}}$

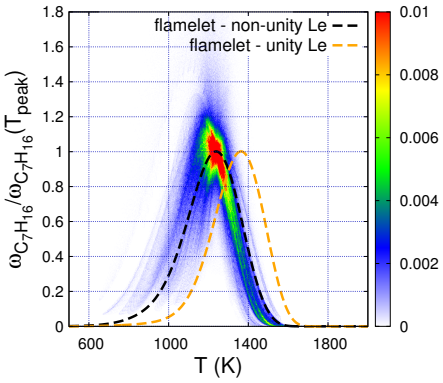

(c) $Le \neq 1$; normalized by closest point on isoterm $T = T_{\text{peak}}$

Figure 6.3: (a)Joint PDF and conditional mean (solid line) of n-C_7H_{16} source term, $\dot{\omega}_{C_7H_{16}}$, normalized by its peak laminar value *vs.* temperature from the unity Lewis number simulation. Joint PDF of n-C_7H_{16} source term, $\dot{\omega}_{C_7H_{16}}$, normalized, in the direction normal to the isoterm $T = T_{\text{peak}}$, by its value on this isoterm *vs.* temperature for the unity Lewis number (b) and the non-unity Lewis number DNS (c). The non-unity and unity Lewis number flamelet solutions are also shown (dashed line).

$T = T_{\text{peak}}$). As can be observed, the fluctuations are significantly reduced now. Figure 6.3(c) shows the same normalized source term for the non-unity Lewis number case. These plots suggest that fuel consumption locally scales like its value at T_{peak}, for both the unity and the non-unity Lewis number flames, *i.e.*

$$\dot{\omega}_{C_7H_{16}}(T) \approx \dot{\omega}_{C_7H_{16}}(T_{\text{peak}}) \frac{\dot{\omega}_{C_7H_{16},\text{lam}}(T)}{\dot{\omega}_{C_7H_{16},\text{lam}}(T_{\text{peak}})}. \tag{6.1}$$

Therefore, only the fuel conssumption term at $T = T_{\text{peak}}$ will be further considered. Figure 6.4

presents three-dimensional views of this reaction surface, *i.e.* the isoterm corresponding to $T = T_{\text{peak}}$, colored by the normalized fuel consumption rate.

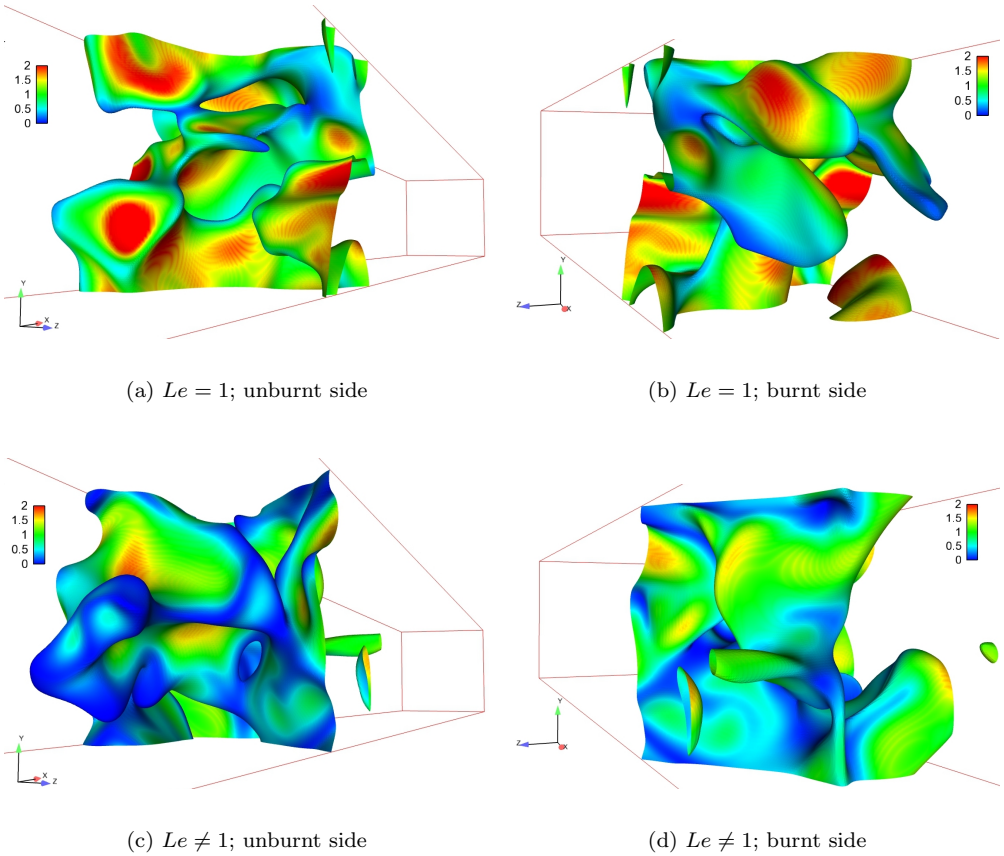

(a) $Le = 1$; unburnt side

(b) $Le = 1$; burnt side

(c) $Le \neq 1$; unburnt side

(d) $Le \neq 1$; burnt side

Figure 6.4: Contours of $\dot{\omega}_{C_7H_{16}}$ normalized by its laminar value on the isosurface corresponding to $T = T_{\text{peak}}$. (a,b) $Le = 1$; (c,d) $Le \neq 1$. (a,c) View from unburnt side; (b,d) view from burnt side.

6.2 Stretching

In order to assess if the fuel consumption rate fluctuations and the local extinctions in the presence of differential diffusion are caused by stretching, it is interesting to first analyze the distribution of curvature and strain rate at the reaction zone. Then, the correlation between fuel consumption rate and strain rate or curvature will be tested.

6.2.1 Curvature and strain rate distributions

The mean curvature is defined as $\kappa = \kappa_1 + \kappa_2$, where κ_1 and κ_2 are the principal curvatures of the reaction surface. The curvature is defined to be positive when the center of curvature is oriented towards the burnt gas. It is expressed as

$$\kappa = \nabla \cdot \boldsymbol{n}, \tag{6.2}$$

where $\boldsymbol{n} = -\nabla T/|\nabla T|$ is the normal to the reaction zone surface, and is positively oriented towards the unburnt gas. As previously performed in Ref. [53], the normal is computed everywhere in the domain and is interpolated on the reaction surface. The probability density distribution of curvature (surface area weighted and averaged over 10 eddy turnover times) is presented in Fig. 6.5(a) for both the unity and the non-unity Lewis number cases. Note that the mean curvature is normalized by the laminar fuel reaction zone thickness $\delta_{C_7H_{16}}$ (full width at half-height). For both cases, $\delta_{C_7H_{16}} = 0.07$ mm $\ll l_F$.

First, it is important to note that the magnitude of curvature is very large. More specifically, the radius of curvature is (with relatively large probability) much smaller than the laminar flame thickness and even as small as the reaction zone thickness. Such intense curvatures are difficult to observe in laminar flames. Second, consistent with the observation that the turbulent reaction zone remains thin for both flames, Fig. 6.5(a) suggests that only velocity perturbations larger than the laminar reaction zone actually reach this reaction zone. Third and most importantly, no differential diffusion effect is visible in Fig. 6.5(a), suggesting that the geometry of the reaction surface is only influenced by turbulence. Note that this might not remain valid for all fuels and all Karlovitz numbers, as thermo-diffusive and Darrius-Landau instabilities might have an effect on the geometry of the reaction surface [53].

The strain rate tangential to the reaction surface is computed as, similarly to Refs. [71, 34],

$$a_t = \nabla \cdot \boldsymbol{u} - \boldsymbol{n} \cdot \nabla \boldsymbol{u} \cdot \boldsymbol{n}, \tag{6.3}$$

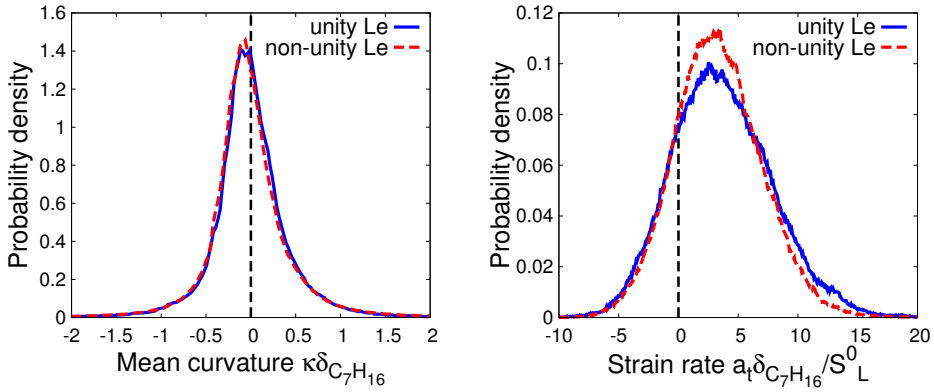

(a) Curvature

(b) Strain rate

Figure 6.5: Probability density function, on the reaction surface, of κ, normalized by the laminar reaction zone thickness (top), and a_t, normalized by the ratio of the laminar reaction zone thickness to the laminar flame speed (bottom).

where $\boldsymbol{u}$ is the velocity. Note that in the limit of an infinitely thin flame, the strain rate is computed in the unburnt gas, where the flow is divergence free, and the tangential strain rate is equal to the normal strain rate. Figure 6.5(b) shows the probability density of the normalized strain rate tangential to the reaction surface. The magnitude of the strain rate, up to 70,000 s^{-1}, is very large (the s-curve turning point of a methane/air premixed flame, with $\phi = 0.7$, $T_u = 800$ K, and $P_0 = 1$ atm in a back-to-back counterflow configuration was found numerically to be approximately 10,000 s^{-1} [96]). Again, the strain rate applied to both the unity Lewis number and the non-unity Lewis number reaction surface are similar. The strain rate for the non-unity Lewis number flame is only marginaly smaller than for the unity Lewis number case. Consistent with values previously-reported by several authors for methane/air and hydrogen/air flames in the thin reaction zone [34, 73, 33, 82], a positive mean tangential strain rate is observed.

With the information presented in this section, it is interesting to go back to Eq. 1.16, which can be rewritten as

$$\frac{S_L}{S_L^0} = 1 - \frac{\mathcal{L}}{\delta_{\mathrm{C_7H_{16}}}} \left(\kappa \delta_{\mathrm{C_7H_{16}}} + \frac{a_t \delta_{\mathrm{C_7H_{16}}}}{S_L^0} \right). \tag{6.4}$$

Under similar unburnt conditions (but with an unburnt temperature of 353K), $\mathcal{L} \approx 1$mm [92], which means $\mathcal{L}/\delta_{\mathrm{C_7H_{16}}} \sim \mathcal{O}(10)$. Figure 6.5 shows that $\kappa\delta_{\mathrm{C_7H_{16}}} \sim \mathcal{O}(0.1)$–$\mathcal{O}(1)$,and $a_t\delta_{\mathrm{C_7H_{16}}}/S_L \sim$

$\mathcal{O}(1)$–$\mathcal{O}(10)$, which means that $\mathcal{L}\left(\kappa + a_t/S_L\right) \gg 1$ and Eq. 6.4 does not hold anymore.

6.2.2 Propagating *vs.* material surface

The results from the last two sections suggest that differential diffusion virtually does *not* affect the reaction zone geometry. This is a consequence of the high Karlovitz number and goes along the results from Bradley *et al.* [22], who observed experimentally a suppresion of thermodiffusive effects at high turbulence levels. This can be explained by an analogy to the work of Yeung *et al.* [185] who analyzed theoretically and numerically the geometry of material and propagating surfaces in the presence of homogeneous isotropic turbulence.

Material surfaces are composed of convected fluid particles. Propagating surfaces have an intrinsic local propagation speed w. For a material surface, w is identically zero. In Yeung *et al.* [185], a premixed flame is seen as a propagating surface, with $w = S_L$. Note that their work is different from that of Ashurst *et al.* [7], who studied the orientation of passive scalar gradients in homogeneous isotropic turbulence (and shear layers). An iso-surface of a passive scalar is neither a material nor a propagating surface.

Yeung *et al.* [185] found that a material surface orientates preferentially with the strain rate tensor. They identified a universal distribution of strain rate on the material surface. In particular, they observed that 80% of the strain rate is positive. They further argued that a propagating surface has the same strain rate distribution as a material surface, independently of the turbulent Reynolds number, under the condition $w/v_\eta \ll 1$, where v_η is the Kolmogorov velocity.

For the present flames analyzed, 81% and 82% of the strain rate was found to be positive for the unity and the non-unity Lewis number flames, respectively. These results are consistent with the ratios S_L^0/v_η as listed in Table 6.1.

In order to further illustrate the difference between propagating and material surfaces, the distributions of tangential strain rate on the reaction surface in the series of DNS of lean H_2/air turbulent flames conducted by Aspden *et al.* [10] are presented in Fig. 6.6. As shown in Table 6.1, the Karlovitz number ranges from 28 to 4200 (consistently with the definition provided in the introduction). The

associated S_L^0/v_η ratios are also listed in Table 6.1. It can be seen that, even though the gas mixtures are different and exhibit Markstein lenghts of opposite signs, the highest Ka H_2/air flame and the present n-C_7H_{16}/air flame show more similar distributions than between the two H_2/air flames. This is consistent with the values of S_L^0/v_η (shown in Table 6.1) and is due to the intense turbulence ahead of the reaction zone.

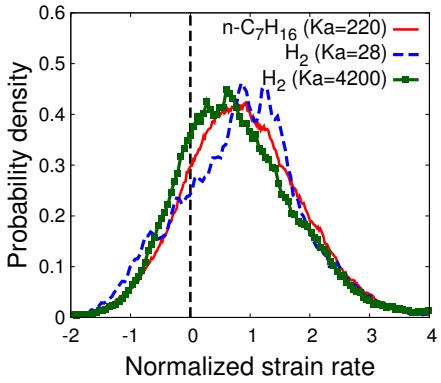

Figure 6.6: Probability density function, on the isoterm $T = T_{\text{peak}}$, of a_t, normalized by the standard deviation of the distributions. Distributions from the H_2/air flame of Aspden *et al.* [10] with $Ka = 28$ and $Ka = 4200$ and from the non-unity Lewis number n-C_7H_{16}/air presented in this thesis.

Fuel	Ka	S_L^0/v_η	% $a_t > 0$
n-C_7H_{16}/air ($Le = 1$)	280	0.08	81
n-C_7H_{16}/air ($Le \neq 1$)	220	0.11	82
H_2/air	28	0.30	80
H_2/air	4200	0.02	80

Table 6.1: S_L^0/v_η ratios (see Ref. [185]) and curvature and strain rate statistics for the flames presented in this thesis and for two lean H_2/air ($\phi = 0.4$) flames presented in [10]. v_η is evaluated at T_{peak}.

The overall conclusion of this subsection and the previous one is that the reaction zone surface behaves as a material surface under the intense turbulent field. Even if the local consumption rates are affected, they are too weak to alter the shape of the flame front. As such, the distributions of curvature and strain rate are independent from differential diffusion effects. Note that curvature and strain rate are also found to be very weakly dependent on one another in both flames (see Appendix B).

6.2.3 Fuel consumption rate *vs.* curvature and strain rate

Figures 6.7(a) and 6.7(b) present the joint probability densities of the normalized fuel consumption term *vs.* strain rate on the isoterm $T = T_{\text{peak}}$, for both the unity Lewis number and the non-unity Lewis number flames (again, the data is averaged over 10 eddy turnover times). Pearson's correlation coefficient and the distance correlation (these two metrics are detailed in Appendix B) are listed in Table 6.2 for these two figures. A stronger correlation (yet still weak) with strain rate is found for the unity Lewis number case. For the non-unity Lewis number case, the source term appears to be more independent from the local strain rate. As a result, strain rate can hardly explain the presence of local extinctions in the non-unity Lewis number case as it can be observed in Fig. 6.7(b).

The sign of the correlation found for both cases (non-unity and unity Lewis number) does not correspond to what would be expected from Eq. 1.16 given the positive sign of the Markstein length. Similarly, Hawkes and Chen [71] have found that, for a lean methane/air mixture, the dependence of the local flame consumption speed (integrated fuel consumption rate normal to the reaction surface) on tangential strain rate is of opposite signs between a laminar flame (exposed to low strain rates) and a high Karlovitz ($Ka \approx 300$, two-dimensional) flame. A similar behavior was also reported by Haworth and Poinsot, albeit for a low Karlovitz number, two-dimensional flame with one-step chemistry [73].

Figures 6.8(a) and 6.8(b) present, similarly to Fig. 6.7(a) and 6.7(b), the joint probability densities of the normalized fuel consumption term *vs.* curvature on the isoterm $T = T_{\text{peak}}$. Again, the correlation coefficients can be found in Table 6.2. This time, there is a much stronger correlation between the fuel consumption rate and the curvature with the presence of differential diffusion. Note that the use of the distance correlation is particularily relevant for this case, as the relation between the fuel consumption rate and curvature is clearly non-linear. Although $\mathcal{L}\kappa > 1$, which implies that Eq. 6.4 is not valid throughout the range of curvatures found, the sign of the correlation found is consistent with Eq. 6.4.

A correlation between the local flame consumption speed and curvature has also been reported previously in turbulent lean hydrogen/air flames [53]. Consistent with the present results, the

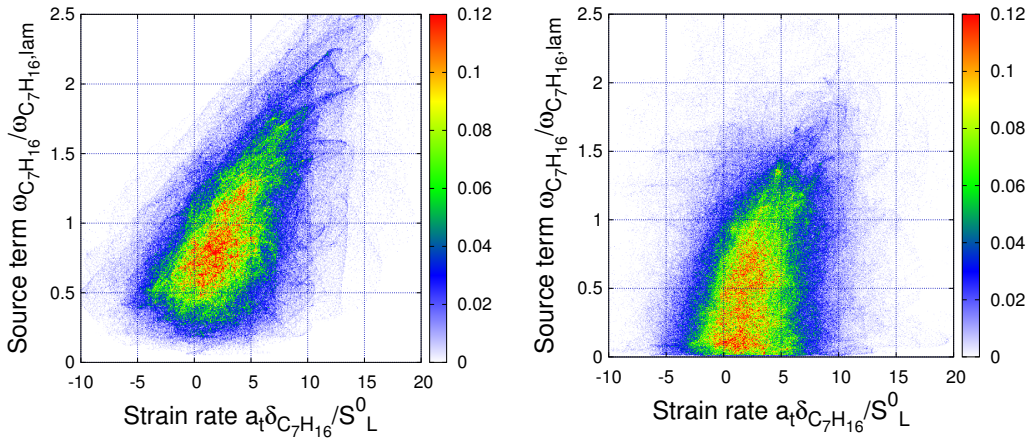

(a) $Le = 1$ (b) $Le \neq 1$

Figure 6.7: Joint probability density function, on the isoterm $T = T_{\text{peak}}$, of n-C_7H_{16} source term, $\dot{\omega}_{C_7H_{16}}$, normalized by its peak laminar value *vs.* the normalized tangential strain rate. (a) $Le = 1$; (b) $Le \neq 1$.

correlation was found to be positive, since such flames are associated with a negative Markstein length.

The fact that the signs of the correlations between fuel consumption rate and curvature are consistent between laminar and turbulent flames is, however, not trivial. More specifically, it has been previously reported that, at sufficiently high Karlovitz numbers, differential diffusion effects are suppressed (see Ref. [142] and Chapter 5). However, the turbulence intensity is not sufficiently high to suppress the differential diffusion effects in the reaction zone for the present flame. This was already evidenced by the characterization of the flame structure (Chapter 5).

	r	dCor_n
Strain / $Le = 1$	0.61	0.57
Strain / $Le \neq 1$	0.49	0.45
Curvature / $Le = 1$	-0.12	0.33
Curvature / $Le \neq 1$	-0.53	0.65

Table 6.2: Pearson's correlation coefficient, r, and distance correlation, dCor_n, between strain rate and fuel consumption, and between curvature and fuel consumption at $T = T_{\text{peak}}$ for both flames presented the unity and the non-unity Lewis number flames.

It is not surprising that the correlations listed in Table 6.2 are relatively weak. First, as mentioned earlier, Eq. 1.16 was derived for much weaker strain rates and curvatures. Second, unsteady effects

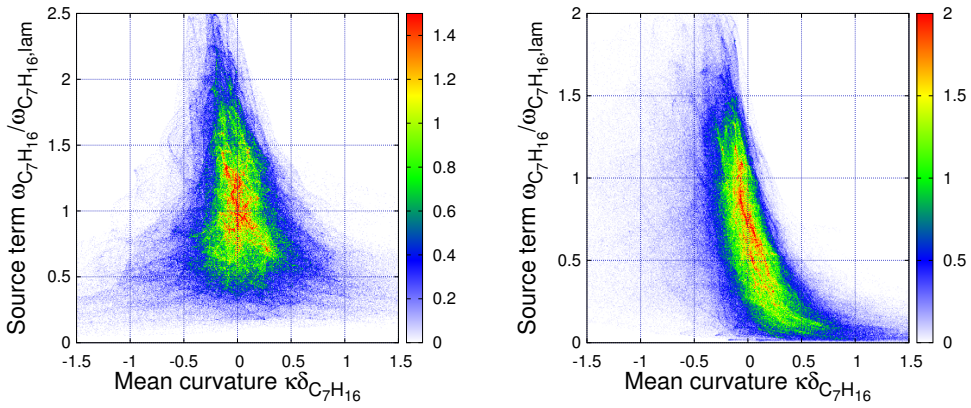

(a) $Le = 1$ (b) $Le \neq 1$

Figure 6.8: Joint probability density function, on the isoterm $T = T_{\text{peak}}$, of n-C_7H_{16} source term, $\dot{\omega}_{C_7H_{16}}$, normalized by its peak laminar value *vs.* the normalized mean curvature. (a) $Le = 1$; (b) $Le \neq 1$.

may also have a strong impact. For instance, considering much weaker stretch, linear theory [84, 42] and results from unsteady counterflow flames [81] have shown an attenuation of Markstein number with the frequency of strain rate fluctuations. Unsteady effects in the response of chemistry to stretch have also been observed experimentally and computationally in flame-vortex interaction [120, 127]. Hence, a loss of correlation with instantaneous stretch is expected for highly turbulent flames [35, 36].

To summarize, it was found that the fluctuations in fuel consumption rate are, to some extent, attributed to strain rate for the unity Lewis number flame, and curvature for the non-unity Lewis number flame. These observations (for premixed flames at the edge of the broken reaction zones regime) are consistent with the results of Haworth and Poinsot (for premixed flames at the edge of the corrugated flamelets regime) [73]. The local extinctions were attributed to high curvatures through differential diffusion for the non-unity Lewis number flame. However, the correlations found may be too weak to be useful for modeling purposes (more details in Chapter 7).

6.2.4 Fuel consumption rate limiting species *vs.* curvature and strain rate

Given the chemical mechanism used in the simulations, the fuel is consumed through six reactions. The following two account for 85% (unity Le) and 90% (non-unity Le) of the overall fuel consumption

rate:

$$n\text{–}C_7H_{16} + H \rightarrow 2\text{–}C_7H_{15} + H_2, \tag{6.5}$$

$$n\text{–}C_7H_{16} + OH \rightarrow 2\text{–}C_7H_{15} + H_2O.$$

Consequently, at the reaction zone (fixing $T = T_{\text{peak}}$), the burning rate is mostly a function of $Y_{C_7H_{16}}$, Y_H, and Y_{OH}. It is interesting to identify which of these species are responsible for the correlations found in the previous section. Their respective correlations with strain rate and curvature are presented in Table 6.3.

In the unity Lewis number case, all three species mass fractions show similar correlations with strain rate and curvature as those obtained for the fuel burning rate (Table 6.2). This is not surprising. In the absence of differential diffusion, all chemical species react to strain and curvature the same way.

In the non-unity Lewis number case, the fuel mass fraction shows the largest correlation with curvature (the joint probability density function is shown in Fig. 6.9) and becomes decorrelated with strain rate. This is qualitatively consistent with the defocusing/focusing differential diffusion effects in laminar flames, which have been widely studied [133, 24, 43]. On the other hand, both radicals show only little correlation with curvature (more for H than OH) and retain their correlation with strain rate.

In Ref. [58], for a two-dimensional stoichiometric methane/air premixed flame in the thin reaction zones regime, Echekki and Chen found a stronger correlation of the hydrogen atom mass fraction with curvature than with strain rate. They attributed this dependence on curvature to focusing/defocusing differential diffusion effect (H has a very low Lewis number). In a similar way, for the present flames, the correlation of hydrogen atom mass fraction with curvature increases from the unity Lewis to the non-unity Lewis number flame (as opposed to OH mass fraction, which has a Lewis number much closer to unity). However, this increase in correlation is overshadowed by that of the fuel mass fraction with curvature, which was not observed in Ref. [58]. It is important to

remark that the Lewis numbers of the reactants in Ref. [58] are very close to unity, while that of the limiting reactant in the present flame is much greater than unity ($Le_{C_7H_{16}} = 2.84$). Important qualitative differences are expected between such flames [36].

	$Le = 1$		$Le \neq 1$	
	r	dCor_n	r	dCor_n
$Y_{C_7H_{16}}$ *vs.* strain	0.50	0.49	0.16	0.22
Y_H *vs.* strain	0.59	0.56	0.52	0.51
Y_{OH} *vs.* strain	0.60	0.57	0.53	0.49
$Y_{C_7H_{16}}$ *vs.* curvature	-0.10	0.34	-0.69	0.74
Y_H *vs.* curvature	-0.15	0.35	-0.33	0.45
Y_{OH} *vs.* curvature	-0.16	0.36	-0.14	0.31

Table 6.3: Pearson's correlation coefficient, r, and distance correlation, dCor_n, between strain rate and species mass fractions, and between curvature and species mass fractions at $T = T_{peak}$ for both (higher-Ka) flames presented in this thesis.

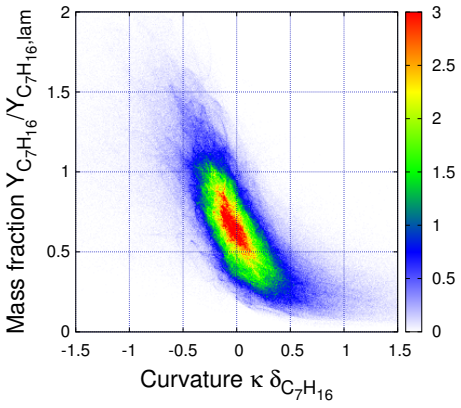

Figure 6.9: Joint probability density function, on the isoterm $T = T_{peak}$, of n-C_7H_{16} mass fraction, $Y_{C_7H_{16}}$, normalized by its peak laminar value *vs.* the normalized mean curvature for the non-unity Lewis number flame.

6.3 Turbulent flame speed

It was shown in the last two sections that the fuel consumption rate was affected by differential diffusion, whereas the curvature distribution on the reaction surface, characteristic of the geometry of this reaction surface, was virtually unaffected by it. In the present section, a link between these two results and the turbulent flame speeds of both flames is discussed.

6.3.1 Computing the turbulent flame speed

The turbulent flame speed may be expressed as

$$S_T = \frac{1}{\rho_u Y_{C_7H_{16},u} L^2 (t_2 - t_1)} \int_{t_1}^{t_2} -\dot{m}_F(t)\,\mathrm{d}t, \tag{6.6}$$

where the subscript u is used for unburnt conditions, $t_2 - t_1$ is the data collection time, and $\dot{m}_F$ is the instantaneous fuel consumption rate, obtained through the following:

$$\dot{m}_F(t) = \int_\Omega \dot{\omega}_{C_7H_{16}}(x, y, z, t)\,\mathrm{d}V, \tag{6.7}$$

with $\mathrm{d}V$ an element of volume, and Ω the whole domain. The values obtained are presented in Table 6.4.

As mentioned in Section 4.1.1, these turbulent flame speeds do not correspond exactly to the inlet bulk velocity (set to 1 m/s). As a result, the flame drifts from its initially position with a relative speed corresponding to the difference between the inlet bulk velocity and the effective turbulent flame speed. This computed drift (linear in time) is compared, in Fig. 6.10, to the instaneous flame drift computed as

$$\Delta x_f = x_f - x_0, \tag{6.8}$$

where x_0 is the position of the flame at time $t = 0$ and x_f is the instantaneous position of the flame, computed as

$$x_f(t) = 11L - \frac{1}{L^2 c_b} \int_\Omega c(x, y, z, t)\,\mathrm{d}V, \tag{6.9}$$

where $c = Y_{H_2} + Y_{H_2O} + Y_{CO} + Y_{CO_2}$ is a progress variable, which takes the value c_b in the burnt gas. The agreement between the drifts computed by both method is very good, suggesting that the turbulent flame speeds presented in Table 6.4 are good estimates over the data collection period.

The difference in the S_T/S_L ratios (between unity and non-unity Lewis numbers) highlights an important differential diffusion effect (the only difference between the flames). The unity Lewis number flame encounters a significantly larger increase in flame speed than the non-unity Lewis

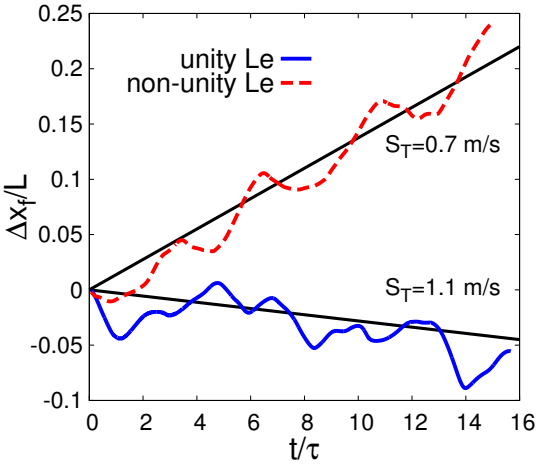

Figure 6.10: Flame drift over time. Recall that the x-axis is positively oriented downstream. A constant inflow of 1 m/s was imposed at the inlet. The straight black lines correspond to the turbulent flame speeds obtained from Eq. 6.6.

number flame, although both flames are subjected to the same incoming turbulent flow. As observed by many authors [172, 99, 94, 100, 50, 69, 21, 125], this further suggests that differential diffusion has to be taken into account in turbulent flame speed models (*e.g.* in the form of a Lewis number dependence). More details can be found in Appendix A.3.

6.3.2 Link between differential diffusion effects and turbulent flame speed

Although the latter observation is interesting in itself, a better understanding of where this difference (in turbulent flame speed) comes from is necessary for modeling purposes. Using continuity, Damköhler proposed that, for a (thin) corrugated flame, the turbulent flame speed is proportional to the turbulent flame surface area A_T, or $S_T/S_L = A_T/A$, with A the cross-section area [48]. In this regime, it is often assumed that the local flame speed is equal to the laminar flame speed. In contrast, for the thin reaction zones regime, Damköhler suggested that the turbulent flame speed should, instead, be proportional to the turbulent diffusivity [48].

Even if the current flames are not in the (thin) corrugated flamelet regime, the reaction zone remains thin and is only weakly corrugated. As a consequence, a reaction surface (isocontour $T = T_{\text{peak}}$, as introduced in Section 6.1.2), as opposed to a flame surface, and a local consumption speed can still be defined. For the present analysis, a similar approach to that used by Damköhler

for the corrugated flamelet regime is taken. This time, the local consumption speed is not fixed to the laminar value.

First, because the reaction zone is only weakly corrugated, one can rewrite exactly Eq. 6.7 as an integral along the isocontour of $T = T_{\text{peak}}$ (surface integral) and an integral in the normal direction, *i.e.*

$$\dot{m}_F(t) = \int_{T=T_{\text{peak}}} \left(\int \dot{\omega}_{\text{C}_7\text{H}_{16}} \mathrm{d}n \right) \mathrm{d}A, \tag{6.10}$$

with $\int \dot{\omega}_{\text{C}_7\text{H}_{16}} \mathrm{d}n$ being the local consumption mass flow rate. Recalling that $\boldsymbol{n} = -\nabla T/|\nabla T|$, the latter can be rewritten as

$$\int \dot{\omega}_{\text{C}_7\text{H}_{16}} \mathrm{d}n = \int \dot{\omega}_{\text{C}_7\text{H}_{16}} \frac{\mathrm{d}T}{|\nabla T|}. \tag{6.11}$$

Second, as previously noted, the reaction zone remains thin, which means that the temperature gradients at the reaction zone are approximately equal to those of a laminar flame, *i.e.* $|\nabla T| \approx |\nabla T_{\text{lam}}|$ and

$$\int \dot{\omega}_{\text{C}_7\text{H}_{16}} \mathrm{d}n \approx \int \dot{\omega}_{\text{C}_7\text{H}_{16}} \frac{\mathrm{d}T}{|\nabla T_{\text{lam}}|}. \tag{6.12}$$

Following Damköhler's argument, the reaction zone thickness scales with the square root of the effective diffusivity (molecular plus turbulent). Therefore, the previous observation of a thin reaction zone is consistent with a negligible turbulent diffusivity at the reaction zone (with respect to the characteristic scales of the reaction zone). As discussed in Section 4.4.1, the intensity of the turbulent flow field decreases dramatically from the preheat zone to the reaction zone.

Third, as shown in Fig. 6.3(b) and 6.3(c), the profiles of $\dot{\omega}_{\text{C}_7\text{H}_{16}}$ in the direction normal to the reaction surface (isocontour of $T = T_{\text{peak}}$) remain fairly unchanged when scaled by their value at $T = T_{\text{peak}}$ (Eq. 6.1). Hence, using Eq. 6.1, 6.10, and 6.12 in Eq. 6.6, the turbulent flame speed can be approximated as

$$S_T \approx S_L^0 \frac{A_T}{A} \left\langle \frac{\dot{\omega}_{\text{C}_7\text{H}_{16}}}{\dot{\omega}_{\text{C}_7\text{H}_{16},\text{lam}}} \right\rangle_{T_{\text{peak}}}, \tag{6.13}$$

where $\langle \dot{\omega}_{\text{C}_7\text{H}_{16}}/\dot{\omega}_{\text{C}_7\text{H}_{16},\text{lam}} \rangle_{T_{\text{peak}}}$ is surface-weighted and averaged in time. It corresponds exactly to the means of the distributions presented in Fig. 6.2. A_T is defined as the surface area of the reaction

zone surface (*i.e.* the isoterm $T = T_{\text{peak}}$) as shown in Fig. 6.11.

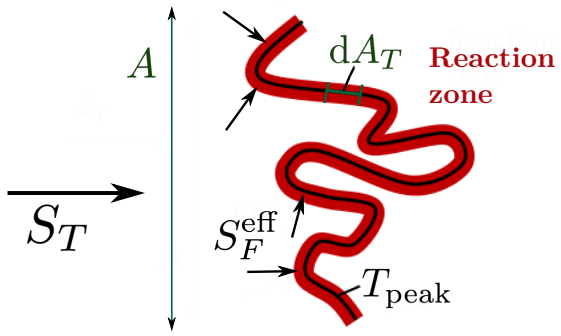

Figure 6.11: Schematic drawing to illustrate Eq. 6.13. $S_F^{\text{eff}} = \langle \dot{\omega}_{C_7H_{16}} / \dot{\omega}_{C_7H_{16},\text{lam}} \rangle_{T_{\text{peak}}} \cdot S_L^0$ is used.

The values for $\langle \dot{\omega}_{C_7H_{16}} / \dot{\omega}_{C_7H_{16},\text{lam}} \rangle_{T_{\text{peak}}}$, S_T/S_L^0, and A_T/A are presented in Table 6.4 for the present flames. First, consistent with the results of Section 6.2.1, differential diffusion has a limited effect on the turbulent surface area. The flame acts as a material surface. Second, the values presented are in very good agreement with Eq. 6.13. Third, the main contribution to the differences in turbulent flame speed due to differential diffusion appears in the $\langle \dot{\omega}_{C_7H_{16}} / \dot{\omega}_{C_7H_{16},\text{lam}} \rangle_{T_{\text{peak}}}$ ratio.

Note that the reduction in this ratio (from the unity to the non-unity Lewis number flames) is not solely due to local flame extinctions. By choosing a threshhold of 5% of the peak laminar burning rate to identify regions of extinctions (similar to Ref. [53]), 3% of the overall surface area undergoes extinction (as opposed to none in the unity Lewis number flame) as shown in Table 6.4. This cannot account for the 30% reduction in the mean local burning rate. However, the conditional PDF of the burning rate at T_{peak} (Fig. 6.2) shows a clear shift towards smaller values from the unity to the non-unity Lewis number flame. For instance, for 77% of the overall surface area, the burning rate is smaller than its peak laminar value in the non-unity Lewis number flame *vs.* 56% in the unity Lewis number flame (see Table 6.4). This shift in the conditional PDF of the burning rate towards smaller values results in the reduction in the mean burning rate, with $\langle \dot{\omega}_{C_7H_{16}} / \dot{\omega}_{C_7H_{16},\text{lam}} \rangle_{T_{\text{peak}}}$ corresponding to its first moment, *i.e.*

$$\left\langle \frac{\dot{\omega}_{C_7H_{16}}}{\dot{\omega}_{C_7H_{16},\text{lam}}} \right\rangle_{T_{\text{peak}}} = \int \frac{\dot{\omega}_{C_7H_{16}}}{\dot{\omega}_{C_7H_{16},\text{lam}}} \text{P}\left(\frac{\dot{\omega}_{C_7H_{16}}}{\dot{\omega}_{C_7H_{16},\text{lam}}} \right) \text{d}\frac{\dot{\omega}_{C_7H_{16}}}{\dot{\omega}_{C_7H_{16},\text{lam}}}. \tag{6.14}$$

	unity Le_i	non-unity Le_i
S_T (m/s)	1.06	0.69
S_T/S_L^0	3.7	1.9
A_T/A	3.5 ± 1.0	2.9 ± 0.8
$\left\langle \frac{\dot{\omega}_{C_7H_{16}}}{\dot{\omega}_{C_7H_{16},\mathrm{lam}}} \right\rangle_{T_{\mathrm{peak}}}$	1.00	0.66
$\frac{A_T}{A}\left\langle \frac{\dot{\omega}_{C_7H_{16}}}{\dot{\omega}_{C_7H_{16},\mathrm{lam}}} \right\rangle_{T_{\mathrm{peak}}}$	3.5	1.9
$A_{5\%}/A_T$	0%	2.9%
$A_{100\%}/A_T$	56.4%	76.6%

Table 6.4: Ratios relevant to the turbulent flame speed (see Eq. 6.13). Confidence intervals correspond to plus or minus one standard deviation.

If the fuel consumption rate at the reaction surface were perfectly correlated with strain rate and/or curvature, the ratio $\langle \dot{\omega}_{C_7H_{16}}/\dot{\omega}_{C_7H_{16},\mathrm{lam}} \rangle_{T_{\mathrm{peak}}}$ could be expressed as

$$\left\langle \frac{\dot{\omega}_{C_7H_{16}}}{\dot{\omega}_{C_7H_{16},\mathrm{lam}}} \right\rangle_{T_{\mathrm{peak}}} = \int \frac{\dot{\omega}_{C_7H_{16}}}{\dot{\omega}_{C_7H_{16},\mathrm{lam}}} (\kappa)\, \mathrm{P}(\kappa)\, \mathrm{d}\kappa, \tag{6.15}$$

or

$$\left\langle \frac{\dot{\omega}_{C_7H_{16}}}{\dot{\omega}_{C_7H_{16},\mathrm{lam}}} \right\rangle_{T_{\mathrm{peak}}} = \int \frac{\dot{\omega}_{C_7H_{16}}}{\dot{\omega}_{C_7H_{16},\mathrm{lam}}} (a_t)\, \mathrm{P}(a_t)\, \mathrm{d}a_t, \tag{6.16}$$

where $\mathrm{P}(\kappa)$ and $\mathrm{P}(a_t)$ are the probability density functions of curvature and strain rate at the reaction surface, respectively (shown in Fig. 6.5). While the correlations found in Section 6.2.3 are not perfect, these equations can help explain the values obtained for $\langle \dot{\omega}_{C_7H_{16}}/\dot{\omega}_{C_7H_{16},\mathrm{lam}} \rangle_{T_{\mathrm{peak}}}$.

For the unity Lewis number case, only strain rate has an effect on the fuel consumption rate (see Section 6.2.3). This effect is approximately symmetric with respect to the mean strain rate (see Fig. 6.7(a)) and this strain rate is symmetrically distributed with respect to its mean (see Fig. 6.5(b)). Therefore, a close-to-unity $\langle \dot{\omega}_{C_7H_{16}}/\dot{\omega}_{C_7H_{16},\mathrm{lam}} \rangle_{T_{\mathrm{peak}}}$ ratio is expected. This is consistent with results previously reported for turbulent flames with a close-to-unity fuel Lewis number [71, 73, 58].

For the non-unity Lewis number case, the fuel consumption rate is correlated with curvature. While curvature is symmetrically distributed with respect to its mean (see Fig. 6.5(a)), its effect on the fuel consumption term is highly non-linear and is not symmetric with respect to its mean. Negative values of curvature have a marginal effect on the fuel consumption rate, while positive curvature has a very strong effect (reduced consumption rate). Consequently, the overall effect is a

reduction in the average fuel consumption rate, *i.e.* $\langle \dot{\omega}_{C_7H_{16}} / \dot{\omega}_{C_7H_{16},\mathrm{lam}} \rangle_{T_{\mathrm{peak}}} < 1$.

6.4 Summary and discussion

The flow chart presented in Fig. 6.12 illustrates the mechanism through which turbulence and differential diffusion affect the overall turbulent flame speed and summarizes the three main results of this chapter.

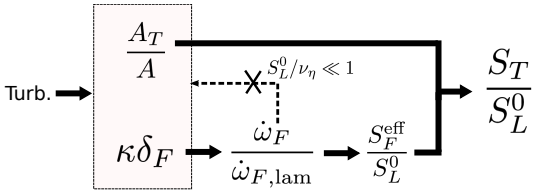

Figure 6.12: Flow chart illustrating the mechanism through which turbulence affects the flame speed for the flames presented in this thesis. $S_F^{\mathrm{eff}} = \langle \dot{\omega}_F / \dot{\omega}_{F,\mathrm{lam}} \rangle_{T_{\mathrm{peak}}} S_L^0$ is used.

First, differential diffusion was found to have limited effect on the strain rate and curvature distribution at the reaction zone. This is a consequence of the high turbulence level ($S_L^0/v_\eta \ll 1$), the reaction surface behaving more like a material (*i.e.* passive) surface than a propagating surface.

Second, a correlation was found between the fuel consumption rate and curvature for the non-unity Lewis number flame, whereas a similar correlation was found between tangential strain rate and fuel consumption rate for the unity Lewis number case.

Finally, local extinctions were shown to have a strong effect on the turbulent flame speed by altering the local consumption rate of the fuel.

This chapter brought a qualitative understanding of the mechanism behind local extinctions and their effect on the turbulent flame speed, highlighting the importance of considering differential diffusion in models. However, quantities that better correlate with source term fluctuations would be required to adequately develop such models. The next chapter introduces such quantities and presents a model for the source term fluctuations.

Chapter 7

Modeling of the reaction zone[1]

As previously identified in Chapters 4 to 6, the n-C_7H_{16}/air premixed turbulent flames considered are found to have a considerably broadened preheat zone, but a thin reaction zone. While this reaction zone is thin, large burning rate fluctuations were observed. More specifically, the following results were identified:

1. largely thickened preheat zone (see Fig. 4.10),
2. thin reaction zone (see Fig. 4.9 and 4.10),
3. large burning rate fluctuations around the mean profile *vs.* progress variable (as previously mentioned, the temperature is a progress variable) (see Fig. 6.1(c) and 6.3(a)),
4. for unity Lewis numbers:

$$< \dot{\omega}_F | c > \approx \dot{\omega}_{F,\mathrm{lam}}(c), \tag{7.1}$$

5. for non-unity Lewis numbers:

$$< \dot{\omega}_F | c > \neq \dot{\omega}_{F,\mathrm{lam}}(c), \tag{7.2}$$

6. for both cases:

$$\dot{\omega}_F(\mathbf{x},t) \neq \dot{\omega}_F(c(\mathbf{x},t)). \tag{7.3}$$

Note that a discussion on the choice of the progress variable (c) for modeling purposes is provided in the first section.

[1]The author of this thesis has contributed to all the work presented in this chapter.

The work in this chapter is directly related to point 6, *i.e.* the first objective is to identify a set of variables $\boldsymbol{\psi}$ such that $\dot{\omega}_F(\mathbf{x},t)$ can be approximated accurately by $\dot{\omega}_F(c(\mathbf{x},t),\boldsymbol{\psi}(\mathbf{x},t))$, while keeping the dimensionality of $\boldsymbol{\psi}$ small. The second objective is to generate the function $\dot{\omega}_F(c,\boldsymbol{\psi})$. The last objective is to provide/discuss a tabulation approach with this reduced set of variables.

7.1 Progress variable

While temperature is a natural choice for the progress variable, this choice is not unique. For modeling purposes, a progress variable with a simpler transport equation than the temperature equation is desired. Typically, a linear combination of species mass fractions is considered:

$$c = \sum_{j=i}^{N} b_j Y_j, \tag{7.4}$$

where b_j is a real coefficient. It is associated with the following transport equation

$$\rho\frac{\partial c}{\partial t} + \rho\mathbf{u}\cdot\nabla c = \nabla\cdot\left(\rho\frac{\alpha}{Le_c}\nabla c\right) + \nabla\cdot\left(\rho\sum_{j=1}^{N} b_j Y_j \mathbf{V}_{\mathbf{c,j}}\right) + \dot{\omega}_c, \tag{7.5}$$

with Le_c such that

$$\sum_{j=1}^{N} b_j \frac{1}{Le_j}\nabla Y_j = \frac{1}{Le_c}\nabla c \tag{7.6}$$

and

$$\dot{\omega}_c = \sum_{j=1}^{N} b_j \dot{\omega}_j. \tag{7.7}$$

In this chapter, all the derivations will be done with the progress variable defined by Eq. 7.4 (more general), but all the figures and calculations will be done with $c = Y_{\mathrm{H_2}} + Y_{\mathrm{H_2O}} + Y_{\mathrm{CO}} + Y_{\mathrm{CO2}}$. The later is typically used in *n*-heptane/air flames [118, 79, 80]. Figure 7.1 shows the joint probability density function of this progress variable *vs.* temperature. Figure 7.2 shows the fuel burning rate as a function of temperature for both the higher-Ka and lower-Ka flames. As one can expect from the strong correlelation between this progress variable and temperature (Fig. 7.1), the results

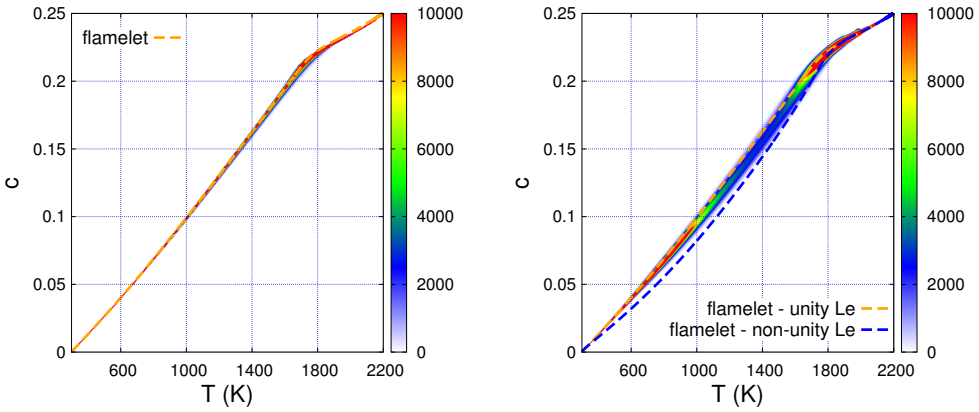

(a) $Le = 1$ (b) $Le \neq 1$

Figure 7.1: Joint PDF of the progress variable $c = Y_{H_2} + Y_{H_2O} + Y_{CO} + Y_{CO2}$ *vs.* temperature in the higher-Ka flame. One-dimensional unstretched flame profiles are shown by dashed lines.

concerning the fuel burning rate obtained in the previous chapters are similar whether temperature or $c = Y_{H_2} + Y_{H_2O} + Y_{CO} + Y_{CO2}$ is considered as the independent variable. Again, for the non-unity Lewis number flames, we want to highlight the fact that differential diffusion effects are still important at the reaction zone (as discussed in Chapter 6) and a single set of effective Lewis number cannot fully characterize the flame structure throughout the flame (as discussed in Chapter 5).

7.2 Coordinate transformation

In order to identify the set of variables $\boldsymbol{\psi}$, a similar approach to the one used in Ref. [184] for non-premixed flames is taken in this section. The following coordinate transformation is proposed (more details can be found in Ref. [184]):

$$(x_1, x_2, x_3, t) \rightarrow (c\,(x_1, x_2, x_3, t)\,, c_2\,(x_1, x_2, x_3, t)\,, c_3\,(x_1, x_2, x_3, t)\,, \tau)\,, \tag{7.8}$$

with

$$\nabla c \cdot \nabla c_2 = 0, \qquad \text{and} \qquad \nabla c \cdot \nabla c_3 = 0, \tag{7.9}$$

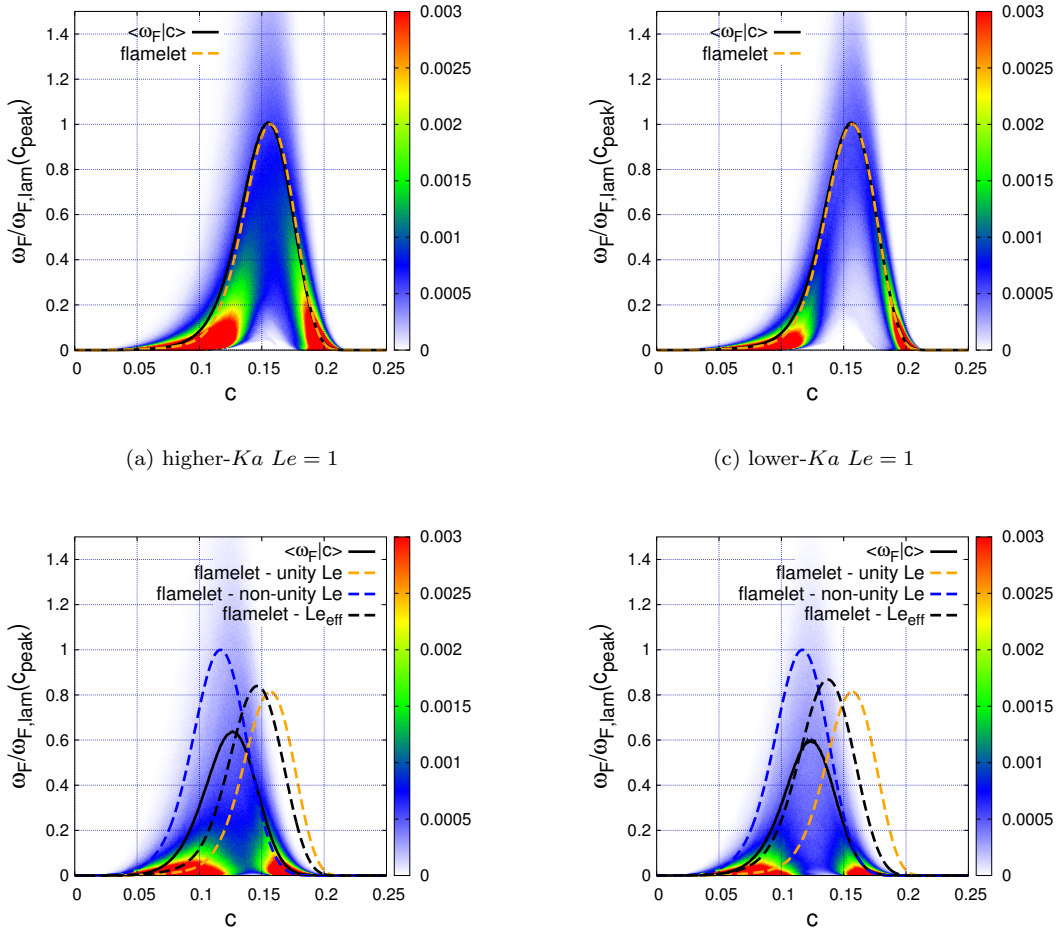

(a) higher-Ka $Le = 1$

(c) lower-Ka $Le = 1$

(b) higher-Ka $Le \neq 1$

(d) lower-Ka $Le \neq 1$

Figure 7.2: Joint PDF and conditional mean (solid line) of the fuel burning rate, $\dot{\omega}_{\mathrm{F}}$, normalized by its peak laminar value *vs.* progress variable c for both the higher-Ka and the lower-Ka flames. The unity, the non-unity, and the effective Lewis number flamelet solutions are also shown (dashed line).

i.e. the variables c_2 and c_3 lie in the surface of constant c. Note that these variables can be curvilinear. The following derivatives result from the coordinate transformation:

$$\begin{aligned}
\frac{\partial}{\partial t} &= \frac{\partial c}{\partial t}\frac{\partial}{\partial c} + \frac{\partial c_2}{\partial t}\frac{\partial}{\partial c_2} + \frac{\partial c_3}{\partial t}\frac{\partial}{\partial c_3} + \frac{\partial}{\partial \tau}, \\
\frac{\partial}{\partial x_1} &= \frac{\partial c}{\partial x_1}\frac{\partial}{\partial c} + \frac{\partial c_2}{\partial x_1}\frac{\partial}{\partial c_2} + \frac{\partial c_3}{\partial x_1}\frac{\partial}{\partial c_3}, \\
\frac{\partial}{\partial x_2} &= \frac{\partial c}{\partial x_2}\frac{\partial}{\partial c} + \frac{\partial c_2}{\partial x_2}\frac{\partial}{\partial c_2} + \frac{\partial c_3}{\partial x_2}\frac{\partial}{\partial c_3}, \\
\frac{\partial}{\partial x_3} &= \frac{\partial c}{\partial x_3}\frac{\partial}{\partial c} + \frac{\partial c_2}{\partial x_3}\frac{\partial}{\partial c_2} + \frac{\partial c_3}{\partial x_3}\frac{\partial}{\partial c_3}.
\end{aligned} \tag{7.10}$$

The only assumption made in this section is that this transformation exists, *i.e.* the Jacobian of the transformation is not singular. Unfortunately, this is not the case everywhere in the flame. Inside pockets of unburnt fuel, or where the reaction zone is closed on itself the Jacobian will be singular point-wise. However, only a discrete number of singularities are found and this local transformation is valid everywhere else.

7.3 Transformed transport equations

Applying the coordinate transformation (Section 7.2) to Eq. 2.5 and 2.4, and using Eq. 7.5, the following transformed equations for the species mass fractions and temperature are obtained:

$$\underbrace{\left\{\nabla\cdot\left[\rho\alpha\left(\frac{1}{Le_c}-\frac{1}{Le_i}\right)\nabla c\right]+\nabla\cdot\left(\rho\sum_{j=1}^{N}b_jY_j\mathbf{V_{c,j}}\right)+\dot{\omega}_c\right\}\frac{\partial Y_i}{\partial c}}_{\text{normal convection}} \tag{7.11}$$

$$-\underbrace{\frac{\rho\chi}{2Le_i}\frac{\partial^2 Y_i}{\partial c^2}}_{\text{normal diffusion}}-\underbrace{\dot{\omega}_i}_{\text{chemical source}}-\underbrace{\nabla\cdot(\rho Y_i\mathbf{V_{c,i}})}_{\text{velocity correction}}$$

$$=-\rho\frac{\partial Y_i}{\partial\tau}-\underbrace{\rho\sum_{k=2}^{3}\left[\frac{\partial Y_i}{\partial c_k}\left(\frac{\partial c_k}{\partial t}+\mathbf{u}\cdot\nabla c_k\right)\right]}_{\text{Lagrangian transport}}$$

$$+\underbrace{\sum_{k=2}^{3}\frac{\rho\chi_k}{2Le_i}\frac{\partial^2 Y_i}{\partial c_k^2}+\frac{2\rho\alpha}{Le_i}\left(\nabla c_2\cdot\nabla c_3\right)\frac{\partial^2 Y_i}{\partial c_2\partial c_3}}_{\text{tangential diffusion}}$$

$$+\underbrace{\nabla\cdot\left(\frac{\rho\alpha}{Le_i}\nabla c_2\right)\frac{\partial Y_i}{\partial c_2}+\nabla\cdot\left(\frac{\rho\alpha}{Le_i}\nabla c_3\right)\frac{\partial Y_i}{\partial c_3}}_{\text{tangential convection}},$$

$$
\begin{aligned}
&\underbrace{c_p\left\{\nabla\cdot\left[\rho\alpha\left(\frac{1}{Le_c}-1\right)\nabla c\right]+\nabla\cdot\left(\rho\sum_{j=1}^{N}b_jY_j\mathbf{V_{c,j}}\right)+\dot{\omega}_c-\frac{\rho\chi}{2c_p}\frac{\partial c_p}{\partial c}\right\}\frac{\partial T}{\partial c}}_{\text{normal convection 1}} \\
&+\underbrace{\left(\sum_{i=1}^{N}\frac{\rho c_{p,i}\chi}{2Le_i}\frac{\partial Y_i}{\partial c}+\sum_{i=1}^{N}\rho c_{p,i}Y_i\mathbf{V_{c,i}}\cdot\nabla c\right)\frac{\partial T}{\partial c}}_{\text{normal convection 2}} \\
&-\underbrace{\frac{\rho c_p\chi}{2}\frac{\partial^2 T}{\partial c^2}}_{\text{normal diffusion}}-\underbrace{\dot{\omega}_T}_{\text{chemical source}} \\
&\qquad=-\rho c_p\frac{\partial T}{\partial\tau}-\underbrace{\rho c_p\sum_{k=2}^{3}\left[\frac{\partial T}{\partial c_k}\left(\frac{\partial c_k}{\partial t}+\mathbf{u}\cdot\nabla c_k\right)\right]}_{\text{Lagrangian transport}} \\
&\qquad\quad+\underbrace{\sum_{k=2}^{3}\frac{\rho c_p\chi_k}{2}\frac{\partial^2 T}{\partial c_k^2}+2\rho c_p\alpha\left(\nabla c_2\cdot\nabla c_3\right)\frac{\partial^2 T}{\partial c_2\partial c_3}}_{\text{tangential diffusion}} \\
&\qquad\quad+\underbrace{\nabla\cdot\left(\rho c_p\alpha\nabla c_2\right)\frac{\partial T}{\partial c_2}+\nabla\cdot\left(\rho c_p\alpha\nabla c_3\right)\frac{\partial T}{\partial c_3}}_{\text{tangential convection 1}} \\
&\qquad\quad+\underbrace{\sum_{k=2}^{3}\left(\sum_{i=1}^{N}\frac{\rho c_{p,i}\chi_k}{2Le_i}\frac{\partial Y_i}{\partial c_k}\frac{\partial T}{\partial c_k}+\sum_{i=1}^{N}\rho c_{p,i}Y_i\mathbf{V_{c,i}}\cdot\nabla c_k\frac{\partial T}{\partial c_k}\right)}_{\text{tangential convection 2}} \\
&\qquad\quad+\underbrace{\sum_{i=1}^{N}\frac{\rho c_{p,i}\alpha}{Le_i}\left(\frac{\partial Y_i}{\partial c_2}\frac{\partial T}{\partial c_3}+\frac{\partial Y_i}{\partial c_3}\frac{\partial T}{\partial c_2}\right)\left(\nabla c_2\cdot\nabla c_3\right)}_{\text{tangential convection 3}},
\end{aligned}
\tag{7.12}
$$

where $\chi = 2\alpha|\nabla c|^2$ and $\chi_k = 2\alpha|\nabla c_k|^2$ for $k = 2, 3$ are the dissipation rates of c, c_2, and c_3, respectively. An additional step in the transformation can be found in Appendix C. In the above equations, the Lagrangian transport corresponds to the convection of the scalar, in the c_2-c_3-direction, *i.e.* in the surface of iso-c, induced by the Lagrangian transport of these c_2 and c_3 coordinates. The normal terms correspond to convection or diffusion of the scalar in the c-direction, whereas the tangential terms correspond to convection or diffusion of the scalar in the c_2-c_3-direction.

7.4 Unity Lewis number limit

As a first step, the unity Lewis number limit is considered. As mentioned throughout this thesis, in the absence of differential diffusion, the effect of turbulence on the chemistry can be directly investigated. In this section, the unity Lewis number flamelet equations are presented first and the extent of their validity in the present turbulent flames is discussed. Then, these equations are used to provide a physical explanation to the fuel burning rate fluctuations. Finally, approaches to model the fuel burning rate are presented.

7.4.1 Flamelet equations

Recall that, in the regime considered, the reaction zone is considered to be thin. It is therefore assumed that, in the vicinity of the reaction zone, $\partial/\partial c_k << \partial/\partial c$, for $k = 2, 3$. With this assumption and in the absence of differential diffusion (*i.e.* by setting all Lewis numbers to unity), Eq. 7.11 and 7.12 reduce to

$$\rho\frac{\partial Y_i}{\partial \tau} + \dot{\omega}_c\frac{\partial Y_i}{\partial c} = \frac{\rho\chi}{2}\frac{\partial^2 Y_i}{\partial c^2} + \dot{\omega}_i. \tag{7.13}$$

$$\rho\frac{\partial T}{\partial \tau} + c_p\dot{\omega}_c\frac{\partial T}{\partial c} = \frac{\rho c_p\chi}{2}\frac{\partial^2 T}{\partial c^2} + \dot{\omega}_T + \frac{\rho\chi}{2}\frac{\partial c_p}{\partial c}\frac{\partial T}{\partial c} + \sum_{i=1}^{N}\frac{\rho c_{p,i}\chi}{2}\frac{\partial Y_i}{\partial c}\frac{\partial T}{\partial c}. \tag{7.14}$$

Note that Eq. 7.11 and 7.12 under unity Lewis number assumption can be found in Appendix D. It is further assumed that the dependence in τ in the transformed coordinate system is negligible. Note that the coordinate c is still a function of time t. With this assumption, the flamelet equations are obtained:

$$\underbrace{\dot{\omega}_c\frac{\mathrm{d}Y_i}{\mathrm{d}c}}_{\text{convection}} = \underbrace{\frac{\rho\chi}{2}\frac{\mathrm{d}^2 Y_i}{\mathrm{d}c^2}}_{\text{diffusion}} + \underbrace{\dot{\omega}_i}_{\text{chemical source}} \tag{7.15}$$

$$\underbrace{c_p\dot{\omega}_c\frac{\mathrm{d}T}{\mathrm{d}c}}_{\text{convection}} = \underbrace{\frac{\rho c_p\chi}{2}\frac{\mathrm{d}^2 T}{\mathrm{d}c^2}}_{\text{diffusion}} + \underbrace{\dot{\omega}_T}_{\text{chemical source}} + \underbrace{\frac{\rho\chi}{2}\frac{\mathrm{d}c_p}{\mathrm{d}c}\frac{\mathrm{d}T}{\mathrm{d}c}}_{\text{grad } c_p\text{-induced convection}} + \underbrace{\sum_{i=1}^{N}\frac{\rho c_{p,i}\chi}{2}\frac{\mathrm{d}Y_i}{\mathrm{d}c}\frac{\mathrm{d}T}{\mathrm{d}c}}_{\text{species mass flux-induced convection}}. \tag{7.16}$$

These equations form a system of ordinary differential equations in which the Y_i and T are the unknowns, c is the variable, and the dissipation rate $\chi(c)$ is the parameter. Given the two

assumptions made in this section, each of the terms in the above equations are only a function of c and χ.

In order to test if these assumptions ($\partial/\partial c_k << \partial/\partial c$, for $k = 2, 3$, and $\partial/\partial\tau = 0$) are valid, each of the terms in Eq. 7.15 (for several species) and Eq. 7.16 are evaluated point-wise in the turbulent flame. Then, the conditional mean and the standard deviation of these terms are computed and the results are presented in Fig. 7.3 (species) and 7.4 (temperature) for both the higher-Ka and the lower-Ka unity Lewis number flames. The species flamelet equations for n-C_7H_{16} (a reactant), CO (an intermediate that contributes to the progress variable), and H_2O (a product that contributes to the progress variable) are considered. Note that due to the large number of grid points covering the reaction zone and the large number of data files considered (spanning over 50 turnover times), the statistics are smooth and well converged. First and foremost, it is clear that the residual of the respective equations (the sum of the neglected terms corresponding to the right hand side of Eq. 7.11 and 7.12) is small in comparison to the other terms in these equations. These results indicate that the assumptions made in this section are valid. This means that, although the flames are highly three-dimensional and unsteady (in physical space), they can be well described by the one-dimensional (in phase space) flamelet equations (Eq. 7.15 and 7.16) parameterized by a single parameter $\chi(c)$.

The unity Lewis number flamelet equations are particularly interesting to study the reaction zone. In contrast with the one-dimensional transport equations in physical space (*e.g.* Fig. 5.9 for hydrogen), the terms in the flamelet equations are only large in the reaction zone. Considering the species transport equations, the convection term and the chemical source term can only be non-zero in the reaction zone. On the other hand, the dissipation term would be non-zero if the tangential and the τ-dependent terms are non-negligible. However, the species mass fraction *vs.* progress variable profiles are linear outside the reaction zone, even in the turbulent flames (see Fig. 5.2). Therefore, the dissipation term is close to zero, and so is the sum of the neglected terms.

Note that although the residuals are small for both flames, they are larger in the higher-Ka flame. It is also interesting to note that these residuals are only large where the diffusion term is large.

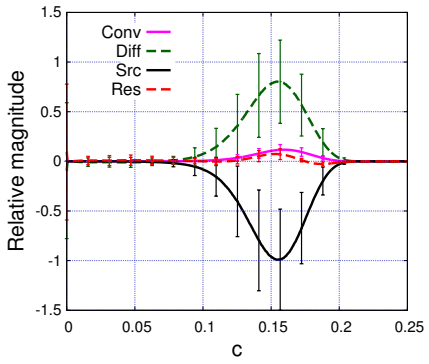

(a) higher-Ka, $Y_{\mathrm{C_7H_{16}}}$

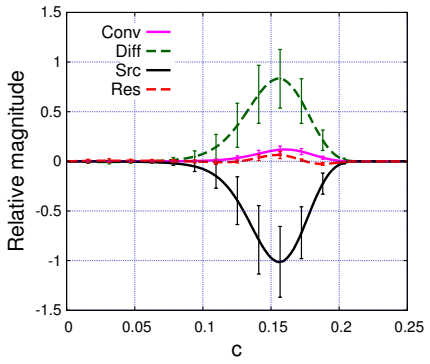

(d) lower-Ka, $Y_{\mathrm{C_7H_{16}}}$

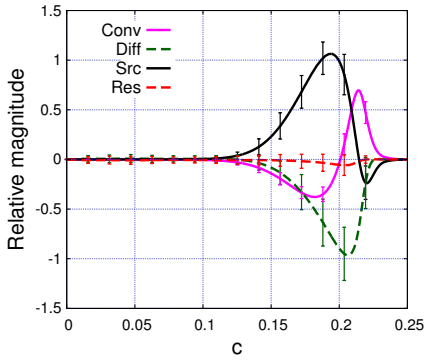

(b) higher-Ka, Y_{CO}

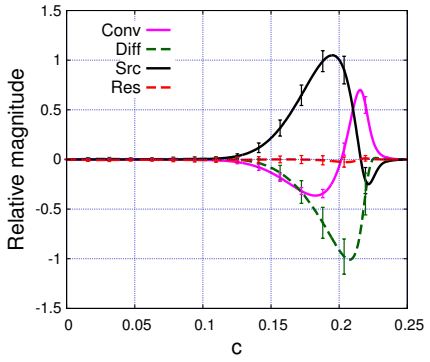

(e) lower-Ka, Y_{CO}

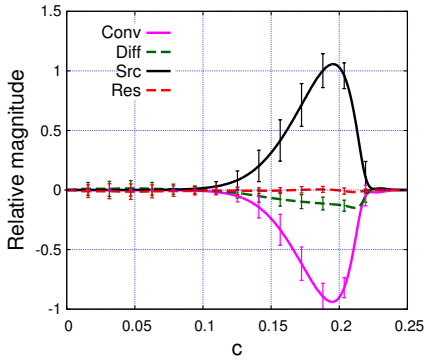

(c) higher-Ka, $Y_{\mathrm{H_2O}}$

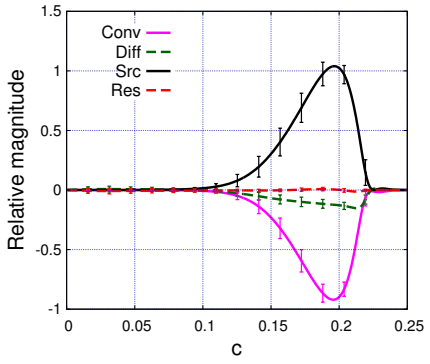

(f) lower-Ka, $Y_{\mathrm{H_2O}}$

Figure 7.3: Mean of the terms in Eq 7.15 (for three different species) conditioned on c for both unity Lewis number flames, $<\mathrm{term}|c>$. The bars correspond the standard deviation of these terms conditioned on c,$<(\mathrm{term}-<\mathrm{term}|c>)^2|c>^{1/2}$. The red dashed line corresponds to the residual of the equation (right hand side of Eq. 7.11 in the unity Lewis number limit). Each term is normalized by the absolute value of the largest term (corresponding to the same equation) in a unity Lewis number one-dimensional unstretched flame.

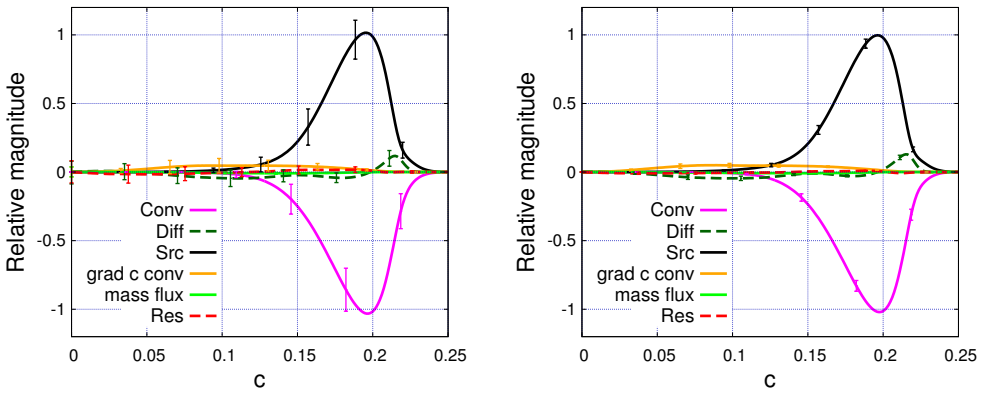

(a) higher-Ka (b) lower-Ka

Figure 7.4: Mean of the terms in Eq 7.16 conditioned on c for both unity Lewis number flames, $<$ term$|c>$. The bars correspond the standard deviation of these terms conditioned on c,$<$ (term$-<$ term$|c>)^2|c>^{1/2}$. The red dashed line corresponds to the residual of the equation (right hand side of Eq. 7.12 in the unity Lewis number limit). Each term is normalized by the absolute value of the largest term (corresponding to the same equation) in a unity Lewis number one-dimensional unstretched flame.

It is hypothesized that the terms left out in Eq. 7.11 contribute to an effective diffusivity, which would result in an effective dissipation rate. Unfortunately, appropriately identifying this effective diffusivity is not a straight forward task, as this effective diffusivity has to be consistent with the (c,c_2,c_3)-coordinate system. In addition, as discussed in Chapter 5, it is expected to vary with c, since turbulent mixing is stronger in the unburnt gas. To verify this hypothesis, a framework that can be used to identify locally the effective diffusivity in this coordinate system would be required. This should be done in future work.

7.4.2 Fuel burning rate

In this section, the flamelet equations are used to model the fuel burning rate in the two unity Lewis number turbulent n-heptane flames considered in this thesis (the higher-Ka and the lower-Ka flames).

7.4.2.1 Dependence of the burning rate on c and χ

Given the validity of the flamelet equations (as shown in the previous section), the fuel burning rate should solely be a function of the progress variable c and its dissipation rate χ. In contrast with Fig. 6.7 and 6.8 shown in the previous chapter, Fig. 7.5 presents the joint probability density function of the fuel consumption rate *vs.* the dissipation rate of the progress variable, both of which are evaluated at c_{peak}, with c_{peak} being the location in c-space of the maximum fuel consumption rate. The correlation coefficients are listed in Table 7.1 and are compared to those obtained with strain rate and curvature (Section 6.2.3). It is clear from Fig. 7.5 and Table 7.1 that the fuel burning rate is far more correlated with χ at c_{peak}. Physically, this means that turbulence affects the fuel burning rate by compressing or extending the isosurfaces of the progress variable. It also means that stretching the flow field is not equivalent to stretching these isosurfaces in the context of high Karlovitz premixed flames.

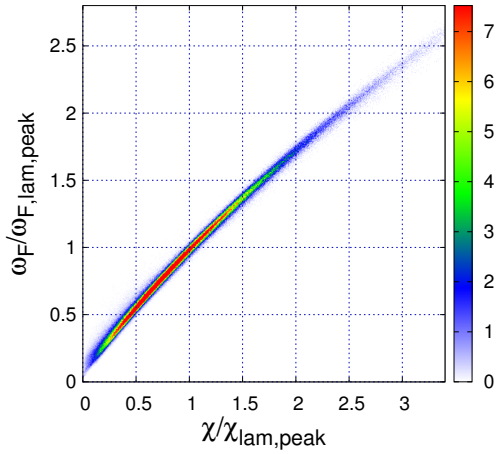

Figure 7.5: Joint PDF of the fuel burning rate *vs.* the dissipation rate of the progress variable, normalized by their peak laminar values, on the isosurface of $c = c_{\text{peak}}$ in the higher-Ka unity Lewis number flame.

This result suggests that there should exist a function $f(c, \chi)$ that estimates accurately the fuel burning rate. Such a function can be easily identified *a posteriori*, *i.e.* using the data from the DNS. We first define the prediction error made by the function f by the following L2-norm over the whole

	r	dCor_n
Strain rate	0.61	0.57
Curvature	-0.12	0.33
Dissipation rate	0.996	0.997

Table 7.1: Pearson's correlation coefficient, r, and distance correlation, dCor_n, between strain rate and fuel consumption rate, curvature and fuel consumption rate, and dissipation rate and fuel consumption rate at $c = c_{\mathrm{peak}}$ for the higher-Ka unity Lewis number flame.

domain:

$$\epsilon_f^F = \frac{1}{V\left(t_2 - t_1\right)} \int_{t_1}^{t_2} \int_{\Omega} \left(f - \dot{\omega}_F\right)^2 \mathrm{d}V\mathrm{d}t. \tag{7.17}$$

A similar approach was used to quantify the error made by LES filters on chemical source terms [123] and by scalar dissipation rate sub-grid-scale models [13]. The function that minimizes this error, given that f is a function of c and χ only, also called the optimal estimator [119, 13], is the mean of the fuel burning rate conditional on c and χ, *i.e.*

$$\underset{f(c,\chi)}{\arg\min} \epsilon_f^F = < \dot{\omega}_F | c, \chi > . \tag{7.18}$$

This result is well described in Ref. [119] and a brief discussion is provided in this paragraph. An optimal estimator Ω defined on an L2-norm, for a set of variables π, and a quantity to estimate, γ, minimizes $||\Omega\left(\pi\right) - \gamma||^2 = < \left(\Omega\left(\pi\right) - \gamma\right)^2 >$ with $< \cdot >$ the statistical mean (or expectation). The quadratic estimation error made from an estimator $g\left(\pi\right)$ satisfies the following orthogonal relation (see proof in Ref. [119]):

$$< \left(\gamma - g\left(\pi\right)\right)^2 > = < \left(\gamma - < \gamma | \pi >\right)^2 > + < \left(< \gamma | \pi > - g\left(\pi\right)\right)^2 > . \tag{7.19}$$

The first term on the right hand side is refered to as the irreducible error, whereas it can be shown the the second term is null if and only if $g\left(\pi\right) = < \gamma | \pi >$. Therefore, the optimal estimator $\Omega\left(\pi\right)$ is $< \gamma | \pi >$.

The optimal estimator given by Eq. 7.18 is evaluated for the two turbulent flames. The prediction errors are listed in Table 7.2. They are compared to the prediction errors made by the following

functions: $< \dot{\omega}_F | c >$ (optimal estimator given that f is a function of the progress variable only), $< \dot{\omega}_F | c, \kappa >$ (optimal estimator given that f is a function of the progress variable and the curvature only), and $< \dot{\omega}_F | c, a_t >$ (optimal estimator given that f is a function of the progress variable and the tangential strain rate only). The last function, $\dot{\omega}_{F,\mathrm{FGM}}(c, \chi)$, will be discussed in the next section. It is clear from this table that, first, allowing a dependence on c and χ instead of c only improves dramatically the prediction of the fuel burning rate. This is illustrated in Fig. 7.6 which shows the probability density function of the point-wise comparison between the predicted and the actual fuel burning rate, for both these functions (higher-Ka flame). Second, the choice of the second variable has a strong effect on the prediction error (Table 7.2). Consistently with the results of Table 7.1, the fuel burning rate appears to be much more correlated with the progress variable dissipation rate than with either curvature or tangential strain rate.

Estimator f	$\left(\epsilon_f^F / \epsilon_0^F\right)^{1/2}$	
	higher-Ka	lower-Ka
$< \dot{\omega}_F \| c >$	0.606	0.426
$< \dot{\omega}_F \| c, \kappa >$	0.489	0.337
$< \dot{\omega}_F \| c, a_t >$	0.459	0.321
$< \dot{\omega}_F \| c, \chi >$	0.084	0.042
$\dot{\omega}_{F,\mathrm{FGM}}(c, \chi)$	0.109	0.067

Table 7.2: Prediction error (Eq. 7.17) for various estimators of the fuel burning rate normalized by the prediction error for $f = 0$ in both unity Lewis number flames.

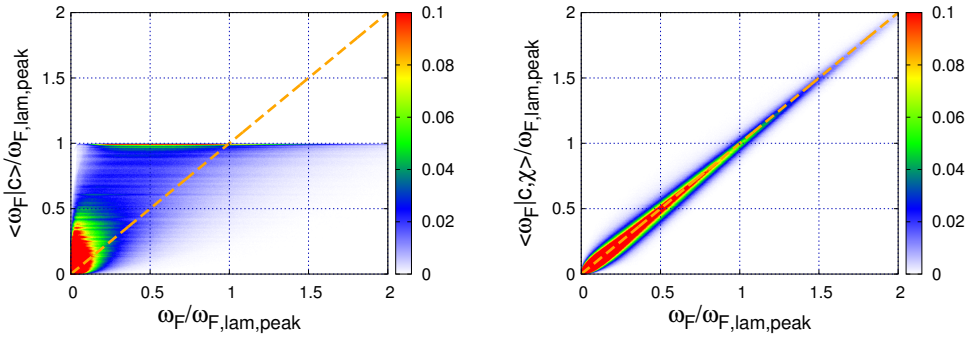

(a) $< \dot{\omega}_F | c >$ *vs.* $\dot{\omega}_F(\mathbf{x}, t)$

(b) $< \dot{\omega}_F | c, \chi >$ *vs.* $\dot{\omega}_F(\mathbf{x}, t)$

Figure 7.6: Joint PDF of the comparison between the predicted fuel burning rate and the actual burning rate in the higher-Ka unity Lewis number flame.

The optimal estimator $< \dot{\omega}_F | c, \chi >$ provides a very good estimation of the fuel burning rate. The

results form this section show that $\dot{\omega}_F(\mathbf{x}, t)$, which lives in a 35-dimensional phase-space (function of $N-1$ species and temperature), collapses very nicely on a two-dimensional manifold. While the optimal estimator $< \dot{\omega}_F | c, \chi >$ provides such an *a posteriori* representation of this manifold, the flamelet equations can also be used to generate a (c, χ)-manifold *a priori*. The quality of the prediction provided by this *a priori* manifold is assessed in the next section.

7.4.2.2 Flamelet-generated manifold

Equations 7.15 and 7.16 are solved numerically (using a modified version of FlameMaster) for a range of β such that $\chi(c) = \beta \chi^0(c)$, with $\chi^0(c)$ the dissipation rate profile in a one-dimensional unstretched flame, to generate a (c, χ)-manifold. Figure 7.7 shows that the solution from the flamelet equation, for $\beta = 1$, is identical to the solution obtained for an unstretched flame solved in physical space (Eq. 2.2 to 2.5). Dirichlet boundary conditions corresponding to the unburnt and the burnt mixture (in a one-dimensional unstretched flame) are used to solve the flamelet equations.

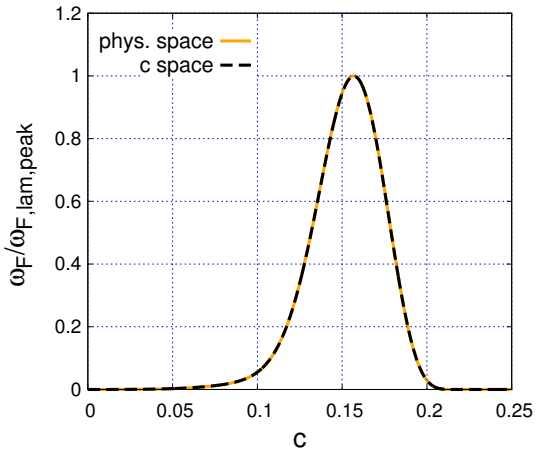

Figure 7.7: Comparison of the fuel burning rate *vs.* progress variable profile between the 1D flame solved in physical space and the flamelet solved in c-space (Eq. 7.15 and 7.16 with $\chi(c) = \chi_{\text{phys}}(c)$).

A model for the fuel burning rate, $\dot{\omega}_{F,\text{FGM}}(c, \chi)$ is extracted from the manifold. Figure 7.8 presents the functional dependence of this function on χ at c_{peak}. It is compared to that of the optimal estimator and the joint PDF previously presented in Fig. 7.5. The FGM agrees very well with the conditional mean at c_{peak}. The prediction error (Eq. 7.17) made by $\dot{\omega}_{F,\text{FGM}}(c, \chi)$ is listed

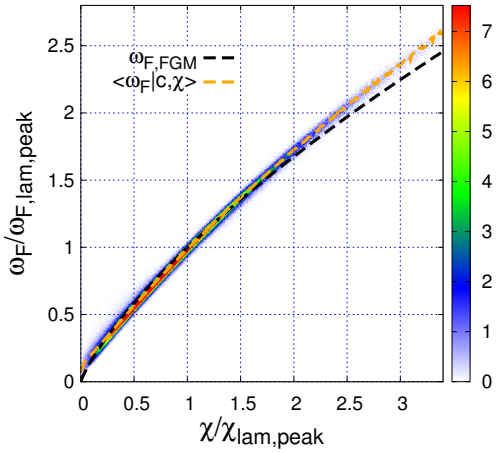

Figure 7.8: Comparison between the fuel burning rate predicted by $\dot{\omega}_{F,\mathrm{FGM}}(c,\chi)$ and $<\dot{\omega}_F|(c,\chi)>$ as a function of the dissipation rate, normalized by their peak laminar values, given $c = c_{\mathrm{peak}}$. The joint PDF on the isosurface of $c = c_{\mathrm{peak}}$ in the higher-Ka unity Lewis number flame is also shown for comparison.

in Table 7.2. This error is very close to that made by the optimal estimator, meaning that the *a priori* manifold generated by the flamelet equations is very close to the optimal (*i.e. a posteriori*) manifold given c and χ as variables.

To summarize, $\dot{\omega}_{F,\mathrm{FGM}}(c,\chi)$ provides a very good prediction of the local and instantaneous fuel burning rate.

7.5 Non-unity Lewis numbers

The previous section provided a framework that was used to physically explain the effect of the turbulence on the fuel burning rate, in the absence of differential diffusion, and to model this fuel burning rate. In the present section, effects of differential diffusion are included in a similar analysis.

7.5.1 Flamelet equations

Similar to Section 7.4.1, we make the same assumptions of local one-dimensionality in phase space, *i.e.* $\partial/\partial c_k << \partial/\partial c$, for $k = 2, 3$, and steady state in phase space, *i.e.* $\partial/\partial\tau = 0$, but no assumption

is made on the species Lewis numbers. Accordingly, Eq. 7.11 and 7.12 simplify to

$$\left\{\nabla\cdot\left[\rho\alpha\left(\frac{1}{Le_c}-\frac{1}{Le_i}\right)\nabla c\right]+\nabla\cdot\left(\rho\sum_{j=1}^{N}b_jY_j\mathbf{V_{c,j}}\right)+\dot{\omega}_c\right\}\frac{\partial Y_i}{\partial c} \tag{7.20}$$
$$=\frac{\rho\chi}{2Le_i}\frac{\partial^2 Y_i}{\partial c^2}+\dot{\omega}_i+\nabla\cdot\left(\rho Y_i\mathbf{V_{c,i}}\right),$$

and

$$c_p\left\{\nabla\cdot\left[\rho\alpha\left(\frac{1}{Le_c}-1\right)\nabla c\right]+\sum_{j=1}^{N}b_j\nabla\cdot\left(\rho Y_j\mathbf{V_{c,j}}\right)+\dot{\omega}_c\right\}\frac{\partial T}{\partial c} \tag{7.21}$$
$$=\frac{\rho c_p\chi}{2}\frac{\partial^2 T}{\partial c^2}+\dot{\omega}_T+\frac{\rho\chi}{2}\frac{\partial c_p}{\partial c}\frac{\partial T}{\partial c}+\sum_{i=1}^{N}\frac{\rho c_{p,i}\chi}{2Le_i}\frac{\partial Y_i}{\partial c}\frac{\partial T}{\partial c}+\sum_{i=1}^{N}\rho c_{p,i}Y_i\mathbf{V_{c,i}}\cdot\nabla T.$$

Let $\xi=\nabla\cdot(\rho\alpha\nabla c)$. Then, Eq. 7.20 and 7.21 can be expended to obtain the non-unity Lewis number flamelet equations:

$$\underbrace{\dot{\omega}_c\frac{\mathrm{d}Y_i}{\mathrm{d}c}}_{\text{convection}}=\underbrace{\frac{\rho\chi}{2Le_i}\frac{\mathrm{d}^2Y_i}{\mathrm{d}c^2}}_{\text{diffusion}}+\underbrace{\dot{\omega}_i}_{\text{chemical source}} \tag{7.22}$$
$$+\underbrace{\left[\xi\left(\frac{1}{Le_i}-\frac{1}{Le_c}\right)+\frac{\rho\chi}{2}\frac{\mathrm{d}}{\mathrm{d}c}\left(\frac{1}{Le_i}-\frac{1}{Le_c}\right)\right]\frac{\mathrm{d}Y_i}{\mathrm{d}c}}_{\text{differential diffusion-induced convection}}$$
$$+\underbrace{\nabla\cdot\left(\rho Y_i\mathbf{V_{c,i}}\right)-\sum_{j=1}^{N}b_j\nabla\cdot\left(\rho Y_j\mathbf{V_{c,j}}\right)\frac{\mathrm{d}Y_i}{\mathrm{d}c}}_{\text{velocity correction}},$$

with

$$\begin{aligned}\nabla\cdot(\rho Y_i\mathbf{V_{c,i}}) =& \frac{1}{Le_i}\left[\xi\frac{Y_i}{W}+\frac{\rho\chi}{2}\frac{\mathrm{d}}{\mathrm{d}c}\left(\frac{Y_i}{W}\right)\right]\frac{\mathrm{d}W}{\mathrm{d}c}\\ &-\left[\xi\frac{Y_i}{W}\sum_{j=1}^{N}\frac{Y_j}{Le_j}+\frac{\rho\chi}{2}\frac{\mathrm{d}}{\mathrm{d}c}\left(\frac{Y_i}{W}\sum_{j=1}^{N}\frac{Y_j}{Le_j}\right)\right]\frac{\mathrm{d}W}{\mathrm{d}c}\\ &-\left(\xi Y_i+\frac{\rho\chi}{2}\frac{\mathrm{d}Y_i}{\mathrm{d}c}\right)\sum_{j=1}^{N}\frac{1}{Le_j}\frac{\mathrm{d}Y_j}{\mathrm{d}c}+\frac{\rho\chi}{2Le_i}\frac{Y_i}{W}\frac{\mathrm{d}^2W}{\mathrm{d}c^2}\\ &-\frac{\rho\chi}{2}\frac{Y_i}{W}\sum_{j=1}^{N}\frac{Y_j}{Le_j}\frac{\mathrm{d}^2W}{\mathrm{d}c^2}-\frac{\rho\chi}{2}Y_i\frac{\mathrm{d}^2}{\mathrm{d}c^2}\left(\sum_{j=1}^{N}\frac{Y_j}{Le_j}\right)\\ &+\frac{\rho\chi}{2}\frac{Y_i}{W}\frac{\mathrm{d}}{\mathrm{d}c}\left(\frac{1}{Le_i}\right)\frac{\mathrm{d}W}{\mathrm{d}c}+\frac{\rho\chi}{2}Y_i\sum_{j=1}^{N}\left[\frac{\mathrm{d}}{\mathrm{d}c}\left(\frac{1}{Le_j}\right)\frac{\mathrm{d}Y_j}{\mathrm{d}c}\right]\\ &+\left(\xi Y_i+\frac{\rho\chi}{2}\frac{\mathrm{d}Y_i}{\mathrm{d}c}\right)\sum_{j=1}^{N}\left[\frac{\mathrm{d}}{\mathrm{d}c}\left(\frac{1}{Le_j}\right)Y_j\right],\end{aligned} \tag{7.23}$$

and

$$\begin{aligned}\underbrace{c_p\dot{\omega}_c\frac{\mathrm{d}T}{\mathrm{d}c}}_{\text{convection}} =& \underbrace{\frac{\rho c_p\chi}{2}\frac{\mathrm{d}^2T}{\mathrm{d}c^2}}_{\text{diffusion}}+\underbrace{\dot{\omega}_T}_{\text{chemical source}}+\underbrace{\frac{\rho\chi}{2}\frac{\mathrm{d}c_p}{\mathrm{d}c}\frac{\mathrm{d}T}{\mathrm{d}c}}_{\text{grad }c_p\text{-induced convection}}+\underbrace{\sum_{i=1}^{N}\frac{\rho c_{p,i}\chi}{2Le_i}\frac{\mathrm{d}Y_i}{\mathrm{d}c}\frac{\mathrm{d}T}{\mathrm{d}c}}_{\text{species mass flux-induced convection}}\\ &+\underbrace{c_p\left[\xi\left(1-\frac{1}{Le_c}\right)-\frac{\rho\chi}{2}\frac{\mathrm{d}}{\mathrm{d}c}\left(\frac{1}{Le_c}\right)\right]\frac{\mathrm{d}T}{\mathrm{d}c}}_{\text{differential diffusion-induced convection}}\\ &+\underbrace{\sum_{i=1}^{N}\rho c_{p,i}Y_i\mathbf{V_{c,i}}\cdot\nabla T-c_p\sum_{j=1}^{N}b_j\nabla\cdot(\rho Y_j\mathbf{V_{c,j}})\frac{\mathrm{d}T}{\mathrm{d}c}}_{\text{velocity correction}},\end{aligned} \tag{7.24}$$

with

$$\sum_{i=1}^{N}\rho c_{p,i}Y_i\mathbf{V_{c,i}}\cdot\nabla T=-\frac{\rho\chi}{2}\left[\sum_{i=1}^{N}\frac{c_p}{Le_i}\frac{\mathrm{d}Y_i}{\mathrm{d}c}+\sum_{i=1}^{N}\frac{c_p-c_{p,i}}{Le_i}\frac{Y_i}{W}\frac{\mathrm{d}W}{\mathrm{d}c}\right]\frac{\mathrm{d}T}{\mathrm{d}c}. \tag{7.25}$$

Note that the inverse of the Lewis number of the progress variable simplifies two $\frac{1}{Le_c}=\sum_{j=1}^{N}\frac{b_j}{Le_j}\frac{\mathrm{d}Y_j}{\mathrm{d}c}$. In this set of equations, a second parameter, $\xi\,(c)$, is involved. It corresponds to the diffusion of c in the original coordinate system. Note that, as one would expect, this parameter includes curvature

effects

$$\xi = \frac{1}{4}\left[\frac{\mathrm{d}}{\mathrm{d}c}\left(\rho\chi\right) + \frac{\chi}{\alpha}\frac{\mathrm{d}}{\mathrm{d}c}\left(\rho\alpha\right)\right] - \rho\kappa\left(\frac{\chi\alpha}{2}\right)^{1/2}, \tag{7.26}$$

with $\kappa = \nabla\cdot(-\nabla c/|\nabla c|)$ (similar to Eq. 6.2 in which T was considered as the progress variable). A detailed derivation of Eq. 7.26 can be found in Ref. [184].

Similar to Section 7.4.1, to verify the validity of the two assumptions made in this section ($\partial/\partial c_k << \partial/\partial c$, for $k = 2, 3$, and $\partial/\partial\tau = 0$), the budget of Eq. 7.22 and 7.24 from the DNS is shown in Fig. 7.9 and 7.10. In contrast with the unity Lewis number limit, non-zero terms are found outside the reaction zone for n-C_7H_{16} and H_2O (diffusion term and differential diffusion-induced convective term). These are associated with relatively large residuals (the sum of the neglected terms corresponding to the right hand side of Eq. 7.11 and 7.12). Recalling that the preheat zone is largely thickened in the turbulent flames, it is not expected that the assumptions made in this section are valid throughout this preheat zone. Nevertheless, the residuals are sufficiently small in the reaction zone to expect some dependence of the source terms on c, χ, and ξ, which will be evaluated in the next section and Section 7.6.2.

As discussed in Section 7.4.1, it is hypothesized that the terms left out in Eq. 7.11 contribute to effective diffusivities, which would result in an effective dissipation rate and effective species Lewis numbers. The fact that the residuals are larger where the diffusion term and the differential diffusion-induced convective term are large is consistent with this hypothesis. For the reasons mentionned in Section 7.4.1 this hypothesis should be validated in future work. In particular, a framework that can be used to identify locally the effective Lewis numbers in the transformed coordinate system would be required.

Consistent with the unity Lewis number case, the residuals are larger in the higher-Ka flame. The terms associated with the velocity correction are negligible for all species considered. The velocity correction terms will therefore be neglected in the rest of the analysis. This is an important result for Section 7.6.2.

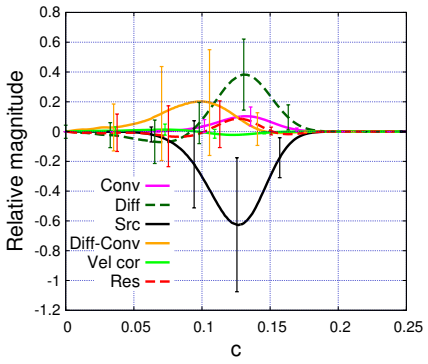

(a) higher-Ka, $Y_{C_7H_{16}}$

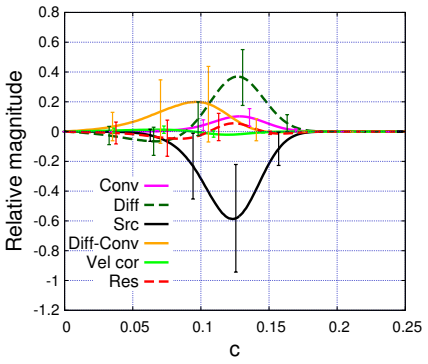

(d) lower-Ka, $Y_{C_7H_{16}}$

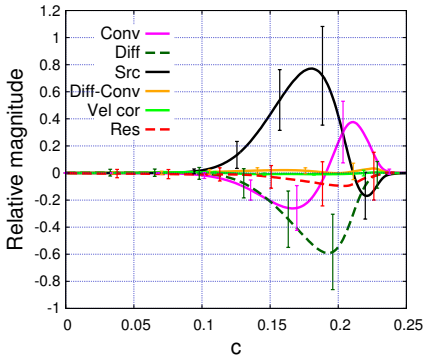

(b) higher-Ka, Y_{CO}

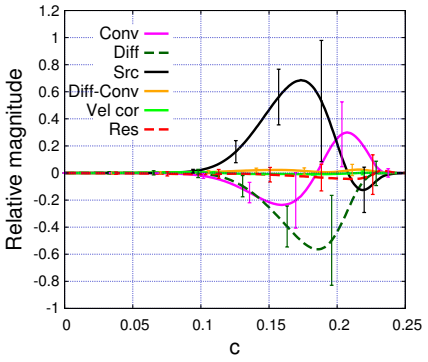

(e) lower-Ka, Y_{CO}

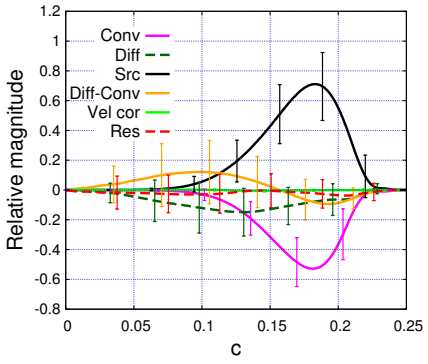

(c) higher-Ka, Y_{H_2O}

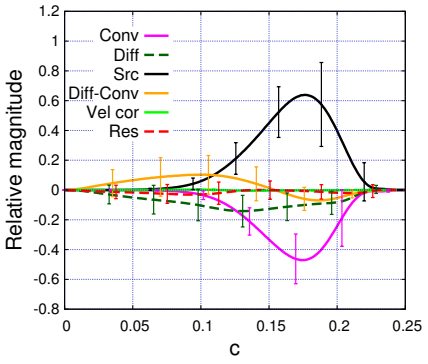

(f) lower-Ka, Y_{H_2O}

Figure 7.9: Mean of the terms in Eq 7.22 (for three different species) conditioned on c for both non-unity Lewis number flames, $< \text{term}|c >$. The bars correspond the standard deviation of these terms conditioned on c,$< (\text{term} - < \text{term}|c >)^2|c >^{1/2}$. The red dashed line corresponds to the residual of the equation (right hand side of Eq. 7.11). Each term is normalized by the absolute value of the largest term (corresponding to the same equation) in a non-unity Lewis number one-dimensional unstretched flame.

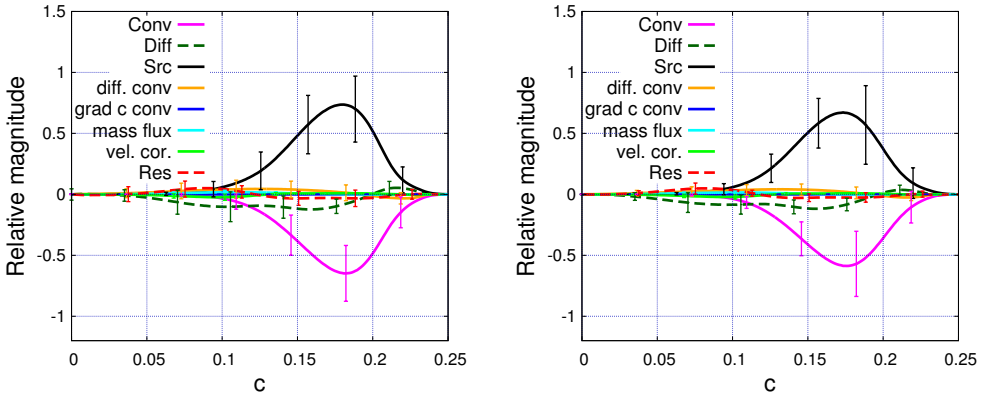

(a) higher-Ka (b) lower-Ka

Figure 7.10: Mean of the terms in Eq 7.24 conditioned on c for both non-unity Lewis number flames, $< \text{term}|c >$. The bars correspond the standard deviation of these terms conditioned on c,$< (\text{term} - < \text{term}|c >)^2|c >^{1/2}$. The red dashed line corresponds to the residual of the equation (right hand side of Eq. 7.12). Each term is normalized by the absolute value of the largest term (corresponding to the same equation) in a non-unity Lewis number one-dimensional unstretched flame.

7.5.2 Fuel burning rate

The results from the previous section are used to model *a posteriori* the fuel burning rate in the non-unity Lewis number flames. An approach to obtain an *a priori* model is discussed.

7.5.2.1 Dependence of the burning rate on c, χ, and ξ

The joint probability density function of the fuel burning rate *vs.* the dissipation rate at c_{peak} is presented in Fig. 7.11. Note that c_{peak} corresponds to the location in c-space of the peak mean (conditional on c) burning rate in the DNS. In contrast, $c_{\text{lam,peak}}$ is the equivalent for a one-dimensional unstretched flame. Recall that, as shown in Fig. 7.2(b) and 7.2(d), these are different. The correlation coefficients associated with Fig. 7.11 are listed in Table 7.3. They are compared to those obtained in Chapter 6 when considering the strain rate or the curvature instead of the dissipation rate. The fuel burning rate correlates better with the dissipation rate than with curvature or strain rate. However, the correlation found in the unity Lewis number flames is significantly stronger than in the non-unity Lewis number case (wide spread in Fig. 7.11).

Given the results of the last section, it is expected that the spread in Fig. 7.11 will be reduced by

allowing a dependence on ξ. This can indeed be observed in Fig. 7.12, where the joint probability density function of the fuel burning rate *vs.* the dissipation rate is presented at c_{peak}, but for three different intervals of ξ. The associated correlation coefficients are listed in Table 7.3. Intervals of ξ are used instead of single values in order to have a sufficient number points from the DNS to obtain statistically relevant correlations. Note that the width of the intervals (in ξ-space) is five times smaller than the difference between the center of these intervals. It is clear from Fig. 7.12 and Table 7.3 that the correlation between the fuel burning rate and the dissipation rate is significantly improved when ξ is set to a fixed value.

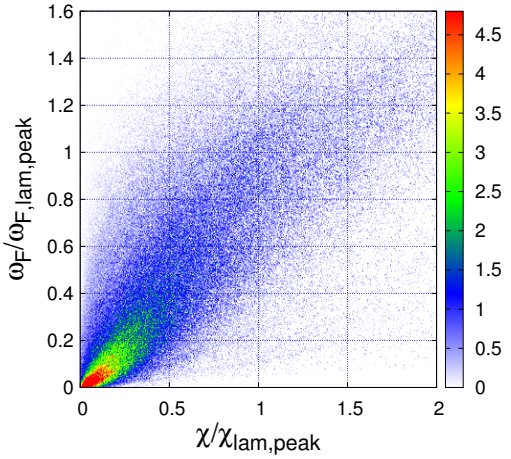

Figure 7.11: Joint PDF of the fuel burning rate *vs.* the dissipation rate of the progress variable, normalized by their peak laminar values (at $c = c_{\text{lam,peak}}$), on the isosurface of $c = c_{\text{peak}}$ in the higher-Ka non-unity Lewis number flame.

	r	dCor_n
Strain rate	0.49	0.45
Curvature	-0.53	0.65
Dissipation rate	0.75	0.72
Dissipation rate $\|\xi \in \Xi_{\text{low}}$	0.94	0.94
Dissipation rate $\|\xi \in \Xi_{\text{mid}}$	0.92	0.92
Dissipation rate $\|\xi \in \Xi_{\text{high}}$	0.87	0.86

Table 7.3: Pearson's correlation coefficient, r, and distance correlation, dCor_n, between fuel burning rate and various variables at $c = c_{\text{peak}}$ for the higher-Ka non-unity Lewis number flame.

This result suggests that the optimal estimator given, c, χ, and ξ should predict the fuel burning rate significantly better than the optimal estimator given, c only or c, χ. Similar to Fig. 7.6, Fig. 7.13 shows the probability density function of the point-wise comparison in the higher-Ka flame between

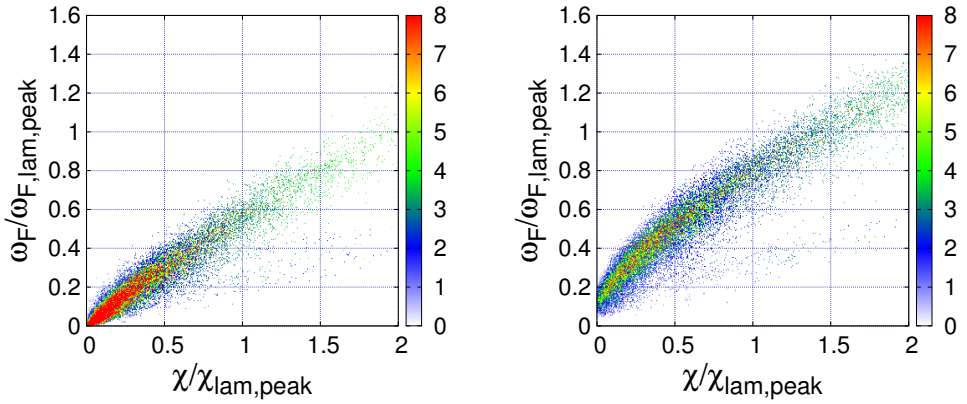

(a) $\xi \in \Xi_{\text{low}}$

(b) $\xi \in \Xi_{\text{mid}}$

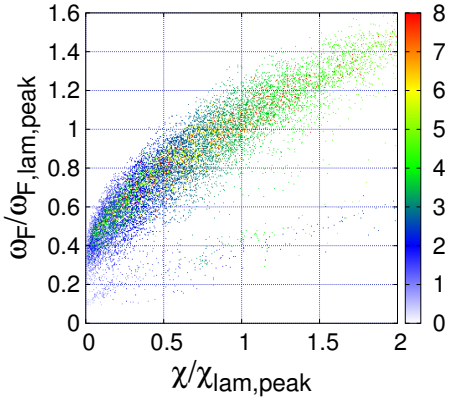

(c) $\xi \in \Xi_{\text{high}}$

Figure 7.12: Joint PDF of the fuel burning rate *vs.* the dissipation rate of the progress variable, normalized by their peak laminar values (at $c = c_{\text{lam,peak}}$), on the isosurface of $c = c_{\text{peak}}$ in the higher-Ka non-unity Lewis number flame, conditional on $\xi \in \Xi_k$, with $k = \text{low, mid, high}$. $\Xi_{\text{low}} = \left[-\frac{4}{3}\xi_{\text{lam,peak}}, -\frac{2}{3}\xi_{\text{lam,peak}}\right]$, $\Xi_{\text{mid}} = \left[\frac{2}{3}\xi_{\text{lam,peak}}, \frac{4}{3}\xi_{\text{lam,peak}}\right]$, $\Xi_{\text{high}} = \left[\frac{8}{3}\xi_{\text{lam,peak}}, \frac{10}{3}\xi_{\text{lam,peak}}\right]$.

the predicted and the actual fuel burning rate, for three optimal estimators: $< \dot{\omega}_F | c >$, $< \dot{\omega}_F | c, \chi >$, and $< \dot{\omega}_F | c, \chi, \xi >$. The prediction errors for these functions are listed in Table 7.4 for both flames. For the lower-Ka flame, $< \dot{\omega}_F | c, \chi, \xi >$ provides a good estimation of the fuel burning rate. In particular, the prediction error is six times smaller than for $< \dot{\omega}_F | c >$. For the higher-Ka, the error associated with $< \dot{\omega}_F | c, \chi, \xi >$ is three times smaller than that for $< \dot{\omega}_F | c >$. Although this error corresponds to a significant improvement with respect to the prediction error associated with $< \dot{\omega}_F | c >$, it is twice larger than for the lower-Ka flame. This shows that, as mentioned in the

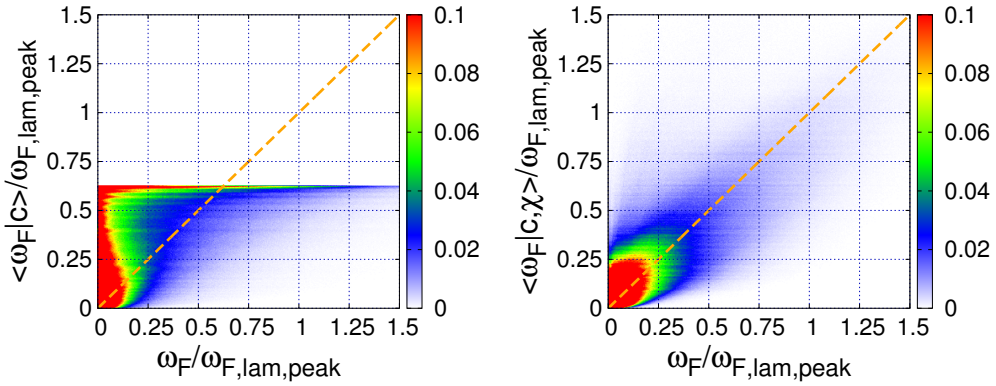

(a) $< \dot{\omega}_F | c >$ *vs.* $\dot{\omega}_F(\mathbf{x}, t)$

(b) $< \dot{\omega}_F | c, \chi >$ *vs.* $\dot{\omega}_F(\mathbf{x}, t)$

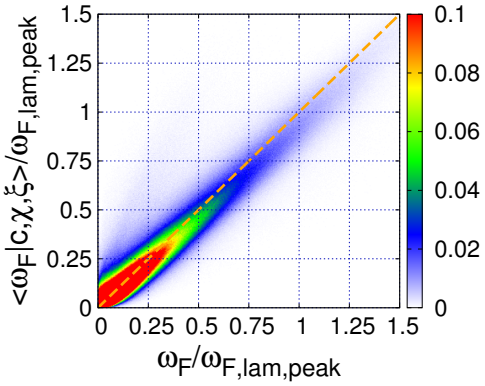

(c) $< \dot{\omega}_F | c, \chi, \xi >$ *vs.* $\dot{\omega}_F(\mathbf{x}, t)$

Figure 7.13: Joint PDF of the comparison between the predicted fuel burning rate and the actual burning rate in the higher-Ka non-unity Lewis number flame.

previous section, the tangential terms are non-negligible in the higher-Ka flame. To reduce this error, further modeling efforts would be required.

7.5.2.2 Flamelet-generated manifold

In a manner similar to what was done in Section 7.4.2.2 for the unity Lewis number cases, Eq. 7.22 and 7.24 can be solved for ranges of β_1 and β_2, such that $\chi(c) = \beta_1 \chi^0(c)$, and $\xi(c) = \beta_2 \xi^0(c)$, with $\xi^0(c)$ the diffusion term of the progress variable (in the original coordinate system) profile in a one-dimensional unstretched flame, in order to generate an *a priori* (c,χ,ξ)-manifold. While theoretically possible, this flamelet-generated manifold would not adequately represent the fuel burning in the

Estimator f	$\left(\epsilon_f^F/\epsilon_0^F\right)^{1/2}$	
	higher-Ka	lower-Ka
$<\dot{\omega}_F\|c>$	0.765	0.680
$<\dot{\omega}_F\|c,\chi>$	0.515	0.341
$<\dot{\omega}_F\|c,\chi,\xi>$	0.256	0.112

Table 7.4: Prediction error (Eq. 7.17) for various estimators of the fuel burning rate normalized by the prediction error for $f = 0$ in both non-unity Lewis number flames.

DNS. Indeed, the residual terms in the preheat zone would need to be modeled (Fig. 7.9). It was suggested in Section 7.5.1 that these could possibly be modeled by effective Lewis numbers. The position of the peak fuel burning rate in Fig. 7.2(b) and 7.2(d) also suggests that effective Lewis numbers are necessary to capture this position in c-space. Similar to the argument made in Chapter 5, since turbulent mixing (and the resulting tangential terms in the flamelet equations) varies accross the flame, a single set of Lewis numbers cannot be considered over the whole range of c. As mentioned, in Sections 7.5.1 and 5.4, to identify such Lewis numbers is not a simple task and this should be done in future work.

Within the framework of this thesis, an *a posteriori* DNS-generated manifold (from which $<\dot{\omega}_F|c,\chi,\xi>$ is extracted) is presented (previous section), but an *a priori* flamelet-generated manifold cannot be provided for the non-unity Lewis number flames.

7.6 Tabulation approach with the reduced-dimension manifold

The results from the previous sections suggest that the 35-dimensional phase space can be replaced by a two-dimensional (c,χ)-manifold in the unity Lewis number case, and, to some extent, by a three-dimensional (c,χ,ξ)-manifold in the non-unity Lewis number case. As mentioned in the introduction, one of the objectives of this thesis is to reduce the dimensionality of the chemistry. With these reduced-chemistry manifolds, the thermodynamic state is given by c and χ in the unity Lewis number case and by c, χ, and ξ in the non-unity Lewis number case. During a simulation of premixed turbulent flames, all chemistry-related quantities can be tabulated as a function of these

controlling variables (tabulated chemistry approach [171, 165, 63, 64, 98]). For the momentum and the continuity equations, the density and the viscosity need to be tabulated

Given the definition of χ and ξ, these can be determined by the field of c, if α is tabulated. However, c needs to be transported and additional properties/terms need to be tabulated.

In this section, the transport equation for the progress variable are provided in these two lower-dimension manifolds and closure for the chemistry-related quantities is provided/discussed in light of the results obtained in this chapter and Chapter 5.

7.6.1 Unity Lewis number limit

The progress variable transport equation in the unity Lewis number limit reads

$$\rho\frac{\partial c}{\partial t}+\rho\mathbf{u}\cdot\nabla c=\nabla\cdot(\rho\alpha\nabla c)+\dot{\omega}_c. \tag{7.27}$$

In this equation, ρ, α, and $\dot{\omega}_c$ need to be closed (tabulated). The viscosity, ν, also requires closure for the momentum equation.

First, as expected from the results presented in Section 5.1.1, and as shown in Fig. 7.14, $\rho\approx\rho_{\mathrm{FGM}}(c)$, $\nu\approx\nu_{\mathrm{FGM}}(c)$ and $\alpha\approx\alpha_{\mathrm{FGM}}(c)$, and these properties do not present modeling challenges.

Second, the progress variable production rate needs to be modeled. Since the reaction zone is thin in the flames studied, both the DNS-generated manifold and the FGM presented in the previous sections should also provide a very good estimator for the progress variable production rate. This is shown in Table 7.5. Therefore, the progress variable source term can be modeled as $\dot{\omega}_c =< \dot{\omega}_c|c,\chi >_{\mathrm{DNS}}$ (tabulation from a DNS-generated manifold) or $\dot{\omega}_c=\dot{\omega}_{c,\mathrm{FGM}}(c,\chi)$. As discussed in Section 7.4.2.1, the DNS-generated manifold provides the optimal predictor given the choice of variables. Unfortunately, this manifold is specific to the mixture and the unburnt conditions considered in the DNS. In contrast, the FGM can be easily generated for any mixtures and unburnt conditions.

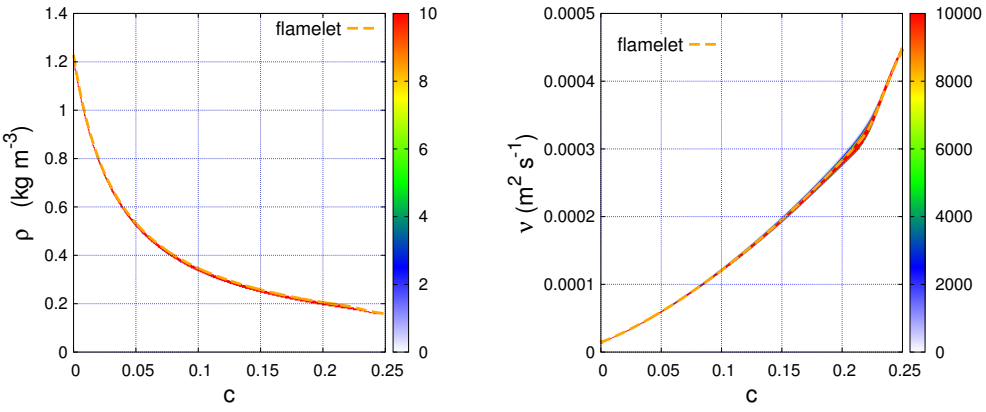

(a) density

(b) viscosity

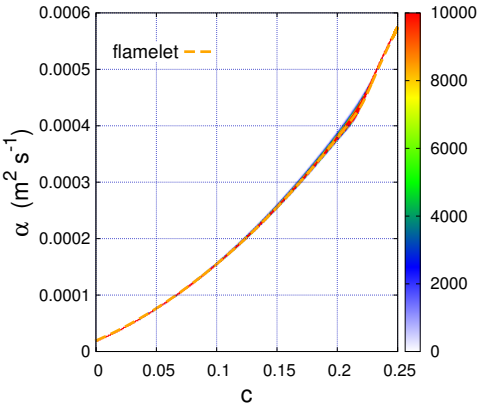

(c) diffusivity

Figure 7.14: Joint PDF of the thermodynamic properties *vs.* progress variable for the higher-Ka unity Lewis number flame. The 1D flame profiles are also shown (dashed lines).

Note that the joint probability density function (along with the correlation coefficients) of $\dot{\omega}_c$ *vs.* χ at c_{peak} is provided in Appendix E. The DNSGM and the FGM predictions are also provided.

7.6.2 Non-unity Lewis numbers

With differential diffusion, the following single scalar equation is considered in the reduced (c,χ,ξ)-manifold:

$$\rho\frac{\partial c}{\partial t} + \rho\mathbf{u}\cdot\nabla c = \nabla\cdot\left(\rho\frac{\alpha}{Le_c}\nabla c\right) + \dot{\omega}_c, \tag{7.28}$$

Estimator f	$\left(\epsilon_f^c/\epsilon_0^c\right)^{1/2}$	
	higher-Ka	lower-Ka
$<\dot{\omega}_c\|c>$	0.222	0.159
$<\dot{\omega}_c\|c,\kappa>$	0.183	0.130
$<\dot{\omega}_c\|c,a_t>$	0.182	0.132
$<\dot{\omega}_c\|c,\chi>$	0.049	0.031
$\dot{\omega}_{c,\mathrm{FGM}}\left(c,\chi\right)$	0.111	0.068

Table 7.5: Prediction error (Eq. 7.17) for various estimators of the progress variable source term normalized by the prediction error for $f = 0$ in both unity Lewis number flames.

which was already provided in Section 7.1 (Eq. 7.5). Recall that the term associated with the velocity correction was found to be negligible in the DNS (see Section 7.5.1) and hence it is not shown in Eq. 7.28. In the non-unity Lewis number case, ρ, ν, α (to evaluate χ and ξ from the field of c), α/Le_c, and $\dot{\omega}_c$ need to be closed (tabulated).

First, as observed in Fig 7.15, ρ, ν, and α are very well predicted by the flamelet with effective Lewis numbers (as computed in Section 5.3). Second, a similar closure for the progress variable diffusivity can also be obtained. Figure 7.16 shows its joint probability density function *vs.* c in both non-unity Lewis number turbulent flames. For values of c between 0 and about 0.22 (beyond which the terms in the flamelet equation are close to zero), little deviation from the conditional mean $<\frac{\alpha}{Le_c}|c>_{\mathrm{DNS}}$ is observed. Again, the flamelet solution with effective Lewis numbers (same as in Section 5.3 and 7.1) is very close to $<\frac{\alpha}{Le_c}|c>_{\mathrm{DNS}}$. Therefore, the thermodynamic properties can be modeled as $\rho = \rho_{\mathrm{FGM}}\left(c;\mathbf{Le_{eff}}\right)$, $\alpha = \alpha_{\mathrm{FGM}}\left(c;\mathbf{Le_{eff}}\right)$, and $\frac{\alpha}{Le_c} = \frac{\alpha}{Le_c}_{\mathrm{FGM}}\left(c;\mathbf{Le_{eff}}\right)$, with $Le_{i,\mathrm{eff}} = \left(1+0.05Ka\right)/\left(1/Le_i+0.05Ka\right)$, where $Ka = \left(u'/S_L\right)^{3/2}\left(l/l_F\right)^{-1/2}$, as introduced in Chapter 5. Third, the closure for the chemical source term of the progress variable can only be provided *a posteriori* (from the DNS) within the framework of this thesis. The prediction errors made with $<\dot{\omega}_c|c,\chi,\xi>_{\mathrm{DNS}}$ are listed in Table 7.6. They are comparable to the errors made for the fuel burning rate (Section 7.5.2.1). Note that the joint probability density function (along with the correlation coefficients) of $\dot{\omega}_c$ *vs.* χ at c_{peak} is provided in Appendix E for three intervals of ξ.

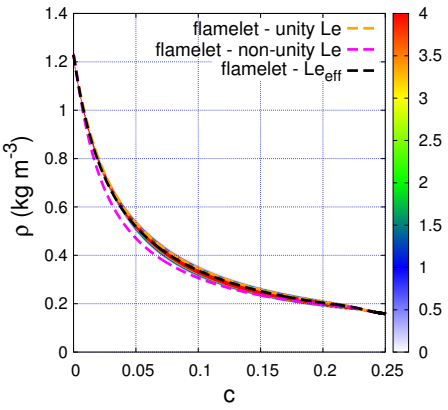

(a) density

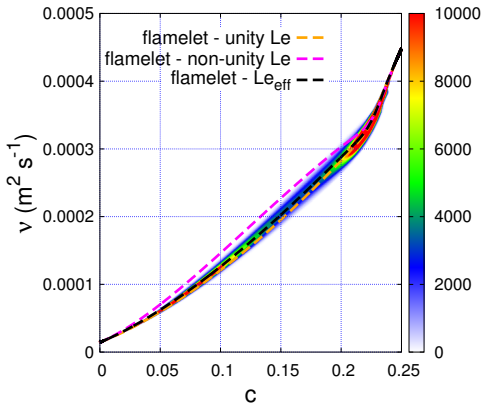

(b) viscosity

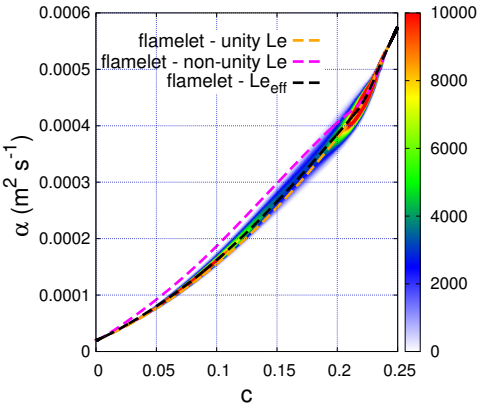

(c) diffusivity

Figure 7.15: Joint PDF of the thermodynamic properties *vs.* progress variable for the higher-Ka non-unity Lewis number flame. The unity, non-unity, and effective Lewis number 1D flame profiles are also shown (dashed lines).

7.7 Summary and discussion

While the flames considered in this work have a thin reaction zone, large fluctuations around the mean burning rate (conditional on c) were observed (Chapter 6). In order to model these fluctuations, a coordinate transformation was performed in this chapter. The following results were identified:

1. for the unity Lewis number flames,

   (a) the turbulent flames can be well represented by a set of one-dimensional (in c-space) flamelet equations parameterized by $\chi(c)$,

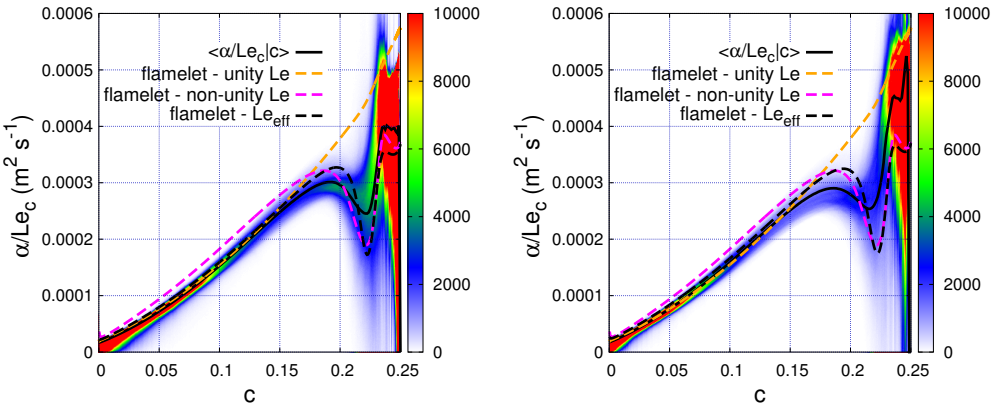

(a) higher-Ka (b) lower-Ka

Figure 7.16: Joint PDF and conditional mean (solid line) of the progress variable diffusivity *vs.* progress variable for both non-unity Lewis number flames. The unity, non-unity, and effective Lewis number 1D flame profiles are also shown (dashed lines).

Estimator f	$\left(\epsilon_f^c/\epsilon_0^c\right)^{1/2}$	
	higher-Ka	lower-Ka
$<\dot{\omega}_c\|c>$	0.483	0.572
$<\dot{\omega}_c\|c,\chi>$	0.401	0.293
$<\dot{\omega}_c\|c,\chi,\xi>$	0.264	0.223

Table 7.6: Prediction error (Eq. 7.17) for various estimators of the progress variable source term normalized by the prediction error for $f = 0$ in both non-unity Lewis number flames.

(b) the fuel burning rate $\dot{\omega}_F(\mathbf{x},t)$ can be approximated accurately by $\dot{\omega}_F(c(\mathbf{x},t),\chi(\mathbf{x},t))$,

(c) the fuel burning rate is well predicted *a priori* by the solution to the set of flamelet equations,

(d) all the chemistry-related quantities relevant to a turbulent flame simulation with this reduced chemistry ((c,χ)-manifold) can be tabulated from an *a priori* FGM;

2. for the non-unity Lewis number flames,

(a) in the vicinity of the reaction zone, the flame can, to a lesser extent (due to non-negligible tangential terms), be represented by a set of one-dimensional flamelet equations (in c) parameterized by $\chi(c)$ and $\xi(c)$,

(b) the fuel burning rate $\dot{\omega}_F(\mathbf{x},t)$ can be approximated accurately (only to some extent in the higher-Ka flame) by $\dot{\omega}_F(c(\mathbf{x},t),\chi(\mathbf{x},t),\xi(\mathbf{x},t))$,

(c) the fuel burning rate cannot be predicted *a priori* by the solution to the set of flamelet equations, unless a model for the effective diffusivities as a function of the progress variable is considered (future work),

(d) the thermodynamic properties relevant to a turbulent flame simulation can be tabulated from an *a priori* 1D-FGM considering the effective Lewis numbers provided in Chapter 5,

(e) the source term of the progress variable (relevant to a turbulent flame simulation with this reduced chemistry) can be closed by an *a posteriori* DNS-generated manifold.

Whether the models provided in this chapter are over-accurate, sufficiently accurate, or insufficiently accurate for practical applications remains unclear. As discussed in the introduction, the simulation of reacting flows in practical devices requires an LES framework. How the accuracy of these models affects that of the LES closure models has yet to be determined. Nevertheless, an important contribution of the analysis made in this chapter is the quantification of the predictive accuracy associated with the proposed models.

Finally, it is important to note that the assumption of a thin reaction zone was made to obtain the premixed flamelet equations. While this assumption is valid in the thin reaction zone regime, it may not be the case for higher turbulence intensities corresponding to the distributed burning regime.

Chapter 8

Conclusions

A time-integration scheme has been proposed for the simulation of stiff reacting flows. Using this scheme, a series of direct numerial simulations of high Karlovitz number, n-C_7H_{16}, turbulent premixed flames have been performed. It was found that the flame structure of these turbulent flames can be well captured by one-dimensional flames accounting for the effective species Lewis numbers. The reaction zone was found to remain thin, yet large fluctuations in the fuel burning rate were identified. Extinctions were observed only in the presence of differential diffusion, and these events were correlated with high curvature regions. A model to capture the burning fluctuations was proposed using a new flamelet approach. Finally, a reduced-chemistry modeling approach using flamelet equations was presented.

8.1 Time-integration

A semi-implicit preconditioning strategy, applied to an iterative method, was proposed for the time-integration of the stiff chemistry in the simulation of unsteady reacting flows, such as turbulent flames. The preconditioner consists of an approximation of the diagonal of the chemical Jacobian. It is integrated into the iterative procedure already implemented in the NGA code, in order to account for the non-linearities of the governing equations.

The proposed semi-implicit preconditioning, in combination with the iterative method, is far less computationally expensive than a fully-implicit method and was shown to be as inexpensive or less expensive than operator-splitting methods, while being more accurate. It was also observed that

the quasi steady-state (QSS) assumption may not be used for conventional species in the turbulent flame presently studied. As such, the proposed method is more suited than alternative methods for the type of flow studied, *i.e.* high Karlovitz flames.

8.2 Direct numerical simulations of high Karlovitz *n*-heptane/air flames

Relying on the new time integration scheme, a series of direct numerical simulations of high Karlovitz number, n-C_7H_{16}, turbulent premixed flames have been performed. These flames fall in the upper part of the thin reaction zone regime, close to the transition to the broken/distributed reaction zone regime.

For both the higher-Ka and the lower-Ka flames, the effects of turbulence on the flame in the absence of differential diffusion have been assessed through a first simulation with unity Lewis number, whereas the effects of turbulence on differential diffusion have been analyzed through a second simulation with non-unity Lewis numbers. Qualitative results indicated that the preheat zone is largely thickened by turbulent mixing, while the reaction zone remained thin.

8.3 Flame structure and differential diffusion

The flame thickness of the unity Lewis number flame was shown to be largely affected by turbulence. However, its structure (defined as the dependence of species mass fractions on temperature) is very similar to that of a one-dimensional, flat flame, suggesting that turbulence has a very limited impact on the flame in temperature space, in the absence of differential diffusion. On the other hand, the structure of the non-unity Lewis number flame is affected more substantially by turbulence. It was argued that turbulence affects the flame structure through an effective Lewis number. At high turbulence levels (*i.e.* high Karlovitz number) turbulence reduces differential diffusion effects.

A model for the effective species Lewis numbers was provided and validated first with a series of DNS of turbulent premixed lean hydrogen flames ($\phi = 0.4$) [10]. The structure of these flames

was found to vary considerably with Karlovitz number. However, this structure was found to be bounded by the structure of two limiting cases: unstretched laminar flamelets with 1) non-unity Lewis numbers, and 2) unity Lewis numbers. Moreover, the turbulent flames were shown to have the same structure in average as unstretched laminar flames with appropriate *effective* Lewis numbers. An *a priori* model for those effective Lewis numbers was derived from RANS transport equations. The model's dependence on a Reynolds versus Karlovitz number was investigated and a dependence on the Karlovitz number was found to be more suitable. While the parameters in the model were estimated with large uncertainties, the model was found to be in very good agreement with the DNS data.

The model, which was validated with the series of hydrogen/air flames, was directly used (with the same parameter) for the *n*-heptane/air flames. The unstretched laminar flamelets computed with these effective Lewis numbers are in good agreement with the mean turbulent flame structure. While the effective Lewis number model captures adequately this mean structure, it does not account for variations in turbulent mixing across the flame (associated with the transformation of turbulence due to the increase in kinematic viscosity). In other words, differential diffusion effects are almost suppressed in the preheat zone, but are still present close to the reaction zone.

8.4 Reaction zone

The reaction zone of both the unity and the non-unity Lewis numbers flames was shown to be thin. However, large source term fluctuations were present in both flames and in particular, local extinction events were found in the flame with non-unity Lewis numbers. This showed that a reaction zone can at the same time be thin and broken. The characterization of the reaction zone provided three main results.

First, differential diffusion was found to have limited effect on the srain rate and curvature distribution at the reaction zone. This is a consequence of the high turbulence level ($S_L^0/v_\eta \ll 1$), the reaction surface behaving more like a material (*i.e.* passive) surface than a propagating surface.

Second, a correlation was found between the fuel consumption rate and curvature for the non-

unity Lewis number flame, whereas a similar correlation was found between tangential strain rate and fuel consumption rate for the unity Lewis number case.

Finally, local extinctions were shown to have a strong effect on the turbulent flame speed by altering the local consumption rate of the fuel.

These results provide a qualitative understanding of the mechanism behind local extinctions and their effects on the turbulent flame speed, highlighting the importance of considering differential diffusion in models. However, a quantity that better correlates with source term fluctuations is required to adequately develop such models.

To identify such a quantity, a different approach was used. A local, flame-based coordinate transformation was applied to the scalar transport equations. For the unity Lewis number flames (both higher-Ka and lower-Ka), a budget analysis showed that the terms in the progress variable (c) direction are far more important than the tangential terms. In other words, around the reaction zone, the flame is very well described by a set of one-dimensional (in progress variable space) equations, or flamelets. These equations are parameterized by the dissipation rate of the progress variable, χ. The fuel burning rate was shown to correlate strongly with this dissipation rate. Two models for the fuel burning rate were provided: one corresponding to the conditional mean of the burning rate in the DNS, $< \dot{\omega}_F | c, \chi >$, and the other being obtained by solving the set of one-dimensional equations (FGM), varying the parameter χ, $\dot{\omega}_{F,\mathrm{FGM}}(c, \chi)$. Both models estimate accurately the local fuel burning rate.

The same approach was used for the non-unity Lewis number flames. In these flames, differential diffusion has a strong effect which results in non-negligible tangential terms, especially in the preheat zone. Nevertheless, these terms are sufficiently small in the reaction zone to consider the flamelet equations (normal terms) for modeling purposes. With differential diffusion, a second parameter appears in these flamelet equations, $\xi = \nabla \cdot (\rho \alpha \nabla c)$. A model for the fuel burning rate was proposed, $< \dot{\omega}_F | c, \chi, \xi >$, which provides relatively good accuracy.

An important contribution is the identification of these two controlling variables, χ and ξ, and the quantification of the best accuracy that can be achieved by models considering these variables

(optimal estimator).

8.5 Reduced-chemistry models

As mentioned in the introduction, an important aspect in the development of LES models is the reduction of the chemistry. It was shown in this thesis that to represent the flame structure of the turbulent unity Lewis number flames, a single progress variable is required. To capture the fuel burning rate, an additional variable is needed, namely the dissipation rate of this progress variable. This means that the 35-dimensional manifold representing the chemistry can be reduced down to a two-dimensional (c,χ)-manifold. The scalar transport equations in this dimensionnally-reduced manifold simplifies to a single transport equation for the progress variable. The thermodynamic properties can be properly closed with a single flamelet solution, while the source term in the equation is closed by the DNS-generated manifold, or the FGM, *i.e.* $< \dot{\omega}_c | c, \chi >_{\mathrm{DNS}}$ or $\dot{\omega}_{c,\mathrm{FGM}}(c, \chi)$.

For the non-unity Lewis number flames, the mean flame structure was shown to be well represented by a single flamelet solved with the appropriate effective species Lewis numbers. To capture the fuel burning rate, two additional variables are required, χ and ξ. Similarly, a single transport equation is required in the reduced (c,χ,ξ)-manifold. Closure for the thermodynamic properties is obtained by a single flamelet solved with the appropriate effective species Lewis numbers, while the source term in the equation is closed by the DNS-generated manifold $< \dot{\omega}_c | c, \chi, \xi >_{\mathrm{DNS}}$. Future work should consider the extension of the model to an FGM with appropriate effective Lewis numbers.

It should be noted that the present results (*i.e.* low dimensional manifold) are expected to be independent of the size of the chemical model used.

8.6 Limitations and suggestions for future work

The model proposed for the effective species Lewis numbers (Chapter 5) should be seen as a first attempt to describe the transition from "laminar" Lewis numbers to unity effective Lewis numbers. Quantification of uncertainties has yet to be performed, and more data points are needed to fully

validate the model. In addition, a framework to identify the effective species Lewis numbers as a function of the progress variable, especially in the transformed coordinates (Chapter 7), would open doors for the generation of FGMs to be used in turbulent non-unity Lewis number flames.

Quantitative prediction errors have been provided for the chemistry-reduction closure models. However, it is unclear what level of precision is required for sub-grid-scale closure models in LES. Future work should be extended to the development of such models that are consistent with the present (c,χ)- and (c,χ,ξ)-manifolds. Depending on the accuracy of the LES, better chemistry-reduction models may be necessary, *i.e.* the tangential terms in the transformed equations (Chapter 7) may need to be modeled.

The analysis in this thesis was done on flames with small integral length scales (relatively low turbulent Reynolds number), due to the expensive computational nature of the DNS. With the increasing capabilities of super-computers, it could be possible to increase the turbulent Reynolds number by close to an order of magnitude, while keeping the Karlovitz number constant, in a relatively close future. This could confirm/disconfirm if the results obtained in this thesis are Karlovitz number dependent, but Reynolds number independent.

In addition to the integral length scale, the domain width considered in the present flames is relatively small. This constrains the mode shapes the flame can exhibit. With the current forcing method, a simulation with a larger integral length scale would also require a larger domain width. With such a simulation, the effects of the additional mode shapes on the results presented in this thesis could be assessed.

The results in this thesis are argued to be valid in the thin reaction zone regime. This is particularly important for the results of Chapter 7, which rely on the fact that the gradients in the progress variable direction are much larger than those in the tangential directions. This assumption is not expected to be valid in the distributed burning regime. It would be interesting to perform simulations in the broken/distributed reaction zone regime to assess the extent of the validity of the results presented in this thesis.

Finally, the effect of the chemical mechanism, the nature of the large hydrocarbon fuel, and the

unburnt temperature on the present results should also be investigated in future work.

Appendix A

Impacts of the effective Lewis number model

A.1 Impact on S_L and l_F

As the effective Lewis numbers of the different species change with the Karlovitz number, the associated laminar flame speed and flame thickness are expected to change as well. This is particularly important as both of these quantities are used in modeling the turbulent flame speed [147, 141] and defining a regime diagram [142].

Figure A.1 shows, in solid lines, the effective laminar flame speed ($S_{L,\text{eff}}$) and flame thickness ($l_{F,\text{eff}}$) obtained from laminar unstretched flamelet simulations, in which the Lewis numbers were modified according to the Ka-based model. These results suggest that these effective Lewis numbers have an important impact on the laminar flame speed and flame thickness. More specifically, both the laminar flame speed and flame thickness vary by almost a factor of 2 between the "laminar" Lewis numbers and the unity Lewis numbers flamelets. Note that this factor is expected to be case dependent, *i.e.* it is expected to be different for different fuels and unburnt conditions.

These strong effects may be understood from simple asymptotic flame theory. For a one-step reaction, matched asymptotic expansion with only the fuel Lewis number different than unity, the following ratios are obtained [140]:

$$\frac{S_{L,2}}{S_{L,1}} = \left(\frac{Le_{F,2}}{Le_{F,1}}\right)^{0.5}, \tag{A.1}$$

$$\frac{l_{F,2}}{l_{F,1}} = \left(\frac{Le_{F,1}}{Le_{F,2}}\right)^{0.5}, \tag{A.2}$$

where $S_{L,i}$ and $l_{F,i}$ are the laminar flame speed and flame thickness of a flame with corresponding fuel Lewis number $Le_{F,i}$. Note that the only different parameter between flames 1 and 2 is the fuel Lewis number. Using the Ka-based model (Eq. 5.34), the effective laminar flame speed and flame thickness obtained from Eq. A.1 and A.2 are plotted as a function of the Karlovitz number in Fig. A.1. The above analytic expressions (Eq. A.1 and A.2) are compared to the flamelet calculation results using the same effective Lewis numbers. The agreement between the curves is relatively good. The discrepancies can be due to the numerous simplifying assumptions made in the matched asymptotic expansion. Note that a 0.6 exponent instead of 0.5 in Eq. A.1 gives better agreement for the effective laminar flame speed with the flamelet calculations. Nevertheless, it is interesting to point out that the complex chemistry mechanism used in the flamelet simulations provides the same behavior as a single-step mechanism.

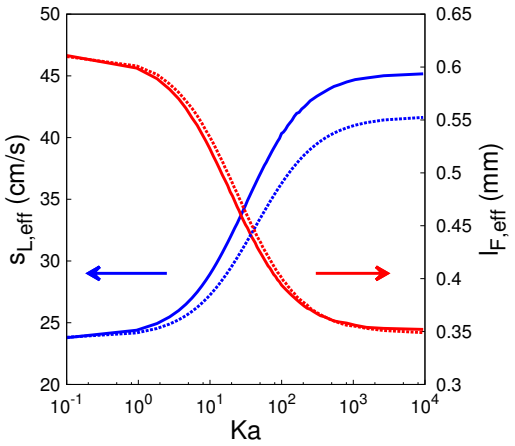

Figure A.1: Effective laminar flame speed and flame thickness versus Karlovitz number from flamelet simulations (solid lines) and analytical expressions (dotted lines).

A.2 Impact on the regime diagram

The result from subsection A.1 suggests that a new effective Karlovitz number should be defined that takes into account the effective flame thickness:

$$Ka_{\text{eff}} = \frac{l_{F,\text{eff}}^2}{\eta^2}. \tag{A.3}$$

Using Eq. A.2, this effective Karlovitz number can be related to the "traditional" Karlovitz number as follows:

$$Ka_{\text{eff}} = \frac{Le_F}{Le_{F,\text{eff}}} Ka. \tag{A.4}$$

Recall the relation derived from Peters [142] from which the iso-Ka lines are obtained in the premixed regime diagram:

$$\frac{u'}{S_L} = Ka^{2/3} \left(\frac{l}{l_F} \right)^{1/3}. \tag{A.5}$$

Note that $S_L l_F = \nu$ is assumed in Eq. A.5.

Following the results shown in Chapter 5, the relevant quantity to differentiate whether the smallest eddies will penetrate the preheat zone or the reaction zone is the effective Karlovitz number (respectively $Ka_{\text{eff}} = 1$ and $Ka_{\text{eff}} = 100$). Using the Ka-based model (Eq. 5.34) in Eq. A.4, Ka can be expressed as a function of Ka_{eff}:

$$\begin{aligned} Ka = \frac{1}{2a^{Ka} Le_F} \Big\{ & \left(a^{Ka} Ka_{\text{eff}} - 1 \right) \\ & + \left[\left(a^{Ka} Ka_{\text{eff}} - 1 \right)^2 + 4a^{Ka} Le_F Ka_{\text{eff}} \right]^{0.5} \Big\}. \end{aligned} \tag{A.6}$$

Fixing Ka_{eff} to its limiting values (1 or 100), the resulting Ka values can be used in Eq. A.5 to obtain a modified regime diagram as shown in Fig. A.2. Note that the $u'/S_L = 1$ line is modified to be the $u'/S_{L,\text{eff}} = 1$ line. The $Re_T = 1$ line is not modified by the fuel effective Lewis number. The lines separating the wrinkled/corrugated flamelet regimes and the thin reaction zone regimes are unchanged. This result is not surprising as, in the wrinkled/corrugated flamelet regimes, eddies

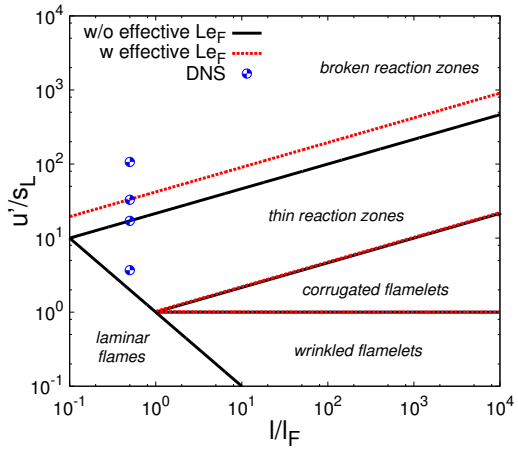

Figure A.2: Regime diagram taking into account the effective Karlovitz number, considering the Ka-based model.

do not penetrate the preheat zone and hence do not lead to an effective Lewis number. On the other hand, the separation between thin reaction and broken reaction zones is affected. As eddies penetrate in the preheat zone, the resulting changes in the effective Lewis numbers lead to an increase in the effective laminar flame speed and a decrease in the effective flame thickness (Fig. A.1). Both of these effects tend to "counteract" the increase in the Karlovitz number (Eq. A.5).

Aspden *et al.* found in Ref. [10] that the two lowest Ka (10 and 100) DNS simulations showed a thin reaction zone-like behavior, whereas the highest Ka (1526) simulation was clearly in the broken reaction or distributed burning zone. The intermediate simulation ($Ka = 266$) was labeled as a transition case, whereas scaling arguments [142] suggest that the transition should be around $Ka = 100$. These observations from Aspden *et al.* agree very well with Fig. A.2, even though the present authors do not claim to explain the transition Ka found in Ref. [10].

A.3 Impact on S_T

Finally, the effective Lewis numbers have an impact on the predicted turbulent flame speed. Numerous experiments have showed a turbulent flame speed dependency on the Lewis number of the fuel [172, 99, 94, 100, 50, 69]. The effects of Reynolds or Karlovitz number on the flame characteristics through the effective Lewis number might explain these dependencies. Consider the most

widely used model for the turbulent flame speed [142]:

$$\frac{S_T}{S_L} = 1 + C\left(\frac{u'}{S_L}\right)^n . \tag{A.7}$$

Using the idea that the effective laminar flame speed is the relevant quantity rather than the laminar flame speed, a new model can be derived. More precisely, we propose

$$\begin{aligned}\frac{S_T}{S_L} &= \frac{S_T}{S_{L,\text{eff}}} \cdot \frac{S_{L,\text{eff}}}{S_L} \\ &= \left(\frac{Le_{\text{eff}}}{Le}\right)^{0.6} \left[1 + C\left(\frac{u'}{S_L}\right)^n \left(\frac{Le}{Le_{\text{eff}}}\right)^{0.6n}\right]\end{aligned} \tag{A.8}$$

where Le_{eff} follows Eq. 5.34. The reason for a 0.6 exponent in Eq. A.8 is explained in subsection A.1. Both a Lewis number and a Karlovtiz number dependency is hence introduced.

In 1992, Bradley *et al.* [21] found the turbulent flame speed to be Lewis number and Reynolds number dependent. After identifying the relevant KLe grouping, where $K = 0.157\left(\frac{u'}{S_L}\right)^2 Re_T^{-0.5}$ is the Karlovitz stretch factor, they obtained the following correlation:

$$\frac{S_T}{S_L} = 0.88\frac{u'}{S_L}\left(KLe\right)^{-0.3} . \tag{A.9}$$

More recently, Muppala *et al.* [125] developed a model that also depends on the Lewis number and the Reynolds number:

$$\frac{S_T}{S_L} = 1 + \frac{A}{\exp\left(Le - 1\right)} Re_T^{0.25}\left(\frac{u'}{S_L}\right)^{0.3} , \tag{A.10}$$

where A is a fitting parameter.

These four models and correlations are compared against one another in Fig. A.3. The parameters C, n, and A are adjusted such that all models fall on each others for unity Lewis number. The integral length scale and the viscosity are taken to be the same as in Section 5.2.1. The Lewis number is then modified to give the solid lines ($Le = 0.3$) and the dotted lines ($Le = 3$). The model proposed in Chapter 5 (C-n with Le_{eff}) agrees very well with the correlation from Bradley *et al.* These results

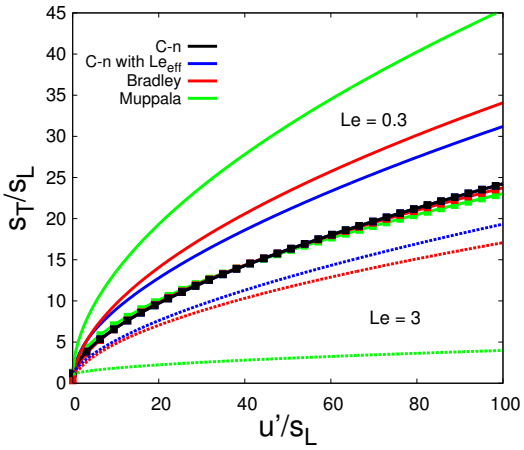

Figure A.3: Normalized turbulent flame speed profiles for the models given by Eq. A.7-A.10 for Le =0.3 (solid lines), 1 (symbols), and 3 (dotted lines).

further suggest that the effective laminar flame speed ($S_{L,\text{eff}}$) is the relevant quantity rather than the laminar unstretched flame speed. A similar analysis has been performed with the Re_T-based model. The results were very similar to those shown in Fig. A.3.

A.4 Summary

The effective laminar flame speed and flame thickness have to be considered. Indeed, those quantities vary by almost a factor of two between the "laminar" Lewis numbers and the unity Lewis numbers for premixed hydrogen flamelet ($\phi = 0.4$) simulations.

In light of these results, an effective Karlovitz number Ka_{eff} was defined and should be used in developing turbulent combustion models. The regime diagram proposed by Peters [142] should therefore be adapted to the fuel considered whenever the fuel has a Lewis number far from unity. Finally, a turbulent flame speed model that takes into account the Lewis number and the Karlovitz number was derived.

Appendix B

Correlations

To better understand the effect of strain rate and curvature on the reaction zone, it is important to assess if they are correlated. Figures B.1(a) and B.1(b) present the joint density distributions for these two quantities, in both flames. The Pearson correlation coefficient [132] and the distance correlation [168] are shown in Table B.1. These measures of correlation will be used further and are described in the following.

The Pearson correlation coefficient, a well established statistical measure, is computed as

$$r = \frac{\sum_{i=1}^{n} \left(X_i - \bar{X}\right)\left(Y_i - \bar{Y}\right)}{\sqrt{\sum_{i=1}^{n} \left(X_i - \bar{X}\right)^2}\sqrt{\sum_{i=1}^{n} \left(Y_i - \bar{Y}\right)^2}}, \tag{B.1}$$

for a sample pair of data (X_i, Y_i), where $\bar{\cdot}$ denotes the sample mean, and n is the sample size. It is important to note that $r = 0$ does not imply independence of the random variables X and Y. Since a measure of dependence is sought, the distance correlation was also computed. This statistical measure was introduced in the previous decade to overcome this issue [168]. Moreover, it is more relevant than Pearson's coefficient for non-linear correlations. To compute the distance correlation,

for a sample pair of data (X_i, Y_i) (assuming $X, Y \in \mathbb{R}$ to simplify), let us first introduce

$$a_{ij} = |X_i - X_j| \qquad \bar{a}_{i\star} = \frac{1}{n}\sum_{j=1}^{n} a_{ij} \tag{B.2}$$

$$\bar{a}_{\star j} = \frac{1}{n}\sum_{i=1}^{n} a_{ij} \qquad \bar{a}_{\star\star} = \frac{1}{n^2}\sum_{i,j=1}^{n} a_{ij}$$

$$A_{ij} = a_{ij} - \bar{a}_{i\star} - \bar{a}_{\star j} + \bar{a}_{\star\star}.$$

Similarly, define $b_{ij} = |Y_i - Y_j|$ and $B_{ij} = b_{ij} - \bar{b}_{i\star} - \bar{b}_{\star j} + \bar{b}_{\star\star}$. The sample distance covariance is then defined as

$$\mathrm{dCov}_n(X, Y) = \frac{1}{n}\sqrt{\sum_{i,j=1}^{n} A_{ij} B_{ij}}. \tag{B.3}$$

Finally, the distance correlation, is computed as

$$\mathrm{dCor}_n(X, Y) = \frac{\mathrm{dCov}_n(X, Y)}{\sqrt{\mathrm{dVar}_n(X)\mathrm{dVar}_n(Y)}}, \tag{B.4}$$

with $\mathrm{dVar}_n(X) = \mathrm{dCov}_n(X, X)$.

Given the values listed in Table B.1, curvature and strain rate show low dependency, as previously observed [71], and, again, differential diffusion has virtually no effect.

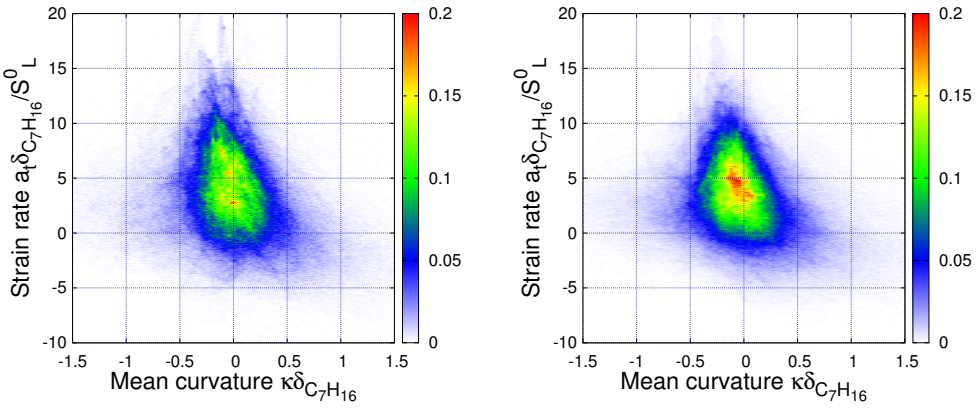

(a) $Le = 1$ (b) $Le \neq 1$

Figure B.1: Joint probability density function, on the isoterm $T = T_{\mathrm{peak}}$, of the normalized strain rate *vs.* the normalized mean curvature. (a) $Le = 1$; (b) $Le \neq 1$.

	r	dCor_n
$Le = 1$	-0.26	0.33
$Le \neq 1$	-0.25	0.35

Table B.1: Pearson's correlation coefficient, r, and distance correlation, dCor_n, between strain rate and curvature at $T = T_{\mathrm{peak}}$ for both (higher-Ka) flames presented in this thesis.

Appendix C

Intermediate step in the transformation of the transport equations

C.1 Species equations

Applying the coordinate transformation (Section 7.2) to Eq. 2.5 yields

$$\begin{aligned}
&\rho\frac{\partial Y_i}{\partial \tau} + \rho\frac{\partial Y_i}{\partial c}\frac{\partial c}{\partial t} + \rho\sum_{k=2}^{3}\left[\frac{\partial Y_i}{\partial c_k}\left(\frac{\partial c_k}{\partial t} + \mathbf{u}\cdot\nabla c_k\right)\right] \\
&+ \rho\frac{\partial Y_i}{\partial c}\mathbf{u}\cdot\nabla c - \frac{\partial Y_i}{\partial c}\nabla\cdot\left(\frac{\rho\alpha}{Le_i}\nabla c\right) \\
&\qquad = \frac{\rho\chi}{2Le_i}\frac{\partial^2 Y_i}{\partial c^2} + \dot{\omega}_i + \sum_{k=2}^{3}\frac{\rho\chi_k}{2Le_i}\frac{\partial^2 Y_i}{\partial c_k^2} + \frac{2\rho\alpha}{Le_i}\left(\nabla c_2\cdot\nabla c_3\right)\frac{\partial^2 Y_i}{\partial c_2\partial c_3} \\
&\qquad\quad + \nabla\cdot\left(\frac{\rho\alpha}{Le_i}\nabla c_2\right)\frac{\partial Y_i}{\partial c_2} + \nabla\cdot\left(\frac{\rho\alpha}{Le_i}\nabla c_3\right)\frac{\partial Y_i}{\partial c_3} + \nabla\cdot\left(\rho Y_i\mathbf{V}_{\mathbf{c,i}}\right).
\end{aligned} \tag{C.1}$$

Using Eq. 7.5, Eq. 7.11 is obtained.

C.2 Temperature equation

Applying the coordinate transformation (Section 7.2) to Eq. 2.4 yields

$$
\begin{aligned}
&\rho c_p \frac{\partial T}{\partial \tau} + \rho c_p \frac{\partial T}{\partial c}\frac{\partial c}{\partial t} + \rho c_p \sum_{k=2}^{3}\left[\frac{\partial T}{\partial c_k}\left(\frac{\partial c_k}{\partial t} + \mathbf{u}\cdot\nabla c_k\right)\right] \\
&+ \rho c_p \frac{\partial T}{\partial c}\mathbf{u}\cdot\nabla c - \frac{\partial T}{\partial c}\nabla\cdot(\rho c_p \alpha \nabla c) \\
&+ \left(\sum_{i=1}^{N}\frac{\rho c_{p,i}\chi}{2Le_i}\frac{\partial Y_i}{\partial c} + \sum_{i=1}^{N}\rho c_{p,i} Y_i \mathbf{V_{c,i}}\cdot\nabla c\right)\frac{\partial T}{\partial c} \\
&\qquad = \frac{\rho c_p \chi}{2}\frac{\partial^2 T}{\partial c^2} + \dot{\omega}_T + \sum_{k=2}^{3}\frac{\rho c_p \chi_k}{2}\frac{\partial^2 T}{\partial c_k^2} + 2\rho c_p \alpha\left(\nabla c_2\cdot\nabla c_3\right)\frac{\partial^2 T}{\partial c_2 \partial c_3} \\
&\qquad\quad + \nabla\cdot(\rho c_p \alpha \nabla c_2)\frac{\partial T}{\partial c_2} + \nabla\cdot(\rho c_p \alpha \nabla c_3)\frac{\partial T}{\partial c_3} \\
&\qquad\quad + \sum_{k=2}^{3}\left(\sum_{i=1}^{N}\frac{\rho c_{p,i}\chi_k}{2Le_i}\frac{\partial Y_i}{\partial c_k}\frac{\partial T}{\partial c_k} + \sum_{i=1}^{N}\rho c_{p,i} Y_i \mathbf{V_{c,i}}\cdot\nabla c_k \frac{\partial T}{\partial c_k}\right) \\
&\qquad\quad + \sum_{i=1}^{N}\frac{\rho c_{p,i}\alpha}{Le_i}\left(\frac{\partial Y_i}{\partial c_2}\frac{\partial T}{\partial c_3} + \frac{\partial Y_i}{\partial c_3}\frac{\partial T}{\partial c_2}\right)\left(\nabla c_2\cdot\nabla c_3\right),
\end{aligned}
\tag{C.2}
$$

Using Eq. 7.5, Eq. 7.12 is obtained.

Appendix D

Transformed transport equations in the unity Lewis number limit

D.1 Species equation

In the unity Lewis number limit, Eq. 7.11 reads

$$\rho\frac{\partial Y_i}{\partial \tau} + \underbrace{\rho\sum_{k=2}^{3}\left[\frac{\partial Y_i}{\partial c_k}\left(\frac{\partial c_k}{\partial t} + \mathbf{u}\cdot\nabla c_k\right)\right]}_{\text{Lagrangian transport}} \tag{D.1}$$

$$+ \underbrace{\dot{\omega}_c\frac{\partial Y_i}{\partial c}}_{\text{normal convection}}$$

$$= \underbrace{\frac{\rho\chi}{2}\frac{\partial^2 Y_i}{\partial c^2}}_{\text{normal diffusion}} + \underbrace{\dot{\omega}_i}_{\text{chemical source}} + \underbrace{\sum_{k=2}^{3}\frac{\rho\chi_k}{2}\frac{\partial^2 Y_i}{\partial c_k^2} + 2\rho\alpha\left(\nabla c_2\cdot\nabla c_3\right)\frac{\partial^2 Y_i}{\partial c_2\partial c_3}}_{\text{tangential diffusion}}$$

$$+ \underbrace{\nabla\cdot\left(\rho\alpha\nabla c_2\right)\frac{\partial Y_i}{\partial c_2} + \nabla\cdot\left(\rho\alpha\nabla c_3\right)\frac{\partial Y_i}{\partial c_3}}_{\text{tangential convection}}.$$

D.2 Temperature equation

In the unity Lewis number limit, Eq. 7.12 reads

$$
\begin{aligned}
&\rho c_p \frac{\partial T}{\partial \tau} + \underbrace{\rho c_p \sum_{k=2}^{3} \left[\frac{\partial T}{\partial c_k} \left(\frac{\partial c_k}{\partial t} + \mathbf{u} \cdot \nabla c_k \right) \right]}_{\text{Lagrangian transport}} \\
&+ c_p \underbrace{\left(\dot{\omega}_c - \frac{\rho \chi}{2 c_p} \frac{\partial c_p}{\partial c} \right) \frac{\partial T}{\partial c}}_{\text{normal convection 1}} \\
&+ \underbrace{\sum_{i=1}^{N} \frac{\rho c_{p,i} \chi}{2} \frac{\partial Y_i}{\partial c} \frac{\partial T}{\partial c}}_{\text{normal convection 2}} \\
&\quad = \underbrace{\frac{\rho c_p \chi}{2} \frac{\partial^2 T}{\partial c^2}}_{\text{normal diffusion}} + \underbrace{\dot{\omega}_T}_{\text{chemical source}} + \underbrace{\sum_{k=2}^{3} \frac{\rho c_p \chi_k}{2} \frac{\partial^2 T}{\partial c_k^2} + 2 \rho c_p \alpha \left(\nabla c_2 \cdot \nabla c_3 \right) \frac{\partial^2 T}{\partial c_2 \partial c_3}}_{\text{tangential diffusion}} \\
&\qquad + \underbrace{\nabla \cdot \left(\rho c_p \alpha \nabla c_2 \right) \frac{\partial T}{\partial c_2} + \nabla \cdot \left(\rho c_p \alpha \nabla c_3 \right) \frac{\partial T}{\partial c_3}}_{\text{tangential convection 1}} \\
&\qquad + \underbrace{\sum_{k=2}^{3} \sum_{i=1}^{N} \frac{\rho c_{p,i} \chi_k}{2} \frac{\partial Y_i}{\partial c_k} \frac{\partial T}{\partial c_k}}_{\text{tangential convection 2}} \\
&\qquad + \underbrace{\sum_{i=1}^{N} \rho c_{p,i} \alpha \left(\frac{\partial Y_i}{\partial c_2} \frac{\partial T}{\partial c_3} + \frac{\partial Y_i}{\partial c_3} \frac{\partial T}{\partial c_2} \right) \left(\nabla c_2 \cdot \nabla c_3 \right)}_{\text{tangential convection 3}} .
\end{aligned}
\tag{D.2}
$$

Appendix E

Joint probability density function of $\dot{\omega}_c$ *vs.* χ at c_{peak}

E.1 Unity Lewis number limit

Figure E.1 shows the joint probablity density function of $\dot{\omega}_c$ *vs.* χ at c_{peak} for both unity Lewis number flames. The DNSGM and the FGM solutions are shown for comparison. The correlation coefficients for this figure are listed in Table. E.1.

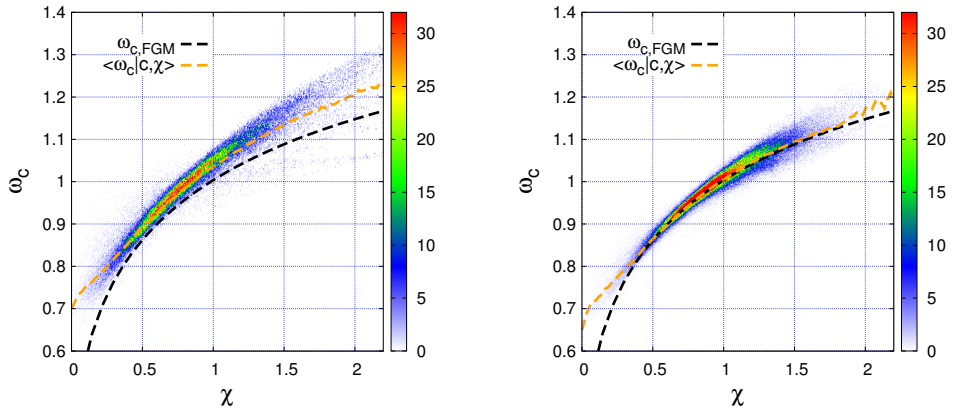

(a) higher-Ka (b) lower-Ka

Figure E.1: Comparison between the fuel burning rate predicted by $\dot{\omega}_{c,\text{FGM}}(c,\chi)$ and $<\dot{\omega}_c|(c,\chi)>$ as a function of the dissipation rate, normalized by their peak laminar values, given $c = c_{\text{peak}}$. The joint PDF on the isosurface of $c = c_{\text{peak}}$ in the turbulent flames is also shown for comparison.

	r	dCor_n
Dissipation rate, higher-Ka	0.96	0.96
Dissipation rate, lower-Ka	0.96	0.96

Table E.1: Pearson's correlation coefficient, r, and distance correlation, dCor_n, between dissipation rate and progress variable source term at $c = c_{\mathrm{peak}}$ for the higher-Ka unity Lewis number flame.

E.2 Non-unity Lewis numbers

Figure E.2 shows the joint probablity density function of $\dot{\omega}_c$ *vs.* χ at c_{peak} for three intervals of ξ, for the higher-Ka non-unity Lewis number flame. The correlation coefficients for this figure are listed in Table. E.2.

	r	dCor_n
Dissipation rate $\|\chi \in \Xi_{\mathrm{low}}$	0.90	0.89
Dissipation rate $\|\chi \in \Xi_{\mathrm{mid}}$	0.86	0.86
Dissipation rate$\|\chi \in \Xi_{\mathrm{high}}$	0.78	0.80

Table E.2: Pearson's correlation coefficient, r, and distance correlation, dCor_n, between dissipation rate and progress variable source terms for various intervals of ξ at $c = c_{\mathrm{peak}}$ for the higher-Ka non-unity Lewis number flame.

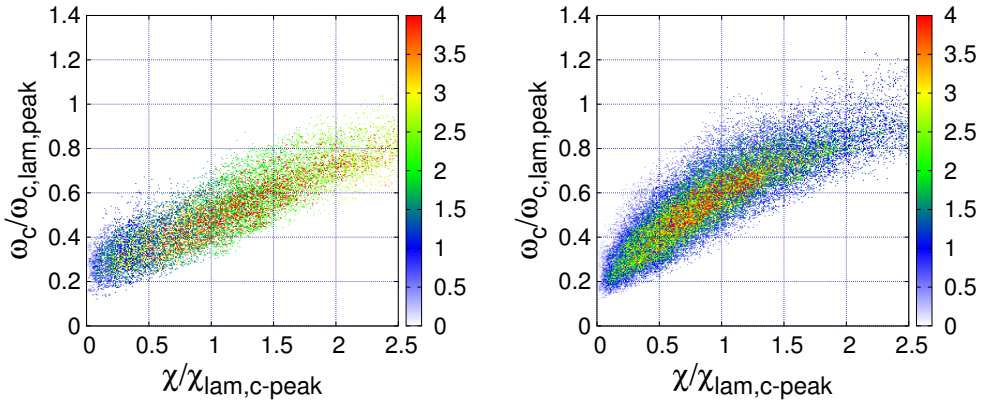

(a) $\chi \in \Xi_{\text{low}}$

(b) $\chi \in \Xi_{\text{mid}}$

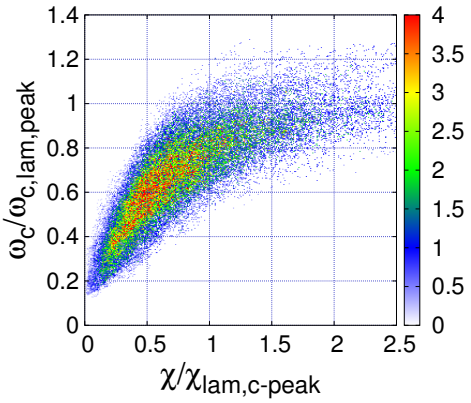

(c) $\chi \in \Xi_{\text{high}}$

Figure E.2: Joint PDF of the progress variable source term *vs.* the dissipation rate of the progress variable, normalized by their peak laminar values (at $c = c_{\text{lam,peak}}$), on the isosurface of $c = c_{\text{peak}}$ in the higher-Ka non-unity Lewis number flame, conditional on $\xi \in \Xi_k$, with $k = \text{low}, \text{mid}, \text{high}$. $\Xi_{\text{low}} = \left[\frac{5}{4}\xi_{\text{lam,c-peak}}, \frac{3}{2}\xi_{\text{lam,c-peak}}\right]$, $\Xi_{\text{mid}} = \left[\frac{7}{8}\xi_{\text{lam,c-peak}}, \frac{9}{8}\xi_{\text{lam,c-peak}}\right]$, $\Xi_{\text{high}} = \left[\frac{1}{2}\xi_{\text{lam,c-peak}}, \frac{3}{4}\xi_{\text{lam,c-peak}}\right]$.

Bibliography

[1] Abdel-Gayed, R., and Bradley, D. Combustion regimes and the straining of turbulent premixed flames. *Combust. Flame 76* (1989), 213–218.

[2] Alexander, R. Diagonally implicit runge-kutta methods for stiff O.D.E.'s. *SIAM J. Numer. Anal. 14*, 6 (1977), 1006–1021.

[3] Almgren, A., Bell, J., Colella, P., Howell, L., and Welcome, M. A conservative adaptive projection method for the variable density incompressible Navier–Stokes equations. *J. Comput. Phys. 142* (1998), 1–46.

[4] Altantzis, C., Frouzakis, C., Tomboulides, A., Matalon, M., and Boulouchos, K. Hydrodynamic and thermodiffusive instability effects on the evolution of laminar planar lean premixed hydrogen flames. *J. Fluid Mech. 700* (2012), 329–361.

[5] Amato, A., Day, M., Cheng, R., Bell, J., and Lieuwen, T. Leading edge statistics of turbulent, lean, H_2/air flames. *Proc. Comb. Inst.* (2014), http://dx.doi.org/10.1016/j.proci.2014.05.143.

[6] Aro, C. J., and Rodrigue, G. H. Preconditioned time differencing for stiff ODEs in diurnal atmospheric kinetics. *Comput. Phys. Commun. 92*, 1 (1995), 27–53.

[7] Ashurst, W., Kerstein, A., Kerr, R., and Gibson, C. Alignment of vorticity and scalar gradient with strain rate in simulated Navier-Stokes turbulence. *Phys. Fluids 30* (1987), 2343–2353.

[8] Aspden, A., Bell, J., and Woosley, S. Distributed flames in type Ia supernovae. *Astrophys. J. 710* (2010), 1654–1663.

[9] Aspden, A., Day, M., and Bell, J. Lewis number effects in distributed flames. *Proc. Comb. Inst. 33* (2011), 1473–1480.

[10] Aspden, A., Day, M., and Bell, J. Turbulence-flame interactions in lean premixed hydrogen: transition to the distributed burning regime. *J. Fluid Mech. 680* (2011), 287–320.

[11] Aspden, A., Day, M., and Bell, J. Turbulence-chemistry interaction in lean premixed hydrogen combustion. *Proc. Comb. Inst. 35*, 2 (2015), 1321–1329.

[12] Bagrinovskii, K., and Godunov, S. Difference schemes for multidimensional problems (in Russian). *Dokl. Akad. Nauk. USSR 115* (1957), 431–433.

[13] Balarac, G., Pitsch, H., and Raman, V. Modeling of the subfilter scalar dissipation rate using the concept of optimal estimators. *Phys. Fluids 20* (2008), 091701.

[14] Barlow, R., Frank, J., Karpetis, A., and Chen, J.-Y. Piloted methane/air jet flames: Transport effects and aspects of scalar structure. *Combust. Flame 143* (2005), 433–449.

[15] Bhagatwala, A., Chen, J. H., and Lu, T. Direct numerical simulations of HCCI/SACI with ethanol. *Combust. Flame 161* (2014), 1826–1841.

[16] Bisetti, F. Integration of large chemical kinetic mechanisms via exponential methods with Krylov approximations to Jacobian matrix functions. *Combust. Theory Model. 16*, 3 (2012), 387–418.

[17] Bisetti, F., Blanquart, G., Mueller, M., and Pitsch, H. On the formation and early evolution of soot in turbulent nonpremixed flames. *Combust. Flame 159* (2012), 317–335.

[18] Blanquart, G. CaltechMech v2.1. Available at http://theforce.caltech.edu/resources/.

[19] Blanquart, G., Pepiot-Desjardins, P., and Pitsch, H. Chemical mechanism for high temperature combustion of engine relevant fuels with emphasis on soot precursors. *Combust. Flame 156*, 3 (Mar. 2009), 588–607.

[20] Borghi, R. *Recent Advances in the Aerospace Science*. Plenum, New York, 1985, ch. On the structure and morphology of turbulent premixed flames, pp. 117–138.

[21] Bradley, D., Lau, A., and Lawes, M. Flame stretch rate as a determinant of turbulent burning velocity. *Phil. Trans. R. Soc. Lond. 338* (1992), 359–387.

[22] Bradley, D., Lawes, M., Liu, K., and Mansour, M. Measurements and correlations of turbulent burning velocities over wide ranges of fuels and elevated pressures. *Proc. Comb. Inst. 34* (2013), 1516–1526.

[23] Brenan, K. E., and Campbell, S. L. A Description of DASSL: a differential/algebraic equation solver. In *Scientific Computing*. North-Holland, Amsterdam, The Netherlands, 1983, pp. 65–68.

[24] Brenblatt, G., Zel'dovich, Y., and Istratov, A. On diffusional thermal stability of laminar flame. *Prikl. Mekh. Tekh. Fiz. 2* (1962), 21–26.

[25] Brown, P. N., Byrne, G. D., and Hindmarsh, A. C. VODE: A variable-coefficient ODE solver. *SIAM J. Sci. Stat. Comput. 10*, 5 (1989), 1038–1051.

[26] Brown, P. N., Shumaker, D. E., and Woodward, C. S. Fully implicit solution of large-scale non–equilibrium radiation diffusion with high order time integration. *J. Comput. Phys. 204*, 2 (Apr. 2005), 760–783.

[27] Candler, G., and Olynick, D. Hypersonic flow simulations using a diagonal implicit method. In *Computing Methods in Applied Sciences and Engineering*, R. Glowinski, Ed. Nova Science Publishers, 1991, pp. 29–47.

[28] Candler, G., Subbareddy, P., and Nompelis, I. Decoupled implicit method for aerothermodynamics and reacting flows. *AIAA J. 51*, 5 (2013), 1245–1254.

[29] Cao, R., and Pope, S. The influence of chemical mechanisms on PDF calculations of nonpremixed piloted jet flames. *Combust. Flame 143* (2005), 450–470.

[30] Carbone, F., Smolke, J., Fincham, A., and Egolfopoulos, F. Characteristics of piloted premixed turbulent-jet flames of methane and C_6-C_8 hydrocarbons. In *Spring Technical Meeting of the WSSCI* (Pasadena, USA, March 2014).

[31] Carroll, P., and Blanquart, G. A proposed modification to Lundgren's physical space velocity forcing method for isotropic turbulence. *Phys. Fluids 25* (2013), 105114.

[32] Carroll, P., and Blanquart, G. The effect of velocity field forcing techniques on the Karman-Howarth equation. *J. Turbul. 15* (2014), 429–448.

[33] Chakraborty, N., and Cant, R. Unsteady effects of strain rate and curvature on turbulent premixed flames in an inflow-outflow configuration. *Combust. Flame 137* (2004), 129–147.

[34] Chakraborty, N., Hawkes, E., Chen, J., and Cant, R. The effects of strain rate and curvature on surface density function in turbulent premixed methane-air and hydrogen-air flames: a comparative study. *Combust. Flame 154* (2008), 259–280.

[35] Chen, J., and Im, H. Correlation of flame speed with stretch in turbulent premixed methane/air flames. *Twenty-Seventh Symposium (International) on Combustion 1-2* (1998), 819–826.

[36] Chen, J., and Im, H. Stretch effects on the burning velocity of turbulent premixed hydrogen/air flames. *Proc. Comb. Inst. 28* (2000), 211–218.

[37] Chen, J. H. Petascale direct numerical simulation of turbulent combustion - fundamental insights towards predictive models. *Proc. Comb. Inst. 33*, 1 (2011), 99–123.

[38] Chen, Y., and Bilger, R. Experimental investigation of three-dimensional flame-front structure in premixed turbulent combustion - II. Lean hydrogen/air Bunsen flames. *Combust. Flame 138* (2004), 155–174.

[39] Chen, Z., Burke, M. P., and Ju, Y. Effects of Lewis number and ignition energy on the determination of laminar flame speed using propagating spherical flames. *Proc. Comb. Inst. 32*, 1 (2009), 1253–1260.

[40] Cheng, R., Littlejohn, D., Nazeer, W., and Smith, K. Laboratory studies of the flow field characteristics of low-swirl injectors for adaptation to fuel-flexible turbines. *J. Eng. Gas Turb. Power 130* (2008), 021501.

[41] Cheng, R., Littlejohn, D., Strakey, P., and Sidwell, T. Laboratory investigations of low-swirl injectors with H_2 and CH_4 at gas turbine conditions. *Proc. Comb. Inst. 32* (2009), 3001–3009.

[42] Clavin, P., and Joulin, G. High-frequency response of premixed ames to weak stretch and curvature: a variable-density analysis. *Combust. Theory Modelling 1* (1997), 429–446.

[43] Clavin, P., and Williams, F. Effects of molecular diffusion and of thermal expansion on the structure and dynamics of premixed flames in turbulent flows of large scale and low intensity. *J. Fluid Mech. 116* (1982), 251–282.

[44] Colket, M., Edwards, T., Williams, S., Cernansky, N., Miller, D., Egolfopoulos, F., Lindstedt, P., Seshadri, K., Dryer, F., Law, C., Friend, D., Lenhert, D., Pitsch, H., Sarofim, A., Smooke, M., and Tsang, W. "Development of an experimental database and kinetic models for surrogate jet fuels" in 45th AIAA Aerospace Sciences Meeting and Exhibit (Reno, Nevada) (Jan. 8-11 2007).

[45] Cook, A., and Riley, J. Subgrid-scale modeling for turbulent, reacting flows. *Combust. Flame 112* (1998), 593–606.

[46] Curran, H.J. Gaffuri, P., Pitz, W., and Westbrook, C. A comprehensive modeling study of *n*-heptane oxidation. *Combust. Flame 114* (1998), 149–177.

[47] Dagaut, P., and Cathonnet, M. The ignition, oxidation, and combustion of kerosene: A review of experimental and kinetic modeling. *Prog. Energy Combust. Sci. 32* (2006), 48–92.

[48] Damkhöler, G. Der einfluss der turbulenz auf die flammengeschwindigkeit. *Z. Elektrochem. 46* (1940), 601–652.

[49] D'Angelo, Y., and Larrouturou, B. Comparison and analysis of some numerical schemes for stiff complex chemistry problems. *Modélisation mathématique et analyse numérique 29*, 3 (1995), 259–301.

[50] Daniele, S., Mantzaras, J., Jansohn, P., Denisov, A., and Boulouchos, K. Flame front/turbulence interaction for syngas fuels in the thin reaction zones regime: turbulent and stretched laminar flame speeds at elevated pressures and temperatures. *J. Fluid Mech. 724* (2013), 36–68.

[51] Davis, S., and Law, C. Determination of and fuel structure effects on laminar flame speeds of C_1 to C_8 hydrocarbons. *Comb. Sci. Tech. 140* (1998), 427–449.

[52] Day, M., and Bell, J. Numerical simulation of laminar reacting flows with complex chemistry. *Combust. Theory Model. 4*, 4 (1999), 535–556.

[53] Day, M., Bell, J., Bremer, P.-T., Pascucci, V., Beckner, V., and Lijewski, M. Turbulence effects on cellular burning structures in lean premixed hydrogen flames. *Combust. Flame 156* (2009), 1035–1045.

[54] Dennis Jr, J. E., and Schnabel, R. B. *Numerical methods for unconstrained optimization and nonlinear equations*, vol. 16. SIAM, 1996.

[55] Desjardins, O., Blanquart, G., Balarac, G., and Pitsch, H. High order conservative finite difference scheme for variable density low Mach number turbulent flows. *J. Comput. Phys. 227*, 15 (2008), 7125–7159.

[56] Dworkin, S., Smooke, M., and Giovangigli, V. The impact of detailed multicomponent transport and thermal diffusion effects on soot formation in ethylene/air flames. *Proc. Comb. Inst. 32*, 1 (2009), 1165–1172.

[57] Eberhardt, S., and Imlay, S. Diagonal implicit scheme for computing flows with finite rate chemistry. *J. Thermophys. Heat Tr. 6*, 2 (1992), 208–216.

[58] Echekki, T., and Chen, J. Unsteady strain rate and curvature effects in turbulent premixed methane-air flames. *Combust. Flame 106* (1996), 184–202.

[59] Ern, A., and Giovangigli, V. Impact of multicomponent transport on planar and counterflow hydrogen/air and methane/air flames. *Comb. Sci. Tech. 149* (1999), 157–181.

[60] Eucken, A. The heat-carrying capabilities, the specific heat and the internal friction of gas. *Phys. Z. 14* (1913), 324–333.

[61] Falgout, R. D., and Yang, U. M. HYPRE: A library of high performance preconditioners. In *Computational Science—ICCS 2002*. Springer, 2002, pp. 632–641.

[62] Ferreira, J. *Flamelet modelling of stabilization in turbulent non-premixed combustion.* Dissertation, ETH Zürich, 1996.

[63] Fiorina, B., Vicquelin, R., Auzillon, P., Darabiha, N., Gicquel, O., and Veynante, D. A filtered tabulated chemistry model for LES of premixed combustion. *Combust. Flame 157*, 3 (2010), 465–475.

[64] Gicquel, L., Staffelbach, G., and Poinsot, T. Large Eddy Simulations of gaseous flames in gas turbine combustion chambers. *Prog. Energy Combust. Sci. 38*, 6 (2012), 782–817.

[65] Gicquel, O., Darabiha, N., and Thévenin, D. Laminar premixed hydrogen/air counterflow flame simulations using flame prolongation of ILDM with differential diffusion. *Proc. Comb. Inst. 28* (2000), 1901–1908.

[66] Gou, X., Sun, W., Chen, Z., and Ju, Y. A dynamic multi-timescale method for combustion modeling with detailed and reduced chemical kinetic mechanisms. *Combust. Flame 157*, 6 (2010), 1111–1121.

[67] Goyal, G., Paul, P., Mukunda, H., and Deshpande, S. Time dependent operator-split and unsplit schemes for one dimensional premixed flames. *Comb. Sci. Tech. 60*, 1-3 (1988), 167–189.

[68] Gruber, A., Sankaran, E. R., Hawkes, E. R., and Chen, J. Turbulent flame-wall interaction: a direct numerical simulation study. *J. Fluid Mech. 658* (2010), 5–32.

[69] Halter, F., Chauveau, C., and Gökalp, I. Characterization of the effects of hydrogen addition in premixed methane/air flames. *Int. J. Hydrogen Energy 32* (2007), 2585–2592.

[70] Hawkes, E., Chatakonda, O., Kolla, H., Kerstein, A., and Chen, J. A petascale direct numerical simulation study of the modelling of flame wrinkling for large-eddy simulations in intense turbulence. *Combust. Flame 159* (2012), 2690–2703.

[71] Hawkes, E., and Chen, J. Comparison of direct numerical simulation of lean premixed methane-air flames with strained laminar flame calculations. *Combust. Flame 144* (2006), 112–125.

[72] Hawkes, E., Sankaran, R., Sutherland, C., and Chen, J. Direct numerical simulation of turbulent combustion: fundamental insights towards predictive models. *J. Phys. Conf. Ser. 16* (2005), 65–79.

[73] Haworth, D., and Poinsot, T. Numerical simulations of Lewis number effects in turbulent premixed flames. *J. Fluid Mech. 244* (1992), 405–436.

[74] Herrmann, M., Blanquart, G., and Raman, V. Flux corrected finite volume scheme for preserving scalar boundedness in reacting large–eddy simulations. *AIAA Journal 44*, 12 (2006), 2879–2886.

[75] Hiremath, V., Lantz, S., Wang, H., and Pope, S. Large-scale parallel simulations of turbulent combustion using combined dimension reduction and tabulation of chemistry. *Proc. Comb. Inst. 34* (2013), 205–215.

[76] Hirschfelder, O., Curtiss, C., and Bird, R. *Molecular Theory of Gases and Liquids*. John Wiley and Sons, New York, 1954.

[77] Hong, Z., Davidson, D., and Hanson, R. An improved H-2/O-2 mechanism based on recent shock tube/laser absorption measurements. *Combust. Flame 158*, 4 (2011), 633–644.

[78] Hult, J., Gashi, S., Chakraborty, N., Klein, M., Jenkins, K., Cant, S., and Kaminski, C. Measurement of flame surface density for turbulent premixed flames using PLIF and DNS. *Proc. Comb. Inst. 31* (2007), 1319–1326.

[79] Ihme, M., and Pitsch, H. Prediction of extinction and reignition in nonpremixed turbulent flames using a flamelet/progress variable model. 1. A priori study and presumed PDF closure. *Combust. Flame 155*, 1-2 (Oct. 2008), 70–89.

[80] Ihme, M., and Pitsch, H. Prediction of extinction and reignition in nonpremixed turbulent flames using a flamelet/progress variable model. 2. A posteriori study with application to Sandia flames D and E. *Combust. Flame 155*, 1-2 (Oct. 2008), 90–107.

[81] Im, H., and Chen, J. Effects of flow transients on the burning velocity of laminar hydrogen/air premixed flames. *Proc. Comb. Inst. 28* (2000), 1833–1840.

[82] Im, H., and Chen, J. Preferential diffusion effects on the burning rate of interacting turbulent premixed hydrogen-air flames. *Combust. Flame 131* (2002), 246–258.

[83] Jay, L. Inexact simplified newton iterations for implicit runge-kutta methods. *SIAM J. Numer. Anal. 38*, 4 (2000), 1369–1388.

[84] Joulin, G. On the response of premixed flames to time-dependent stretch and curvature. *Combust. Sci. Technol. 97* (1994), 219–229.

[85] Ju, Y. Lower-upper scheme for chemically reacting flow with finite rate chemistry. *AIAA J. 33*, 8 (1995), 1418–1425.

[86] Ju, Y., Sun, W., Burke, M., Gou, X., and Chen, Z. Multi-timescale modeling of ignition and ame regimes of *n*-heptane-air mixtures near spark assisted homogeneous charge compression ignition conditions. *Proc. Comb. Inst. 33*, 1 (2011), 1245–1251.

[87] Kailasanathan, R. K. A., Book, E., Fang, T., and Roberts, W. Hydrocarbon species concentrations in nitrogen diluted ethylene-air laminar jet diffusion flames at elevated pressures. *Proc. Comb. Inst. 34*, 1 (2013), 1035–1043.

[88] Kailasanathan, R. K. A., Yelverton, T., Fang, T., and Roberts, W. Effect of diluents on soot precursor formation and temperature in ethylene laminar diffusion flames. *Combust. Flame 160*, 3 (2013), 656–670.

[89] Kanevsky, A., Carpenter, M., Gottlieb, D., and Hesthaven, J. Application of implicit-explicit high order Runge-Kutta methods to discontinuous-Galerkin schemes. *J. Comput. Phys. 225* (2007), 1753–1781.

[90] Kassam, A.-K., and Trefethen, L. N. Fourth-order time-stepping for stiff PDEs. *SIAM J. Sci. Comput. 26*, 4 (2005), 1214–1233.

[91] Kee, R., Warnatz, J., and Miller, J. A Fortran computer code package for the evaluation of gas-phase viscosities, conductivities, and diffusion coefficients. Tech. rep., Sandia National Laboratories, 1983.

[92] Kelly, A., Smallbone, A., Zhu, D., and Law, C. Laminar flame speeds of C_5 to C_8 *n*-alkanes at elevated pressures and temperatures. In *48th AIAA Aerospace Sciences Meeting* (Orlando, USA, January 2010).

[93] Kennedy, C. A., and Carpenter, M. H. Additive Runge-Kutta schemes for convection-diffusion-reaction equations. *Appl. Numer. Math. 44*, 1–2 (2003), 139–181.

[94] Kitagawa, T., Nakahara, T., Maruyama, K., Kado, K., Hayakawa, A., and Kobayashi, S. Turbulent burning velocity of hydrogen-air premixed propagating flames at elevated pressures. *Int. J. Hydrogen Energy 33* (2008), 5842–5849.

[95] Knio, O. M., Najm, H. N., and Wyckoff, P. S. A semi-implicit numerical scheme for reacting flow: II. Stiff, operator-split formulation. *J. Comput. Phys. 154*, 2 (1999), 428–467.

[96] Knudsen, E., Kolla, H., Hawkes, E., and Pitsch, H. LES of a premixed jet flame DNS using a strained flamelet model. *Combust. Flame 160* (2013), 29112927.

[97] Knudsen, E., and Pitsch, H. A general flamelet transformation useful for distinguishing between premixed and non-premixed modes of combustion. *Combust. Flame 156* (2009), 678–696.

[98] Knudsen, E., and Pitsch, H. Capabilities and limitations of multi-regime flamelet combustion models. *Combust. Flame 159* (2012), 242–264.

[99] Kobayashi, H., Kawabata, Y., and Maruta, K. Experimental study on general correlation of turbulent burning velocity at high pressure. *Proc. Comb. Inst. 27* (1998), 941–948.

[100] Kobayashi, H., Otawara, Y., Wang, J., Matsuno, F., Ogami, Y., Okuyama, M., Kudo, T., and Kadowaki, S. Turbulent premixed flame characteristics of a $CO/H_2/O_2$ mixture highly diluted with CO_2 in a high-pressure environment. *Proc. Comb. Inst. 34* (2013), 1437–1445.

[101] Lam, S. Singular perturbation for stiff equations using numerical methods. In *Recent Advances in the Aerospace Sciences*. Springer, 1985, pp. 3–19.

[102] Lam, S., and Coussis, D. Understanding complex chemical kinetics with computational singular perturbation. In *Symposium (International) on Combustion* (1989), vol. 22, Elsevier, pp. 931–941.

[103] Li, J., Zhao, Z., Kazakov, A., and Dryer, F. L. An updated comprehensive kinetic model of hydrogen combustion. *Int. J. Chem. Kinet. 36*, 10 (2004), 566–575.

[104] Lignell, D. O., Chen, J. H., and Smith, P. J. Three-dimensional direct numerical simulation of soot formation and transport in a temporally evolving nonpremixed ethylene jet flame. *Combust. Flame 155*, 1–2 (2008), 316–333.

[105] Lignell, D. O., Chen, J. H., Smith, P. J., Lu, T., and Law, C. K. The effect of flame structure on soot formation and transport in turbulent nonpremixed flames using direct numerical simulation. *Combust. Flame 151*, 1–2 (2007), 2–28.

[106] Lu, T., and Law, C. K. A directed relation graph method for mechanism reduction. *Proc. Comb. Inst. 30*, 1 (2005), 1333–1341.

[107] Lu, T., and Law, C. K. A criterion based on computational singular perturbation for the identification of quasi steady state species: A reduced mechanism for methane oxidation with NO chemistry. *Combust. Flame 154*, 4 (2008), 761–774.

[108] Lu, T., and Law, C. K. Strategies for mechanism reduction for large hydrocarbons: *n*-heptane. *Combust. Flame 154*, 1–2 (2008), 153–163.

[109] Lu, T., and Law, C. K. Toward accommodating realistic fuel chemistry in large-scale computations. *Prog. Energy Combust. Sci. 35*, 2 (2009), 192–215.

[110] Lu, T., Law, C. K., Yoo, C. S., and Chen, J. H. Dynamic stiffness removal for direct numerical simulations. *Combust. Flame 156*, 8 (2009), 1542–1551.

[111] Lundgren, T. "Linear forced isotropic turbulence" in Annual Research Briefs (Center for Turbulence Research, Stanford) (2003) 461-473.

[112] Maas, U., and Pope, S. Simplifying chemical kinetics: Intrinsic low-dimensional manifolds in composition space. *Combust. Flame 88*, 3–4 (1992), 239–264.

[113] Markstein, G. Cell structure of propane flames burning in tubes. *J. Chem. Phys. 17* (1949), 428.

[114] Matalon, M., and Matkowsky, B. Flames as gasdynamic discontinuities. *J. Fluid Mech. 124* (1982), 239–259.

[115] Mathur, S., Tondon, P., and Saxena, S. Thermal conductivity of binary, ternary and quaternary mixtures of rare gases. *Mol. Phys. 12*, 6 (1967), 569–579.

[116] McNenly, M. J., Whitesides, R. A., and Flowers, D. L. Faster solvers for large kinetic mechanisms using adaptive preconditioners. *Proc. Comb. Inst. 35*, 1 (2015), 581–587.

[117] Mehl, M., Pitz, W. J., Westbrook, C. K., and Curran, H. J. Kinetic modeling of gasoline surrogate components and mixtures under engine conditions . *Proc. Comb. Inst. 33* (2011), 193 – 200.

[118] Menon, S., Boettcher, P., and Blanquart, G. Enthalpy based approach to capture heat transfer effects in premixed combustion. *Combust. Flame 160* (2002), 1242–1253.

[119] Moreau, A., Teytaud, O., and Bertoglio, J. Optimal estimation for large-eddy simulation of turbulence and application to the analysis of subgrid models. *Phys. Fluids 18* (2006), 105101.

[120] Mueller, C., Driscoll, J., Sutkus, D., Roberts, W., Drake, M., and Smooke, M. Effect of unsteady stretch rate on OH chemistry during a flame-vortex interaction: to assess flamelet models. *Combust. Flame 100* (1995), 323–331.

[121] Mueller, M. A., Kim, T. J., Yetter, R. A., and Dryer, F. L. Flow reactor studies and kinetic modeling of the H_2/O_2 reaction. *Int. J. Chem. Kinet. 31*, 2 (1999), 113–125.

[122] Mueller, M. E., and Pitsch, H. LES model for sooting turbulent nonpremixed flames. *Combust. Flame 159*, 6 (June 2012), 2166–2180.

[123] Mukhopadhyay, S. *Modeling turbulent combustion using filtered flamelets.* Dissertation, Technische Universiteit Eindhoven, 2014.

[124] Muller, J.-M. *Elementary functions: algorithms and implementation*, 2 ed. Birkhäuser, 2005.

[125] Muppala, S., Papalexandris, M., Manickam, B., Aluri, N, K., and Dinkelacker, F. Numerical simulation of lean premixed turbulent hydrogen/hydrocarbon flames at elevated pressures. In *10th International Workshop on Premixed Turbulent Flames* (Mainz, Germany, August 2006).

[126] Mydlarski, L., and Warhaft, Z. On the onset of high-Reynolds-number grid-generated wind tunnel turbulence. *J. Fluid Mech. 320* (1996), 331–368.

[127] Najm, H., and Wyckoff, P. Premixed flame response to unsteady strain rate and curvature. *Combust. Flame 110* (1997), 92–112.

[128] Najm, H. N., Wyckoff, P. S., and Knio, O. M. A semi-implicit numerical scheme for reacting flow: I. Stiff chemistry. *J. Comput. Phys. 143*, 2 (1998), 381–402.

[129] Niemeyer, K., and Sung, C. Mechanism reduction for multicomponent surrogates: A case study using toluene reference fuels. *Combust. Flame 161*, 11 (2014), 2752–2764.

[130] Ober, C. C., and Shadid, J. N. Studies on the accuracy of time-integration methods for the radiation-diffusion equations. *J. Comput. Phys. 195*, 2 (2004), 743–772.

[131] Park, C., and Yoon, S. Fully coupled implicit method for thermochemical nonequilibrium air at suborbital flight speeds. *AIAA J. 28*, 1 (1991), 31–39.

[132] Pearson, K. Notes on regression and inheritance in the case of two parents. *P. R. Soc. London 58* (1895), 240–242.

[133] Pelce, P., and Clavin, P. Influence of hydrodynamics and diffusion upon the stability limits of laminar premixed flames. *J. Fluid Mech. 124* (1982), 219–237.

[134] Pepiot-Desjardins, P., and Pitsch, H. An efficient error-propagation-based reduction method for large chemical kinetic mechanisms. *Combust. Flame 154*, 1 (2008), 67–81.

[135] Perini, F., Galligani, E., and Reitz, R. D. A study of direct and Krylov iterative sparse solver techniques to approach linear scaling of the integration of chemical kinetics with detailed combustion mechanisms. *Combust. Flame 161*, 5, 1180–1195.

[136] Peters, N. Local quenching due to flame stretch and non-premixed turbulent combustion. *Combust. Sci. Technol 30*, 1 (1983), 1–17.

[137] Peters, N. Laminar flamelet concepts in turbulent combustion. *Twenty-First Symposium (International) on Combustion* (1986), 1231–1250.

[138] Peters, N. *Numerical Approaches to Combustion Modelling, Progress in Astronautics and Aeronautics, Vol. 135.* 1991, ch. Length scales in laminar and turbulent flames, pp. 155–182.

[139] Peters, N. Reducing mechanisms. In *Reduced kinetic mechanisms and asymptotic approximations for methane-air flames*, M. D. Smooke, Ed., vol. 384 of *Lecture Notes in Physics.* Springer Berlin Heidelberg, 1991, pp. 48–67.

[140] Peters, N. Fifteen lectures on laminar and turbulent combustion. Ercoftac Summer School, September 1992.

[141] Peters, N. The turbulent burning velocity for large-scale and small-scale turbulence. *J. Fluid Mech. 384* (1999), 107–132.

[142] Peters, N. *Turbulent Combustion.* Cambridge University Press, Cambridge, 2000.

[143] Petzold, L. R. A Description of DASSL: a differential/algebraic system solver. *Sandia National Laboratories Report, SAND282-8637* (1982).

[144] Pierce, C., and Moin, P. Progress-variable approach for large-eddy simulation of non-premixed turbulent combustion. *J. Fluid Mech. 504* (2004), 73–97.

[145] Pierce, C. D. *Progress-variable approach for large-eddy simulation of turbulent combustion.* PhD thesis, Stanford University, 2001.

[146] Pitsch, H. Flamemaster: A C++ computer program for 0D combustion and 1D laminar flame calculations. available at http://www.itv.rwth-aachen.de/downloads/flamemaster/. 1998.

[147] Pitsch, H. A consistent level set formulation for large-eddy simulation of premixed turbulent combustion. *Combust. Flame. 143* (2005), 587–598.

[148] Pitsch, H. Large-eddy simulation of turbulent combustion. *Ann. Rev. Fluid Mech. 38* (2006), 453–482.

[149] Pitsch, H., and Steiner, H. Large-eddy simulation of a turbulent piloted methane/air diffusion flame (sandia flame D). *Phys. Fluids 12* (2000), 2541–2554.

[150] Poinsot, T., Veynante, D., and Candel, S. Diagrams of premixed turbulent combustion based on direct simulation. *Twenty-Third Symposium (International) on Combustion* (1990), 613–619.

[151] Poludnenko, A., and Oran, E. The interaction of high-speed turbulence with flames: Global properties and internal flame structure. *Combust. Flame 157* (2010), 995–1011.

[152] Pope, S. *Turbulent Flows*. Cambridge University Press, Cambridge, 2000.

[153] Quinlan, J., McDaniel, J., Drozda, T., Lacaze, G., and Oefelein, J. A priori analysis of flamelet-based modeling for a dual-mode scramjet combustor. *50th AIAA/ASME/SAE/ASEE Joint Propulsion Conference 2014* (2014), 2879–2886.

[154] Richardson, L. F. The approximate arithmetical solution by finite differences of physical problems involving differential equations, with an application to the stresses in a masonry dam. *Philos. Trans. R. Soc. Lond. A 210* (1911), 307–357.

[155] Robertson, H. The solution of a set of reaction rate equations. *Numerical analysis: an introduction* (1966), 178–182.

[156] Ropp, D. L., Shadid, J. N., and Ober, C. C. Studies of the accuracy of time integration methods for reaction-diffusion equations. *J. Comput. Phys. 194*, 2 (2004), 544–574.

[157] Rosales, C., and Meneveau, C. Linear forcing in numerical simulations of isotropic turbulence: Physical space implementations and convergence properties. *Phys. Fluids 17* (2005), 095106.

[158] Sandu, A., Verwer, J., Blom, J., Spee, E., Carmichael, G., and Potra, F. Benchmarking stiff ode solvers for atmospheric chemistry problems II: Rosenbrock solvers. *Atmos. Environ. 31*, 20 (1997), 3459–3472.

[159] Sandu, A., Verwer, J., Loon, M. V., Carmichael, G., Potra, F., Dabdub, D., and Seinfeld, J. Benchmarking stiff ode solvers for atmospheric chemistry problems-I. implicit vs explicit. *Atmos. Environ. 31*, 19 (1997), 3151–3166. EUMAC: European Modelling of Atmospheric Constituents.

[160] Sankaran, R., Hawkes, E., Chen, J., Lu, T., and Law, C. Structure of a spatially developing turbulent lean methane-air bunsen flame. *Proc. Comb. Inst. 31* (2007), 1291–1298.

[161] Saylor, R. D., and Ford, G. D. On the comparison of numerical methods for the integration of kinetic equations in atmospheric chemistry and transport models. *Atmos. Environ. 29*, 19 (1995), 2585–2593.

[162] Shunn, L., Ham, F., and Moin, P. Verification of variable-density flow solvers using manufactured solutions. *J. Comput. Phys. 231*, 9 (2012), 3801–3827.

[163] Smith, G. P., Golden, D. M., Frenklach, M., Moriarty, N. W., Eiteneer, B., Goldenberg, M., Bowman, C. T., Hanson, R. K., Song, S., Gardiner, W. C., Lissianski, V. V., and Qin, Z. GRI-Mech 3.0. Available at http://www.me.berkeley.edu/gri_mech/.

[164] Smooke, M., Mitchell, R., and Keyes, D. Numerical-solution of 2-dimensional axisymmetric laminar diffusion flames. *Combust. Sci. Technol 67*, 4–6 (1989), 85–122.

[165] Staffelbach, G., Gicquel, L., Boudier, G., and Poinsot, T. Large Eddy Simulations of self excited azimuthal modes in annular combustors. *Proc. Comb. Inst. 32* (2009), 2909–2916.

[166] Strang, G. On the construction and comparison of difference schemes. *SIAM J. Numer. Anal. 5*, 3 (1968), 506–517.

[167] Swanson, R., Turkel, E., and Rossow, C.-C. Convergence acceleration of Runge-Kutta schemes for solving the Navier-Stokes equations. *J. Comput. Phys. 224* (2007), 365–388.

[168] Székely, G., Rizzo, M., and Bakiroz, N. Measuring and testing dependence by correlation of distances. *Ann. Stat. 35* (2007), 2769–2794.

[169] Tranquilli, P., and Sandu, A. Rosenbrock-Krylov methods for large systems of differential equations. *SIAM J. Sci. Comput. 36*, 3 (2014), A1313–A1338.

[170] van Lipzig, J., Nilsson, E., de Goey, L., and Konnov, A. Laminar burning velocities of *n*-heptane, iso-octane, ethanol and their binary and tertiary mixtures. *Fuel 90* (2011), 2773–2781.

[171] van Oijen, J., Lammers, F., and de Goey, L. Modeling of complex premixed burner systems by using flamelet-generated manifolds. *Combust. Flame 127* (2001), 2124–2134.

[172] Venkateswaran, P., Marshall, A., Shin, D., and Noble, D. Measurements and analysis of turbulent consumption speeds of H_2/CO mixtures. *Combust. Flame 158* (2011), 1602–1614.

[173] Verma, S., Xuan, Y., and Blanquart, G. An improved bounded semi-Lagrangian scheme for the turbulent transport of passive scalars. *J. Comput. Phys. 272*, 0 (2014), 1 – 22.

[174] Viswanathan, S., Wang, H., and Pope, S. Numerical implementation of mixing and molecular transport in LES/PDF studies of turbulent reacting flows. *J. Comp. Phys. 230* (2011), 6916–6957.

[175] Wang, H., and Frenklach, M. A detailed kinetic modeling study of aromatics formation in laminar premixed acetylene and ethylene flames. *Combust. Flame 110*, 1–2 (1997), 173–221.

[176] Wang, W., Luo, K., and Fan, J. Direct numerical simulation and conditional statistics of hydrogen/air turbulent premixed flames. *Energ. Fuel 27* (2013), 549–560.

[177] Warnatz, J. *Numerical methods in laminar flame propagation.* Friedr. Vieweg and Sohn Verlagsgesellschaft mbH, Braunschweig, ch. Influence of transport models and boundary conditions on flame structure.

[178] Wilcox, D. *Turbulence Modeling for CFD.* DCW Industries, Anaheim, 2000.

[179] Wilke, C. A viscosity equation for gas mixtures. *J. Chem. Phys. 18*, 4 (1950), 517–519.

[180] Williams, F. A. *Combustion Theory 2nd Edition.* Addison-Wesley, 1985.

[181] Xin, Y., and Law, C. K. A mechanistic evaluation of Soret diffusion in heptane/air ames. *Combust. Flame 159* (2012), 2345–2351.

[182] Xuan, Y., and Blanquart, G. Numerical modeling of sooting tendencies in a laminar co-flow diffusion flame. *Combust. Flame 160*, 9 (2013), 1657–1666.

[183] Xuan, Y., and Blanquart, G. Effects of aromatic chemistry-turbulence interactions on soot formation in a turbulent non-premixed flame. *Proc. Comb. Inst. 35*, 2 (2015), 1911–1919.

[184] Xuan, Y., Blanquart, G., and Mueller, M. E. Modeling curvature effects in diffusion flames using a laminar flamelet model. *Combust. Flame 161*, 5 (2014), 1294–1309.

[185] Yeung, P., Girimaji, S., and Pope, S. Straining and scalar dissipation on material-surfaces in turbulence - implications for flamelets. *Combust. Flame 79* (1990), 340–365.

[186] Yoo, C. S., Lu, T., Chen, J. H., and Law, C. K. Direct numerical simulations of ignition of a lean *n*-heptane/air mixture with temperature inhomogeneities at constant volume: Parametric study. *Combust. Flame 158*, 9 (2011), 1727–1741.

[187] Yoo, C. S., Luo, Z., Kim, H., and Chen, J. H. A DNS study of ignition characteristics of a lean *iso*-octane/air mixture under HCCI and SACI conditions. *Proc. Comb. Inst. 34* (2013), 2985–2993.

[188] Yoo, C. S., Richardson, E., Sankaran, R., and Chen, J. H. A DNS study on the stabilization mechanism of a turbulent lifted ethylene jet flame in highly-heated coflow. *Proc. Comb. Inst. 33*, 1 (2011), 1619–1627.

[189] Yoshida, H. Construction of higher order symplectic integrators. *Phys. Lett. A 150*, 5 (1990), 262–268.

[190] Yu, R., Yu, J., and Bai, X.-S. An improved high-order scheme for DNS of low Mach number turbulent reacting flows based on stiff chemistry solver. *J. Comput. Phys. 231*, 16 (2012), 5504–5521.

[191] Zhong, X. Additive semi-implicit Runge–Kutta methods for computing high-speed nonequilibrium reactive flows. *J. Comput. Phys. 128*, 1 (1996), 19–31.